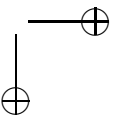
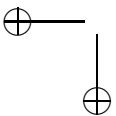
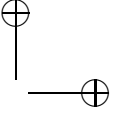
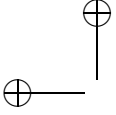
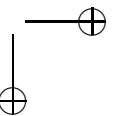
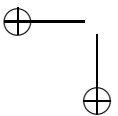
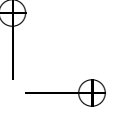
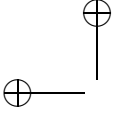


**Flow Characteristics**  
**in**  
**Lean Direct Injection Combustors**





**Flow Characteristics**  
**in**  
**Lean Direct Injection Combustors**

Proefschrift

ter verkrijging van de graad van doctor  
aan de Technische Universiteit Delft,  
op gezag van de Rector Magnificus prof. ir. K.C.A.M. Luyben,  
voorzitter van het College voor Promoties,  
in het openbaar te verdedigen op maandag 15 oktober 2012 om 12:30 uur  
door

**Dipanjay DEWANJI**

Master of Engineering in Space Engineering and Rocketry  
Birla Institute of Technology, India  
geboren te Calcutta, India.

Dit proefschrift is goedgekeurd door de promotor:  
Prof.ir. J.P. van Buijtenen

Samenstelling promotiecommissie:

Rector Magnificus	voorzitter
Prof.ir. J.P. van Buijtenen	Technische Universiteit Delft, promotor
Dr. A.G. Rao	Technische Universiteit Delft, copromotor
Prof.dr. D.J.E.M. Roekaerts	Technische Universiteit Delft
Prof.dr.ir. H. Bijl	Technische Universiteit Delft
Prof.dr.ir. T.H. van der Meer	University of Twente
Prof.dr. C.O. Paschereit	Technische Universität Berlin
Dr.ir. M.J.B.M. Pourquie	Technische Universiteit Delft
Prof.dr.ir. B.J. Boersma	Technische Universiteit Delft, reservelid

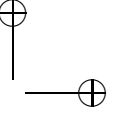
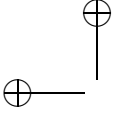
keywords: lean direct injection, spray, combustion, turbulence, low  $\text{NO}_x$ , aero engines, gas turbine, two-phase flow, drop breakup, turbulent dispersion, Discrete Phase Model.

ISBN 978-94-6191-467-5

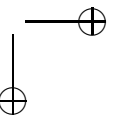
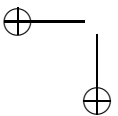
Copyright © 2012 by Dipanjay Dewanji

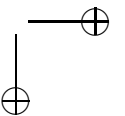
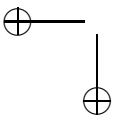
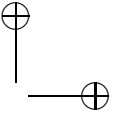
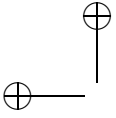
All rights reserved. No part of the material protected by this copyright notice may be reproduced or utilized in any form or by any means, electronic or mechanical, including photocopying, recording, or by any information storage and retrieval system, without written permission from the author.

Printed in the Netherlands.



*To,  
my mother,  
my brother,  
Pia, and  
in loving memory of my father, Milan Dewanji (1946-2012).*





## Summary

### Flow Characteristics in Lean Direct Injection Combustors

Aero engine emissions are becoming a global environmental concern as air traffic continues to rise. As a consequence, governing organizations for pollution controls continue to tighten existing emission certification standards and apply new policies to mitigate pollutant emissions from the future-generation of aero-propulsion systems. Current international regulations for aviation emissions only cover ground level emissions of hydrocarbons, carbon monoxide, and oxides of nitrogen ( $\text{NO}_x$ ) based on landing and take-off cycles. To be able to restrict global emissions, it is expected that future environmental laws will regulate exhaust products at different altitudes in the atmosphere. Therefore, advanced combustion methods will be required to overcome the challenges posed by impending strict emission standards while satisfying mission objectives.

Lean direct injection (LDI) concept is developed as an ultra-low  $\text{NO}_x$  combustion scheme for future aviation gas turbines. The LDI concept is defined as one in which the fuel and air are directly injected into the reaction zone without having an external premixing. All the combustion air enters the front end of the combustor and there is no dilution zone. The architecture of the combustor makes itself very compact, leading to less liner cooling and longer liner life. Furthermore, this combustion technique is not limited to any specific fuel and alternate fuels such as biofuels and gaseous hydrogen can be used for combustion.

The LDI strategy facilitates rapid, stable and uniform combustion under lean operation, resulting in lower peak temperatures and flow residence time, which in turn reduce thermal  $\text{NO}_x$ . A rapid fuel evaporation process and fuel-air mixing also eliminate local hot spots, thereby producing a uniform temperature distribution within the combustion chamber. Nevertheless, direct fuel injection process is more susceptible to non-uniform combustion due to greater chances of inadequate mixing prior to chemical reactions. Therefore, low- $\text{NO}_x$  performance is affected in an LDI combustor if the fuel and air are not perfectly mixed before combustion.

To enhance the fuel atomization quality and expedite the mixing of the resulting fine fuel drops with air, a highly swirling air stream is admitted into LDI combustor. In addition to the highly swirling flow, the mixing rate is further augmented by breaking

a few large injectors into several small air swirler-fuel injector modules, thus increasing the number and decreasing the size of the air jets. This direct injection concept is referred to as the Multi-Point Lean Direct Injection (MPLDI).

This thesis presents a numerical analysis of the flow field in a single-element and a MPLDI combustors. Numerical investigations include non-reacting cold flow and reacting spray simulations for the two configurations. The study of the single-element LDI provides an insight into the aerodynamic characteristics of the swirling flow and spray-turbulence interactions inside the combustion chamber. The simulations of the MPLDI illustrate a strong influence of the complex array of the swirler-injector modules on the flow field.

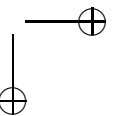
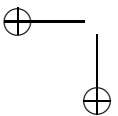
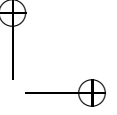
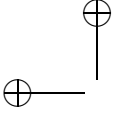
The non-reacting cold flow simulation for the single-element LDI is carried out using the Unsteady Reynolds-averaged Navier Stokes (URANS) code with the realizable  $k - \varepsilon$  and the Reynolds stress turbulence models. The results exhibit a few essential features of LDI, such as the complex flow structures inside the swirler vanes, a single large recirculation zone originating from the injector tip, and reverse flow regions at the corners of the chamber wall and on the wall of the diverging venturi, with good accuracy. The reacting spray simulations involve the modeling of several spray sub-processes and the combustion of the fuel and air. The Euler-Lagrange approach is implemented to resolve the two-phase flow. The gas-phase is treated as a continuum and it is calculated by solving the Navier-Stokes equations. The liquid-phase is resolved by tracking the liquid particles through the calculated flow field. The results show that the high axial momentum induced by combustion and momentum transfer between the liquid and gas phases decrease the length and volume of the central recirculation zone. However, the heat release due to combustion results in a strong recirculation region. The spray mean diameter profiles indicate the influence of the swirling shear layer on the spray drop distribution. The drop velocity plots illustrate the interactions between the gas-phase and the liquid drops of various size groups and reflect a strong momentum exchange between the two phases. The computational results for the single-element LDI are compared and validated with the available measurement data.

The URANS and large eddy simulation (LES) methodologies are applied separately to characterize the non-reacting flow field of the MPLDI. Each of the nine swirlers produces a compact recirculation zone. The magnitude of the velocity components close to chamber inlet and the length and volume of the recirculation zones predicted by the LES scheme differ significantly from that of the URANS. Farther downstream, the results using both the methods display identical flow structures with almost the same velocity magnitude. The LES results illustrate the dynamic behavior of large turbulent structures such as the precessing vortex cores (PVC) and vortex breakdown bubbles (VBB), indicating a large degree of unsteadiness in the flow field. The numerical predictions for the mean velocity field and the flow structures show good agreement with the experimental data available in the literature.

The computational results of the combustng spray in the MPLDI show that by increasing the swirl velocity, a large number of fine liquid drops are produced, thereby enhancing fuel atomization and fuel-air mixing. The drop mean diameters and drop size distribution are uniform along both the axial and radial directions with increasing swirl velocities. The complex geometry of the MPLDI also plays an important role

in the drop distribution process. The rotating motion of the vortex structures in the vicinity of the injectors enhances the drop dispersion into the gas, thereby expediting drop vaporization and improving the mixture quality. The high fluid shear and rapid mixing significantly influence the instantaneous temperature profiles. The peak combustion temperature is reduced with increasing fluid shear, which reduces thermal  $\text{NO}_x$ . The unified swirling flow downstream of the reaction zone assists the higher temperature zones to rapidly spread out and mix with the lower temperature zones. The simulations demonstrate that the mixture with a low equivalence ratio and high velocity gradients produces a uniformly low temperature distribution in almost the entire volume of the MPLDI combustion chamber. Short flames are noticed from the individual injectors, which reduce the residence times in the flames, resulting in low thermal  $\text{NO}_x$  formation.

Overall, the numerical results are able to explain the underlying features of the LDI combustion technique, which primarily influence its  $\text{NO}_x$  reduction capabilities. The results bring to a conclusion that the multi-point injection system with the LDI concept has the potential to reduce  $\text{NO}_x$  much more than the conventional combustion system used in aviation gas turbines.



# Samenvatting

## Stromingskarakteristieken in Branders met Brandstofarme, Directe Inspuiting

De uitstoot van vliegtuigmotoren wordt een mondiale milieukwestie met de aanhoudende toename van het vliegverkeer. Als gevolg hiervan worden bestaande standaarden in de milieuwetgeving voor uitstootcertificering steeds krappere en wordt nieuw beleid toegepast om de uitstoot van de toekomstige generaties vliegtuigvoorstuwingsystemen te verminderen. De huidige internationale regels voor de uitstoot in de luchtvaart beslaan slechts de uitstoot van koolwaterstoffen, koolstofmonoxide en stikstofoxiden ( $\text{NO}_x$ ) aan de grond, gebaseerd op de cycli van landen en opstijgen. Om mondiale uitstoot te kunnen beperken, wordt verwacht dat milieuwetten in de toekomst de uitlaatproducten ook op verschillende hoogten in de atmosfeer zullen reguleren. Daarom zullen geavanceerde verbrandingsmethoden nodig zijn om de uitdagingen, opgelegd door de dreigende strenge emissiecriteria, het hoofd te kunnen bieden en tegelijk aan de doelstellingen van de missie te voldoen.

Het concept van brandstofarme, directe inspuiting (LDI) is ontwikkeld als een verbrandingsmethode voor toekomstige vliegtuiggasturbines met uiterst lage uitstoot van  $\text{NO}_x$ . LDI wordt gedefinieerd als een concept waarbij de brandstof en lucht direct in de reactiezone worden ingespoten zonder dat externe voormenging plaatsvindt. Alle lucht voor de verbranding komt binnen via de voorkant van de brander en er is geen verdunningszone. De architectuur van de brander is op deze manier zeer compact, wat minder koeling van de voering en minder onderhoudsvereisten met zich meebrengt. Bovendien is deze verbrandingstechniek niet beperkt tot één bepaalde brandstof: ook alternatieve brandstoffen zoals biobrandstof en gasvorming waterstof kunnen worden gebruikt voor de verbranding.

De LDI strategie zorgt voor een vlotte, stabiele en uniforme verbranding in brandstofarm bedrijf, wat resulteert in lagere piektemperaturen en kortere verblijfstijd in de vlam en een verminderde vorming van thermische  $\text{NO}_x$ . Een korte duur van het verdampingsproces van de brandstof en het mengen van brandstof en lucht elimineren tevens lokale hete punten, zodat een uniforme temperatuurverdeling in de verbrandingskamer wordt bereikt. Desalniettemin is directe inspuiting van de brandstof vatbaarder voor niet-uniforme verbranding vanwege de grotere kans op onvoldoende vermenging nog voor het plaatsvinden van de chemische reacties. Daarom wordt de lage  $\text{NO}_x$  prestatie in een LDI brander beïnvloed als de brandstof en lucht niet perfect

met elkaar zijn vermengd voor de verbranding.

Om de kwaliteit van de brandstofverstuiving te verbeteren en het mengen te bespoedigen van de zo ontstane fijne brandstofdruppels met lucht, wordt een zeer kolkende luchtstroom in de LDI brander ingelaten. Naast de kolkende stroming wordt de mengsnelheid verder verbeterd door een klein aantal grote spuitstukken op te breken in verscheidene modules van lucht en brandstof wervelkransinjectoren, waardoor het aantal toeneemt en de grootte van de luchtstralen afneemt. Dit concept van directe inspuiting wordt multi-punts brandstofarme, directe inspuiting (MPLDI) genoemd.

Dit proefschrift presenteert een numerieke analyse van het stromingsveld in één enkel element alsook in een MPLDI brander. De numerieke onderzoeken omvatten de niet-reagerende koude stroming en de reagerende sproeistraalsimulaties voor de beide configuraties. De bestudering van het enkele LDI-element geeft inzicht in de aerodynamische karakteristieken van de kolkstroming en de interactie tussen de sproeistraal en turbulentie binnenin de verbrandingskamer. De simulaties van de MPLDI laten een sterke invloed zien van de complexe rangschikking van de kolkinjectiemodules op het stromingsveld.

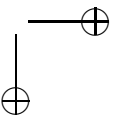
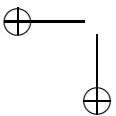
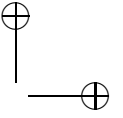
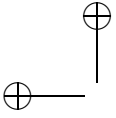
De simulatie van de niet-reagerende koude stroming in het enkele LDI-element is uitgevoerd met de instationaire Reynolds-gemiddelde Navier-Stokes (URANS) code met het realiseerbare  $k - \varepsilon$  en de Reynoldsspanningsmodellen voor turbulentie. De resultaten belichten met grote nauwkeurigheid een aantal essentiële karakteristieken van LDI, zoals de complexe structuren in de stroming in de wervelkransschoppen, één enkel, groot recirculatiegebied dat ontstaat aan het mondstuk van de injector en terugstromingsgebieden in de hoeken van de wand van de kamer en aan de wand van het divergerende venturi-kanaal. De simulaties van de reagerende sproeistraal behelzen het modelleren van diverse sproeistraal sub-processen alsmede de verbranding van brandstof en lucht. De Euler-Lagrange aanpak is geïmplementeerd om de meerfasenstroming op te lossen. De gasfase wordt beschouwd als een continuüm en wordt berekend door het oplossen van de Navier-Stokes vergelijkingen. De vloeistoffase wordt opgelost door de vloeistofdeeltjes door het berekende stromingsveld te volgen. De resultaten laten zien dat de grote axiale impuls, die door de verbranding wordt opgewekt, en de uitwisseling van impuls tussen de vloeistof- en gasfase de grootte en lengte van het centrale recirculatiegebied doen verminderen. Echter, de warmteafgifte door verbranding resulteert in een sterk recirculatiegebied. De profielen van de gemiddelde diameter in de sproeistraal wijzen op de invloed van de afschuiflaag in de kolk op de druppelverdeling in de sproeistraal. De grafieken met de snelheden van de druppels illustreren de interactie tussen de gasfase en vloeistofdruppels van diverse afmetingen en laten een sterke uitwisseling van impuls tussen de twee fasen zien. De berekende resultaten voor het enkele LDI-element worden vergeleken en gevalideerd met de beschikbare meetdata.

De URANS en grote wervelsimulatie (LES) methodologieën worden apart van elkaar toegepast om het niet-reagerende stromingsveld van de MPLDI te karakteriseren. Elk van de negen wervelkransen brengt een compact recirculatiegebied voort. De grootte van de snelheidscomponenten vlakbij de inlaat en de grootte en lengte van de recirculatiegebieden, zoals deze door het LES-schema worden voorspeld, verschillen significant van die van URANS. Verder stroomafwaarts laten de resultaten van beide methoden identieke stromingsstructuren zien met nagenoeg dezelfde snelheid. De

LES resultaten illustreren het dynamische gedrag van grote turbulente structuren, zoals de precederende wervelkernen (PVC) en wervelafbraakbellen (VBB), wat wijst op een grote mate van instationaire stroming. De numerieke voorspellingen van het gemiddelde snelheidsveld en de stromingsstructuren laten een goede overeenstemming zien met de experimentele data die beschikbaar is in de literatuur.

De berekende resultaten van de sproeistraalverbranding in de MPLDI laten zien dat door toename van de kolk snelheid een groot aantal kleine vloeistofdruppels wordt geproduceerd, zodat de brandstofverstuiving en vermenging van de brandstof met lucht wordt verbeterd. De gemiddelde diameter en de verdeling van de grootte van de druppels zijn uniform langs zowel de axiale als de radiale richting met toenemende kolk snelheid. De complexe geometrie van de MPLDI speelt ook een belangrijke rol in het verdelingsproces van de druppels. De roterende beweging van de wervelstructuren in de nabijheid van de spuitstukken verbetert de verspreiding van de druppels in het gas, waardoor verdamping van de druppels bespoedigd wordt en de kwaliteit van het mengsel verbetert. De hoge mate van afschuiving in de stroming en het vlotte mengen beïnvloeden de instantane temperatuurprofielen significant. De piektemperatuur in de vlam vermindert met toenemende afschuiving in de stroming, wat de thermische  $\text{NO}_x$  reduceert. De verenigde kolkstroming stroomafwaarts van de reactiezone helpt om de gebieden met hogere temperatuur vlot uit te spreiden en te vermengen met de gebieden met lagere temperatuur. De simulaties demonstreren dat het mengsel met een lage equivalentieverhouding en hoge snelheidsgradienten en uniform lage temperatuursverdeling produceert in vrijwel het gehele volume van de MPLDI verbrandingskamer. Korte vlammen worden waargenomen vanaf de individuele injectoren, wat de verblijfstijd in de vlam vermindert en zo resulteert in een lage vorming van thermische  $\text{NO}_x$ .

Over het algemeen is het mogelijk met de numerieke resultaten de onderliggende eigenschappen, die voornamelijk de  $\text{NO}_x$  verminderen, van LDI verbranding te verklaren. De resultaten leiden tot de conclusie dat het multi-punts inspuitsysteem samen met het LDI-concept de potentie heeft om  $\text{NO}_x$  – veel meer dan het conventionele verbrandingssysteem dat wordt gebruikt in vliegtuiggasturbines – te verminderen.



# Contents

<b>Summary</b>	<b>vii</b>
<b>Samenvatting</b>	<b>xi</b>
<b>1 Low NO<sub>x</sub> Combustion Systems for Aviation</b>	<b>1</b>
1.1 Gas Turbine Combustion . . . . .	1
1.2 NO <sub>x</sub> Formation in Gas Turbines . . . . .	3
1.3 Low NO <sub>x</sub> Combustion Scheme for Aircraft Engines . . . . .	6
1.3.1 Rich-Burn/Quick-Quench/Lean-Burn (RQL) Combustion . . . . .	7
1.3.2 Staged Combustion . . . . .	8
1.4 Lean Combustion . . . . .	11
1.4.1 Lean Premixed Prevaporized (LPP) Concept . . . . .	12
1.4.2 Lean Direct Injection (LDI) Concept: A Step Forward . . . . .	13
1.5 Thesis Goals . . . . .	14
1.6 Thesis Overview . . . . .	15
<b>2 Lean Direct Injection Combustion</b>	<b>17</b>
2.1 Introduction . . . . .	17
2.2 Effects of Swirling Flow . . . . .	18
2.3 MPLDI Combustor versus Conventional Combustor . . . . .	21
2.4 Past Studies on LDI Combustors . . . . .	22
2.5 Recent Studies on LDI Combustors . . . . .	25
<b>3 Fundamentals of Sprays</b>	<b>29</b>
3.1 Introduction . . . . .	29

xvi		Contents
<hr/>		
3.2	Governing Equations . . . . .	30
3.2.1	Two-phase Flow Characteristics . . . . .	30
3.2.2	Gas-phase Equations . . . . .	31
3.2.3	Discrete-phase Equations . . . . .	34
3.3	Classifications of Models . . . . .	35
3.4	Spray Sub-processes . . . . .	36
3.4.1	Atomization and Drop Breakup . . . . .	36
3.4.2	Drop Drag and Deformation . . . . .	40
3.4.3	Drop-Turbulence Interactions . . . . .	41
3.4.4	Drop Collision and Coalescence . . . . .	42
3.4.5	Drop Vaporization . . . . .	44
3.5	Properties of Sprays . . . . .	46
3.5.1	Drop Size . . . . .	46
3.5.2	Drop Size Distribution . . . . .	48
3.5.3	Spray Cone Angle . . . . .	49
3.5.4	Spray Penetration . . . . .	50
<b>4</b>	<b>Turbulence Modeling and Numerical Methods</b>	<b>51</b>
4.1	Introduction . . . . .	51
4.2	RANS Turbulence Models . . . . .	52
4.2.1	Governing Equations . . . . .	52
4.2.2	Realizable $k - \varepsilon$ model . . . . .	54
4.2.3	Reynolds Stress Turbulence Models . . . . .	57
4.3	Large Eddy Simulation Model . . . . .	59
4.4	Numerical Methods . . . . .	61
<b>5</b>	<b>Spray Combustion Modeling</b>	<b>65</b>
5.1	Introduction . . . . .	65
5.2	The Euler-Lagrange Approach . . . . .	66
5.3	Turbulent Dispersion Modeling of Spray Drops . . . . .	67
5.4	Atomization and Drop Breakup Modeling . . . . .	69
5.4.1	The Pressure-Swirl Atomizer Model . . . . .	69
5.4.2	Drop Breakup Modeling . . . . .	75

Contents	xvii
5.5 Drop Collision and Coalescence Modeling . . . . .	77
5.6 Drop Vaporization Modeling . . . . .	79
5.7 Combustion Modeling . . . . .	80
<b>6 Non-Reacting Flow Study in the Single-Element LDI Combustor</b>	<b>85</b>
6.1 Introduction . . . . .	85
6.2 Geometrical Configuration and Grid . . . . .	86
6.3 Boundary Conditions and Numerical Procedure . . . . .	87
6.4 Non-Reacting Cold Flow Field Analysis . . . . .	88
6.5 Concluding Remarks . . . . .	96
<b>7 Spray Combustion Study in the Single-Element LDI Combustor</b>	<b>99</b>
7.1 Introduction . . . . .	99
7.2 Geometrical Configuration and Grid . . . . .	100
7.3 Boundary Conditions and Numerical Procedure . . . . .	100
7.4 Reacting Spray Analysis . . . . .	102
7.4.1 Gas-Phase Flow Field . . . . .	102
7.4.2 Liquid Spray Characteristics . . . . .	106
7.5 Concluding Remarks . . . . .	112
<b>8 Non-Reacting Flow Study in the MPLDI Combustor</b>	<b>113</b>
8.1 Introduction . . . . .	113
8.2 Geometrical Configuration and Grid . . . . .	114
8.3 Boundary Conditions and Numerical procedure . . . . .	116
8.4 Non-Reacting Cold Flow Field Analysis . . . . .	117
8.5 Concluding Remarks . . . . .	127
<b>9 Spray Combustion Study in the MPLDI Combustor</b>	<b>129</b>
9.1 Introduction . . . . .	129
9.2 Geometrical Configuration and Grid . . . . .	130
9.3 Boundary Conditions, Mathematical Models, and Numerical approach	131
9.4 Reacting Spray Analysis . . . . .	132
9.5 Concluding Remarks . . . . .	151

xviii	Nomenclature
<b>10 Conclusions</b>	<b>153</b>
<b>Bibliography</b>	<b>159</b>
<b>A Code for Calculating Drop Mean Diameters</b>	<b>169</b>
<b>B Code for Computing Drop Velocity Distributions</b>	<b>171</b>
<b>Acknowledgements</b>	<b>173</b>
<b>Publications</b>	<b>175</b>
<b>The Author</b>	<b>177</b>

# Nomenclature

## Latin Symbols

$\dot{j}$	rate of change of oscillation velocity	$[\text{m s}^{-2}]$
$\dot{m}$	mass flow rate	$[\text{m s}^{-1}]$
$\dot{Q}_d$	heat flux	$[\text{W m}^{-2}]$
$\dot{T}_d$	rate of change of drop temperature	$[\text{K s}^{-1}]$
$\dot{y}$	rate of change of drop distortion	$[\text{m s}^{-1}]$
$\mathbf{F}$	drop acceleration	$[\text{m s}^{-2}]$
$\mathbf{s}$	displacement vector	$[\text{m}]$
$\mathbf{u}'$	turbulent gas velocity	$[\text{m s}^{-1}]$
$\mathbf{U}$	gas mean velocity	$[\text{m s}^{-1}]$
$\mathbf{u}$	instantaneous gas velocity	$[\text{m s}^{-1}]$
$\mathbf{v}$	drop velocity	$[\text{m s}^{-1}]$
$\mathbf{v}_{rel}$	relative velocity between two drops	$[\text{m s}^{-1}]$
$A$	surface area	$[\text{m}^2]$
$a$	jet radius	$[\text{m}]$
$A_2$	swirler minimum throat area	$[\text{m}^2]$
$A_3$	swirler exit area	$[\text{m}^2]$
$A_a$	air core area	$[\text{m}^2]$
$A_o$	discharge orifice area	$[\text{m}^2]$
$A_P$	total inlet port area	$[\text{m}^2]$
$A_S, A_0$	model constant	$[-]$
$A_t$	total area of tangential inlet	$[\text{m}^2]$
$B$	mass transfer number	$[-]$
$B_0$	model constant	$[-]$
$B_1$	breakup time constant	$[-]$
$c$	specific heat	$[\text{J kg}^{-1} \text{K}^{-1}]$
$C_\mu$	model coefficient	$[-]$

xx Nomenclature

---

$C_c$	swirler contraction coefficient	[–]
$C_D$	drag coefficient	[–]
$C_i$	vapor concentration	[mol m <sup>-3</sup> ]
$C_{ij}$	cross-stress tensor	[Pa]
$C_{SGS}$	Smagorinsky constant	[–]
$D$	diffusion coefficient	[m <sup>2</sup> s <sup>-1</sup> ]
$D_h$	hydraulic mean diameter of air exit duct	[m]
$d_o$	orifice diameter	[m]
$D_p$	hydraulic mean diameter of pre-filmer	[m]
$D_S$	swirl chamber diameter	[m]
$D_{10}$	arithmetic mean diameter	[m]
$D_{32}$	Sauter mean diameter	[m]
$D_{ij}$	transport of Reynolds stress by diffusion	[m <sup>2</sup> s <sup>-3</sup> ]
$f$	droplet distribution function	[–]
$f_m$	mixture fraction	[–]
$g$	acceleration due to gravity	[m s <sup>-2</sup> ]
$G_\phi$	axial flux of angular momentum	[N m]
$G_x$	axial flux of axial momentum	[N]
$G_b$	generation of turbulent kinetic energy due to buoyancy	[m <sup>2</sup> s <sup>-3</sup> ]
$H$	instantaneous enthalpy	[J]
$h$	specific enthalpy	[J kg <sup>-1</sup> ]
$I$	specific internal energy	[J kg <sup>-1</sup> ]
$K$	wave number	[m <sup>-1</sup> ]
$k$	turbulent kinetic energy	[m <sup>2</sup> s <sup>-2</sup> ]
$k_c$	mass transfer coefficient	[m s <sup>-1</sup> ]
$k_t$	turbulent thermal conductivity	[W m <sup>-1</sup> K <sup>-1</sup> ]
$k_v$	velocity coefficient	[–]
$L$	ligament length	[m]
$L$	specific latent heat of vaporization	[J kg <sup>-1</sup> ]
$l$	length	[m]
$L_{ij}$	Leonard stress tensor	[Pa]
$m$	mass	[kg]
$M_w$	molecular weight	[kg mol <sup>-1</sup> ]
$n$	number of collision	[–]
$n$	pressure exponent	[–]
$N_i$	flux of liquid vapor into gas	[mole m <sup>-2</sup> s <sup>-1</sup> ]
$Nu$	Nusselt number	[–]
$Oh$	Ohnesorge number	[–]
$P$	thermodynamic pressure	[Pa]

Nomenclature

xxi

$P_3$	combustor inlet pressure	[Pa]
$P_{ij}$	rate of production of Reynolds stress	[m <sup>2</sup> s <sup>-3</sup> ]
$p_{sat}$	saturated vapor pressure	[Pa]
$Pr$	Prandtl number	[-]
$Q$	volume fraction	[-]
$q$	spread parameter	[-]
$R$	rate of change of drop radius	[m s <sup>-1</sup> ]
$R$	universal gas constant	[J mol <sup>-1</sup> k <sup>-1</sup> ]
$r$	drop radius	[m]
$r_h$	swirler hub radius	[m]
$r_t$	swirler tip radius	[m]
$r_e$	swirler exit radius	[m]
$Re_{ij}$	kinematic Reynolds stress	[m <sup>2</sup> s <sup>-2</sup> ]
$Re$	Reynolds number	[-]
$S$	source term	[various units]
$S$	swirl number	[-]
$S_{ij}$	mean rate-of-strain tensor	[s <sup>-1</sup> ]
$Sc$	Schmidt number	[-]
$Sh$	Sherwood number	[-]
$St$	Stokes number	[-]
$T$	temperature	[K]
$t$	time	[s]
$T_3$	combustor inlet temperature	[K]
$T_d$	drop temperature	[K]
$T_l$	Lagrangian integral time	[s]
$t_s$	liquid sheet thickness	[m]
$t_l$	liquid film thickness	[m]
$Ta$	Taylor number	[-]
$U, V, W$	mean velocity component	[m s <sup>-1</sup> ]
$u, v, w$	instantaneous velocity component	[m s <sup>-1</sup> ]
$u', v', w'$	turbulent velocity component	[m s <sup>-1</sup> ]
$U_{rel}$	relative velocity between liquid and air	[m s <sup>-1</sup> ]
$V$	cell volume	[m <sup>3</sup> ]
$We$	Weber number	[-]
$X$	impact parameter	[m]
$x$	non-dimensional impact parameter	[-]
$X, Y, Z$	position	[m]
$Y$	random number	[-]
$y$	drop distortion	[m]

$y^+$	non dimensional wall distance	[—]
$Y_D$	Rosin-Rammler distribution function	[—]
$Y_i$	species mass fraction	[—]

## Greek Symbols

$\alpha$	collision angle	deg
$\alpha_h$	heat transfer coefficient	[W m <sup>-2</sup> K <sup>-1</sup> ]
$\Delta$	cutoff width	[m]
$\delta$	characteristic length	[m]
$\delta_l$	drop diameter ratio	[—]
$\delta_{ij}$	Kronecker delta	[—]
$\Delta P$	pressure drop	[Pa]
$\eta$	wave amplitude	[rad s <sup>-1</sup> ]
$\gamma$	drop size ratio	[—]
$\Lambda$	maximum wavelength	[m]
$\lambda$	wavelength	[m]
$\Phi$	mean scalar quantity	[various units]
$\mu$	molecular viscosity	[N s m <sup>-2</sup> ]
$\nu$	kinematic viscosity	[m <sup>2</sup> s <sup>-1</sup> ]
$\Omega$	maximum wave growth rate	[s <sup>-1</sup> ]
$\omega$	angular velocity	[rad s <sup>-1</sup> ]
$\Omega_{ij}$	transport of Reynolds stress due to rotation	[rad s <sup>-1</sup> ]
$\phi$	equivalence ratio	[—]
$\phi$	instantaneous scalar quantity	[various units]
$\phi'$	fluctuating scalar quantity	[various units]
$\phi_{sw}$	swirler vane angle	[deg]
$\Pi_{ij}$	transport of Reynolds stress due to pressure-strain interaction	[m <sup>2</sup> s <sup>-3</sup> ]
$\rho$	density	[kg m <sup>-3</sup> ]
$\sigma_l$	surface tension	[m <sup>-1</sup> ]
$\sigma_{ij}$	stress tensor due to molecular viscosity	[Pa]
$\tau_F$	time characteristic of a flow system	[s]
$\tau_m$	particle response time	[s]
$\theta$	half spray cone angle	[rad s <sup>-1</sup> ]
$\theta$	void fraction	[—]
$\tau_{ij}$	viscous stress tensor	[Pa]
$\tau_{xx}, \tau_{yy}, \tau_{zz}$	normal stress component	[N m <sup>-2</sup> ]
$\tau_{xy}, \tau_{yz}, \tau_{zx}$	shear stress component	[N m <sup>-2</sup> ]

$\varepsilon$	turbulent dissipation rate	$[\text{m}^2 \text{s}^{-3}]$
$\lambda$	thermal conductivity	$[\text{W m}^{-1} \text{K}^{-1}]$

## Subscripts

$0$	initial state
$a$	air
$bu$	breakup
$coll$	collision
$crit$	critical
$c$	collision
$D$	drag force
$d$	drop
$e$	eddy
$fg$	fuel species in gas form
$fl$	fuel species in liquid form
$fv$	fuel vapor
$f$	an arbitrary face
$g$	gas
$int$	interaction
$L$	ligament
$l$	liquid
$ox$	oxidizer
$rel$	relative
$s$	liquid sheet

## Abbreviations

<b>ALR</b>	Air-to-liquid ratio
<b>CFD</b>	Computational fluid dynamics
<b>CFL</b>	Courant-Friedrich-Lewy
<b>DDB</b>	Dynamic drop breakup
<b>DDM</b>	Dynamic Drag Model
<b>DPM</b>	Discrete Phase Model
<b>DRW</b>	Discrete Random Walk
<b>LDI</b>	Lean direct injection
<b>LES</b>	Large eddy simulation

---

<b>LHF</b>	Locally homogeneous-flow
<b>LISA</b>	Linearized Instability Sheet Atomization
<b>LPM</b>	Lean Premixed
<b>LPP</b>	Lean Premixed Prevaporized
<b>MPLDI</b>	Multi-Point lean direct injection
<b>MUSCL</b>	Monotone upstream centered schemes for conservation laws
<b>PDF</b>	Probability Density Function
<b>PRESTO</b>	PREssure STaggering Option
<b>PVC</b>	Precessing vortex core
<b>RANS</b>	Reynolds-averaged Navier Stokes
<b>RQL</b>	Rich burn-Quick quench-Lean burn
<b>RSTM</b>	Reynolds stress turbulence model
<b>RT</b>	Rayleigh-Taylor
<b>SGS</b>	Subgrid-scale
<b>TAB</b>	Taylor analogy breakup
<b>UHC</b>	Unburned hydrocarbon
<b>URANS</b>	Unsteady Reynolds-averaged Navier Stokes
<b>VBB</b>	Vortex breakdown bubble

# 1. Low $\text{NO}_x$ Combustion Systems for Aviation

*If I knew what I was doing, it wouldn't be called research.*

Albert Einstein

## 1.1 Gas Turbine Combustion

The fundamental challenge for the aviation gas turbine industry of the 21<sup>st</sup> century is to increase engine cycle efficiency, while keeping the emissions at the lowest possible levels. During the early years of introduction of gas turbine into aviation, the engine design was primarily driven by a need to achieve greater thrusts at higher altitudes. In the beginning, this design philosophy quietly overlooked other performance aspects, such as fuel economy, engine noise, and pollutant emissions. With the growth in aviation, it was soon envisaged that the huge consumption of fuel by civil transport might lead the aircraft industry to become one of the rapidly growing energy-use sectors. Meanwhile, the soaring fuel price in the eighties compelled the industry to explore fuel efficient aero engine concepts. Nevertheless, it was only in the nineties when aviation gas turbine emissions received serious attention, leading the International Civil Aviation Organization (ICAO) to respond to concerns regarding air quality in the vicinity of airports. Limits were set for emissions of oxides of nitrogen ( $\text{NO}_x$ ), carbon monoxide (CO), and unburned hydrocarbons (UHC), for a reference aircraft landing and take-off (LTO) cycle below 915 meters of altitude (3000 ft).

Over the last decade and a half, environmental impact of aero engines in terms of emissions and noise has moved more and more into the center of public attention. As a consequence, the standard for the emissions of pollutants and noise becomes increasingly stringent. For instance, the standard for  $\text{NO}_x$  was first adopted in 1981, then made more stringent in 1993, 1999, and 2005. Most recently, the eighth meeting of the Committee on Aviation Environmental Protection (CAEP/8) agreed on a new  $\text{NO}_x$  standard, which improves on the current standard by up to 15% with an effective date of 31<sup>st</sup> December 2013. Demand for air traffic is projected to grow substantially in the foreseeable future driven mainly by sustained economic growth in the developing countries and reduced airfares, but the environmental consequences of this rate of growth are increasingly called into question. Therefore, the coming years are likely to witness more stringent standards of emissions from the regulatory bodies, which will

create a step change to the existing gas turbine technologies.

Development of a clean and efficient combustion technology is essential as emissions are primarily governed by the combustion process. The exhaust from an aircraft gas turbine combustor is composed of CO, carbon dioxide (CO<sub>2</sub>), water vapor (H<sub>2</sub>O), UHC, particulate matter, NO<sub>x</sub>, and excess atmospheric oxygen and nitrogen. CO<sub>2</sub>, and H<sub>2</sub>O are the natural products of complete combustion of a hydrocarbon fuel; therefore, they are not regarded as pollutants. Nevertheless, they both contribute to global warming and can be controlled only by burning less fuel or non-hydrocarbon fuels. On the other hand, the principal pollutants, such as NO<sub>x</sub>, CO, UHC, and particulate matter have several adverse impacts on health and the environment.

In order to design a low emission gas turbine combustor, it is necessary to provide adequate time and sufficiently high temperatures to complete the hydrocarbon reactions. However, both residence time and temperatures must be low enough to keep the formation of NO<sub>x</sub> to a minimum, because its formation rate is an exponential function of flow residence time and temperature. Fortunately, over the past two decades, combustion technologies for aviation engines have been improved steadily to limit NO<sub>x</sub> and other pollutant emissions. Regardless of combustion chamber design and associated benefits, every gas turbine combustion system must undergo detailed analysis and rigorous component testing to balance the overall system design, as illustrated in Fig. 1.1.

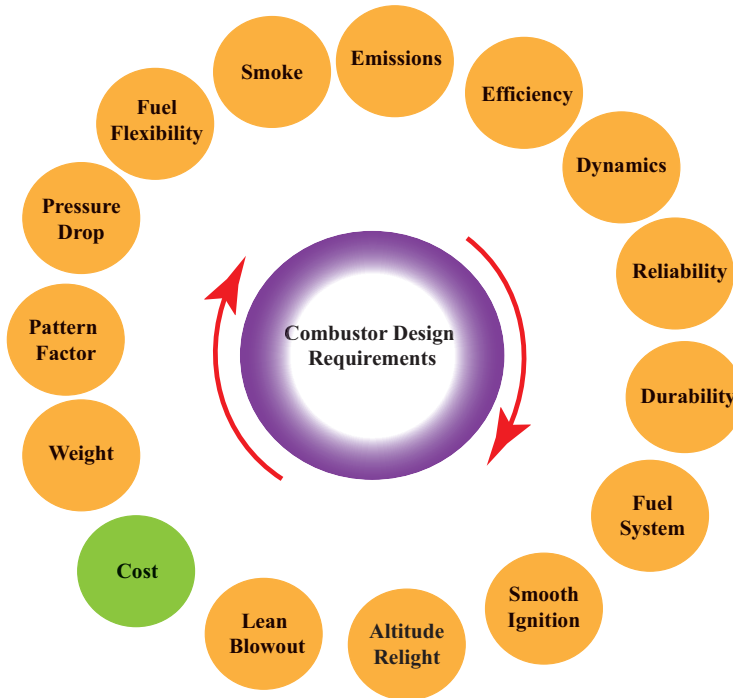


Figure 1.1: Detailed analysis and component-testing required to balance design

## 1.2 NO<sub>x</sub> Formation in Gas Turbines

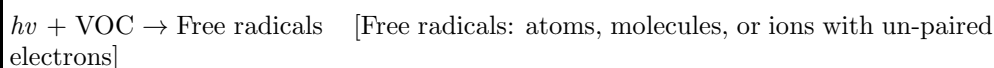
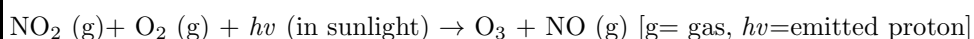
The contribution of aircraft to total NO<sub>x</sub> emissions is low, but the effect of NO<sub>x</sub> emissions is magnified because they are emitted in concentrated regions near airports and at higher altitudes in the atmosphere [1, 2]. Over the past two decades, NO<sub>x</sub> emissions have been reduced to very low levels with the development of cleaner-burning engines. Nevertheless, NO<sub>x</sub> contributes more than 80 percent by weight of aircraft engine emissions during a 926 km (500 nautical miles) mission. It is most severe at takeoff, climb, and cruise, which represent nearly 90 percent of the time of an average flight.

In this chapter, a few experimentally demonstrated low NO<sub>x</sub> combustion concepts are described. However, before reviewing these concepts, it is important to understand the fundamental mechanisms that are responsible for NO<sub>x</sub> production in gas turbines.

### NO<sub>x</sub> Formation and its Consequences

A major implication of NO<sub>x</sub> emissions in the lower atmosphere is the formation of ozone (O<sub>3</sub>) and smog. Tropospheric ozone, which is a primary constituent of smog, has been one of the main causes of air-pollution problems (see Fig. 1.2). Nitrogen dioxide (NO<sub>2</sub>) forms ozone and nitric oxide (NO) when it reacts with air in the presence of ultraviolet (UV) light in sunlight. The UV light also creates free radicals by reacting with volatile organic compounds (VOC) in the atmosphere. NO then reacts with the free radicals present in the atmosphere to form NO<sub>2</sub>. Therefore, NO<sub>2</sub> is recycled and in this way, each molecule of NO produces ozone multiple times.

*At lower atmosphere*



It's a repetitive process which may continue a few times until the VOCs are reduced to a short chain of carbon compounds that cease to be photo-reactive.

The VOCs are carbon-based chemicals that easily evaporate at room temperature. Some common examples include Acetone, Benzene, Xylene, and Formaldehyde.

The influence of NO<sub>x</sub> emissions on ozone levels depends on the altitude of the emissions for both chemical and dynamical reasons. As aircraft emissions occur near the tropopause, only a small shift in flight altitude will lead to large changes in the fraction of emissions released into the stratosphere, where pollutants accumulate more efficiently due to less vertical mixing [3]. In the sunlit troposphere and lower stratosphere, NO<sub>x</sub> leads to efficient ozone production through oxidation of CO, methane (CH<sub>4</sub>), and higher hydrocarbons. At higher altitudes in the stratosphere, this source



Figure 1.2:  $\text{NO}_x$  effect: Beijing airport on a smoggy day ©2011AFP

becomes less important, due to the limited availability of hydrocarbons. The catalytic ozone depletion cycles involving  $\text{NO}_x$  [4] gain importance, and the injection of  $\text{NO}_x$  actually destroys ozone rather than producing it. Increasing occurrences of skin cancer are being attributed to the thinning of this protective ozone layer in the upper atmosphere. In addition to ozone and  $\text{NO}_2$  concerns,  $\text{NO}_x$  in the lower atmosphere is captured by moisture to produce acid rain, which affects the ecosystem. Figure 1.3 depicts one such incident caused by acid rain.



Figure 1.3: Trees burnt by acid rain on the Mount Mitchell State Park, North Carolina ©Tina Manley

### **$\text{NO}_x$ Formation Mechanisms from Gas Turbine Combustion Standpoint**

There are two distinct mechanisms which are primarily responsible for the production of  $\text{NO}_x$  in gas turbine combustors [5].

1. The oxidation of atmospheric nitrogen present in the air for combustion (thermal  $\text{NO}_x$  and prompt  $\text{NO}_x$ ).
2. The conversion of nitrogen that is chemically bound in the fuel (fuel  $\text{NO}_x$ ).

**Thermal NO<sub>x</sub>**

Thermal NO<sub>x</sub> is formed by a series of chemical reactions in which oxygen and nitrogen present in the combustion air dissociate and subsequently react to form NO<sub>x</sub>. The chemical mechanisms, representing the major pathways for NO<sub>x</sub> formation, are as follows.

*Extended Zeldovich Mechanism*

- |   |   |
|---|---|
| <p>Nitric Oxide</p> <ol style="list-style-type: none"> <li>1. <math>O + N_2 \leftrightarrow NO + N</math></li> <li>2. <math>N + O_2 \leftrightarrow NO + O</math></li> <li>3. <math>N + OH \leftrightarrow NO + H</math></li> </ol> | <p>Nitrous Oxide</p> <ol style="list-style-type: none"> <li>4. <math>N_2 + O + M \leftrightarrow N_2O + M</math></li> <li>5. <math>N_2O + O \leftrightarrow NO + NO</math></li> <li>6. <math>N_2O + H \leftrightarrow NO + NH</math></li> </ol> |
|---|---|

[M= inert substance]

**Prompt NO<sub>x</sub>**

Prompt NO<sub>x</sub> is a form of thermal NO<sub>x</sub>, which is formed close to the flame front when intermediate combustion products (e.g., HCN) are oxidized.

*Prompt Mechanism*

- |  |  |
|--|--|
| <ol style="list-style-type: none"> <li>1. <math>N_2 + CH \leftrightarrow HCN + N</math></li> <li>2. <math>N + O_2 \leftrightarrow NO + O</math></li> </ol> | <ol style="list-style-type: none"> <li>3. <math>HCN + OH \leftrightarrow CN + H_2O</math></li> <li>4. <math>CN + O_2 \leftrightarrow NO + CO</math></li> </ol> |
|--|--|

**Fuel NO<sub>x</sub>**

Fuel NO<sub>x</sub> is produced when fuel containing nitrogen is burned. Typical examples are some types of natural gas that contain molecular nitrogen and some synthetic fuels that contain nitrogen in the form of ammonia. When these fuels are burned, the nitrogen bonds break and some of the resulting free nitrogen oxides form NO<sub>x</sub>.

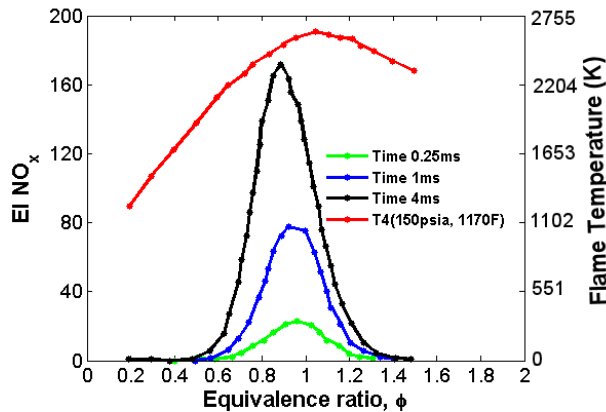


Figure 1.4: EINO<sub>x</sub> related to equivalence ratio, flame temperature, and residence time (Courtesy of Pratt & Whitney)

NO<sub>x</sub> production in gas turbines is mostly governed by combustor operating conditions, fuel and air injection scheme, fuel-air mixing, and the resulting combustion process. It is a time-integral of the NO<sub>x</sub> formation rate and the residence time of the gas mixture. This formation rate is driven exponentially by the local flame temperature. Non-uniform fuel-air mixtures cause local hot spots that contribute to NO<sub>x</sub> production. Figure 1.4 shows that the emission index of NO<sub>x</sub> (EINO<sub>x</sub>) is a function of flame temperature and residence time. It is evident that NO<sub>x</sub> production in a gas turbine can be minimized significantly if combustion is performed in either fuel-rich or fuel-lean conditions, while reducing gas mixture residence times at near stoichiometric conditions. Unfortunately, burning rich in a combustion chamber has other adverse impacts rather than just NO<sub>x</sub> reduction benefits. On the contrary, lean combustion scheme holds promise for a reduction in emissions and fuel consumption by a significant amount. This motivates the aviation gas turbine industry to develop lean combustion technologies for future engines.

In addition to chamber temperature and flow residence time, the effects of combustion chamber pressure on NO<sub>x</sub> formation have received special attention due to the continual trend toward engines of higher pressure ratio to meet the demand for lower fuel consumption. The effect of chamber pressure on NO<sub>x</sub> formation varies from one combustor design to another. For instance, in conventional combustors, it is generally found that NO<sub>x</sub> ∝ P<sup>n</sup>, where the pressure exponent, *n*, has values ranging from 0.5 to 0.8 [5]. For a rich-burn/quick-quench/lean-burn (RQL) type combustor, Rizk and Mongia [6] predicted that the value of pressure exponent varied with rich-zone equivalence ratio according to the relationship

$$n = 116.5 \exp(-\phi/0.222) \quad (1.1)$$

where  $\phi$  is the equivalence ratio, which is defined as the ratio of the fuel-to-oxidizer ratio to the stoichiometric fuel-to-oxidizer ratio.

Leonard and Correa [7] showed that for the lean premixed combustor operating at relatively low equivalence ratio, NO<sub>x</sub> is independent of pressure. Their results confirm that the low temperatures of lean flames preclude significant formation of NO by the thermal mechanism and the prompt mechanism is dominant. An increase in flame temperature (above 1800 K), corresponding to an increase in equivalence ratio, causes the pressure exponent, *n*, to increase. This trend continues until equivalence ratio is close to the stoichiometric region and *n* attains the value of 0.5, corresponding to NO formation by the thermal mechanism. For the lean direct injection (LDI) combustor, Lee et al. [8] used two EINO<sub>x</sub> correlations to compare with the measured NO<sub>x</sub> data, in which the pressure exponent values were 0.595 and 0.68, respectively.

### 1.3 Low NO<sub>x</sub> Combustion Scheme for Aircraft Engines

From the above discussions, it can be summarized that NO<sub>x</sub> formation in a combustor can be minimized if

- the combustion is performed in either fuel rich or lean conditions, thereby de-

creasing the combustion chamber temperature.

- the flow residence time is reduced.
- the operating pressure and temperature are decreased.
- local hot spots are eliminated.

All the concepts which will be introduced in the following subsections make use of these fundamental principles. Nevertheless, they differ in their  $\text{NO}_x$  reduction potential and their impact on other pollutant emissions and performance characteristics.

### 1.3.1 Rich-Burn/Quick-Quench/Lean-Burn (RQL) Combustion

Most of the combustors of modern aero engines are working according to the Rich-Burn/Quick-Quench/Lean-Burn (RQL) (see Fig. 1.5) principle. The concept was first introduced in 1980 as a strategy to reduce  $\text{NO}_x$  emissions from gas turbines [9] and it is still actively studied for aircraft applications worldwide. The basic principle

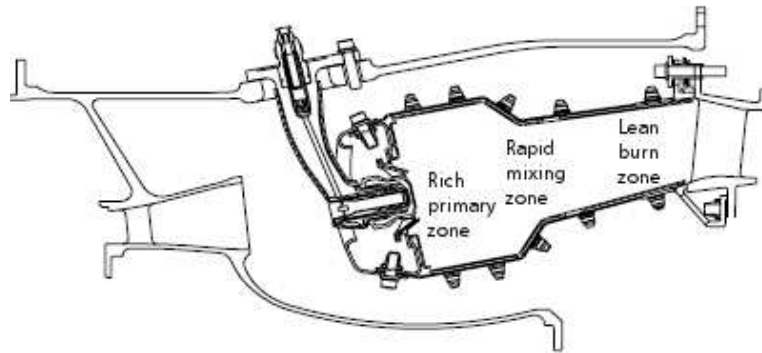


Figure 1.5: Schematic of an RQL combustor (Courtesy of Pratt & Whitney)

of an RQL combustor concept is illustrated in Fig.1.6. In this system, combustion is initiated in a fuel-rich primary zone. The rich primary zone essentially enhances the stability of the combustion reaction by producing a large concentration of energetic hydrogen and hydrocarbon radical species. In addition, the rich-burn condition minimizes  $\text{NO}_x$  production due to the effects of relatively low temperatures and low concentration of oxygen. The mixture from the primary zone generally contains partially oxidized and pyrolyzed hydrocarbon species, hydrogen, and CO. As the fuel rich combustion products emerge from the primary zone, they interact with jets of air. This air quenching process is rather rapid and it reduces the temperature of the products, leading to low  $\text{NO}_x$  formation. Nevertheless, this process involves challenges as the transformation from a rich-burn zone to a lean-burn zone must take place quickly to avoid the formation of local near stoichiometric regions which otherwise will cause excessive  $\text{NO}_x$  production. In the lean-burn zone, the primary zone effluent, which contains high concentrations of CO, hydrogen, and hydrocarbon species, is oxidized.

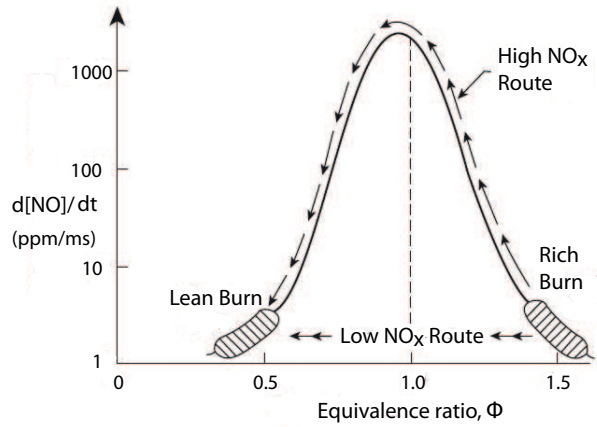


Figure 1.6: Principle of RQL combustion [5]

The temperature in this region must be controlled to prevent NO<sub>x</sub> formation. On the other hand, the temperature has to be high enough to consume the remaining CO, UHC, and soot. Therefore, it requires a careful consideration of the equivalence ratio. The success of the RQL technology lies in the rapid mixing between the air and the effluent exiting from the primary zone. Other major challenges associated with this combustion scheme include liner cooling and the selection of liner wall material. Various types of cooling techniques have been investigated for the liner wall cooling in the primary zone, such as backside convection cooling and more advanced impingement cooling, since the conventional film cooling would generally create local stoichiometric mixtures, resulting in high levels of NO<sub>x</sub> [5]. However, the most limiting aspect of the NO<sub>x</sub> reduction capability of the RQL concept is the NO<sub>x</sub>-exhaust smoke tradeoff. Therefore, the optimization of an RQL combustor needs conscientious consideration of both NO<sub>x</sub>-smoke and the thermodynamic cycle of the engine.

In comparison with conventional combustors, the RQL concept has so far been proven very successful for aero engine applications due to its intrinsically better ignition and lean blowout performance and lower NO<sub>x</sub> production capability. However, with respect to the emission targets for 2020 and beyond, the RQL design seems to have limited potential to further significantly decrease NO<sub>x</sub> emissions.

### 1.3.2 Staged Combustion

In the staged combustors, air flow distribution within the combustor remains constant, but the fuel flow is switched from one zone to another in order to maintain a fairly constant temperature. A well known method for this concept is the Selective Fuel Injection [10], in which fuel is supplied only to selected combinations of fuel injectors during altitude relight, light-off, and engine idle conditions. This method is mainly useful for extending the lean blowout limit to lower overall equivalence ratios and for

reducing CO and UHC emissions. However, there is no special advantage concerning  $\text{NO}_x$  reduction in this technique. Moreover, this method might cause chilling of the chemical reactions at the outer edges of the individual combustion zones and can also cause non-uniform distribution of combustor exit temperature, thereby affecting the turbine efficiency. These limitations led to the development of staged combustors, in which two or more combustion zones are employed within the combustor, either in parallel or in series. Each stage is designed to optimize certain aspects of combustion chamber performance.

A typical staged combustor comprises a lightly loaded primary zone, which provides the temperature rise needed at low-power conditions. On the other hand, at high-power settings, it works as a pilot source of heat for the main combustion zone. At maximum power conditions, the equivalence ratio in both the primary and main zones are kept low to minimize  $\text{NO}_x$  and smoke.

### Parallel/Radial Staging

The General Electric developed the parallel/radial staging concept for civil aircraft engines using the Dual Annular Combustor (DAC) (see Fig. 1.7). As the name indicates, the DAC has two combustion domes [10]. The outer dome is optimized for operability and low power operation. It is generally lightly loaded and provides a relatively high temperature that is required during some specific engine operating conditions, such as startup, altitude relight, and engine idle. At idle, the equivalence ratio is selected to reduce CO and UHC formations. On the contrary, the inner (main) dome is optimized for high-power settings. It has a small highly loaded combustion zone of short residence time and low equivalence ratio to minimize  $\text{NO}_x$  and smoke. At high power, both stages are operational but the majority of the fuel and air is burned in the inner stage. The higher flow velocities in the inner stage reduce combustor residence time.

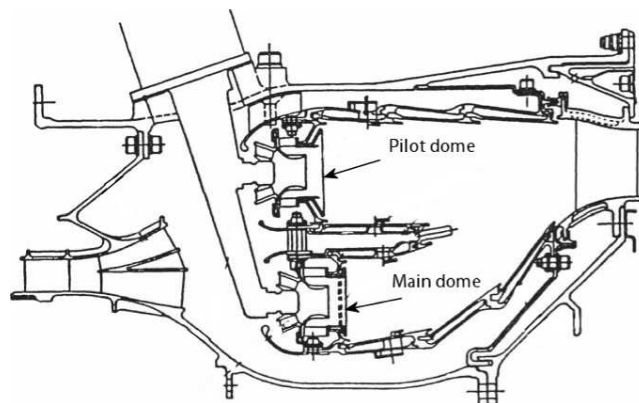


Figure 1.7: Schematic of a radial staged combustor [10]

The radial staged combustor essentially accomplishes low emissions within approximately the same overall length as a conventional combustor. The General Electric

reportedly achieved around 45 percent reduction in NO<sub>x</sub> using the DAC, in comparison with the corresponding single annular combustor (SAC) [10].

A major challenge for the parallel staging concept is to obtain the desired performance during the intermediate power settings when both the annular chambers are operating far away from their optimum design points. Another drawback is that the pollutant reduction is achieved at the expense of increased design complexity and an increase in the number of fuel injectors. Furthermore, the combustor has relatively large liner wall surface area, resulting in additional cooling requirements.

### Series/Axial Staging

In a series/axial staged combustor, a part of the total amount of fuel is injected into a somewhat conventional primary (pilot) zone. The secondary (main) combustion zone is located downstream. A premixed fuel and air mixture is introduced into the main combustion zone, which operates at low equivalence ratios, resulting in low NO<sub>x</sub> and smoke. The primary combustion zone is used to raise the temperature during engine startup. The fuel is admitted into the main combustion zone when the engine demands for high power. At maximum power conditions, the primary zone provides the heat needed to promote a rapid combustion of the fuel supplied to the main combustion zone.

In an axial staged combustor (see Fig. 1.8), the combustion process in the main zone is relatively rapid and reliable, in comparison with a radial staged combustor, since in the former, the ignition process in the main stage is directly driven by the pilot. In addition, the hot gas flow from the pilot to the main zone results in high combustion efficiency, even at low equivalence ratios.

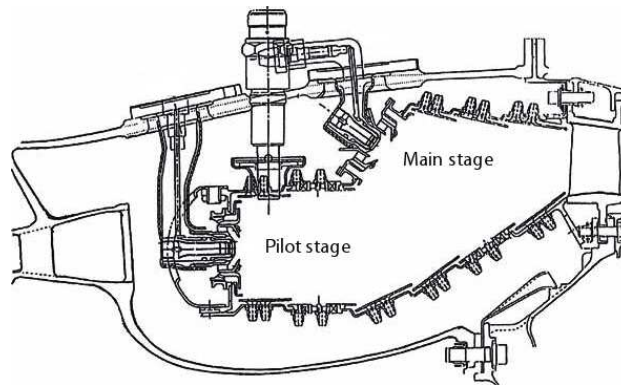


Figure 1.8: Schematic of an axial staged combustor (Courtesy of Pratt & Whitney)

An increased combustor length due to the in-line arrangement of stages is a major disadvantage of this system. This also leads to an increase in liner wall surface area and additional cooling requirements. Furthermore, using this concept, NO<sub>x</sub> reduction can be achieved only at the expense of increased costs, weight, and design complexity.

### Twin Annular Premixing Swirler (TAPS)

The General Electric recently introduced the Twin Annular Premixing Swirler (TAPS) combustion concept (see Fig. 1.9) in view of the future emission targets for  $\text{NO}_x$  and other pollutants [11]. The concept has evolved primarily from the staged combustion methods. However, it can also be viewed as a lean combustion concept.

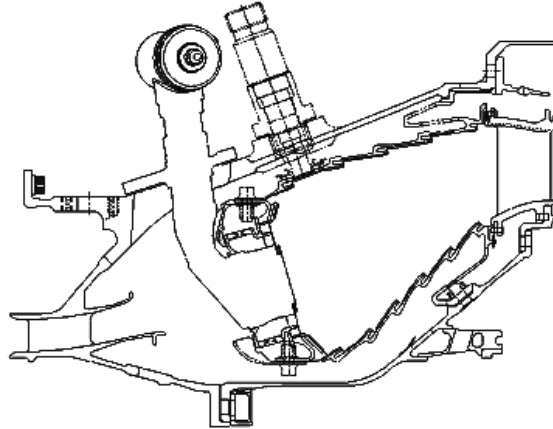


Figure 1.9: Schematic of a TAPS combustor [11]

The TAPS issues two co-annular swirling flow streams produced by a pilot and a main mixer, respectively. The swirling streams are the result of multi-swirler arrangement designed for achieving certain aspects of combustion performance. The pilot uses a high flow number simplex atomizer surrounded by two co-rotating swirlers that assist in developing a fine spray suitable for engine startup and low-power operations. On the other hand, the main mixer consists of a cyclone or radial inflow swirler. The fuel is injected into it by discrete traversed jets. The pilot swirling jets, which are initially controlled by the fuel nozzle geometry, interact with the swirling jets from the main-mixer. They are separated by a step height to provide a thermal environment needed to meet the design requirements. All the combustor air except cooling air required for the dome and liners passes through the pilot and cyclone swirlers. Fuel staging between the pilot and main mixer is done within the fuel nozzle by discrete flow splits that vary from 100% through the pilot at low-power to 5 – 10% at the maximum power.

## 1.4 Lean Combustion

Low- $\text{NO}_x$  combustion in gas turbines can be best achieved by using gaseous fuel with the Lean-Premixed (LPM) concept. As a matter of fact, in industrial gas turbines, LPM systems have accomplished significant  $\text{NO}_x$  reduction levels compared to diffusion flames. In this combustion system, vaporized fuel and air are mixed uniformly

at a very low equivalence ratio to reduce the flame temperature, which essentially reduces EINO<sub>x</sub>. Nevertheless, an implementation of the LPM technology into aircraft engines requires some specific considerations to be made, since aircraft engines use liquid fuel rather than natural gas and they operate under different conditions.

### 1.4.1 Lean Premixed Prevaporized (LPP) Concept

The underlying principle of the Lean Premixed Prevaporized (LPP) concept is to supply a homogenous mixture of fuel and air into the combustion zone, and then to operate the combustion process at an equivalence ratio very close to the lean blowout limit. The smaller the difference between stable combustion and flame blowout, the lower the chances of NO<sub>x</sub> formation.

A schematic of an LPP combustor is illustrated in Fig. 1.10. Air discharged from the compressor enters the combustor through a faired pre-diffuser before it is dumped into the annulus. As the air accelerates through the annulus, a portion is admitted by holes in the liner to dilute the hot combustion gases. The other portion of the air flows through the annulus where it cools the outside of the liner wall. This cooling effect can be enhanced by the use of trip strips. Annulus air used for cooling is then dumped into a plenum and enters the premixer. Inside the premixer, the air passes through axial swirlers to mix with an evaporating liquid fuel spray. The exiting fuel and air mixture is dumped into the primary zone by another axial swirler where it ignites and burns. The resulting hot products are diluted with relatively cooler air and accelerated out of the combustor by a converging nozzle.

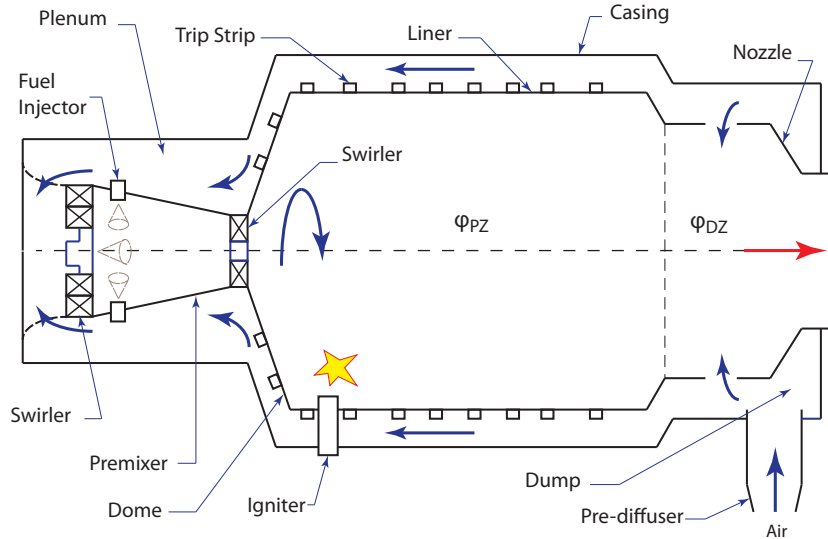


Figure 1.10: Schematic of an LPP combustor

In the premixer, the processes, such as fuel injection, fuel drop evaporation, and fuel-air mixing have to be optimized, because a small degree of unmixedness could affect

the  $\text{NO}_x$  formation process. Therefore, from an emission standpoint, long residence times are beneficial. However, excessive residence times result in a longer pre-mix duct and a heavier engine. Most importantly, under high pressure and temperature conditions, the fuel-air mixture could be susceptible to auto-ignition inside the pre-mix duct. Therefore, the residence time needs to be shorter than the auto-ignition time. On the other hand, auto-ignition itself is a function of air temperature and pressure and fuel properties.

Aircraft engines typically operate at higher overall pressure ratios (OPRs) than the maximum pressure ratios of industrial gas turbines. In addition, the auto-ignition delay times of jet fuel are shorter than those of natural gas for the same pressure and temperature conditions [12]. Flashback is another major problem which is associated with LPP combustors [13]. Flashback into the pre-mix duct takes place when the local flame speed is faster than the velocity of the fuel-air mixture exiting the duct. Unexpected engine transients and the resultant change in air velocity often results in flashback. Furthermore, as soon as the flame-front approaches the exit of the pre-mixer, the flame pressure drop will cause a reduction in the velocity of the mixture through the duct, thereby amplifying the effect of the original disturbance and prolonging flashback [14].

Therefore, it is evident that the LPP combustion concept has certain operational risks for aero engine applications. If it is used for large engines operating at high OPRs, narrow stability limits, auto-ignition of mixture, and flame flashback could pose some serious challenges to the engine performance. For small engine applications, the system is too complex to be considered as an economically feasible design. Nevertheless, LPP combustors have been widely used in industrial gas turbines due to its ability to produce very low  $\text{NO}_x$ .

#### 1.4.2 Lean Direct Injection (LDI) Concept: A Step Forward

The existing single annular combustor technology is most likely to be phased out soon as further optimization will not contribute any significant improvement to its  $\text{NO}_x$  reduction capability. Classical staged combustor designs largely suffer from poor economy due to their increased complexity, high part count, and large liner wall area that needs to be cooled. The most widely used RQL technology also has limited potential to further significantly decrease  $\text{NO}_x$  emissions whilst maintaining the other emissions criteria and satisfying all operability requirements. These challenges lead the aviation gas turbine industry to step up its efforts toward the development of lean combustion technologies with low emissions performance while they remain economically viable. However, the main challenge in aircraft applications lies in devising a lean combustion system which can perform stably under all operating conditions.

The trick to overwhelm the short ignition delay associated with the LPP method is to use the lean direct injection (LDI) scheme in which fuel and air are injected directly into the combustion chamber without any pre-mixing. As the name implies, in LDI the combustor operates fuel-lean without a rich front end: all of the combustor air except that used for liner cooling enters through the combustor dome. Like other lean burn combustor concepts, LDI reduces thermal  $\text{NO}_x$  by minimizing flame temperature. To eliminate local hot spots that produce high levels of  $\text{NO}_x$ , the LDI concept relies

on a rapid and efficient fuel-air mixing before burning occurs. The simplest way of enhancing the mixing process is to increase the air pressure drop across the injector, which will generate more turbulence to rip apart the liquid fuel streams. Nevertheless, an increase in pressure loss essentially represents system efficiency loss. Therefore, to be able to improve the mixing with out increased loss, it is imperative to reduce the distance over which the fuel and air streams need to be mixed. By breaking up a few large fuel injectors into many small fuel injectors, it is possible to speed up fuel-air mixing and make the combustor front end more uniform. Each small fuel injector is surrounded by an air-swirler which creates a high degree of swirling airflow to atomize the fuel streams into very fine drops, then evenly disperse the fuel drops into the gaseous medium, and create rapidly a homogenous mixture of air and the resulting fuel vapor before the mixture undergoes combustion. This injection scheme is referred to as the Multi-Point Lean Direct Injection (MPLDI)[15]. The set-up makes it possible to control the individual injectors to redistribute fuel on the fly in time and space to reduce hot-streak reduction as well as instabilities. Several series of the MPLDI have been tested recently by the NASA Glenn Research Center [16]. It has been found that the best of these have the  $\text{EINO}_x$  performances approaching that of the LPP combustors. The MPLDI combustion concept is discussed further in Chapter 2.

## 1.5 Thesis Goals

The lean direct injection (LDI) concept is anticipated as a potential candidate to replace the existing combustion systems for the future aircraft engines. It shows promise as an ultra low- $\text{NO}_x$  concept which can reduce  $\text{NO}_x$  emissions much more than the combustion systems used currently in aero gas turbines, whilst maintaining the other emissions criteria. Furthermore, the experiments demonstrated its good flame-holding ability and wide stability limits. The results are quite encouraging, but the measurements are rather limited to an observation of exhaust emissions. In other words, the experiments have not described completely the dynamics of the mixing and combustion process that resulted in measured low emissions. Therefore, the present research is primarily aimed at achieving a physical insight into the underlying physics of the LDI combustor. The results presented in this dissertation are part of an effort to explain the fundamental features of the LDI concept which contribute to the reduced  $\text{NO}_x$  emissions as measured by the experiments. In this regard, two LDI combustor configurations are numerically investigated: the single element LDI and the MPLDI. Calculations are performed for both non-reacting cold flow and reacting spray combustion within the two combustors. The computations for the single-element LDI are the first step ahead of the investigations for the more complex MPLDI combustor. The results are compared with the experimental data available in the literature.

Overall, the thesis provides a comprehensive description of the complex swirling flow field associated with the LDI combustors. The results offer an insight into the effects of highly swirling flows on various spray sub-processes, such as drop breakup, drop drag and distortion, turbulent dispersion of spray, drop collision and coalescence, drop evaporation, and spray combustion. Furthermore, from the calculated flow field, the

$\text{NO}_x$  emission characteristics are predicted.

## 1.6 Thesis Overview

The thesis is structured as follows.

Chapter 1 starts with a discussion on the basic mechanisms of  $\text{NO}_x$  formation in gas turbine combustors. Various existing low- $\text{NO}_x$  combustion schemes for aero engines are described. The fundamentals of the lean combustion concept and the associated major challenges for aircraft applications are illustrated. The chapter then discusses how the LDI concept could solve the inherent problems of a lean premixed system, thus emerging as a viable combustion scheme for future aircraft propulsion. Finally, the goals of the thesis and the outline of the thesis are presented.

Chapter 2 provides an overview of the LDI concept. The influence of swirling flow on combustion performance is discussed. The MPLDI combustor is compared with a conventional annular combustor. Furthermore, this chapter highlights a few from the past and the more recent studies on LDI combustors.

Chapter 3 introduces the fundamentals of sprays, which include the governing equations of two-phase flow and a detailed description of various spray sub-processes. In addition, the basic spray properties are discussed, which include drop size, drop size distribution, spray cone angle, and spray penetration.

Chapter 4 presents the turbulence models and the numerical schemes applied in this research to compute the turbulent and swirling flow field of the LDI combustors.

In Chapter 5, discussion is focussed on the sub-models that are used to compute combusting sprays in the LDI combustors. The chapter starts with a description of the Euler-Lagrange approach applied in the Discrete Phase Model (DPM) of the Fluent<sup>®</sup> solver to simulate the multi-phase flow. The dispersion modeling of liquid spray drops is explained. In addition, the modeling techniques for atomization, drop breakup, and drop distortion are elaborated. It is followed by a discussion on the drop collision and spray vaporization modeling schemes used in the simulations. The chapter ends with the theory of the combustion model being applied and its implementation into the present research.

Chapter 6 is the first among the four chapters on the results obtained from the simulations of the LDI combustors. The chapter reports the non-reacting cold flow field in a single-element LDI combustor. An unsteady Reynolds Averaged Navier Stokes (URANS) code is used to compute the entire flow field of the combustor. Both the mean velocity field and the turbulence are analyzed. The results are compared and validated with the available experimental data.

In Chapter 7, the computational results are illustrated for the reacting spray simulations of the single-element LDI configuration. Properties of both the liquid and gas phases are analyzed to get an insight into the effects of the highly swirling flow on the spray characteristics and the combustion process. The computational results are compared with the available experimental data. In addition, a comparison is made between the non-reacting and reacting flow velocity fields.

Chapter 8 presents the numerical results of the cold flow analysis of the MPLDI combustor. The URANS and large eddy simulation (LES) methods are employed separately to study the aerodynamic characteristics of the flow field for the same inlet flow conditions. The results of the two numerical methods are compared. Furthermore, the results are compared with the measurement data available in the literature.

Chapter 9 discusses the computational results of the reacting spray in a Multi-Point Lean Direct Injection (MPLDI) combustor to demonstrate some of its fundamental features that essentially explain its ability to achieve low NO<sub>x</sub>. Three cases are studied for different operating conditions. Each case is analyzed and its results are compared with the results of the two other cases. Furthermore, the reacting spray results of the MPLDI are compared with that of the single-element LDI.

Finally, the major conclusions of this research are drawn in Chapter 10. It ends with a few recommendations for future research.

## 2. Lean Direct Injection Combustion

### 2.1 Introduction

The lean direct injection (LDI) concept has been developed as a low  $\text{NO}_x$  alternative to the Lean Premixed Prevaporized (LPP) combustion scheme for aviation gas turbines, since LPP combustion suffers from operational risks for aircraft applications. In this concept, fuel and air are directly injected into the combustion chamber at an equivalence ratio close to the lean blowout limit and the fuel-air mixing takes place in the shortest possible distance. There is no premixing duct attached upstream of the combustion chamber. The main purpose is to provide a lean premixed fuel-air mixture that burns in a low- $\text{NO}_x$  flame, similar to LPP combustors. As discussed in the previous chapter,  $\text{NO}_x$  performance in gas turbines not only depends on overall lean mixture and flow residence time in a combustor, but it also depends on the quality of the fuel-air mixture and the efficiency of the mixing process. In the LDI concept, direct fuel injection may cause non-uniform combustion and create local hot spots. Therefore, low- $\text{NO}_x$  performance is affected in an LDI combustor if the fuel and air are not perfectly mixed before combustion, resulting in regions with higher fuel content that burn hotter and generate more  $\text{NO}_x$ .

In LDI, a highly swirling air flow is admitted into the combustor to atomize the fuel stream and mix the resulting fuel drops rapidly with the incoming air. In addition to the swirling air flow, the mixing is further enhanced by breaking a few large fuel injectors into several small fuel injectors, thus increasing the number and decreasing the size of the air jets. This direct injection concept is referred to as the Multi-Point Lean Direct Injection (MPLDI) [16]. Each small injector in MPLDI generates a stable and short flame which reduces the flame residence time, thereby leading to reduced  $\text{NO}_x$  production. The multi-swirler fuel injector concept significantly shortens the fuel-air mixing time inside the flame tube by dispersing liquid fuel drops quickly and uniformly. The small drops immediately vaporize and mix with the air/gas. The homogenous mixture also leads to a uniform distribution of combustion products and smooth temperature profiles across the combustion chamber.

This chapter is structured as follows. In the next section, the discussion is focussed on the effects of swirling flow on combustion performance as discussed in the literature. It also includes a description of the swirl number, which determines the degree of swirl

imparted to the flow. This is followed by a brief comparison between conventional and MPLDI combustors in Section 2.3. A few notable past studies on LDI combustors are discussed in Section 2.4. Finally, Section 2.5 highlights some current research on the LDI technology.

## 2.2 Effects of Swirling Flow

Swirling flow is generally used for flame stabilization and improved mixing in combustion chambers. It induces a highly turbulent recirculation zone, which anchors the flame, resulting in better mixing and combustion [17]. The aerodynamics of swirling flow influences the combustion performance significantly as it directly affects the fuel-air mixing and the flow residence time. An extensive amount of studies has been conducted on the effects of swirling motion in a variety of combustor configurations. In this section, a few of them are discussed.

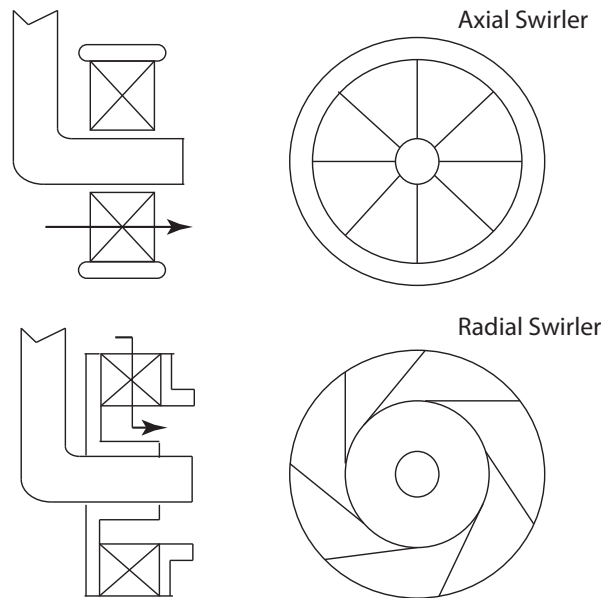


Figure 2.1: Schematics of axial and radial swirlers

Gupta et al. [18] observed that the large toroidal recirculation zone played a major role in the flame stabilization process by acting as a store for heat and chemically active species. They opined that the well mixed region induced by the swirling flow served to transport heat and mass to the fresh combustible mixture of air and fuel.

The most common method of generating a swirling flow is by using radial angled vanes in the passages of air. The characteristics of the swirling flow depend on the swirler vane angle. Beer and Chigier [19] demonstrated a few methods of inducing rotation in a stream of fluid. In conventional liquid fuel burners, axial-flow type swirlers (see Fig.

2.1) are generally employed. The axial swirl vanes are easy to manufacture as they are relatively flat. However, curved vanes can yield better performance in aerodynamic properties [5]. Syred and Beer [20] illustrated that for tangential entry including radial vanes, the swirling flow produced high efficiency for isothermal performance and low loss of pressure coefficient compared to that for axial straight vanes. On the other hand, Al-Kabie [21] observed that the discharge coefficient for the radial swirlers (see Fig. 2.1) is low in comparison with the zero angle vane. A low discharge coefficient implies that flow separation has occurred in the passage in spite of the curved vane. However, both axial and radial swirlers are commonly used in gas turbine combustors. Axial and radial swirler configurations in a can combustor were evaluated by Smith et al. [22] using natural gas and by Cowell and Smith [23] using liquid fuel. They observed that the emission performance of the radial swirler was better than for the axial swirler. The properties of recirculation zone generated by each swirler type could be the major contributing factor to this difference. Both swirlers had the same swirl number, but the radial swirler produced a stronger central recirculation zone than its axial counterpart, due to differences in the expansion ratio, channel height, and exit velocity of the swirlers. Etemad and Forbes [24] conducted a numerical investigation of the effect of radial and axial swirler configurations on the flow field in a gas turbine combustor. They observed that the radial swirler provided a widely dispersed, flat swirling pattern attached to the swirler face, with the possibility of fuel impingement on the swirler and liner wall. On the other hand, the axial swirler provided a narrower, centralized fuel pattern, influenced partially by primary air jets, with less chance of fuel impingement on the wall.

Wang et al. [25] performed a large eddy simulation (LES) study for the CFM56 gas turbine swirl injector with axial jet entry. They investigated the flows generated with co-rotating and counter-rotating swirlers by reversing the orientation of the secondary swirl vanes. The mean velocity field in the co-rotating case has a close resemblance to its counterpart in the counter-rotating case, except that the former possesses a much larger recirculation zone, due to the stronger swirling motion. Merkle et al. [26] measured the isothermal flow and mixture fields in a double swirler airblast fuel atomizer. The counter-swirl configuration exhibited a considerable attenuation of the turbulent exchange of momentum perpendicular to the main flow direction. As a consequence, the mixture field with counter-rotating airflows featured a reduction in the turbulent mass transfer rate in the radial direction. Li and Gutmark [27] investigated the effects of swirler configurations on the flow structures and combustion characteristics in a triple annular research swirler (TARS) fuel injector. The co-swirling configuration was demonstrated to have lower  $\text{NO}_x$  emission levels than the counter-swirling configuration for both gaseous and liquid fuels.

## Swirl Number

The swirl number,  $S$ , is used for quantifying the amount or degree of swirl imparted to the flow. Based on the swirl number, the swirling flow can be divided into two regions: weak swirling flow ( $S < 0.6$ ) and strong swirling flow ( $S > 0.6$ ). In a weak swirling flow, the axial pressure gradients are insufficient to cause on-axis recirculation. On the contrary, strong swirling flow has high radial and axial pressure gradients near the exit of the swirler, resulting in a recirculation zone at the center.

The swirl number is usually defined as the ratio of the axial flux of the tangential momentum to the product of the axial momentum flux and a characteristic radius [19], i.e.,

$$S = \frac{G_\phi}{G_x r_t} \quad (2.1)$$

where the axial flux of angular momentum,  $G_\phi$ , is given by

$$\begin{aligned} G_\phi &= \int_{r_h}^{r_t} (Wr) \rho U (2\pi r) dr \\ &= (U \tan \alpha_{sw}) 2\pi \rho U \int_{r_h}^{r_t} r^2 dr \\ &= \frac{2}{3} \pi \rho U^2 (r_t^3 - r_h^3) \end{aligned} \quad (2.2)$$

and the axial flux of momentum,  $G_x$ , is expressed in the following form

$$G_x = \int_{r_h}^{r_t} \rho U^2 (2\pi r) dr + \int_{r_h}^{r_t} p (2\pi r) dr \quad (2.3)$$

where  $r_h$  and  $r_t$  are the inner (hub) radius and outer (tip) radius of the swirler, respectively and  $\alpha_{sw}$  is the swirler vane angle. The terms  $U$  and  $W$  are the axial and tangential components of velocity at radius  $r$ , respectively.

The pressure term in Eqn.2.3 is difficult to calculate, since pressure varies with position in the swirling jet. Therefore, the pressure term is sometimes omitted to make a simplified definition of the swirl number, i.e.,

$$S = \frac{G_\phi}{G'_x r_t} \quad (2.4)$$

where  $G'_x$  is given by

$$\begin{aligned} G'_x &= \int_{r_h}^{r_t} \rho U^2 (2\pi r) dr \\ &= 2\pi \rho U^2 \int_{r_h}^{r_t} r dr \\ &= \pi \rho U^2 (r_t^2 - r_h^2) \end{aligned} \quad (2.5)$$

Therefore, the swirl number becomes

$$S = \frac{2}{3} \tan \alpha_{sw} \left[ \frac{1 - (r_h/r_t)^3}{1 - (r_h/r_t)^2} \right] \quad (2.6)$$

Claypole and Syred [28] related the swirl number to the geometry of the combustor by assuming a perfect mixing and conservation of momentum:

$$S = \frac{r_o \pi r_e}{A_t} \left[ \frac{\text{tangential flow}}{\text{total flow}} \right]^2 \quad (2.7)$$

where  $r_e$  is the radius of the swirler exit and  $A_t$  is the total area of tangential inlet.

Al-Kabie [21] formulated the geometric swirl number using the following relation

$$S = \frac{\sin\theta}{1 + \frac{1}{\tan\theta}} \left[ \frac{A_3}{C_c A_2} \right] \quad (2.8)$$

where  $A_3$  is the swirler exit area,  $A_2$  is the swirler minimum throat area, and  $C_c$  refers to the swirler contraction coefficient.

## 2.3 MPLDI Combustor versus Conventional Combustor

Figures 2.2 and 2.3 illustrate the schematics of a conventional combustor and an MPLDI combustor, respectively. In conventional combustor, one third of the total air is mixed in the front end with the fuel. As the spray comes out in the conical shape, some of hot gas recirculates backward in the center, which ignites the incoming fresh mixture. Therefore, the vortex formed in this region stabilizes the flame and acts as a primary flame holding mechanism. However, the mixture in the primary region is close to stoichiometric, with very high temperature. This is where a lot of  $\text{NO}_x$  is produced. The rest two third of the air enters through the dilution holes to bring the gas temperature down to a level acceptable to the first stage of turbine, and through the cooling systems. The fuel rich region in the frontal section produces a lot of CO. Therefore, a long combustor length is required to burn off the CO. The long residence time of the gas mixture at high temperatures results in additional  $\text{NO}_x$ .

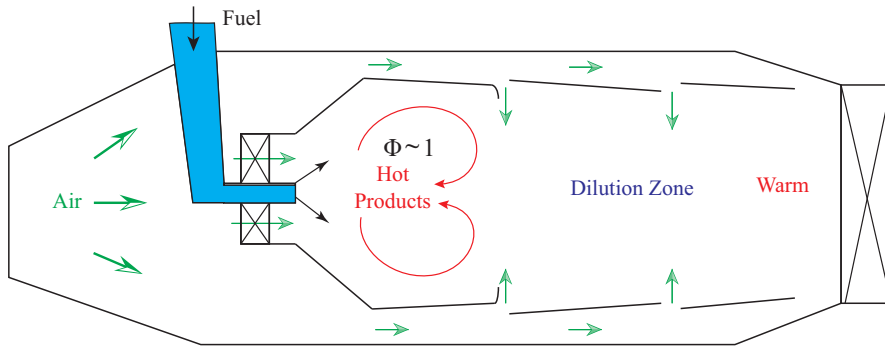


Figure 2.2: Schematic of a conventional combustor

On the other hand, in the MPLDI system, all the combustor air except that used for liner cooling enters through the combustor dome. As a result, the mixture is lean. It burns at a lower temperature and produces less  $\text{NO}_x$  to start with. An efficient mixing process in the MPLDI combustor also produces less CO. Therefore, the combustor length can be made shorter, which means that the flow residence time shortens. This reduces  $\text{NO}_x$  production further. Consequently, the more compact combustor requires less liner cooling and a shorter engine shaft, thus reducing the engine weight significantly. Furthermore, the design of the MPLDI combustor allows

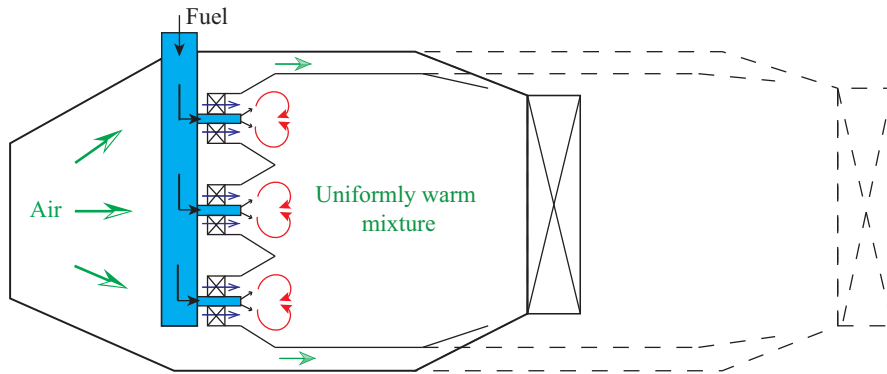


Figure 2.3: Schematic of an MPLDI combustor

controlling the individual fuel injectors to modulate the fuel in time and space to reduce local hot streaks inside the chamber. In addition to the conventional aviation fuel, this system can be used for combustion of alternative fuels, such as biofuels and gaseous hydrogen, without making any major design modifications.

## 2.4 Past Studies on LDI Combustors

Early studies on the direct fuel injection concept were carried out by a few researchers. Al-Kabie et al. [29, 30, 31] and Andrews et al. [32] investigated radial swirlers in LDI combustors. Low  $\text{NO}_x$  and short residence time were reported. Al-Kabie et al. [31] also reported very good flame stability. However, these investigations were conducted by using natural gas, instead of liquid fuel. In principle,  $\text{NO}_x$  levels increase for liquid fuel injection depending on the degree of atomization, vaporization, and mixing that can be achieved before combustion occurs.

Anderson [33] studied the effect of fuel atomization and vaporization on  $\text{NO}_x$  levels in an automotive gas turbine using liquid diesel. The study also reported the consequence of fuel-bound nitrogen on  $\text{NO}_x$ . At a reference velocity of 32 m/s, the  $\text{NO}_x$  levels decreased as the inlet air temperature increased from 1100 to 1250 K. Anderson attributes this to faster vaporization at the higher inlet temperature. By increasing the air velocity, the same effect was observed. The higher air velocity decreases the drop sizes and provides faster vaporization and a closer approximation of a premixed flame. Anderson concluded that thermal  $\text{NO}_x$  was not a major contributor since the temperature inside the combustor was sufficiently low and the  $\text{NO}_x$  was mainly from fuel-bound nitrogen and prompt  $\text{NO}_x$ .

The potential for low- $\text{NO}_x$  LDI combustors has also been demonstrated by Shaffar and Samuelson [34], Terasaki and Hayashi [35], and Tacina [36]. Their results showed that  $\text{NO}_x$  emissions from an LDI combustor could approach those of LPP combustors.

Based on the experiments carried out by different workers, a comparison is made between the  $\text{NO}_x$  data of LDI [31, 33, 37] and RQL [38, 39, 40, 41, 42] combustion

systems (see Fig. 2.4). RQL combustor architecture has been commonly used for aero engine combustion and its basic principles are discussed in Chapter 1. The RQL experiments were mainly conducted to determine the rich zone equivalence ratio that would minimize  $\text{NO}_x$  production. The LDI experiments were performed using both gaseous [31, 37] and liquid fuels [33] at different inlet flow conditions. Figure 2.4 illustrates that the  $\text{NO}_x$  levels for the LDI experiments are lower than for the LDI experiments.

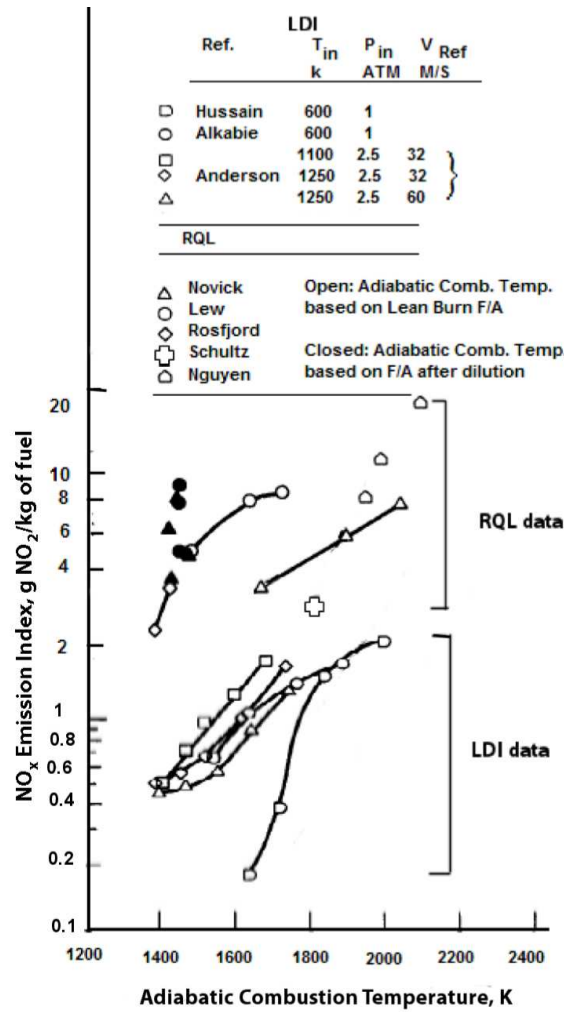


Figure 2.4: Comparison between LDI and RQL  $\text{NO}_x$  data

Tacina et al. [43, 44, 45] implemented the multi-point fuel-injection/multi-burning zone concept in LDI combustors. Each of the fuel injection devices consists of a simplex atomizer and an air swirler. All the air swirlers swirl the air in the same direction. The fuel injector tips were fed by two manifolds to evaluate fuel staging.



Figure 2.5: Multi-point fuel injector module [45]

Tests were conducted with the modules containing 25 [44], 36 [43] and 49 (see Fig. 2.5) [45] fuel injectors in a 76x76 mm area. Test conditions included inlet air temperatures up to 810 K, inlet pressures up to 2700 kPa and the fuel was JP8. Low  $\text{NO}_x$  levels were reported over the range of test conditions. The results showed that the  $\text{NO}_x$  levels were about 70% lower than the 1996 ICAO standard. Furthermore, the data showed that the  $\text{NO}_x$  emissions followed the expected trends of increasing with increasing inlet pressure and temperature and decreasing with increasing air pressure drop. The NASA Glenn Research Center developed a correlation [8, 44] relating the emission index of  $\text{NO}_x$  ( $E\text{INO}_x$ ) to inlet temperature, inlet pressure, equivalence ratio and pressure drop, based on several LDI configurations tested in the Advanced Subsonic Technology (AST) and the Ultra Efficient Engine Technology (UEET) programs. The correlation is given by:

$$E\text{INO}_x = 0.104 \exp(T_3/185) \text{FAR}^{1.32} P_3^{0.68} (\Delta P/P_3)^{-0.36} \quad (2.9)$$

where FAR is the fuel-to-air ratio,  $T_3$  is the combustor inlet temperature,  $P_3$  is the combustor inlet pressure, and  $\Delta P$  is the pressure drop across the combustion chamber.

To demonstrate the potential of LDI combustors, Marek et al. [46] studied various low  $\text{NO}_x$  LDI concepts for pure hydrogen combustion in aircraft gas turbine combustors. Five fuel injector designs were tested in 2.5 and 3.5 inch diameter flame tubes with non-vitiated heated air and gaseous hydrogen. To minimize the risk of flashback, design mixing times were kept short and velocities high. Results showed that for some configurations,  $\text{NO}_x$  emissions were comparable to that of LDI combustors using Jet-A fuel. No flashback or auto-ignition phenomena were encountered. The results also demonstrated that a lower level of  $\text{NO}_x$  was achieved with an increasing number of injection points. Nevertheless, Marek et al. cited the difficulties in constructing such small injectors. In addition, they acknowledged the problems concerning cooling of the combustors.

Cai et al. [47] studied the LDI concept having a single injection system. Experiments were conducted for both non-reacting and reacting flows at ambient temperature and pressure. Figure 2.6 shows the test section (flame tube) setup of the single-element LDI. The element consists of an air swirler, a fuel injector, and a converging-diverging

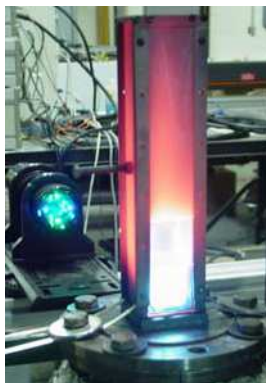


Figure 2.6: Test section setup for the single-element LDI [47]

venturi that ends at the dump plane of a square combustion chamber. The air swirler is a vane annular swirler comprising six helicoidal axial vanes with downstream vane angles of  $60^\circ$ . The inner and outer diameters of the swirler are 22.5 mm and 8.8 mm, respectively. The fuel is injected through the center of the swirler and the fuel tip is at the throat of the venturi. Both the converging and diverging angle of the venturi are  $45^\circ$ . In accordance with Eqn. 2.6, the calculated swirl number is 1.23.

For spray measurements, an Aerometrics two-component Phase Doppler Particle Analyzer (PDPA) was used which had a 3 watt argon laser and a transmitter with 500 nm focus lens. The data rate was 3000 to 20,000 Hz and an average of 10,000 data points were collected during a seven second period at each measurement location. Results were presented for the gas velocity components, spray velocity, and drop size distributions at several axial locations within the combustion chamber.

Cai et al. found that the strong swirl generated by the helicoidal vanes affected mean diameter profiles, thereby providing more uniform drop sizes. The results indicate that heat released during combustion increases the mean and turbulent velocities relative to the non-reacting case. They concluded that the interaction between liquid and gas phases caused a decrease in the recirculation zone during combustion.

## 2.5 Recent Studies on LDI Combustors

The work of Cai et al. is of special importance since the same physical geometry for the air swirler-fuel injector module was used later in the baseline MPLDI configuration developed by the NASA Glenn Research Center [15]. The baseline MPLDI (see Fig. 2.7) has nine air swirler-fuel injector modules arranged in a 3x3 array that are designed to fit within a 76.2 mm square section with the center-to-center distance between the

modules equal to 25.4 mm. All the nine swirlers rotate in the same direction. A few experiments have been conducted recently on this configuration, which are discussed in this section.

Heath et al. [15] performed a series of tests at high inlet pressures (1034 – 1379 kPa) and temperatures (672 – 828 K) using Jet-A fuel to characterize operation of the



Figure 2.7: Perspective view of the MPLDI test hardware (Courtesy of NASA)

baseline MPLDI strategy for potential use in future gas turbine combustor applications. The total equivalence ratio was varied between 0.41 and 45. They measured fuel velocities and fuel drop sizes by employing optical diagnostic methods, such as phase Doppler interferometry (PDI) and particle image velocimetry (PIV). The results showed that average arithmetic mean diameters ( $D_{10}$ ) of drops were typically less than  $20\mu\text{m}$ . PDI measurements revealed that close to the dump plane, the highest drop velocities occurred where the jets from adjacent injectors mix. On the other hand, the lowest velocities were found along the injector centerline within the injector’s hollow cone. Local turbulence levels are at a maximum where adjacent fuel jets mix and at a minimum in the boundary regions of the spray cones. PIV measurements yielded similar results for average drop velocity and RMS fields.

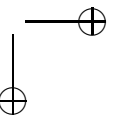
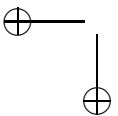
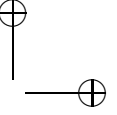
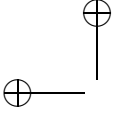
Most recently, Hicks et al. [48] presented data from the measurements taken in an optically-accessible, JP8-fueled, flame tube combustor using the baseline MPLDI hardware. Test conditions for the experiments were the same as for the work of Heath et al. Experiments were performed by splitting the fuel evenly to all the injectors and fueling the central injector only. PIV and chemiluminescence measurements exhibited that the burning zone extended farther downstream for the center-only cases than it did for the corresponding equally-fueled cases. However, the local equivalence ratio for the center-only cases was much higher than it was for the evenly-fueled cases. Results from the high speed chemiluminescence tests indicate that combustion reduces the size of the recirculation zone.

In addition to the experimental works, a few numerical investigations have been performed on LDI. It includes the work of Patel and Menon [49], which describes spray-turbulence-flame interactions in the single-element LDI using the LES method. The simulations were carried out by using a NASA developed in-house code, namely, the National Combustion Code (NCC) [50]. The results illustrate a few unsteady features, such as the dispersion of the spray by the precessing vortex core (PVC) structure and the flame stabilization by the vortex breakdown bubble (VBB). Furthermore, the work analyzes liquid drop-drop and gas-liquid drop correlations.

Davoudzadeh et al. [51] investigated non-reacting cold flow in the single-element and MPLDI combustors. For the single-element LDI, the Reynolds-averaged Navier-Stokes (RANS) and the LES results for the mean velocity components exhibited some discrepancy close to the chamber inlet. This was attributed to the coarse grid used for the LES calculations. The results are also comparable with the measurement data. The cold flow simulation for the MPLDI was discussed briefly with the results depicting a small recirculation zone generated from each of the nine swirlers.

Dewanji et al. [52] also performed non-reacting cold flow simulations for the single-element and MPLDI combustors. The unsteady RANS (URANS) results of both mean and turbulent velocity components for the single-element LDI are in good agreement with the experiments of Cai et al. [47]. The simulations for the MPLDI were carried out using the URANS and LES methods. Between the two numerical methods, the magnitude of velocities differ significantly near the combustion chamber inlet, although the velocity contour structures display similarities at all of the computed locations. The simulations captured the fundamental aerodynamic flow features, such as the recirculation zone of the individual swirlers and the highly complex flow structures at the chamber entrance and at the interface of the adjacent swirlers. The strong turbulent flow and the presence of dynamic vortex structures in the proximity of the combustion chamber inlet indicate a large degree of unsteadiness in the flow field. Dewanji et al. further studied reacting sprays in LDI combustors [53, 54, 55, 56]. Several numerical spray models were applied to model various spray sub-processes. The studies indicate that the swirling flow strongly influences the spray velocity and the drop size distribution and show the momentum exchange between the liquid and gas phases.

Liu [57] performed two-phase turbulent combustion modeling and simulations for the single-element LDI using the time filtered Navier-Stokes (TFNS) methodology ranging from steady RANS, URANS, to the dynamic flow structure simulation (DFS). Furthermore, the LES method was used for the calculations. The sub-grid models employed for turbulent mixing and combustion included the well mixed model, the linear eddy mixing (LEM) model, the filtered mass density function (FDF/PDF) model, and the flamelet based model. All the calculations were conducted using the same grid that was built for the RANS simulations. The results show that the PVC enhances spray particle dispersion. Liu observed that the premixed, partially-premixed and non-premixed flames were in close proximity to each other in the combustor. Nevertheless, the author considered the results being preliminary, due to the uncertainty in the imposed starting condition for the spray, the use of a five-species single step global chemistry model, and the non-optimized coupling between the CFD finite-volume module and the LEM or FDF/PDF module. Furthermore, the role of the grid size in the performance of these sub-grid models was not investigated.



## 3. Fundamentals of Sprays

### 3.1 Introduction

Spray combustion is important in many applications, including spark-ignited engines, diesel engines, gas turbines, and liquid rocket engines. It is a complicated subject because it involves many different processes. A typical sequence of events would be the injection and atomization of liquid fuel into gas, mixing of droplets with the gas, heat transfer to droplets causing evaporation of liquid, mixing of fuel vapor with the gas, and gas-phase combustion. Furthermore, these processes are accompanied by various additional aspects of finite-rate chemistry, such as fuel pyrolysis, production of oxides of nitrogen, and extinction phenomena.

A spray is generally considered as a system of droplets immersed in a gaseous phase. Sprays belong to a specific type of two-phase flow, which includes liquid phase in the discrete form and gas phase as the continuum. In a gas turbine combustion chamber, liquid fuel jets or sheets are injected through one or several injector orifices. The atomization process causes the disintegration of liquid streams into ligaments and then droplets. Finally, the fuel droplets evaporate and the vaporized fuel mixes with the oxidizer to produce a combustible mixture.

Sprays may be produced in various ways, but there are some fundamental processes associated with all the methods of atomization. In principle, a spray is generated as a result of a high relative velocity between the liquid to be atomized and the surrounding air or gas. Different atomizers accomplish this in different ways. For instance, pressure atomizers and rotary atomizers eject the liquid at a high velocity from the periphery of a rotating cup or disk into a relatively slow-moving air or gas. On the contrary, air-assist and air-blast atomizers release the liquid at a relatively slow velocity into a high-velocity air or gas stream.

The atomization process has a great deal of influence on spray evaporation rates because it increases the total surface area of the liquid, which in turn significantly influences the combustion process. The hydraulics of the flow within the atomizer determines the turbulence properties of the emerging liquid stream. The growth of initially small disturbances over the liquid surface is responsible for the disintegration of the liquid core into ligaments and then droplets. The development of the liquid jet or sheet emerging from the atomizer and the disintegration of the liquid surface are taken into consideration to determine the essential spray characteristics, such as the shape and penetration of the spray, number density, drop velocity, and drop size

distribution as a function of space and time. To be able to describe spray combustion, it is necessary to get a detailed understanding of the fundamentals of various spray regimes and spray sub-processes. Detailed modeling of spray sub-processes can lead to significant improvements in quality and performance of spraying systems and reduction of emission of pollutants.

The theory of spray combustion and its modeling are split into two chapters. This chapter discusses the main principles of spray combustion and its sub-processes. The numerical models related to various spray processes, which are applied in this research to simulate the reacting spray in the LDI combustors, are described in Chapter 5. The present chapter is structured as follows. In the next section, the equations governing the various spray regimes are briefly described. This is followed by a discussion on the basic principles of various spray sub-processes. Finally, the main properties of sprays are discussed.

## 3.2 Governing Equations

### 3.2.1 Two-phase Flow Characteristics

The various important spray regimes due to liquid injection from a single hole nozzle are summarized in Fig. 3.1. It shows that near the injector nozzle exit, the spray drops occupy a significant fraction of the total volume of the two-phase mixture. This region is typically known as the thick or dense spray regime. As the spray diverges away from the nozzle, the size of the drops is reduced due to drop breakup and evaporation. Consequently, at the locations far away from the nozzle, the drops become isolated with negligible mass and volume compared to that of the surrounding gas. This region is termed the very thin or dilute spray regime. Although the drops in this regime continue to exchange mass, momentum, and energy with the gas-phase, the state of the gas is hardly affected by the exchange processes. The intermediate spray regime, which falls between the thick and the very thin regime, is known as the thin regime. Since volume fraction of the liquid in the very thin spray regime is negligible,

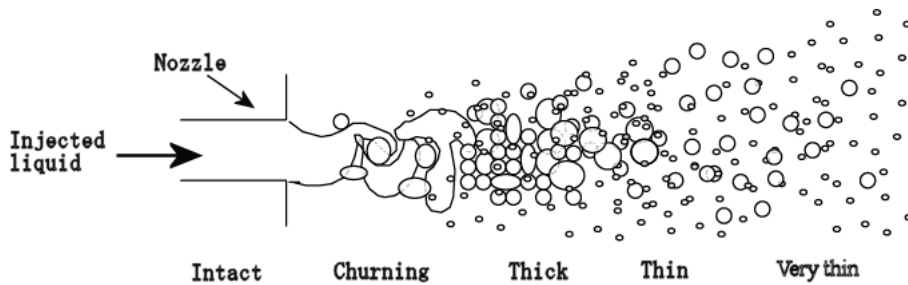


Figure 3.1: Schematic representation of various spray regimes for liquid injection from a nozzle

the drops can be tracked using a spray equation [58], which describes the evolution of

the droplet distribution function  $f$ . For the dilute spray regime,  $f$  has 9 independent variables including three drop position coordinates  $\mathbf{x}$ , three velocity components  $\mathbf{v}$ , the drop radius  $r$ , and the drop temperature  $T_d$ . Therefore,

$$f(\mathbf{x}, r, \mathbf{v}, T_d, t) dx dr d\mathbf{v} dT_d \quad (3.1)$$

is the probable number of droplets located at position  $\mathbf{x}$  and time  $t$  with drop radii in the interval  $(r, r + dr)$ , velocities in the interval  $(\mathbf{v}, \mathbf{v} + d\mathbf{v})$ , and temperatures in the interval  $(T_d + dT_d)$ . The above expression considers a uniform temperature within the drop. The total fraction of the volume occupied by the gas-phase is termed the gas-phase void fraction,  $\theta_g$ . For the very thin spray,  $\theta_g$  is found by integrating the liquid volume over all the drops

$$\theta_g = 1 - \int_{Vol} \left( \int \int \int \frac{4}{3} \pi r^3 f dr d\mathbf{v} dT_d \right) dVol / Vol \quad (3.2)$$

Furthermore, in this spray regime, the isolated drop correlations [58] are used to characterize the exchanges of mass, momentum, and energy between the drops and the gas-phase, while neglecting the effects of drop interactions.

In the thin spray regime, although the liquid volume fraction is still low, the drops have a significant mass compared to the gas. Therefore, the drops can also affect the state of the gas.

Unlike both the thin and very thin spray regimes, the thick spray regime contains a significant amount of drops. The volume fraction of the liquid is much higher in this region. In addition, the liquid can be recognized as discrete drops in the gas-phase. However, the effects of drop interactions such as collision and coalescence become very important, and they in turn influence the exchange rates. The earlier results suggest that a practical definition for the beginning of the thick spray regime can be considered as  $\theta_g < 0.9$  [59].

The churning flow, as shown in Fig. 3.1, essentially occurs in the region where the intact liquid core starts to break up into a spray. In this regime, the volume fraction of the liquid equals or exceeds that of the gas. In addition, the liquid is not dispersed in the gas-phase. In the past, some works were done to calculate the exchange rates between the two phases. However, the form and the applicability of the coupling terms between the two phases are not clear yet. As a consequence, most spray simulations assume the spray being in the thin or very thin regime.

### 3.2.2 Gas-phase Equations

The governing equations for the gas-phase include equations of mass, momentum, and energy conservation, supplemented by the equations of a turbulence model. The interactions between the liquid drops and the gas-phase is accounted for by considering the exchange functions.

In the absence of the liquid drops, the gas-phase mass conservation equation is

$$\int_{Vol_g} \left\{ \frac{\partial \rho_g}{\partial t} + \nabla \cdot (\rho_g \mathbf{u}) \right\} dVol_g = 0 \quad (3.3)$$

where  $\rho_g$  is the gas density and  $\mathbf{u}$  is the velocity of the gas. When the liquid drops are not considered, the volume occupied by the gas,  $Vol_g$ , represents the total volume.

When the spray drops are present, the differential form of the gas-phase mass conservation equation becomes

$$\int_{Vol} \left\{ \frac{\partial \rho}{\partial t} + \nabla \cdot (\rho \mathbf{u}) \right\} dVol = - \int_{Surf_d} \rho_g (\mathbf{u} - \mathbf{w}) \cdot \mathbf{n}_d dA \quad (3.4)$$

where  $\rho$  is the gas mass per unit volume of the mixture,  $Surf_d$  are the inner surfaces of the control volume in contact with the drops,  $\mathbf{w}$  refers to the interface velocity, and  $dA$  is an element of total surface area. The total volume now becomes  $Vol$ , which consists of the volume of the gas ( $Vol_g$ ) and the volume occupied by the drops ( $Vol_d$ ). The integral on the right-hand side represents the source or sink of gas mass due to evaporation or condensation from the drops.

For an individual drop, the rate of change of liquid mass due to evaporation can be expressed as

$$\frac{\partial}{\partial t} \left( \frac{4}{3} \pi r^3 \rho_l \right) = \int_{Surf_d} \rho_l (\mathbf{w} - \mathbf{v}) \cdot \mathbf{n}_d dA \quad (3.5)$$

where  $\rho_l$  is the liquid density,  $\mathbf{v}$  is the drop velocity and the integration is over the surface of the drop. For mass conservation, the right hand sides of the Eqns. 3.4 and 3.5 must be equal. When Eqn. 3.5 is summed over all of the drops, and the liquid density is assumed to be constant, Eqn. 3.4 becomes

$$\frac{\partial \rho}{\partial t} + \nabla \cdot (\rho \mathbf{u}) = - \int \int \int \rho_l 4\pi r^2 R f dr d\mathbf{v} dT_d \quad (3.6)$$

This is the final form of the mass conservation equation, where  $R$  is time rate of change of drop radius  $r$ , and  $T_d$  is the temperature of the drop.

Similarly, the momentum equation can be obtained. For a single drop, linear momentum conservation gives

$$\frac{4}{3} \pi r^3 \rho_l \mathbf{F} = \int_{Surf_d} [\rho_g (\mathbf{u} - \mathbf{v})(\mathbf{v} - \mathbf{w}) \cdot \mathbf{n} - P_g \mathbf{n} + \tau_g \cdot \mathbf{n} + \sigma \nabla \cdot \mathbf{n}] dA \quad (3.7)$$

where  $\mathbf{F}$  is the acceleration of the drops,  $\tau_g$  is the viscous stress tensor of the gas,  $P_g$  is the thermodynamic pressure of the gas, and  $\sigma$  is the surface tension. Equation 3.7 implies that if the evaporation is symmetric, the first term on the right-hand side is equal to zero, because the thrust imparted to the drop is zero.

For a mixture of reacting gases, the mass conservation equation for species  $m$  has source terms arising from the chemical reactions and the vaporization of drops.

$$\frac{\partial \rho_m}{\partial t} + \nabla \cdot (\rho_m \mathbf{u}) = \nabla \cdot \left[ \rho D \nabla \left( \frac{\rho_m}{\rho} \right) \right] + \dot{\rho}_m^c + \dot{\rho}^s \delta_{m1} \quad (3.8)$$

where  $\rho_m$  is the mass density of species  $m$ ,  $\rho$  is the total mass density,  $D$  is the diffusion coefficient,  $\dot{\rho}_m^c$  is the source term due to chemical reactions, and  $\dot{\rho}^s \delta_{m1}$  corresponds to the source term due to evaporation of species (1 corresponds to the fuel and  $\delta$  is the Kronecker delta function).

The momentum equation (including turbulence modeling) for the fluid mixture becomes

$$\frac{\partial \rho \mathbf{u}}{\partial t} + \nabla \cdot (\rho \mathbf{u} \mathbf{u}) = -\nabla p - \nabla \left( \frac{2}{3} \rho k \right) + \nabla \tau + F^s + \rho g \quad (3.9)$$

where  $P$  is the fluid pressure,  $k$  is the turbulent kinetic energy,  $\tau$  is the total viscous stress tensor, and  $F^s$  is the rate of momentum gain per unit volume due to the spray. In this equation, the body force  $g$  is assumed to be constant.

The viscous stress tensor is related to the diffusion coefficient  $D$  as follows:

$$\tau = \rho D [(\nabla \mathbf{u} + \nabla \mathbf{u}^T) - \frac{2}{3} \nabla \cdot \mathbf{u} \mathbf{I}] \quad (3.10)$$

where  $\mathbf{I}$  is a unit dyadic.

The energy conservation equation for a single drop introduces the terms that account for the energy required to heat the drop and the work associated with the stresses plus heat transfer. The equation for the internal energy becomes

$$\frac{\partial \rho I}{\partial t} + \nabla \cdot (\rho \mathbf{u} I) = -P \nabla \cdot \mathbf{u} - \nabla \cdot J + \rho \varepsilon + \dot{Q}^c + \dot{Q}^s \quad (3.11)$$

where  $I$  is the specific internal energy,  $J$  is the heat flux vector,  $\varepsilon$  is the turbulent dissipation rate, and  $\dot{Q}^c$  and  $\dot{Q}^s$  are the source terms arising from the heat release due to chemical reactions and spray interactions respectively. Chemical energy is not included in the specific internal energy term,  $I$ .

The heat flux vector  $J$  includes the effects of turbulent heat conduction and enthalpy diffusion.

$$J = -\lambda \nabla T - \rho D \sum_m h_m \nabla (\rho_m / \rho) \quad (3.12)$$

where  $\lambda$  is the thermal conductivity and  $h_m$  is the specific enthalpy of species  $m$ .

Equations 3.8-3.12 indicate that the diffusion coefficient term  $D$  influences the transport of mass, momentum, and energy. The diffusion coefficient is related to the transport of turbulent kinetic energy  $k$  and its dissipation rate  $\varepsilon$  as follows:

$$D = C_\mu k^2 / \varepsilon \quad (3.13)$$

where  $C_\mu$  is a constant.

The turbulent kinetic energy  $k$  and its dissipation rate  $\varepsilon$  are modeled by selecting a suitable turbulence model. For instance, the standard  $k - \varepsilon$  turbulence model yields:

$$\frac{\partial \rho k}{\partial t} + \nabla \cdot (\rho \mathbf{u} k) = -\frac{2}{3} \rho k \nabla \cdot \mathbf{u} + \tau \cdot \mathbf{u} + \nabla \cdot \left[ \left( \frac{\mu}{Pr_k} \right) \nabla k \right] - \rho \varepsilon + \dot{W}^s \quad (3.14)$$

$$\frac{\partial \rho \varepsilon}{\partial t} + \nabla \cdot (\rho \mathbf{u} \varepsilon) = - \left( \frac{2}{3} C_{\varepsilon 1} - C_{\varepsilon 3} \right) \rho \varepsilon \nabla \cdot \mathbf{u} + \nabla \cdot \left[ \left( \frac{\mu}{Pr_\varepsilon} \right) \nabla \varepsilon \right] + \frac{\varepsilon}{k} (C_{\varepsilon 1} \tau \cdot \mathbf{u} - C_{\varepsilon 2} \rho \varepsilon + C_s \dot{W}^s) \quad (3.15)$$

Equations 3.14 and 3.15 include some source terms. The source term  $-\left(\frac{2}{3}C_{\varepsilon 1} - C_{\varepsilon 3}\right)\rho\varepsilon\nabla\cdot\mathbf{u}$  accounts for the changes in the length scale due to velocity dilatation. The terms linking to the shear stress tensor,  $\tau$ , refer to the rate of turbulence production. Source terms involving  $\dot{W}^s$  imply interactions with the spray.  $C_{\varepsilon 1}$ ,  $C_{\varepsilon 2}$ ,  $C_{\varepsilon 3}$ ,  $Pr_k$ ,  $Pr_\varepsilon$ , and  $C_s$  are the model constants for the standard  $k - \varepsilon$  model.

### 3.2.3 Discrete-phase Equations

The governing equation of spray [58] explains the development of the droplet distribution by using a distribution function  $f$ . The function  $f$  represents the probable number of droplets.

$$f(\mathbf{x}, r, \mathbf{v}, T_d, y, \dot{y}, t) d\mathbf{x} dr d\mathbf{v} dT_d dy d\dot{y} \quad (3.16)$$

Therefore,  $f$  has 11 independent variables including three droplet position coordinates  $\mathbf{x}$ , the drop radius coordinate  $r$ , three velocity components  $\mathbf{v}$ , the drop temperature  $T_d$ , the drop distortion  $y$ , the rate of change of drop distortion  $\dot{y}$ , and time  $t$ .

Equation 3.16 can be solved to obtain the time rate of change of the distribution function  $f$ ,

$$\frac{\partial f}{\partial t} + \nabla_{\mathbf{x}} \cdot (f\mathbf{v}) + \nabla_{\mathbf{v}} \cdot (f\mathbf{F}) + \frac{\partial}{\partial r}(fR) + \frac{\partial}{\partial T_d}(f\dot{T}_d) + \frac{\partial}{\partial y}(f\dot{y}) + \frac{\partial}{\partial \dot{y}}(f\ddot{y}) = \dot{f}_{coll} + \dot{f}_{bu} \quad (3.17)$$

where the properties  $\mathbf{F}$ ,  $R$ ,  $\dot{T}_d$ , and  $\dot{y}$  are the time rates of changes of velocity, radius, temperature, and oscillation velocity ( $\dot{y}$ ) of an individual drop, respectively.  $\dot{f}_{coll}$  and  $\dot{f}_{bu}$  are the source terms arising from droplet collision and breakup.

By solving the spray equation, the source terms or the exchange functions  $\dot{\rho}^s$ ,  $F^s$ ,  $\dot{Q}^s$ , and  $W^s$  are obtained, which can be used in the reacting mixture equations of mass conservation, momentum, internal energy, and the transport of turbulent kinetic energy and its dissipation rate. The exchange functions can be calculated by adding the rate of mass, momentum, and energy for all the droplets present in the spray at position  $\mathbf{x}$  and time  $t$ .

The mass source term arising from vaporization of spray becomes

$$\dot{\rho}^s = - \int f \rho_l 4\pi r^2 R d\mathbf{v} dr dT_d dy d\dot{y} \quad (3.18)$$

The droplet drag is responsible in transmitting force to the gas, which gives rise to the exchange function  $F^s$ , i.e.,

$$F^s = - \int f \rho_l \left( \frac{4}{3} \pi r^3 \mathbf{F}' + 4\pi r^2 R \mathbf{v} \right) d\mathbf{v} dr dT_d dy d\dot{y} \quad (3.19)$$

where  $\mathbf{F}' = \mathbf{F} - g$ .

The function  $\dot{Q}^s$ , which determines the exchange of energy in the multi-phase flow, accounts for the energy transmission to the gas by drop evaporation, heat transfer into the drop, and work done due to turbulent fluctuations. It can be expressed in the following form:

$$\dot{Q}^s = - \int f \rho_l \left[ 4\pi r^2 R [I_l + \frac{1}{2}(\mathbf{v} - \mathbf{u})^2] + \frac{4}{3} \pi r^3 [c_l \dot{T}_d + \mathbf{F}' \cdot (\mathbf{v} - \mathbf{u} - \mathbf{u}')] \right] d\mathbf{v} dr dT_d dy d\dot{y} \quad (3.20)$$

where  $I_l$  and  $c_l$  are the internal energy and specific heat of liquid drops, respectively.  $(\mathbf{v} - \mathbf{u})$  is the relative velocity between the droplet and gas.  $\mathbf{u}'$  is the turbulent velocity of the gas.

The transport of turbulent kinetic energy,  $k$ , and its rate of dissipation,  $\varepsilon$ , as shown in Eqns. 3.14 and 3.15, yields a source term  $\dot{W}^s$ . This exchange term essentially arises due to the interactions between the gas-phase and spray. It is written in the following form:

$$\dot{W}^s = - \int f \rho_l \frac{4}{3} \pi r^3 \mathbf{F}' \cdot \mathbf{u}' dv dr dT_d dy dj \quad (3.21)$$

The exchange function in Eqn. 3.21 is negative. This is due to the fact that the turbulent eddies do work in dispersing the liquid droplets, which results in the loss of energy in the gas-phase.

### 3.3 Classifications of Models

The governing equations for spray can be simplified by adopting different assumptions for spray combustion modeling. In general, to simplify interpretation of multiphase flow phenomena in reacting sprays, effects of evaporation and combustion are treated as a separate subject. For premixed combustions, the idea behind treating combustion separately can be justified, because the fuel is essentially premixed and prevaporized before combustion. Although spray evaporation and multiphase flow phenomena intersect in these applications, an assumption of non-evaporating sprays still represents a reasonable first step toward understanding premixed combustions. Furthermore, it has been realized that evaporation does not dominate the behavior of other multiphase flow phenomena [60].

For non-premixed combustions, separating combustion and multiphase flow processes can also be considered as a reasonable assumption, because these processes take place at different levels of mixing. This behavior was demonstrated by approximating locally homogeneous-flow (LHF) [61]. The LHF approximation is adopted in an idealized spray consisting of infinitely small drops, where both liquid and gas phases can be safely assumed to have the same velocity and temperature and are in thermodynamic equilibrium at each point in the flow. Predictions based on the LHF approximation of scalar properties as a function of mixture fraction were shown by burning an  $n$ -pentane spray in air at both normal temperature and pressure (NTP) and high pressure conditions [62, 63, 64]. It has been found that liquid is present for mixture fractions greater than 0.9. On the other hand, combustion phenomena associated with the maximum temperature region are restricted to mixture fractions less than 0.1. The low mixture fraction region is similar to a gaseous diffusion flame, involving temperature and density extrema, and the disappearance of fuel vapor and oxygen near the stoichiometric mixture ratio [63, 64]. Therefore, most spray phenomena occur in a situation remote from combustion phenomena, so that neglecting the effects of combustion is a logical first step toward understanding non-premixed reacting sprays.

For LHF models, the spray equation is not required. Furthermore, the source terms in the gas-phase equations due to spray are neglected. As a result, the gas-phase equations are modified. For instance, the gas-phase equations must introduce a mixture density,  $\rho$ , which includes the partial density of species both in the liquid and gas phases, i.e.,

$$\rho = (Y_{fl}/\rho_{fl} + Y_{fg}/\rho_{fg} + Y_a/\rho_a)^{-1} \quad (3.22)$$

where  $Y$  is the species mass fraction, the subscripts  $a$ ,  $fl$ , and  $fg$  refer to the air and the fuel species in its liquid and gaseous forms, respectively.

Unlike the LHF approximations, the separated flow (SF) models do not consider equal phase velocities and account for effects due to finite rates of mass, momentum, and energy exchange between the liquid and gas phases, thus retaining all the terms in the liquid and gas conservation equations [65]. The concept of unequal phase velocities is most important when the densities between the phases are different in the presence of large pressure gradients or a gravitational potential field. The buoyancy effects, as a result of density difference, tend to induce a drift velocity of the lighter phase into the heavier phase. It has been noticed that as the density ratio between the phases approaches zero, the use of the LHF models becomes more practical, because the drift velocity would be reduced as the buoyancy of the lighter phase diminishes. Nevertheless, an accurate modeling of flow around individual droplets in a spray is computationally very expensive. As a result, the exchange functions between the phases are often modeled by implementing semi-empirical correlations.

### 3.4 Spray Sub-processes

This section briefly discusses various sub-processes that are associated with spray phenomena. This includes atomization and drop breakup, drop drag and deformation, turbulent dispersion, drop collision and coalescence, and spray vaporization.

#### 3.4.1 Atomization and Drop Breakup

The atomization process converts bulk liquid into small drops by disrupting the consolidating influence of surface tension. In most cases, both internal and external influences, such as turbulence in the liquid, cavitation in the nozzle, and external aerodynamic forces on the liquid surface contribute to atomization. In general, the atomization process is divided into primary atomization and secondary atomization processes, due to their distinctive influences on the outcomes. During primary atomization, the liquid fuel stream is split up into ligaments and large drops, while secondary atomization further disintegrates the ligaments and large drops into smaller droplets. The two atomization processes together determine the detailed characteristics of the fuel spray, which include size, distribution, and velocity of liquid droplets. Nevertheless, these properties of the liquid spray are significantly influenced by the internal geometry of the atomizer, the effects of the surrounding medium (gas-phase flow), and the physical attributes of the fuel being injected.

#### Drop Breakup

The mechanisms involved in the drop breakup process can be explained by using the Weber number,  $We$ , which is the ratio of the disruptive force to the consolidating

surface tension force. For example, in a non-evaporating spray,  $We$  becomes

$$\begin{aligned} We &= \frac{\rho_a U_{rel}^2}{\sigma_l / d_l} \\ &= \frac{\rho_a U_{rel}^2 d_l}{\sigma_l} \end{aligned} \quad (3.23)$$

where  $\rho_a$  is the air density,  $U_{rel}$  is the relative velocity between the liquid and the air,  $\sigma$  is the surface tension of the liquid, and  $d_l$  is the diameter of the liquid drop.

The drop breakup reaches the critical condition, when the aerodynamic force is equal to the surface tension force, i.e.,

$$\begin{aligned} C_D \frac{1}{2} \rho_a U_{rel}^2 \frac{\pi}{4} d_l^2 &= \pi d_l \sigma_l \\ (\rho_a U_{rel}^2 d_l / \sigma_l)_{crit} &= 8 / C_D \end{aligned} \quad (3.24)$$

where  $C_D$  is the drag coefficient of the drop.

Combining Eqns. 3.23 and 3.24 gives

$$We_{crit} = 8 / C_D \quad (3.25)$$

where  $We_{crit}$  is the critical Weber number for the onset of drop breakup.

Another important dimensionless number is Ohnesorge number,  $Oh$ , which accounts for the influence of liquid viscosity on drop breakup. It is expressed in the following form:

$$\begin{aligned} Oh &= \frac{\sqrt{We}}{Re} \\ &= \frac{\mu_l}{\rho_l \sigma_l d_l} \end{aligned} \quad (3.26)$$

where  $Re$  is the Reynolds number,  $\mu_l$  is the liquid viscosity, and  $\rho_l$  is the liquid density. Essentially,  $Oh$  relates the viscous forces to inertial and surface tension forces.

A high relative velocity between the fuel and the surrounding air is essential for drop breakup. However, in turbulent flow field, it is difficult to determine the relative velocities since the drops become airborne shortly after leaving the injector. In such scenarios, the dynamic pressure forces of the turbulent air stream is considered to determine the size of the largest drop in the spray [5]. The critical Weber number becomes

$$We_{crit} = \frac{\rho_a \overline{u'^2} d_{lmax}}{\sigma_l} \quad (3.27)$$

where  $\sqrt{\overline{u'^2}}$  is the root mean square (RMS) value of the velocity fluctuations and  $d_{lmax}$  is the maximum drop diameter.

### Drop Breakup Regimes and Mechanisms

Based on the relative velocity between the liquid drops and the surrounding medium, drop breakup regimes can be classified into three main groups: the bag breakup

regime, the shear or boundary layer stripping breakup regime, and the catastrophic breakup regime [66]. On the other hand, the breakup processes of the liquid drops can be classified into two stages. During the first stage, in all the three breakup regimes, the drops experience a shape change. However, during the second stage, the distorted drops undergo disintegration, and the three breakup regimes exhibit contrasting breakup mechanisms.

### First Breakup Stage

A spherical liquid drop in a steady air stream experiences a variable air pressure distribution. Under equilibrium conditions, the internal pressure at any point on the drop surface is sufficient to balance the external aerodynamic pressure and the surface tension pressure. Nevertheless, as the steady air stream flows around the drop, the distributions of air velocity and pressure at any point on the drop surface become non-uniform. The air velocity has a maximum at the drop’s equator and equals zero at the drop’s poles. Therefore, from the Bernoulli’s Law, the air pressure becomes higher at the poles and lower at the equators. Consequently, the external aerodynamic pressure causes the drop to distort from its undisturbed spherical shape to a flat ellipsoid, normal to the air flow direction. The drop further flattens with an increase in Bernoulli pressure difference, and finally forms a disk-shaped profile. In all drop breakup regimes, the flattening process occurs as soon as the injected drops enter the air jet [66].

### Second Breakup Stage

As the relative velocity between the liquid drops and surrounding gas increases, various breakup regimes are encountered. During the second breakup stage, the flattened drops produced in the first stage undergo disintegration to form small droplets. However, different breakup regimes display different disintegration mechanisms.

1. *Bag breakup*: The bag breakup phenomenon, as shown in Fig. 3.2, appears when the relative velocity is low [67]. It occurs at about  $We = 6$ . The flattened disk-shaped drop produced during the first breakup stage is accelerated, and at

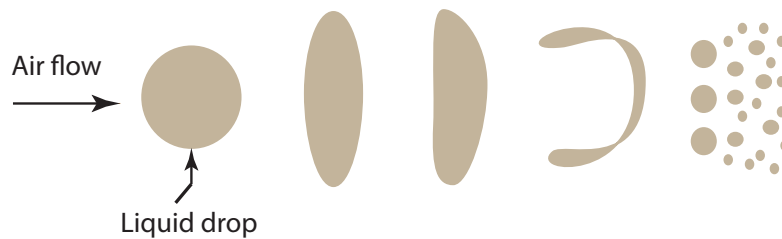


Figure 3.2: Schematic representation of the bag breakup mechanism

a critical velocity, its surface becomes concave near a pole. After that, the pole is blown out and the disk deforms into a thin hollow bag-like structure. The

bag-shaped drop is stretched and swept off in the downstream direction. The rupture of the bag produces small drops and the liquid located in the rim of the distorted disk eventually breaks up into relatively large drops.

2. *Shear breakup*: If the velocity of the surrounding medium is further increased, breakup occurs at the edges of the equator of the flattened drop. The shear breakup phenomenon, as shown in Fig. 3.3, essentially commences at about  $We > 80$ . Unlike the bag breakup process, where the pole region is blown out into a thin hollow bag, the shear breakup causes the drop to deform in

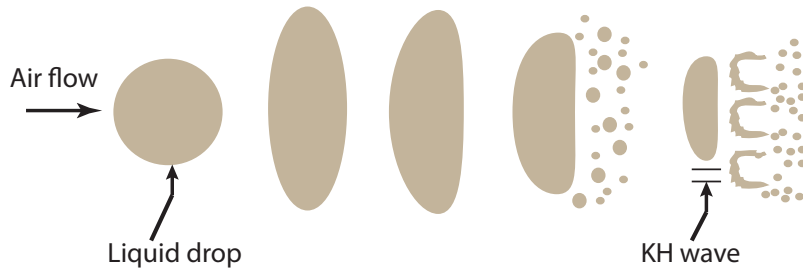


Figure 3.3: Schematic representation of the shear breakup mechanism

the opposite direction, resulting in a convex surface facing toward the flow of air/gas. The edges of the saucer-shaped drop are drawn out into a thin sheet, and then the sheet is split up into ligaments, which later break up into drops [66]. The unstable growth of surface waves of short wavelength is primarily involved in this breakup process. These waves are known as Kelvin-Helmholtz (KH) waves.

3. *Catastrophic breakup*: This breakup regime (see Fig. 3.4) starts at about  $We > 350$ . The breakup mechanisms of the shear and catastrophic breakup regimes have some similarities. For instance, in both regimes (1) the liquid drop is flattened significantly and the edge of the flattened drop is bent in the

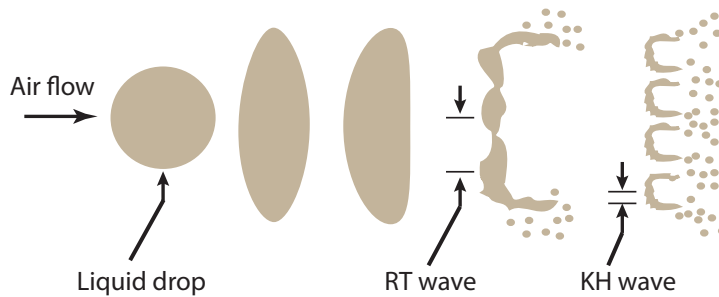


Figure 3.4: Schematic representation of the catastrophic breakup mechanism

direction of the flow of the surrounding gas by the high velocity gas stream blowing, which makes the flattened drop display a convex surface facing the

gas flow, (2) the edges of the saucer-shaped droplet are pulled out into a thin sheet, which is split up into ligaments and then into small drops. The KH waves originate on the fragmented surfaces to form small droplets. However, further investigations revealed the presence of some additional breakup features in the catastrophic regime. The growth of unstable surface waves were observed on the flattened drop surfaces in the azimuthal direction [68]. The Rayleigh-Taylor (RT) instabilities were believed to promote these waves due to the large acceleration of drop in the gas stream.

### 3.4.2 Drop Drag and Deformation

From the drop breakup theory, it is realized that a drop undergoes shape change during its breakup process, resulting in a variation of drop drag. Drag affects the acceleration of drop, which in turn, influences its physical location, velocity, and penetration in the surrounding gas medium. Furthermore, drop drag can also affect the gas-phase properties. Therefore, in order to accurately predict the properties of drop and gas, it is important to include the dynamic behavior of drop drag during the course of drop breakup. Drag is often specified by its coefficient  $C_D$ .

For thin sprays,  $C_D$  is specified as a function of the drop Reynolds number considering it remains spherical throughout the domain. Therefore, the following solid sphere correlations are applied to calculate the drag coefficient [69].

$$C_{D,sphere} = \begin{cases} \frac{24}{Re} (1 + \frac{1}{6} Re^{2/3}) & Re \leq 1000 \\ 0.424 & Re > 1000 \end{cases} \quad (3.28)$$

For thick sprays, the equation of  $C_D$  for  $Re \leq 1000$  [59, 70] becomes

$$C_{D,sphere} = \frac{24}{Re} (\theta_g^{-2.65} + Re^{2/3} \theta_g^{-1.78} / 6) \quad (3.29)$$

where  $C_{D,sphere}$  is the drag coefficient of a spherical drop and  $\theta_g$  is the local void fraction.

At high relative velocities, oscillation and distortion of drop during the breakup process have an impact on the drop drag coefficient [68, 69]. Under such conditions,  $C_D$  is also a function of the oscillation amplitude, i.e.,

$$C_D = C_{D,sphere} (1 + 2.632y) \quad (3.30)$$

where  $y$  is the drop's distortion from sphericity, and it is calculated by solving the spring-mass analogy equation,

$$\frac{d^2y}{dt^2} = \frac{2}{3} \frac{\rho_g U_{rel}^2}{\rho_l r^2} - \frac{8\sigma_l}{\rho_l r^3} y - \frac{5\mu_l}{\rho_l r^2} \frac{dy}{dt} \quad (3.31)$$

where  $(\frac{dy}{dt})$  is the oscillation velocity ( $\dot{y}$ ),  $(\frac{d^2y}{dt^2})$  is the time rate of change of  $\dot{y}$  ( $\ddot{y}$ ), and  $\rho_g$  is the density of gas medium.

Equation 3.30 indicates that in the limit of no distortion, i.e.,  $y = 0$ , the drag coefficient corresponding to a sphere is obtained. On the other hand, at maximum

distortion, i.e.,  $y = 1$ , the drag coefficient of a disk is obtained, which is about 3.6 times higher than that of a sphere. Therefore, Eqn. 3.30 implies that the drag coefficient of a distorting drop lies between the drag coefficient of a sphere and a disk. In this thesis, for the reacting spray simulation of the LDI combustors, the dynamic drag model (DDM) [71] is used along with the Wave breakup model to include the effects of drop drag.

### 3.4.3 Drop-Turbulence Interactions

In addition to the drop breakup process, subsequent interactions between the phases to produce gaseous reactants are important for spray combustion. The drop-turbulence interactions arise mainly due to the following phenomena.

1. the dispersion of drops by turbulence
2. the modification of turbulence properties by the motion of drops
3. the modification of interphase transport rates by turbulent fluctuations

The dispersion of spray drops by turbulence results in the modulation of gas-phase turbulence. In other words, a portion of the turbulent kinetic energy of gas is spent to do work in dispersing the drops [60]. On the contrary, if the size of the drops are larger than one-tenth of the integral scale of turbulence, wakes produced by the drops will act as a source of turbulence energy, thus increasing the gas-phase turbulence kinetic energy [72]. By evaluating the relative magnitude of these effects, it can be determined whether turbulence modification will increase or decrease turbulence levels [73].

From the experiments, it was observed that in a turbulent flow, small drops had a tendency to follow the large eddies in gas-phase flow, while the larger drops left the large-scale vortex structures [74]. These contrasting phenomena can be described using the Stokes number ( $St$ ), which is a time-scaling ratio of the aerodynamic response time ( $\tau_m$ ) and the time scale associated with large-scale structures ( $\tau_F$ ), i.e.,

$$\begin{aligned} St &= \frac{\tau_m}{\tau_F} \\ &= \frac{\rho_l d_l^2 \Delta U}{18\mu\delta} \end{aligned} \quad (3.32)$$

where  $\Delta U$  is the velocity difference across the large-scale structure and  $\delta$  is the characteristic size of the structure.

The aerodynamic response time is a measure of the responsiveness of a particle to a change in fluid velocity. In essence, the Stokes number assesses the effects of the large-scale vortices on particle dispersion. As shown in Fig. 3.5, for small values of the Stokes number, particles follow the surrounding fluid and disperse as a fluid particle. On the other hand, for particles with large Stokes numbers, the particle to fluid dispersion ratio becomes less than unity, because the large-scale structures have insufficient time to influence the motion of particles. Particles with intermediate

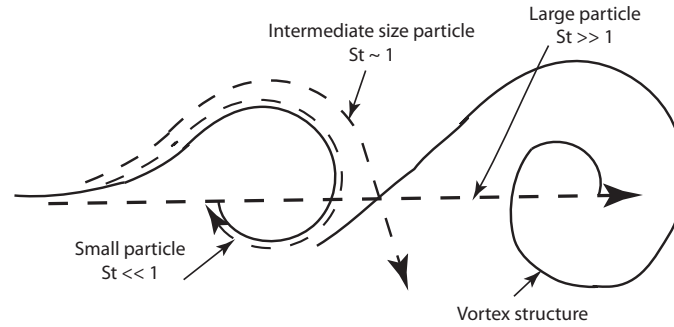


Figure 3.5: Effect of Stokes number on particle dispersion in large-scale turbulent structures [74]

Stokes numbers (the order of unity) are likely to be centrifuged by the eddy. Therefore, in this regime, the particle dispersion can exceed that of the fluid particle.

From the above discussions, it is understood that a turbulent gas-phase strongly influences the motion of small drops and the interactions of small drops with the gas-phase turbulence reduces the rate of production of turbulence kinetic energy. As a result, the source term,  $\dot{W}^s$  in Eqn. 3.21 becomes negative, indicating the depletion of turbulent kinetic energy from the gas-phase.

### 3.4.4 Drop Collision and Coalescence

In dense sprays, drop collision and coalescence can significantly alter the spray characteristics, such as drop size and velocity distribution [70]. An accurate study of drop collision can give an insight into the collision outcomes and the parameters that define the boundaries between different types of collisions. Early experiments categorized the outcomes of drop collision into four general types, namely bouncing, coalescence, separation, and shattering collisions [75]. In bouncing collision, drops bounce apart due to the intervening gas film, which prevents the contact of drop surfaces. Coalescence collision occurs when two drops permanently combine to generate one single drop. Separation collision refers to collisions in which drops combine temporarily and later separate into two or more drops. Finally, shattering collision occurs at a high relative velocity collision, resulting in the disintegration of drops into a cluster of several smaller droplets. Nevertheless, it was later found that there were many sub-categories of drop collision within the four generalized collision types, depending primarily on the operating conditions [76, 77].

The main parameters that govern the outcomes of binary drop collision are the relative velocity of the two drops, liquid drop density, viscosity and surface tension, the diameters and velocities of the drops, and the density and velocity of the surrounding medium. The relative velocity of the two drops,  $\mathbf{v}_{rel}$  is an important parameter, because it contains the information of the trajectories of the drops which form a collision

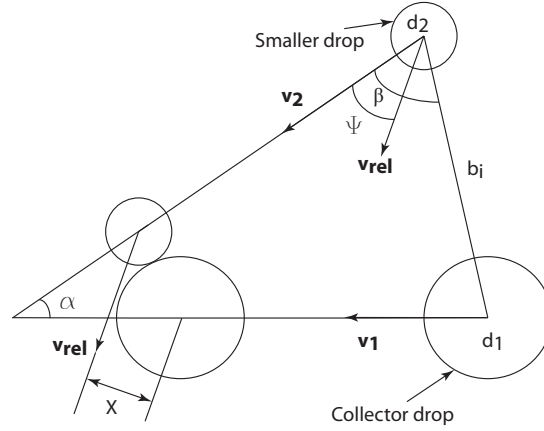


Figure 3.6: Schematic of the collision of two moving drops at a collision angle of  $\alpha$  [76]

angle  $\alpha$  (see Fig. 3.6), i.e.,

$$\mathbf{v}_{rel} = (\mathbf{v}_1^2 + \mathbf{v}_2^2 - 2\mathbf{v}_1\mathbf{v}_2 \cos \alpha)^{\frac{1}{2}} \quad (3.33)$$

where  $\mathbf{v}_1$  and  $\mathbf{v}_2$  are the velocities of the larger (collector) and smaller drops respectively.

In addition to these main parameters, another parameter that governs the collision phenomenon is the impact parameter,  $X$ , which is essentially proportional to the distance between the centers of the colliding drops [76]. By dimensional analysis, the above parameters can be grouped into five dimensionless numbers, namely Reynolds number ( $Re$ ), collision Weber number ( $We_c$ ), drop diameter ratio ( $\Delta_l$ ), non-dimensional impact parameter ( $x$ ), and Weber number of the surrounding gas-phase ( $We$ ). The Weber number for the gas-phase was described previously in the section discussing on drop breakup. The other dimensionless parameters are defined as follows:

$$Re = \frac{\rho_l d_1 \mathbf{v}_{rel}}{\mu_l}; We_c = \frac{\rho_l d_2 \mathbf{v}_{rel}^2}{\sigma_l}; \Delta_l = \frac{d_2}{d_1}; x = \frac{2X}{d_1 + d_2}.$$

where  $d_1$  and  $d_2$  are the diameters of the larger and smaller drops, respectively.

The experiments conducted on binary water drop collisions with Reynolds numbers in the range of 500 to 4000, did not exhibit any major influence of the Reynolds number and the gas-phase Weber number on the outcome of collisions [76]. Therefore, for low drop Reynolds numbers and low gas-phase Weber numbers, the major parameters that influence collision outcome are collision Weber number, drop diameter ratio, and impact parameter. As an example, the influence of these parameters on collision outcome are presented in Fig 3.7. The figure demonstrates the regions for different types of collision outcomes for two equal-size drops in the collision Weber number range of  $5 \leq We_c \leq 100$  and all impact parameters,  $0 \leq x \leq 1$ .  $x = 0$  represents a head-on collision, while  $x = 1$  refers to a tangential or grazing collision. The symbols show the experimental results, while the solid lines represent the boundaries of the

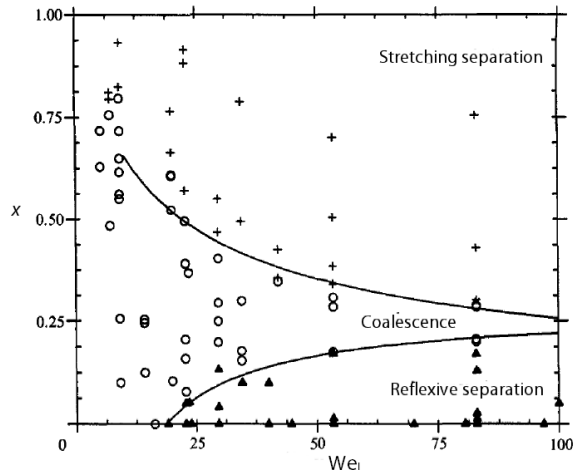


Figure 3.7: Binary drop collision for drop size ratio  $\Delta_l = 1.0$  (+, stretching separation; O, coalescence;  $\Delta$ , reflexive separation) [76]

collision regimes obtained from the measurements. As shown in Fig. 3.7, for a fixed value of the impact parameter ( $x$ ), coalescence occurs at low drop collision Weber numbers. On the other hand, as the collision Weber number is increased beyond a critical value, the collision outcome is in either stretching separation or reflexive separation mode, depending on the impact parameter.

In general, the outcome of a binary drop collision depends on the forces acting on the coalesced pair of drops. At low relative velocities of the two drops, surface tension forces are greater than liquid inertia forces, resulting in a permanent coalescence of the drops. The collision Weber number,  $We_l$ , is then very low. Nevertheless, at higher  $We_l$ , liquid inertia forces dominate, and the drops separate from each other. Furthermore, during such type of collision, satellite droplets around the main drops are formed. This process is generally termed grazing collision [59]. At very high relative velocities, the two drops are likely to shatter after collision to form small droplets.

In this research, the model being used to predict the collision outcome is discussed in Chapter 5. Instead of considering binary drop collision and its outcome, the model determines the collision outcome of two colliding parcels, with each parcel has a given number of drops.

### 3.4.5 Drop Vaporization

The rate of change in drop radius ( $R$ ), as shown in Eqns. 3.6 and 3.18, due to vaporization takes the following term [78].

$$R = \frac{dr}{dt}$$

$$= -\frac{\rho_a DBSh}{2\rho_{fv}r} \quad (3.34)$$

where  $D$  is the mass diffusivity of fuel vapor in air of density  $\rho_a$  and  $B$  is the mass transfer number, which is related to the fuel mass fraction, i.e.,

$$B = \frac{Y_{fv}^* - Y_{fv}}{1 - Y_{fv}^*} \quad (3.35)$$

where  $Y_{fv}^*$  refers to the fuel mass fraction at the drop surface,  $Y_{fv}$  is the fuel mass fraction in the computational cell, the subscript  $fv$  refers to the fuel vapor, and  $Sh$  is the Sherwood number. The expression for the Sherwood number [78] is as follows.

$$Sh = (2 + 0.6Re_d^{1/2}Sc^{1/3})\frac{\ln(1+B)}{B} \quad (3.36)$$

where  $Re_d$  is the drop Reynolds number,  $Sc$  is the Schmidt number of the air, and  $\ln(1+B)/B$  is the Spalding heat-transfer modification function. The fuel mass fraction at the drop surface is obtained by assuming that the partial pressure of fuel vapor equals to the equilibrium vapor pressure, i.e.,

$$Y_{fv}^* = \frac{W_{fv}}{W_{fv} + W_a \left( \frac{p_a}{p_{fv}T_d} - 1 \right)} \quad (3.37)$$

where  $W_{fv}$  and  $W_a$  are the molecular weights of the fuel vapor and air, respectively,  $p_{fv}$  and  $p_a$  are the fuel vapor pressure and air pressure, respectively, and  $T_d$  is the drop temperature.

The drop temperature also changes with the time, which gives rise to the term  $\dot{T}_d$  in Eqns. 3.17 and 3.20. The time rate of change in drop temperature,  $\dot{T}_d$  is obtained by balancing the energy, which involves the latent heat of vaporization and the heat of conduction from the gas, i.e.,

$$\begin{aligned} m_d c_l \dot{T}_d - \rho_l A_d R L &= A_d \dot{Q}_d \\ \rho_l \frac{4}{3} \pi r^3 c_l \dot{T}_d - \rho_l 4\pi r^2 R L &= 4\pi r^2 \dot{Q}_d \end{aligned} \quad (3.38)$$

where  $m_d$  is mass of the drop,  $A_d$  is the surface area of the drop,  $c_l$  refers to the specific heat of the liquid,  $L$  is the specific latent heat of vaporization at a constant temperature  $T_d$ , and  $\dot{Q}_d$  is the rate of heat conduction to the drop or the heat flux.

The heat flux,  $\dot{Q}_d$  is given by

$$\dot{Q}_d = \alpha_h (T_g - T_d) \quad (3.39)$$

where  $\alpha_h$  is the heat transfer coefficient and  $T_g$  refers to the gas temperature.

The equation for the heat transfer coefficient [79] can be written as

$$\alpha_h = \frac{Nu}{2r} \lambda_{eff} \frac{\ln(1+B)}{B} \quad (3.40)$$

where  $Nu$  is the Nusselt number and  $\lambda_{eff}$  refers to the effective thermal conductivity.

The equation for the Nusselt number [80, 81] becomes

$$Nu = 2 + 0.6Re^{1/2}Pr^{1/3} \quad (3.41)$$

where  $Re$  and  $Pr$  are the Reynolds number and Prandtl number, respectively.

## 3.5 Properties of Sprays

In this section, the spray properties of most practical importance, such as mean drop size, drop size distribution, spray angle, and drop penetration, are briefly discussed in the context of the most common atomization processes. As mentioned earlier, there are some fundamental processes involved with all modes of atomization, which determine the essential spray properties. These basic processes include the development of the liquid jet or sheet, the growth of small disturbances on the liquid surfaces, and the impending disintegration of the liquid stream into ligaments and then drops. The action of external and internal forces and the liquid properties, such as surface tension and viscosity play a major role in influencing the liquid atomization process. The impact of atomization on the spray properties determines the spray quality, which in turn, influences mixing, ignition, and combustion performances [82].

### 3.5.1 Drop Size

The basics of the atomization process have been reported in the literature. However, the physical processes involved in atomization under various operating conditions are not interpreted completely to make an accurate judgement on drop size. A majority of investigations on drop size distribution are limited to empirical estimations. Nevertheless, this information provides a general idea about the effects of liquid properties, gas properties, and injector dimensions on mean drop size. The influence of the atomization process on drop size is discussed here with respect to the pressure-swirl atomizer and air-blast atomizer, which are commonly used in many spray applications.

#### Pressure-Swirl Atomizer

A pressure-swirl atomizer consists of a swirl chamber, which causes the liquid to emerge from the nozzle as an annular sheet that spreads radially outward to produce a hollow conical spray. It is simple in design, but the various processes involved in this atomization scheme are highly complex in nature.

A few definitions of the mean drop diameter are available in the literature, of which the Sauter mean diameter (SMD) or  $D_{32}$  is widely used. Several empirical correlations of the SMD have been proposed for pressure swirl atomizer applications in terms of atomizer hydrodynamic parameters and the properties of liquid [83, 84, 85]. A general empirical equation for the SMD of drops is

$$D_{32} \propto \sigma_l^a \nu_l^b \dot{m}_l^c \Delta P_l^d \quad (3.42)$$

where  $\sigma_l$ ,  $\nu_l$ , and  $\dot{m}_l$  are the surface tension, kinematic viscosity, and mass flow rate of liquid, respectively.  $\Delta P_l$  is the liquid injection pressure. The superscripts  $a$ ,  $b$ ,  $c$ , and  $d$  are the exponents.

An alternative approach has been proposed to derive the equation for mean drop size [86], which includes the effects of both external aerodynamic forces and turbulence or other disruptive forces within the liquid on the disintegration of a liquid sheet issuing from a nozzle. During the first stage of atomization, the disturbances within the flow have a strong influence on sheet disintegration. Subsequently, and to some extent simultaneously, the relative velocity between the liquid and the surrounding medium plays a major role in atomization through its influence on the development of waves on the initially smooth liquid surface and the production of unstable ligaments. As the relative velocity is increased, the size of the ligaments is decreased, resulting in the disintegration of ligaments into smaller drops [86, 87]. The proposed formulation of an equation for mean drop size is as follows.

$$D_{32} = 4.52 \left( \frac{\sigma_l^{0.5} \mu_l}{\rho_a^{0.5} \Delta P_l} \right)^{0.5} (t_l \cos \theta)^{0.25} + 0.39 \left( \frac{\sigma_l \rho_l}{\rho_a \Delta P_l} \right)^{0.25} (t_l \cos \theta)^{0.75} \quad (3.43)$$

where  $t_l$  is the liquid film thickness at the plane of discharge from the nozzle and  $\theta$  refers to the half spray cone angle.

In pressure-swirl atomizers, the thickness of the liquid film,  $t_l$ , in the orifice is related to the area of the air core by the equation

$$\frac{A_a}{A_o} = \frac{(d_o - 2t_l)^2}{d_o^2} \quad (3.44)$$

where  $A_a$  and  $A_o$  are the air core area and discharge orifice area, respectively.  $d_o$  is the discharge orifice diameter.

Several expressions have been derived to estimate liquid film thickness. A majority of such expressions indicate that film thickness is mainly dependent on atomizer geometry and is virtually independent of liquid properties and nozzle operating conditions [88, 89, 90]. Nevertheless, film thickness values predicted by several workers showed a wide disparity for a given discharge orifice diameter,  $d_o$  [91]. Therefore, the existing empirical correlations of mean drop sizes from pressure swirl atomizers must be regarded as less than satisfactory.

### Airblast Atomizers

The airblast atomizer allows fuel to flow at a low pressure over a lip located in a high-velocity airstream, resulting in the atomization of the fuel. The air carries the fuel drops along with it to the combustion zone. By providing maximum physical contact between the air and fuel, minimum drop sizes are obtained. Several studies have been conducted on airblast atomization. Studies on plain-jet airblast atomization led to the discovery of the following mean drop size equation, which was found to provide an excellent data correlation, especially for low-viscosity fuels [92, 93, 94].

$$\frac{D_{32}}{d_o} = 0.48 \left( \frac{\sigma_l}{\rho_a U_{rel}^2 d_o} \right) 60.4 \left( 1 + \frac{1}{ALR} \right)^{0.4} + 0.15 \left( \frac{\mu_l^2}{\sigma_l \rho_l d_o} \right)^{0.5} \left( 1 + \frac{1}{ALR} \right) \quad (3.45)$$

where ALR is the air-to-liquid ratio.

For pre-filming airblast atomizers, the mean drop size is correlated by the following dimensionally correct equation [95].

$$\frac{D_{32}}{D_h} = \left[ 0.33 \left( \frac{\sigma_l}{\rho_a u_a D_p} \right)^{0.6} \left( \frac{\rho_l}{\rho_a} \right)^{0.1} + 0.068 \left( \frac{\mu_l^2}{\rho_l \sigma_l D_p} \right)^{0.5} \right] \left( 1 + \frac{1}{ALR} \right) \quad (3.46)$$

where  $D_h$  and  $D_p$  are the hydraulic mean diameters of the air exit duct and pre-filmer, respectively and  $u_a$  is the air velocity.

Experiments conducted on many different types of airblast atomizers by several workers show that the mean drop size ( $D_{32}$ ) of the spray increases with increasing liquid surface tension and viscosity and with decreasing air-to-liquid ratio. The studies further show that the air property of most importance is air velocity. In general, the mean drop size is inversely proportional to atomizing air velocity. Nevertheless, the equations for mean drop size do not incorporate the time required for atomization. The considerations of the time element is important, since various fluid properties, such as liquid viscosity and air or gas density have an effect on mean drop size through their influence on liquid drop breakup time. For instance, an increase in air pressure improves atomization quality by reducing the breakup time. On the other hand, an increase in liquid viscosity decreases the wave growth rate on the liquid surface, thus resulting in a poor quality of atomization.

### 3.5.2 Drop Size Distribution

Practical atomizers do not produce sprays of uniform drop size at any given operating condition. The drop size may vary from a few microns up to several hundred microns. A spray is generally considered as a spectrum of drops of different sizes, which are distributed about some arbitrarily mean value. Therefore, in addition to mean drop size, the definition of spray must include the distributions of drop sizes it contains. The existing theories of atomization are not capable yet to completely describe the hydrodynamic and aerodynamic phenomena involved in jet and sheet disintegration processes under normal atomizing conditions. As a result, a few functions have been proposed to mathematically represent the measured drop size distributions. They include normal, log-normal, Nukiyama and Tanasawa [96], Rosin-Rammler [97], upper limit, and log-hyperbolic distributions. However, there is no single function that can represent all drop-size data. Therefore, for any given application, comparative assessments of the available distribution functions are necessary to find out the one that provides the best fit to the measurement data.

The Rosin-Rammler approach [97] of drop size distribution is the most widely used method in many practical applications. The distribution function proposed by Rosin and Rammler is based on the assumption that an exponential relationship exists between the droplet diameter,  $D_l$ , and the mass fraction of droplets with diameter greater than  $D_l$ ,  $Y_{D_l}$ , i.e.,

$$\begin{aligned} Y_{D_l} &= 1 - Q \\ &= \exp - \left( \frac{D_l}{D_l} \right)^q \end{aligned} \quad (3.47)$$

where  $Q$  is the fraction of the total volume that contains drops of diameter less than  $D_l$ ,  $\overline{D}_l$  is the mean diameter and  $q$  is the spread parameter.  $\overline{D}_l$  and  $q$  are constants and their values can be determined from experiments. In essence, the exponent  $q$  is a measure of the spreads of drop sizes in the spray. A higher value of  $q$  will make the spray more uniform by having more smaller drops.

A major advantage of the Rosin-Rammler expression is that it is applicable to any range of drop sizes, including the range of very fine drops, where measurements are not so accurate. Furthermore, in the Rosin-Rammler drop distributions, all the representative diameters are exclusively linked to each other through the distribution parameter,  $q$ .

Although the Rosin-Rammler expression provides a satisfactory match over a wide drop size range, it sometimes tends to deviate from the measurement data for the larger drops. A modified expression [98] was proposed in the form

$$1 - Q = \exp - \left( \frac{\ln D_l}{\ln \overline{D}_l} \right)^q \quad (3.48)$$

Equation 3.48 produced better representation of large drops for various types of pressure-swirl and airblast atomizer configurations [98, 99, 100, 101]. Nevertheless, as noted earlier, this expression may not provide the best representation in all cases.

In addition to the Rosin-Rammler formulation, several analytical approaches have been proposed to the development of mathematical descriptions of drop size distributions in sprays. In the past, due to the lack of accurate drop size information, the analytical models were not expected to produce precise representation of drop size distributions. Recently, with the advent of phase-Doppler anemometry, it has become possible to measure local size and velocity distributions in sprays. Therefore, the information gathered from the experiments can be used to develop robust analytical methods, which may provide more insights into the fundamental mechanisms involved in atomization.

### 3.5.3 Spray Cone Angle

Spray cone angle has a significant influence on fuel atomization, since an increase in cone angle essentially enhances the interactions between the spray droplets and the surrounding air or gas stream, leading to improved atomization and more efficient exchange of mass and energy between the two phases.

In pressure-swirl atomizers, spray is generally produced in the form of a hollow cone of wide angle, with the majority of the drops being at the spray periphery. Various studies conducted on pressure-swirl atomizers demonstrate the influence of nozzle geometry, liquid properties, and the density of the surrounding medium on the spray cone angle [102]. Initially, several expressions for the spray cone angle were derived, mostly with the assumption of non-viscous or low viscous liquids. For example, by assuming a constant axial velocity across the liquid film, the mean cone angle has been derived in the form [102]

$$\tan \theta_m = \tan \theta \left( 1 - \frac{t_l}{d_o} \right) \quad (3.49)$$

Later, for viscous liquids, a dimensionally-correct spray cone angle equation [103] was proposed in the form

$$2\theta_m = 6 \left( \frac{A_P}{d_o D_S} \right)^{-0.15} \left( \frac{\Delta P_l d_o^2 \rho_l}{\mu_l^2} \right)^{0.11} \quad (3.50)$$

where  $2\theta_m$  represents the mean cone angle in the near-nozzle region,  $A_P$  refers to the total inlet ports area, and  $D_S$  is the swirl chamber diameter. The term  $\left( \frac{A_P}{d_o D_S} \right)$  is often referred to as the atomizer constant. Although the equation provides a useful insight into the effects of liquid injection pressure and liquid properties on spray angle, the effects of ambient pressure on cone angle is not addressed. Experiments conducted on different simplex nozzles by Ortman and Lefebvre [104] show the effects of gas pressure on spray cone angle. The tests were performed using aviation kerosene as liquid. The results indicate that an increase in gas pressure above normal atmospheric causes the spray to contract sharply. However, the rate of spray contraction decreases with continuing increase in gas pressure and eventually, a point is reached where further increase in ambient pressure has no impact on the equivalent spray angle.

### 3.5.4 Spray Penetration

Spray penetration is another important aspect of atomizers in internal combustion engines, since over penetration of spray leads to impingement of fuel on the combustion chamber walls, while under penetration causes insufficient fuel-air mixing. The penetration of a spray is determined by the maximum distance it reaches when injected into a quiescent surrounding medium. Both kinetic energy of the initial liquid jet or sheet and the aerodynamic resistance of the surrounding gas affect spray penetration. As atomization proceeds, the surface area of the spray increases, resulting in a gradual dissipation of the liquid kinetic energy caused by frictional losses to the gas. Finally, when the liquid drops exhaust their kinetic energy, their trajectories are primarily influenced by the motion of the surrounding gas and gravity. Although a well-atomized spray of wide cone angle is desirable in many applications, it incurs more resistance from the surrounding medium, leading to low penetration of spray drops. Some correlations exist for the spray tip penetration for diesel jets in stagnant air, but very little information is available on the penetration of sprays from pressure-swirl atomizers. For simplex and dual-orifice nozzles operating in gas turbine combustors, the spray penetration has been found to be inversely proportional to the cube root of the ambient gas pressure [105].

## 4. Turbulence Modeling and Numerical Methods

### 4.1 Introduction

Numerical simulation has recently gained tremendous importance in determining the design process of modern gas-turbine combustion systems. In order to allow a suitable and reliable design, the CFD methods need to characterize the aerodynamics and the combustion driven dynamics accurately. Different approaches are presently available to determine flow fields, such as the Reynolds-averaged Navier Stokes (RANS), large eddy simulation (LES), and hybrid RANS/LES methods. The unsteady RANS (URANS) approach, which is widely used for many practical applications, employs complete statistical averaging of the turbulence. This allows for determining the time-mean or ensemble averaged quantities for velocity, temperature, and species concentration of non-reacting and reacting flow fields. Nevertheless, it has been experienced that the RANS approach can cause an excess of turbulence dissipation, which might lead the crucial flow structures to be dissipated. Additionally, for the flow field where swirl, wall effects, flow separation, and recirculation regions are present, the RANS alone will not be sufficient. Therefore, in order to avoid the possible errors, a turbulence model needs to be applied. In advanced CFD codes, the most widely used turbulence model is the  $k - \varepsilon$  model. Although the  $k - \varepsilon$  model is relatively easy to implement, it has considerable drawbacks to resolve flows with high gradients of velocity and swirl. Owing to the assumption of isotropy in modeling eddy viscosity, the  $k - \varepsilon$  model has a tendency to yield inconsistent and diffusive results for complex flows. Therefore, for the calculations of more complex flow field with high degree of swirl, a higher order turbulence model, such as the Reynolds Stress Turbulence Model (RSTM) [106] can produce results that more accurately represent the physical and statistical features of the flow.

Unlike the  $k - \varepsilon$  models, the RSTM has a transport equation for each Reynolds-stress component. As a result, it can naturally resolve flow anisotropy, streamline curvature, sudden changes in strain rate, and swirl in turbulent flow. In general, the RSTM model describes turbulent flows most comprehensively within the framework of a Reynolds averaging approach at an expense of increased complexity resulting from additional equations in the modeling.

Simulation of gas-turbine combustion systems using LES has been demonstrated by

several authors [49, 107]. However, the LES modeling approach needs to be validated for more case-specific combustion problems. In this approach, the larger eddies are computed for each problem with a time-dependent simulation. On the other hand, the universal behavior of the smaller eddies is modeled and their effects on the resolved flow is included by means of a so called sub-grid scale model. The physics of turbulent flows in combustion chambers involving combustion, swirl, dilution jets, and instabilities is highly complex, and the information yielded by LES calculations can be applied to the development of combustion technology.

In this dissertation, the URANS approach with the realizable  $k - \varepsilon$  and RSTM turbulence models are used to simulate the non-reacting cold flow in a single-element and a Multi-Point Lean Direct Injection (MPLDI) combustor. In addition, LES is used to compute the non-reacting turbulent flow field of the MPLDI combustor. In all cases, a steady-state RANS calculation is performed to create an initial flow field before conducting the unsteady calculation. In the reacting spray simulation for both single-element and MPLDI combustors, the gas-phase is modeled using the steady-state RANS with the realizable  $k - \varepsilon$  turbulence model. On the other hand, the discrete phase is solved by tracking the liquid particles through the calculated flow field in an unsteady manner, while incorporating all the necessary spray sub-models. The numerical models used for the discrete phase calculations are discussed in Chapter 5.

The present chapter is organized as follows. In the next section, a description of the RANS turbulence models, such as the realizable  $k - \varepsilon$  and RSTM, implemented in the flow computations of the LDI combustors, are presented. In Section 4.3, the LES formulation and the sub-grid closure model, employed in the non-reacting flow calculation, are described. This is followed by a discussion of the solution methods applied in the numerical simulations.

## 4.2 RANS Turbulence Models

This section briefly discusses the effects of turbulence on the Navier-Stokes equations and the turbulence models used in this research to predict the Reynolds stresses and the scalar transport terms.

### 4.2.1 Governing Equations

The system of equations that governs all turbulent flows are as follows.

Continuity

$$\frac{\partial \rho}{\partial t} + \text{div}(\rho \mathbf{u}) = 0 \quad (4.1)$$

Momentum

$$\frac{\partial(\rho u)}{\partial t} + \text{div}(\rho u \mathbf{u}) = -\frac{\partial p}{\partial x} + \text{div}(\mu \text{grad}(u)) + S_{M_x} \quad (4.2)$$

$$\frac{\partial(\rho v)}{\partial t} + \text{div}(\rho v \mathbf{u}) = -\frac{\partial p}{\partial y} + \text{div}(\mu \text{grad}(v)) + S_{M_y} \quad (4.3)$$

$$\frac{\partial(\rho w)}{\partial t} + \text{div}(\rho w \mathbf{u}) = -\frac{\partial p}{\partial z} + \text{div}(\mu \text{grad}(w)) + S_{Mz} \quad (4.4)$$

where the fluid velocity vector  $\mathbf{u}$  has the velocity components  $u$ ,  $v$ , and  $w$  along the  $x$ ,  $y$ , and  $z$  directions, respectively in a Cartesian coordinate system,  $\rho$  is the density of the fluid,  $\mu$  refers to the fluid dynamic viscosity,  $p$  is the fluid pressure, and  $S_{Mx}$ ,  $S_{My}$  and  $S_{Mz}$  are the source terms.

For an incompressible fluid with constant viscosity, the above equations of mass and momentum are reduced to the following forms.

$$\text{div}(\mathbf{u}) = 0 \quad (4.5)$$

$$\frac{\partial u}{\partial t} + \text{div}(u \mathbf{u}) = -\frac{1}{\rho} \frac{\partial p}{\partial x} + \nu \text{div}(\text{grad}(u)) + S_{Mx} \quad (4.6)$$

$$\frac{\partial v}{\partial t} + \text{div}(v \mathbf{u}) = -\frac{1}{\rho} \frac{\partial p}{\partial y} + \nu \text{div}(\text{grad}(v)) + S_{My} \quad (4.7)$$

$$\frac{\partial w}{\partial t} + \text{div}(w \mathbf{u}) = -\frac{1}{\rho} \frac{\partial p}{\partial z} + \nu \text{div}(\text{grad}(w)) + S_{Mz} \quad (4.8)$$

where  $\nu = \mu/\rho$  is the fluid kinematic viscosity.

To illustrate the consequences of turbulence on the mean flow, the flow variables in Eqns. 4.5-4.8 are replaced by the sum of a mean and a fluctuating component, i.e.,  $\mathbf{u} = \mathbf{U} + \mathbf{u}'$ ,  $u = U + u'$ ,  $v = V + v'$ ,  $w = W + w'$ ,  $p = P + p'$

If time average is taken, the continuity equation for the mean flow becomes

$$\text{div}(\mathbf{U}) = 0 \quad (4.9)$$

Similarly, the time-averages of individual terms in the momentum equations yield

$$\frac{\partial U}{\partial t} + \text{div}(U \mathbf{U}) + \text{div}(\overline{u' \mathbf{u}'}) = -\frac{1}{\rho} \frac{\partial P}{\partial x} + \nu \text{div}(\text{grad}(U)) + S_{Mx} \quad (4.10)$$

$$\frac{\partial V}{\partial t} + \text{div}(V \mathbf{U}) + \text{div}(\overline{v' \mathbf{u}'}) = -\frac{1}{\rho} \frac{\partial P}{\partial y} + \nu \text{div}(\text{grad}(V)) + S_{My} \quad (4.11)$$

$$\frac{\partial W}{\partial t} + \text{div}(W \mathbf{U}) + \text{div}(\overline{w' \mathbf{u}'}) = -\frac{1}{\rho} \frac{\partial P}{\partial z} + \nu \text{div}(\text{grad}(W)) + S_{Mz} \quad (4.12)$$

The process of time averaging introduces new terms in Eqns. 4.10-4.12. The terms include time-averaged products of turbulent velocities, caused by convective momentum transfer due to the presence of turbulent eddies. To demonstrate the role of these terms as additional turbulent stresses on the mean flow, they are moved to the right hand side of the momentum equations as follows.

Time-average  $x$ -momentum

$$\begin{aligned} \frac{\partial U}{\partial t} + \text{div}(U \mathbf{U}) &= -\frac{1}{\rho} \frac{\partial P}{\partial x} + \nu \text{div}(\text{grad}(U)) \\ + \frac{1}{\rho} \left[ \frac{\partial(-\rho \overline{u'^2})}{\partial x} + \frac{\partial(-\rho \overline{u'v'})}{\partial y} + \frac{\partial(-\rho \overline{u'w'})}{\partial z} \right] &+ S_{Mx} \end{aligned} \quad (4.13)$$

Time-average  $y$ -momentum

$$\begin{aligned} \frac{\partial V}{\partial t} + \text{div}(V\mathbf{U}) &= -\frac{1}{\rho} \frac{\partial P}{\partial x} + \nu \text{div}(\text{grad}(V)) \\ + \frac{1}{\rho} \left[ \frac{\partial(-\rho \overline{u'v'})}{\partial x} + \frac{\partial(-\rho \overline{v'^2})}{\partial y} + \frac{\partial(-\rho \overline{v'w'})}{\partial z} \right] &+ S_{My} \end{aligned} \quad (4.14)$$

Time-average  $z$ -momentum

$$\begin{aligned} \frac{\partial W}{\partial t} + \text{div}(W\mathbf{U}) &= -\frac{1}{\rho} \frac{\partial P}{\partial x} + \nu \text{div}(\text{grad}(W)) \\ + \frac{1}{\rho} \left[ \frac{\partial(-\rho \overline{u'w'})}{\partial x} + \frac{\partial(-\rho \overline{v'w'})}{\partial y} + \frac{\partial(-\rho \overline{w'^2})}{\partial z} \right] &+ S_{Mz} \end{aligned} \quad (4.15)$$

Equations 4.13-4.15 show six additional stresses, which include three normal stress terms and three shear stress terms.

Normal stresses

$$\tau_{xx} = -\rho \overline{u'^2}, \tau_{yy} = -\rho \overline{v'^2}, \tau_{zz} = -\rho \overline{w'^2} \quad (4.16)$$

Shear stresses

$$\tau_{xy} = \tau_{yx} = -\rho \overline{u'v'}, \tau_{xz} = \tau_{zx} = -\rho \overline{u'w'}, \tau_{yz} = \tau_{zy} = -\rho \overline{v'w'} \quad (4.17)$$

These additional normal and shear stresses are termed the Reynolds stresses. Therefore, Eqns. 4.13-4.15 are often referred to as the Reynolds equations.

In a similar way, additional turbulent terms would arise in the time-average transport equation for a scalar quantity,  $\phi$  i.e.,

$$\frac{\partial \Phi}{\partial t} + \text{div}(\Phi\mathbf{U}) = \frac{1}{\rho} \text{div}(\Gamma_\phi \text{grad}(\Phi)) + \left[ -\frac{\partial(\overline{u'\phi'})}{\partial x} - \frac{\partial(\overline{v'\phi'})}{\partial y} - \frac{\partial(\overline{w'\phi'})}{\partial z} \right] + S_\phi \quad (4.18)$$

where the fluctuating scalar quantity,  $\phi = \Phi + \phi'$ ,  $\Gamma_\phi$  is the diffusion coefficient for property  $\phi$ , and  $S_\phi$  refers to the rate of change of  $\phi$  due to sources.

The governing equations for the continuity, momentum, and scalar transport shown above are mainly related to a non-reacting flow field. For flows involving liquid spray combustion, the corresponding governing equations are presented in Chapters 3 and 5.

The following subsections discuss briefly the RANS turbulence models applied to simulate the flow field of the LDI combustors.

## 4.2.2 Realizable $k - \varepsilon$ model

The realizable  $k - \varepsilon$  model [108] contains a new transport equation for the turbulent dissipation rate, which is different from the other  $k - \varepsilon$  models. In addition, this model contains a new formulation for the turbulent viscosity. This allows the model to satisfy certain mathematical constraints on the normal stresses consistent with the physics

of turbulence. The model is reported to be able to provide better performance for the flows involving rotation, boundary layers under strong adverse pressure gradients, separation, and recirculation [108]. The realizable  $k-\varepsilon$  model is applied in the current study since some of these complex features are present in the flow field of the LDI combustor.

The realizable  $k-\varepsilon$  model combines the Boussinesq relationship and the definition of the eddy viscosity. The Boussinesq hypothesis [109] connects the Reynolds stresses to mean rates of deformation using

$$\begin{aligned}\tau_{ij} &= -\rho \overline{u'_i u'_j} = 2\mu_t \overline{S_{ij}} - \frac{2}{3} \left( \rho k + \mu_t \frac{\partial \overline{u_k}}{\partial x_k} \right) \delta_{ij} \\ &= \mu_t \left( \frac{\partial \overline{u_i}}{\partial x_j} + \frac{\partial \overline{u_j}}{\partial x_i} \right) - \frac{2}{3} \left( \rho k + \mu_t \frac{\partial \overline{u_k}}{\partial x_k} \right) \delta_{ij}\end{aligned}\quad (4.19)$$

where  $\tau_{ij}$  is the Reynolds stress tensor,  $\mu_t$  is the turbulent or molecular eddy viscosity,  $\overline{S_{ij}}$  refers to the mean rate-of-strain tensor,  $k$  is the turbulent kinetic energy, and  $\delta_{ij}$  is the Kronecker delta.

The eddy viscosity,  $\mu_t$ , is computed from

$$\mu_t = \rho C_\mu \frac{k^2}{\varepsilon} \quad (4.20)$$

where  $C_\mu$  is a model coefficient.

For incompressible flow:  $\frac{\partial \overline{u_k}}{\partial x_k} = 0$ . Therefore, from Eqns. 4.16 and 4.19, the following normal Reynolds stress equations for incompressible flow are obtained

$$\begin{aligned}\tau_{xx} &= -\rho \overline{u'^2} \\ \overline{u'^2} &= \frac{2}{3}k - 2\nu_t \frac{\partial U}{\partial x}\end{aligned}\quad (4.21)$$

$$\begin{aligned}\tau_{yy} &= -\rho \overline{v'^2} \\ \overline{v'^2} &= \frac{2}{3}k - 2\nu_t \frac{\partial V}{\partial y}\end{aligned}\quad (4.22)$$

$$\begin{aligned}\tau_{zz} &= -\rho \overline{w'^2} \\ \overline{w'^2} &= \frac{2}{3}k - 2\nu_t \frac{\partial W}{\partial z}\end{aligned}\quad (4.23)$$

where  $\nu_t = \frac{\mu_t}{\rho}$  is the kinematic eddy viscosity.

The value of the turbulence quantity,  $\overline{u_i'^2}$ , by definition is positive (realizability). However, the quantity  $\overline{u_i'^2}$  in Eqns. 4.21-4.23 becomes negative or non-realizable, when the mean strain rate satisfies the following condition

$$\begin{aligned}\frac{2}{3}k - 2\nu_t \frac{\partial U_i}{\partial x_j} &< 0 \\ \nu_t \frac{\partial U_i}{\partial x_j} &> \frac{1}{3}k\end{aligned}\quad (4.24)$$

Applying the kinematic eddy viscosity expression,  $\nu_t = C_\mu \frac{k^2}{\varepsilon}$ , into Eqn. 4.24, the non-realizability condition for the mean strain rate becomes

$$\frac{k}{\varepsilon} \frac{\partial U_i}{\partial x_j} > \frac{1}{3C_\mu} \approx 3.7 \quad (4.25)$$

To keep the normal Reynolds stresses positive (realizability), the concept of variable  $C_\mu$  was introduced to the realizable  $k - \varepsilon$  model, where  $C_\mu$  is sensitive to the mean flow and turbulence. This is unlike other  $k - \varepsilon$  models, where  $C_\mu$  is a constant. The expression for  $C_\mu$  in the realizable  $k - \varepsilon$  model is as follows

$$C_\mu = \frac{1}{A_0 + A_S \frac{kU^*}{\varepsilon}} \quad (4.26)$$

In the above equation,  $U^* \equiv \sqrt{S_{ij}S_{ij} + \tilde{\Omega}_{ij}\tilde{\Omega}_{ij}}$

and

$$\tilde{\Omega}_{ij} = \Omega_{ij} - 2\varepsilon_{ijk}\omega_k; \quad \Omega_{ij} = \overline{\Omega_{ij}} - \varepsilon_{ij}\omega_k$$

where  $\overline{\Omega_{ij}}$  is the mean rate of rotation with the angular velocity  $\omega_k$ .

$A_0$  and  $A_S$  are model constants, which are given by

$$A_0 = 4.04, \quad A_S = \sqrt{6} \cos \phi$$

where

$$\phi = \frac{1}{3} \cos^{-1}(\sqrt{6}W_s); \quad W_s = S_{ij}S_{jk}S_{ki}/\tilde{S}^3; \quad \tilde{S} = \sqrt{S_{ij}S_{ij}}; \quad S_{ij} = \frac{1}{2} \left( \frac{\partial u_j}{\partial x_i} + \frac{\partial u_i}{\partial x_j} \right)$$

Equation 4.26 shows that the coefficient  $C_\mu$  is a function of the mean strain and rotation rates, the angular velocity of the system rotation, and the turbulence fields.

In the realizable  $k - \varepsilon$  turbulence model, the transport equation for turbulent kinetic energy,  $k$ , is identical to that of the other  $k - \varepsilon$  models, i.e.,

$$\frac{\partial}{\partial t}(\rho k) + \frac{\partial}{\partial x_i}(\rho k u_i) = \frac{\partial}{\partial x_j} \left[ \left( \mu + \frac{\mu_t}{Pr_k} \right) \frac{\partial k}{\partial x_j} \right] + G_k + G_b - \rho\varepsilon - Y_M + S_k \quad (4.27)$$

where  $G_k$  and  $G_b$  represent the generation of turbulence kinetic energy due to the mean velocity gradients and buoyancy, respectively,  $Y_M$  refers to the contribution of the fluctuating dilatation in compressible turbulence to the overall dissipation rate,  $Pr_k$  is the Prandtl number for  $k$ , and  $S_k$  is a user-defined source term.

However, the transport equation for the turbulent dissipation rate,  $\varepsilon$ , differs from the other models. The transport equation for  $\varepsilon$  is based on the dynamic equation of the mean-square vorticity fluctuation, and is expressed in the following form

$$\begin{aligned} \frac{\partial}{\partial t}(\rho\varepsilon) + \frac{\partial}{\partial x_i}(\rho\varepsilon u_i) &= \frac{\partial}{\partial x_j} \left[ \left( \mu + \frac{\mu_t}{Pr_\varepsilon} \right) \frac{\partial \varepsilon}{\partial x_j} \right] + \rho C_1 S_\varepsilon \\ &\quad - \rho C_2 \frac{\varepsilon^2}{k + \sqrt{\nu_t \varepsilon}} + C_{1\varepsilon} \frac{\varepsilon}{k} C_{3\varepsilon} G_b + S_\varepsilon \end{aligned} \quad (4.28)$$

where

$$C_1 = \max \left[ 0.43, \frac{\eta}{\eta + 5} \right], \quad \eta = S \frac{k}{\varepsilon}, \quad S = \sqrt{2S_{ij}S_{ij}}$$

In the above equation,  $C_1$ ,  $C_2$ ,  $C_{1\varepsilon}$ , and  $C_{3\varepsilon}$  are constants,  $Pr_\varepsilon$  is the Prandtl number for  $\varepsilon$ , and  $S_\varepsilon$  is a user-defined source term.

The main difference between the dissipation rate transport equation for the realizable and the other  $k - \varepsilon$  models can be found in the production and diffusion terms, which are defined by the second and third terms on the right-hand side of Eqn. 4.28, i.e.,

Rate of production of  $\varepsilon$ :

$$G_\varepsilon = \rho C_1 S \varepsilon \quad (4.29)$$

Rate of diffusion of  $\varepsilon$ :

$$Y_\varepsilon = \rho C_2 \frac{\varepsilon^2}{k + \sqrt{\nu_t \varepsilon}} \quad (4.30)$$

Similarly to the standard  $k - \varepsilon$  model, the eddy viscosity is computed from Eqn. 4.20, although  $C_\mu$  is not a constant and it is calculated using Eqn. 4.26.

### 4.2.3 Reynolds Stress Turbulence Models

For flows with complex strain fields or significant body forces, individual Reynolds stresses are poorly represented by the  $k - \varepsilon$  model, even though the turbulent kinetic energy,  $k$ , is computed with reasonable accuracy. However, an exact Reynolds stress transport equation can account for the anisotropy of the turbulence. The exact transport equation of each of the six kinematic Reynolds stress,  $R_{ij}$  is given by

$$\frac{DR_{ij}}{Dt} = P_{ij} + D_{ij} - \varepsilon_{ij} + \Pi_{ij} + \Omega_{ij} \quad (4.31)$$

where  $R_{ij} = -\frac{\tau_{ij}}{\rho} = \overline{u'_i u'_j}$

The above equation essentially describes six partial differential equations: one for the transport of each of the six independent Reynolds stresses. If it is compared with the exact transport equation for the turbulent kinetic energy in the  $k - \varepsilon$  model, the transport equation of  $R_{ij}$  brings out two new physical processes: the pressure-strain interaction term  $\Pi_{ij}$ , and the rotation term  $\Omega_{ij}$ .

The stress production term,  $P_{ij}$ , in the transport equations retains its exact form

$$P_{ij} = - \left( R_{ik} \frac{\partial U_j}{\partial x_k} + R_{jk} \frac{\partial U_i}{\partial x_k} \right) \quad (4.32)$$

The diffusion term,  $D_{ij}$  is modeled with the assumption that the rate of transport  $R_{ij}$  by diffusion is proportional to the gradients of  $R_{ij}$  [110]:

$$D_{ij} = \frac{\partial}{\partial x_k} \left( \frac{\nu_t}{Pr_k} \frac{\partial R_{ij}}{\partial x_k} \right) = \text{div} \left( \frac{\nu_t}{Pr_k} \text{grad}(R_{ij}) \right) \quad (4.33)$$

The turbulent kinematic viscosity,  $\nu_t$  is computed from Eqn. 4.20 and a value of  $Pr_k = 0.85$  [110] is considered, which differs from  $Pr_k = 1.0$  [108] used for the realizable  $k - \varepsilon$  model.

The dissipation rate of Reynolds stress,  $\varepsilon_{ij}$  is modeled with the assumption of the isotropic characteristics of small dissipative eddies present in the flow field. It only affects the normal Reynolds stresses ( $i = j$ ) with equal measure and is given by

$$\varepsilon_{ij} = \frac{2}{3}\varepsilon\delta_{ij} \quad (4.34)$$

The Kronecker delta,  $\delta_{ij}$ , is given by  $\delta_{ij} = 1$  if  $i = j$  and  $\delta_{ij} = 0$  if  $i \neq j$ .

The pressure-strain interaction term,  $\Pi_{ij}$ , is the most difficult term to model accurately. Their effect on Reynolds stresses is caused by two physical processes:

1. a slow process that diminishes anisotropy of the turbulent eddies due to their mutual interactions and
2. a fast process due to interactions between turbulent fluctuations and the mean flow strain that produce the eddies, such that the anisotropic production of turbulent eddies is countered.

The overall effect of both processes is to redistribute energy amongst the normal Reynolds stresses so as to make them more isotropic and to reduce the Reynolds shear stresses. In the present study, the linear pressure-strain model [111, 112, 113] is used. The term  $\Pi_{ij}$  is modeled by using the following decomposition:

$$\Pi_{ij} = \Pi_{ij,1} + \Pi_{ij,2} + \Pi_{ij,w} \quad (4.35)$$

where  $\Pi_{ij,1}$  is the return-to-isotropy pressure-strain term,  $\Pi_{ij,2}$  is the rapid pressure-strain term, and  $\Pi_{ij,w}$  is the wall-reflection term.

$\Pi_{ij,1}$  is modeled as follows

$$\Pi_{ij,1} \equiv -c_1 \frac{\varepsilon}{k} \left[ R_{ij} - \frac{2}{3}\delta_{ij}k \right] \quad (4.36)$$

where  $c_1 = 1.8$  [114].  $k$  is the turbulent kinetic energy, which is obtained by adding the three normal stresses together:

$$k = \frac{1}{2}(R_{11} + R_{22} + R_{33}) = \frac{1}{2}(\overline{u_1'^2} + \overline{u_2'^2} + \overline{u_3'^2})$$

$\Pi_{ij,2}$  is defined as

$$\Pi_{ij,2} \equiv -c_2 \left[ (P_{ij} + \Omega_{ij} + G_{ij} - C_{ij}) - \frac{2}{3}\delta_{ij}(P + G - C) \right] \quad (4.37)$$

where  $c_2 = 0.6$  [114]. The terms  $P_{ij}$  and  $\Omega_{ij}$  are described in Eqns. 4.32 and 4.38, respectively,  $G_{ij}$  refers to buoyancy production,  $C_{ij}$  represents the transport of  $R_{ij}$  by convection, and the terms  $P = \frac{1}{2}P_{kk}$ ,  $G = \frac{1}{2}G_{kk}$ , and  $C = \frac{1}{2}C_{kk}$ .

The wall-reflection term,  $\Pi_{ij,w}$ , distributes the normal stresses near the wall. It tends to damp the normal stress perpendicular to the wall, while increasing the stresses parallel to the wall.

Finally, the rotation term,  $\Omega_{ij}$  is given by

$$\Omega_{ij} = -2\omega_k (R_{jm}e_{ikm} + R_{im}e_{jkm}) \quad (4.38)$$

where  $\omega_k$  is the rotation vector and  $e_{ijk}$  is the Levi-Civita symbol.  $e_{ijk} = +1$  if  $i, j,$  and  $k$  are different and in cyclic order,  $e_{ijk} = -1$  if  $i, j,$  and  $k$  are different and in anti-cyclic order, and  $e_{ijk} = 0$  if any two indices are the same.

### 4.3 Large Eddy Simulation Model

Unlike time-averaging in the URANS approach, LES uses a spatial filtering operation on the time-dependent flow equations to separate the larger and smaller eddies in the flow field. The spatial filtering operation separates the small scale turbulent motions which are smaller than the filter cutoff width. The separated scales are called sub-filter or sub-grid-scale (SGS) motions.

#### Filtered Unsteady Navier-Stokes Equations

A spatial filtering operation in LES is defined by means of a filter function,  $G(\mathbf{x}, \mathbf{x}', \Delta)$ , which is used to filter out the eddies whose scales are smaller than the filter width or grid spacing used in the computations.

The filtered variable is given by

$$\bar{\phi}(\mathbf{x}, t) \equiv \int_D G(\mathbf{x}, \mathbf{x}', \Delta) \phi(\mathbf{x}', t) d\mathbf{x}' \quad (4.39)$$

where  $D$  is the fluid domain, and  $\Delta$  is filter cutoff width. The above equation implies that the spatial filtering is a linear operation and is carried out in three-dimensional space.

There are a few forms of the filtering function available in 3D LES computations. However, in the present computations, the top-hat or box filter is used, which is common in finite-volume implementation of LES. The finite-volume discretization describes the filtering operations as follows:

$$\bar{\phi}(\mathbf{x}, t) = \frac{1}{V^3} \int_v \phi(\mathbf{x}') d\mathbf{x}', \mathbf{x}' \in \nu \quad (4.40)$$

The filter function,  $G(\mathbf{x}, \mathbf{x}', \Delta)$  is thus designed by

$$G(\mathbf{x}, \mathbf{x}', \Delta) = \begin{cases} 1/V, \mathbf{x}' \in \nu \\ 0, \mathbf{x}' \text{ otherwise} \end{cases} \quad (4.41)$$

where  $V$  is the volume of a computational cell and is related to the cutoff width,  $\Delta$ , as follows:  $V = \Delta^3 = \Delta x \Delta y \Delta z$ .

$\Delta x$ ,  $\Delta y$ , and  $\Delta z$  are the length, width, and height of the grid cell, respectively. The cutoff width is an indicative measure of the size of eddies that are retained in the

computations, and the eddies that are rejected. The most common practice is to take the cutoff width to be of the same order as the grid size.

Filtering of Navier Stokes equations yields the following LES equations:

$$\frac{\partial \rho}{\partial t} + \frac{\partial}{\partial x_i}(\rho \bar{u}_i) = 0 \quad (4.42)$$

and

$$\frac{\partial}{\partial t}(\rho \bar{u}_i) + \frac{\partial}{\partial x_j}(\rho \bar{u}_i \bar{u}_j) = \frac{\partial}{\partial x_j}(\sigma_{ij}) - \frac{\partial \bar{p}}{\partial x_i} - \frac{\partial \tau_{ij}}{\partial x_j} \quad (4.43)$$

where  $\bar{u}_i$  and  $\bar{p}$  are the filtered velocity and filtered pressure field, respectively.

The term  $\sigma_{ij}$  in Eqn.4.43 represents the stress tensor due to molecular viscosity, which can be defined as:

$$\sigma_{ij} \equiv \left[ \mu \left( \frac{\partial \bar{u}_i}{\partial x_j} + \frac{\partial \bar{u}_j}{\partial x_i} \right) \right] - \frac{2}{3} \mu \frac{\partial \bar{u}_k}{\partial x_k} \delta_{ij} \quad (4.44)$$

The averaging procedure for the momentum equations gives rise to the SGS stresses,  $\tau_{ij}$ . The SGS stresses are defined by

$$\tau_{ij} = \rho \overline{u_i u_j} - \rho \bar{u}_i \bar{u}_j \quad (4.45)$$

The major contributions of the SGS stresses can be determined by decomposing a flow variable,  $\phi(\mathbf{x}, t)$  as the combination of the filtered function  $\bar{\phi}(\mathbf{x}, t)$  with spatial variations that are larger than the cutoff width and resolved by the LES computation and  $\phi'(\mathbf{x}, t)$ , which contains unresolved spatial variations at a length scale smaller the cutoff width:

$$\phi(\mathbf{x}, t) = \bar{\phi}(\mathbf{x}, t) + \phi'(\mathbf{x}, t) \quad (4.46)$$

Using this decomposition in Eqn. 17, the following final form of the SGS stresses can be obtained:

$$\tau_{ij} = \rho \overline{u_i u_j} - \rho \bar{u}_i \bar{u}_j = (\rho \overline{\bar{u}_i \bar{u}_j} - \rho \bar{u}_i \bar{u}_j) + (\rho \overline{\bar{u}_i u'_j} + \rho \overline{u'_i \bar{u}_j}) + \rho \overline{u'_i u'_j} \quad (4.47)$$

In the above equation, the contributions of the SGS stresses are shown in three groups, namely the Leonard Stresses  $L_{ij} = \rho \overline{\bar{u}_i \bar{u}_j} - \rho \bar{u}_i \bar{u}_j$ , the cross-stresses  $C_{ij} = \rho \overline{\bar{u}_i u'_j} + \rho \overline{u'_i \bar{u}_j}$ , and the LES Reynolds stresses  $R_{ij} = \rho \overline{u'_i u'_j}$ . The Leonard stresses arise from the effects at the resolved scale. The cross stresses are due to interactions between SGS eddies and the resolved flow. The LES Reynolds stresses are induced by convective momentum transfer as a result of interactions of SGS eddies, which are modeled with a so-called SGS turbulence model. A modeling approach, which is considered for SGS eddies in the present study, is discussed below.

### Smagorinsky-Lilly SGS Model

Smagorinsky’s SGS model [115] is based on the assumption of an isotropic nature of the smallest turbulent eddies thereby following the Boussinesq hypothesis [109] to describe the effects of the unresolved eddies on the resolved flow. Therefore, the model

considers the local SGS stresses or the LES Reynolds stresses,  $R_{ij}$ , being proportional to the local rate-of-strain of the resolved flows. They are given by

$$R_{ij} = -2\mu_{SGS}\overline{S_{ij}} + \frac{1}{3}R_{ii}\delta_{ij} = -\mu_{SGS}\left(\frac{\partial\overline{u}_i}{\partial x_j} + \frac{\partial\overline{u}_j}{\partial x_i}\right) + \frac{1}{3}R_{ii}\delta_{ij} \quad (4.48)$$

where the average local rate-of-strain is defined by

$$\overline{S_{ij}} = \frac{1}{2}\left(\frac{\partial\overline{u}_i}{\partial x_j} + \frac{\partial\overline{u}_j}{\partial x_i}\right) \quad (4.49)$$

The term,  $\mu_{SGS}$  in Eqn. 4.48 represents dynamic SGS viscosity. The term  $\frac{1}{3}R_{ii}\delta_{ij}$  ensures that the sum of the modeled normal SGS stresses,  $R_{ii}$ , is equal to the kinetic energy of the SGS eddies.

The Smagorinsky-Lilly SGS model [116], which is based on the Prandtl mixing length model, assumes that a kinematic SGS viscosity,  $\nu_{SGS}$  ( $\nu_{SGS} = \mu_{SGS}/\rho$ ) can be described by one length scale and one velocity scale. The length scale is considered as the filter cutoff width,  $\Delta$ , whereas the velocity scale is defined as a product of the length scale,  $\Delta$  and the average strain rate of the resolved flow  $|\overline{S}|$ . The SGS eddy-viscosity is modeled by

$$\mu_{SGS} = \rho(C_{SGS}\Delta)^2|\overline{S}| \quad (4.50)$$

where  $C_{SGS}$  is the Smagorinsky constant. In the present work, a  $C_{SGS}$  value of 0.1 is considered, which has been found reasonable for the present type of flow calculation. The average strain rate in Eqn. 4.50 is computed from

$$|\overline{S}| = \sqrt{2\overline{S_{ij}}\overline{S_{ij}}} \quad (4.51)$$

## 4.4 Numerical Methods

In this dissertation, numerical simulation of the flow in the LDI combustors is conducted using the commercial CFD software, Fluent<sup>®</sup>. The pressure-based numerical method is applied to calculate the flow field, since this method performs well to resolve incompressible flows. The pressure-based solver employs the projection method [117], in which the constraint of the mass conservation of the velocity field is obtained by solving a pressure equation. The pressure equation is derived from the continuity and momentum equations in such a way that the velocity field, corrected by pressure, satisfies the continuity.

The pressure-based solver has two algorithms: a segregated algorithm and a coupled algorithm. The coupled algorithm is employed in the present study for the following reasons. A comparison between the computed flow fields using the two algorithms showed that the coupled algorithm could resolve the complex swirling flow structures better and the simulated velocity field with this approach also exhibited better agreements with the measurements.

## The Pressure-based Coupled Algorithm

In the coupled algorithm, the momentum equations and the pressure-based continuity equation are solved in a coupled manner, leading to a significant improvement in the rate of solution convergence. However, the memory requirement for the coupled algorithm is more than for the segregated algorithm since the discrete system of all momentum and pressure-based continuity equations have to be stored in the memory when solving for the velocity and pressure fields, rather than solving a single equation at a time in the segregated algorithm.

With the coupled algorithm, each iteration consists of the following steps that are continued until the solution convergence criteria are satisfied.

1. Updating the fluid properties based on the current solution. The properties include density, viscosity, specific heat, and diffusivity.
2. Solving the system of momentum and pressure-based continuity equations.
3. Updating the mass fluxes.
4. Solving the equations for additional scalars, such as energy (for the reacting flow), turbulent quantities, and species using the current values of the solution variables.
5. Updating the source terms arising from the interactions between the liquid and gas phases.
6. Checking the convergence of all the equations.

## Discretization

Using the pressure-based coupled algorithm, the Fluent<sup>®</sup> code solves the governing integral balances for the conservation of mass, momentum, and energy and other scalars such as turbulence and chemical species. The code employs a control-volume-based technique to convert the governing equations to algebraic equations, which can be resolved numerically [71]. This technique consists of integrating the governing equations about each control volume, yielding discrete equations that conserve each quantity on a control-volume basis.

For example, discretization of the steady conservation equation for transport of a scalar quantity,  $\phi$ , can be written as follows

$$\oint \rho \phi \mathbf{u} \cdot d\mathbf{A} = \oint \Gamma_\phi \nabla \phi \cdot d\mathbf{A} + \int_V S_\phi dV \quad (4.52)$$

where  $V$  is the arbitrary control volume,  $\mathbf{u}$  is the velocity vector,  $A$  is the surface area vector,  $\Gamma_\phi$  is the diffusion coefficient for the quantity  $\phi$ , and  $S_\phi$  is the source of  $\phi$  per unit volume.

The equation above is applied to each cell in the computational domain. If the cell has  $N$  number of faces, discretization of Eqn. 4.52 on the cell gives

$$\sum_f^N \rho_f \mathbf{u}_f \phi_f \cdot A_f = \sum_f^N \Gamma_\phi (\nabla \phi)_n \cdot A_f + S_\phi V \quad (4.53)$$

where  $\phi_f$  is the value of  $\phi$  convected through the face  $f$ ,  $\rho_f \mathbf{u}_f \cdot A_f$  is the mass flux through the face,  $A_f$  is area of the face, and  $(\nabla \phi)_n$  is the magnitude of  $\nabla \phi$  normal to the face.

For transient simulation, the governing equation has to be discretized in both space and time. Therefore, discretization of the unsteady conservation equation for the transport of  $\phi$  becomes

$$\frac{\partial \rho \phi}{\partial t} V + \sum_f^N \rho_f \mathbf{u}_f \phi_f \cdot A_f = \sum_f^N \Gamma_\phi (\nabla \phi)_n \cdot A_f + S_\phi V \quad (4.54)$$

In temporal discretization, the expression for the time evolution of the scalar  $\phi$  is given by

$$\frac{\partial \phi}{\partial t} = F(\phi) \quad (4.55)$$

where the function  $F$  includes any spatial discretization. If the time derivative is discretized using backward differences, the first-order accurate temporal discretization is given by

$$\frac{\phi^{n+1} - \phi^n}{\Delta t} = F(\phi) \quad (4.56)$$

On the other hand, the second-order accurate discretization becomes

$$\frac{3\phi^{n+1} - 4\phi^n + \phi^{n-1}}{2\Delta t} = F(\phi) \quad (4.57)$$

where  $n$ ,  $n + 1$ , and  $n - 1$  are the values at the time levels  $t$ ,  $t + \Delta t$ , and  $t - \Delta t$ , respectively.

In the pressure-based solver, once the time derivative is discretized,  $F$  is evaluated either at the future time level (implicit time integration) or the current time level (explicit time integration).

The Fluent<sup>®</sup> solver stores discrete values of the scalar quantity  $\phi$  at the center of each cell. However, as the scalar property is convected through the face a cell, it gives rise to a face value of the scalar,  $\phi_f$ , in the convective term in Eqns. 4.53 and 4.54. The quantity  $\phi_f$  is calculated by interpolating from the cell center values. An upwind scheme is used to obtain the face value  $\phi_f$ . In this scheme,  $\phi_f$  is derived from the quantities in the cell upstream, relative to the direction of the normal velocity. Several upwind schemes are available, which include first-order upwind, second-order upwind, third order MUSCL, power law, and QUICK.

The RANS simulations performed in this dissertation use the PREssure STaggering Option (PRESTO)[71] scheme for pressure interpolation and the second-order upwind scheme to solve the equations for momentum, energy, turbulence properties, and

chemical species since a higher-order scheme is more suitable for the flow simulation involving highly turbulent and swirling flows. In addition, the grid used for the computations has unstructured tetrahedral elements, causing the flow to misalign with the grid. In such a case, a higher-order scheme is expected to yield greater accuracy and minimize numerical discretization error. A brief description of the second-order-upwind scheme is presented below.

### Second-Order-Upwind Scheme

In this scheme, the quantities at the cell faces are computed using a multidimensional linear reconstruction approach [118]. The approach provides a higher-order accuracy at the cell faces through a Taylor series expansion of the cell-centered solution about the cell centroid. The face value  $\phi_f$  is computed from

$$\phi_f = \phi + \nabla\phi \cdot \mathbf{s} \quad (4.58)$$

where  $\phi$  and  $\nabla\phi$  are the cell-centered value and its gradient in the upstream cell, and  $\mathbf{s}$  is the displacement vector from the upstream cell centroid to the face centroid.

In Eqn. 4.58,  $\nabla\phi$  in each cell is determined using the Green-Gauss divergence theorem, which in discrete form is written as follows.

$$\nabla\phi = \frac{1}{V} \sum_f^N \overline{\phi}_f A \quad (4.59)$$

where  $\overline{\phi}_f$  is the average of  $\phi$  computed from the two cells adjacent to the face.

The cell-based gradient approach used in the present study evaluates  $\overline{\phi}_f$  through the arithmetic average of the values at the neighboring cell centers, i.e.,

$$\overline{\phi}_f = \frac{\phi_{c0} + \phi_{c1}}{2} \quad (4.60)$$

where  $\phi_{c0}$  and  $\phi_{c1}$  are the discrete values of the scalar  $\phi$  at the centers of the adjacent cells  $c0$  and  $c1$ , respectively.

## 5. Spray Combustion Modeling

### 5.1 Introduction

In most applications, liquid fuels are injected into the combustion chamber as turbulent sprays. As discussed in Chapter 3, a typical spray process in gas turbine applications involves several sub-processes. The characteristics of turbulent sprays significantly influence combustion performance and pollutant formation in gas turbines. Therefore, a detailed understanding of the spray sub-processes involved in turbulent spray combustion can lead to substantial improvements in combustion performance, quality of product, and in reduction of emissions of pollutants. Over the past few years, numerous theoretical and experimental studies have been conducted on turbulent spray combustion, although knowledge of the atomization process and gas-phase turbulence-spray interactions is far from complete. The underlying physics is not well understood. The validity of the available measurement data and correlations on spray properties are often questionable. Furthermore, a wide disparity exists between the various investigations regarding the exact relationships between liquid properties, surrounding gas properties, nozzle dimensions, and spray properties. In recent years, rapid advancements of spray diagnostic techniques have helped to make considerable progress in understanding more fundamental aspects of atomization and turbulent spray combustion. In addition to the progress in measurement techniques, with the advent of computer modeling and increasing computational power, it has become possible to conduct an in-depth spray analysis, which will further improve the understanding of turbulent spray combustion systems. Nevertheless, the two-way coupling between the liquid and gas-phase poses additional challenges to accurately model these systems. In general, the complexity in modeling and simulating turbulent spray combustion arises due to the presence of several strongly coupled phenomena, such as turbulence, heat and mass transfer between the phases, phase change, and chemical reactions. Furthermore, the challenge of numerical simulation is to find a compromise between computational efficiency including the simplification of mathematical models and detailed mathematical descriptions of relevant processes, which increase the complexity of the models and computational expenses.

This chapter discusses the sub-models that are used to compute the combusting sprays in a single-element and a multi-point LDI combustors. In a practical spray, the spray sub-processes that need to be modeled include atomization, drop breakup, drop distortion and drag, drop collision and coalescence, turbulent dispersion of spray drops, and drop evaporation. To simulate the reacting sprays in a highly turbulent

flow field of the LDI combustors, all these sub-processes are explicitly modeled. The numerical models are discussed here in details. In addition to the relevant spray models, the combustion modeling approach is presented.

As mentioned earlier in Section 3.2, a typical liquid spray has an initial dense spray regime where the liquid jet breaks up and strong interactions among the drops take place. However, the drops disperse downstream to reduce the local liquid volumetric fraction, thus forming a dilute regime. The rapid formation of dilute sprays is desirable to enhance the mixing of fuel and air in the combustion chamber, but it is almost impossible to avoid the dense regime and the associated liquid jet breakup process. Unfortunately, experimental data concerning dense sprays is very limited. On the other hand, the requirements for very high resolution hinder computer models to provide a full resolution of the liquid jet breakup in the dense regime [119].

Considering the difficulties in computing the dense spray regime, the primary breakup is not addressed for the study of reacting sprays in the LDI combustors. Therefore, only secondary breakup of the initially injected liquid drops is considered.

## 5.2 The Euler-Lagrange Approach

The traditional approach of spray combustion modeling is to track the discrete drops using a Lagrangian formulation [120]. The flow field inside and around the particles is not resolved, but its effects are considered in the form of analytical and empirical correlations [120], and inter-phase exchange terms account for interactions between the two phases. Past studies have shown that this approach of drop tracking is reasonable as long as the size of drops are of the order of the Kolmogorov length scale or smaller.

The Discrete Phase Model (DPM) [71] of the Fluent<sup>®</sup> solver is used to simulate the combusting sprays in the LDI combustors, which implements the Euler-Lagrange approach to treat the multiphase flow. The gas-phase is treated as a continuum by solving the Navier-Stokes equations, while the discrete-phase is solved by tracking the liquid particles through the calculated flow field. The discrete-phase exchanges mass, momentum, and energy with the gas-phase. The Eulerian equations for the gas-phase and the Lagrangian equations for the discrete-phase are described in Section 3.2. The source terms in the gas-phase equations for mass ( $\dot{\rho}^s$ ), momentum ( $F^s$ ), and energy ( $\dot{Q}^s$ ) account for the interactions between the gas-phase and the liquid sprays.

A main assumption of the Euler-Lagrange approach is that the discrete-phase occupies a low volume fraction, although high mass loading of liquid particles is acceptable. The trajectories of particles are calculated individually at specified intervals during the continuous-phase calculation. The discrete-phase particle trajectories are computed by integrating the force balance on the particle in a Lagrangian reference frame, i.e.,

$$\frac{d\mathbf{v}}{dt} = F_D(\mathbf{u} - \mathbf{v}) + \frac{g_x(\rho_l - \rho_g)}{\rho_l} + F_x \quad (5.1)$$

where  $\mathbf{v}$  is the liquid particle velocity,  $\mathbf{u}$  represents the gas velocity,  $F_D(\mathbf{u} - \mathbf{v})$  refers to the drag force per unit particle mass,  $F_x$  is an additional force per unit particle mass, and  $\rho_l$  and  $\rho_g$  are the liquid and gas density, respectively.

The above equation has terms for the drag force and gravity force. Furthermore, the equation incorporates additional forces in the particle force balance that can be important under special situations. For combustion applications, however, the drag and the gravity forces are the main influences on particle trajectories.

The term  $F_D$  in Eqn. 5.1 is written in the following form:

$$F_D = \frac{18\mu_g C_D Re}{\rho_l d_l^2} \frac{C_D Re}{24} \quad (5.2)$$

where  $\mu_g$  is the molecular viscosity of the gas,  $d_l$  corresponds to the liquid particle diameter, and  $C_D$  is the drag coefficient. The relative Reynolds number,  $Re$ , is defined as

$$Re \equiv \frac{\rho_g d_l |\mathbf{v} - \mathbf{u}|}{\mu_g} \quad (5.3)$$

The two-way coupling system used in the DPM accounts for the influences of the gas-phase on the combusting liquid particles via drag, turbulence, and momentum transfer, while the particles influence the gas-phase via the source terms of mass, momentum, and energy. Figure 5.1 illustrates how a particle may exchange mass, momentum, and heat with the continuous-phase within the control volumes that are crossed by the trajectory of the particle.

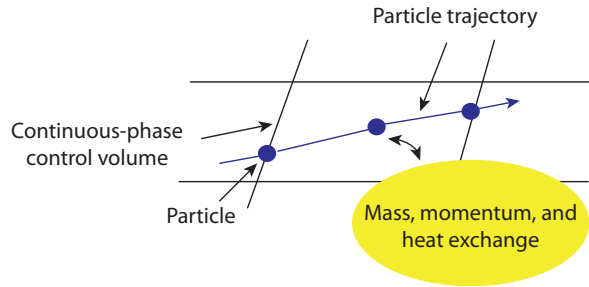


Figure 5.1: Schematic representation of the coupling between the continuous-phase and discrete-phase in the DPM

### 5.3 Turbulent Dispersion Modeling of Spray Drops

The dispersion of liquid drops in the LDI combustors due to fluid phase or gas-phase turbulence is predicted using the stochastic tracking method. The Fluent<sup>®</sup> solver implements the Discrete Random Walk (DRW) model [121] as a stochastic method to determine turbulent dispersion of spray drops. In this approach, the dispersion of particles or liquid drops is predicted by integrating the trajectory equations (Eqn. 5.1) for individual particles and using the instantaneous fluid velocity along the particle path during the integration process. By computing the trajectory for a sufficient number of representative particles, the stochastic effects of turbulence on the particle dispersion can be included. In the DRW model, the fluctuating velocity components

are discrete piecewise constant functions of time. The random value is kept constant over an interval of time given by the characteristics lifetime of the eddies [71].

To predict particle dispersion, the concept of the integral time scale is used, which describes the time spent in a characteristic turbulent eddy along the particle path. Essentially, the integral time scale is proportional to the particle dispersion rate. For small particles that move with the fluid phase, the integral time becomes the fluid Lagrangian integral time, which is written in the form

$$T_l = C_l \frac{k}{\varepsilon} \quad (5.4)$$

where  $C_l$  is the time scale constant,  $k$  is the turbulence kinetic energy, and  $\varepsilon$  is the turbulence dissipation rate.

For the  $k - \varepsilon$  model and its variants, the time scale constant value used is 0.15.

In the DRW model, the interaction of a particle with a sequence of discrete stylized gas-phase turbulent eddies is simulated. Each eddy is characterized by a Gaussian distributed random velocity fluctuation and a time scale. The values of the fluctuating velocity components,  $u'$ ,  $v'$ , and  $w'$ , that prevail during the lifetime of the turbulent eddy are sampled by assuming that they obey a Gaussian probability distribution, i.e.,

$$G(u') = \left( \frac{4}{3\pi k} \right)^{-3/2} \exp \left( \frac{-3|\mathbf{u}'|^2}{4k} \right) \quad (5.5)$$

The above equation shows that the Gaussian distribution has a variance, which is proportional to the turbulent kinetic energy,  $k$ . In the  $k - \varepsilon$  model, by assuming isotropy of stresses, the fluctuating velocity can be defined as

$$\overline{u'^2} = \overline{v'^2} = \overline{w'^2} = 2k/3 \quad (5.6)$$

The motion of the liquid drop is integrated with the gas-phase turbulent velocity field until the drop passes from the eddy. The drop-eddy interaction time can be determined either by the eddy characteristic lifetime or by the time required for the drop to pass through an eddy [74].

The eddy dissipation length scale is given by

$$l_e = \frac{C_\mu^{3/4} k^{3/2}}{\varepsilon} \quad (5.7)$$

where  $C_\mu$  is a constant for the standard  $k - \varepsilon$  model.

On the other hand, the characteristic lifetime of the eddy is defined by the following form

$$t_e = \frac{l_e}{\sqrt{2k/3}} \quad (5.8)$$

The time taken by the drop to pass through an eddy is approximated as

$$t_p = \frac{l_e}{|\bar{\mathbf{u}} - \mathbf{v}|} \quad (5.9)$$

where  $\bar{\mathbf{u}}$  is the gas mean velocity and  $\mathbf{v}$  is the drop velocity.

However, the minimum of the eddy lifetime,  $t_e$ , and the eddy crossing time,  $t_p$ , is considered as the drop-eddy interaction time,  $t_{int}$ , i.e.,

$$t_{int} = \min(t_e, t_p) \quad (5.10)$$

If the eddy crossing time is small compared to the eddy lifetime, then the crossing trajectory effect is important.

## 5.4 Atomization and Drop Breakup Modeling

The atomization model provides the initial conditions for the computations of spray drop size, drop velocities and its position, temperature etc., at the nozzle exit. However, for a realistic atomizer simulation, spray drops have to be randomly distributed. By using a stochastic trajectory selection in the atomizer model, it is possible to attain a random distribution of drops.

The pressure-swirl atomizer model is applied in the DPM to model the liquid spray atomization in the LDI combustion simulations, since a hollow-cone simplex atomizer was used in the experiments [47]. In this section, the discussion is primarily focused on the theory of the pressure-swirl atomizer model and its implementation in the present numerical study.

### 5.4.1 The Pressure-Swirl Atomizer Model

The pressure-swirl atomizer model provides an initial dispersion angle, and the stochastic trajectory selection picks an initial direction within this angle [71]. This approach makes the drops spread uniformly among the computational cells near the atomizer. By evenly spreading the drops over the cells, the coupling with the gas-phase can be improved due to smooth dissemination of drag. Furthermore, the source terms in the energy and species conversion equations are more uniformly distributed among adjacent computational cells, thereby improving solution convergence.

The simplex atomizer is the most simple form of pressure-swirl atomizer, where fuel is fed into a swirl chamber through tangential ports. The swirling liquid fuel has high angular velocity as it enters the swirl chamber, thereby developing an air-cored vortex. The fuel then enters the final orifice through the outlet of the swirl chamber. Under the action of both axial and radial forces, the rotating fuel eventually emerges from the final orifice in the form of a hollow conical sheet. The thinning sheet emerging from the orifice becomes unstable when it encounters the surrounding medium. Consequently, the sheet disintegrates into ligaments and then drops.

The Fluent<sup>®</sup> solver implements the concept of the Linearized Instability Sheet Atomization (LISA) model [122] in the pressure-swirl atomizer model. The LISA model consists of two stages:

1. liquid film formation

2. sheet breakup and atomization

### Liquid Film Formation

The centrifugal motion of the liquid within the pressure-swirler injector creates an air-core surrounded by a liquid film. The thickness of the film,  $t_l$ , is related to the liquid mass flow rate by [123]

$$\dot{m}_l = \pi \rho_l u_l t_l (d_0 - t_l) \quad (5.11)$$

where  $\dot{m}_l$  is the mass flow rate of the liquid,  $d_0$  is the atomizer exit diameter, and  $u_l$  is the axial component of liquid velocity at the atomizer exit. Nevertheless, it is difficult to calculate  $u_l$ , since its value depends on various internal details of the injector. Therefore, using a different approach [124], the total velocity,  $U_l$  is generally measured while assuming its dependence on the injector pressure drop,  $\Delta P$ , i.e.,

$$U_l = k_v \sqrt{\frac{2\Delta P}{\rho_l}} \quad (5.12)$$

where  $k_v$  is the velocity coefficient, which is a function of the injector design and injection pressure [102]. In general the following expression is used for  $k_v$ :

$$k_v = \max \left[ 0.7, \frac{4\dot{m}_l}{\pi d_0^2 \rho_l \cos \theta} \sqrt{\frac{\rho_l}{2\Delta P_l}} \right] \quad (5.13)$$

where  $\theta$  is the initial half spray cone angle, which is assumed to be known.

If the pressure drop is also known,  $U_l$  can be calculated from Eqn. 5.12. Using the value of  $U_l$ , liquid axial velocity,  $u_l$ , can be determined from

$$u_l = U_l \cos \theta \quad (5.14)$$

As shown in Fig. 5.2, the initial liquid sheet thickness,  $t_s$ , can be related to the film thickness within the discharge orifice by the expression

$$t_s = t_l \cos \theta \quad (5.15)$$

Therefore, using Eqns 5.11-5.28, the film thickness and the axial velocity of the liquid film can be determined at the injector exit. The tangential velocity of the liquid is generally assumed to be equal to the radial velocity component of the liquid sheet downstream of the nozzle exit [122], i.e.,

$$v_l = w_l = U_l \sin \theta \quad (5.16)$$

where  $v_l$  and  $w_l$  are radial and tangential components of liquid velocity, respectively.

### Sheet Breakup and Atomization

The LISA model takes into account the effects of the surrounding medium, liquid viscosity, and surface tension on the breakup of the liquid sheet issuing from a pressure-swirl atomizer. The model assumes that a two-dimensional, viscous, incompressible

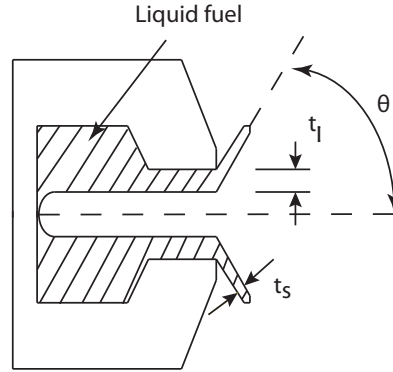


Figure 5.2: Relationship between sheet thickness and half spray cone angle [5]

liquid sheet of thickness  $t_s$  moves with a relative velocity  $U$  through an inviscid, incompressible gas medium. A coordinate system is used that moves with the sheet, and an array of infinitesimal disturbances is imposed on the initially steady motion. The amplitude of the liquid surface wave becomes

$$\eta = \eta_0 \exp(i\kappa x + \omega t) \quad (5.17)$$

where  $\eta_0$  is the initial wave amplitude,  $\kappa$  is the wave number, and  $\omega$  is wave growth rate.

The wave number,  $\kappa$  is written in the form

$$\kappa = \frac{2\pi}{\lambda} \quad (5.18)$$

where  $\lambda$  is the wavelength.

The complex form of the wave growth rate is

$$\omega = \omega_r + i\omega_i \quad (5.19)$$

The most unstable disturbance has the largest value of  $\omega_r$ , which is assumed to be responsible for sheet breakup. In principle, the wave growth rate is a function of the wave number, i.e.,  $\omega = \omega(\kappa)$ . The spectrum of infinitesimal disturbances gives rise to fluctuating velocities and pressures for both liquid and gas. In general, there are two distinct modes that satisfy the governing equations subject to the boundary conditions at the upper and lower interfaces of the liquid sheet [125, 126]. The first mode, as shown in Fig. 5.3a, is the sinuous or anti-symmetric mode, which has waves at the upper and lower sheet interfaces in phase. On the contrary, for the varicose or symmetric mode, the waves at the two sheet interfaces are  $\pi$  radians out of phase (see Fig. 5.3b). At low velocities and low gas-liquid density ratios, it has been observed that the sinuous mode generally dominates the growth of the varicose waves [127]. For high-speed flows, the sinuous and varicose modes become almost indistinguishable. The pressure-swirl atomizer model, therefore, is based upon the growth of anti-symmetric or sinuous waves on the liquid sheet that induces sheet breakup into ligaments [71].

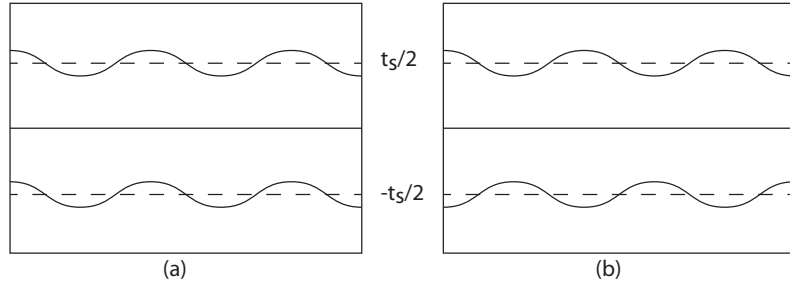


Figure 5.3: Schematic of (a) sinuous waves and (b) varicose waves

The following form gives the dispersion relation for the sinuous mode [127]

$$\omega^2 [\tanh(\kappa \frac{t_s}{2}) + \rho_{g,l}] + [4\nu_l \kappa^2 \tanh(\kappa \frac{t_s}{2}) + 2i\rho_{g,l}\kappa U_{rel}] + 4\nu_l \kappa^4 \tanh(\kappa \frac{t_s}{2}) - 4\nu_l^2 \kappa^3 l \tanh(\frac{t_s}{2}) - \rho_{g,l} U_{rel}^2 \kappa^2 + \frac{\sigma_l \kappa^3}{\rho_l} = 0 \quad (5.20)$$

where the density ratio,  $\rho_{g,l} = \rho_g/\rho_l$ ,  $l = \sqrt{\kappa^2 + \omega/\nu_l}$ ,  $\nu_l$  is the liquid kinematic viscosity,  $\sigma_l$  is the liquid surface tension, and  $t_s/2$  is the sheet half-thickness.

However, assuming that the terms of second order in viscosity is negligible in comparison to the other terms in Eqn. 5.20, the equation reduces to

$$\omega_r = \frac{1}{\tanh(\kappa \frac{t_s}{2}) + \rho_{g,l}} \left[ -2\nu_l \kappa^2 \tanh(\kappa \frac{t_s}{2}) + \sqrt{4\nu_l^2 \kappa^4 \tanh^2(\kappa \frac{t_s}{2}) - \rho_{g,l}^2 U_{rel}^2 \kappa^2 - [\tanh(\kappa \frac{t_s}{2}) + \rho_{g,l}] \left[ -\rho_{g,l} U_{rel}^2 \kappa^2 + \frac{\sigma_l \kappa^3}{\rho_l} \right]} \right] \quad (5.21)$$

For long waves, the wavelengths are large compared with the sheet thickness, so that  $\tanh(\kappa \frac{t_s}{2}) \approx \kappa \frac{t_s}{2}$ . Furthermore, in many applications, the density ratio,  $\rho_{g,l}$ , is on the order of  $10^{-3}$ . It can be assumed that  $\rho_{g,l} \ll \kappa \frac{t_s}{2}$ , thus further reducing Eqn. 5.21 to

$$\omega_r = -2\nu_l \kappa^2 + \sqrt{4\nu_l^2 \kappa^4 + \frac{\rho_{g,l} U_{rel}^2 \kappa}{t_s/2} - \frac{\sigma_l \kappa^2}{\rho_l t_s/2}} \quad (5.22)$$

For short waves on high-speed sheets,  $\tanh(\kappa \frac{t_s}{2}) \approx 1$  and  $\rho_{g,l} \ll 1$ , reducing Eqn. 5.21 to

$$\omega_r = -2\nu_l \kappa^2 + \sqrt{4\nu_l^2 \kappa^4 + \rho_{g,l} U_{rel}^2 \kappa^2 - \frac{\sigma_l \kappa^3}{\rho_l}} \quad (5.23)$$

If the sheet thickness is small compared to the wavelength, ligaments are assumed to form from the sheet breakup process when the unstable waves reach a critical amplitude. Equation 5.22 shows that the growth rate of long waves depends on the sheet thickness. On the other hand, Eqn. 5.23 indicates that the growth rate of short waves is independent of the sheet thickness. Therefore, for short waves, the onset of ligament formation can be formulated based on an analogy with the breakup length of

cylindrical jets [128]. When the surface disturbance reaches a value of  $\eta_{bu}$  at breakup, a breakup time,  $\tau_{bu}$  can be determined using the following equation:

$$\begin{aligned}\eta_{bu} &= \eta_0 \exp(\Omega_s \tau_{bu}) \\ \tau_{bu} &= \frac{1}{\Omega_s} \ln\left(\frac{\eta_{bu}}{\eta_0}\right)\end{aligned}\quad (5.24)$$

where  $\Omega_s$  is the maximum growth rate.  $\Omega_s$  is found from Eqn. 5.21 by maximizing  $\omega_r$  as a function of  $\kappa$ . The liquid sheet eventually breaks up and ligaments will be formed having a length

$$L_{bu} = U_l \tau_{bu} = \frac{U_l}{\Omega_s} \ln\left(\frac{\eta_{bu}}{\eta_0}\right)\quad (5.25)$$

where the quantity  $\ln\left(\frac{\eta_{bu}}{\eta_0}\right)$  is an empirical sheet constant. In the present study, a value of 12 is considered for the sheet constant based on an experimental study that shows this value agrees well with sheet breakup lengths over a wide range of Weber numbers [129].

The diameter of the ligaments formed at the time of breakup can be obtained from a mass balance. For the long waves, it is assumed that the ligaments are formed from tears in the sheet twice per wavelength, the ligament diameter becomes

$$d_L = \sqrt{\frac{4t_s}{K_s}}\quad (5.26)$$

where  $K_s$  is the wave number corresponding to the maximum growth rate,  $\Omega_s$ .

The value of  $K_s$  can be obtained from the relation

$$K_s = \frac{\rho_g U_{rel}^2}{2\sigma_l}\quad (5.27)$$

Equation 5.26 shows that the ligament diameter depends on the sheet thickness. For attenuating sheets, the thickness is inversely proportional the radial distance from the injector nozzle. Figure 5.4 shows a schematic of the conceptual liquid flow at the exit of a hollow cone pressure-swirl atomizer. The sheet thickness at the breakup point can be obtained using the following correlation.

$$t_s = \frac{2r_0 t_0}{r_0 + L \sin \theta}\quad (5.28)$$

where  $t_0$  is the half sheet-thickness at the injector exit,  $r_0$  is the radius at the atomizer exit, and  $L$  refers to the sheet length. In Fig. 5.4, the cone half-angle,  $\theta$ , is measured from the centerline to the mid-line of the sheet.

By substituting  $L = U_l t$  in Eqn. 5.28 and assuming  $r_0 \ll L \sin \theta$ , the sheet thickness,  $t_s$ , becomes

$$t_s = \frac{2K}{U_l t}\quad (5.29)$$

where the dimensional constant  $K = \frac{r_0 t_0}{\sin \theta}$  represents the variation of the sheet thickness with distance from the injector exit.

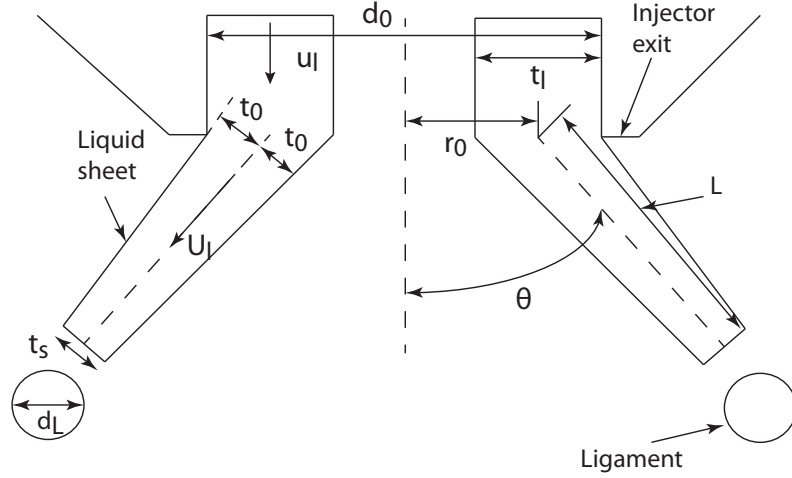


Figure 5.4: Schematic of the liquid flow at the nozzle exit

For short waves, it is assumed that the ligaments are formed from tears in the sheet once per wavelength [127]. The resulting ligament diameter is given by

$$d_L = \sqrt{\frac{8t_s}{K_s}} \quad (5.30)$$

Nevertheless, the pressure-swirl atomizer model in the Fluent<sup>®</sup> code assumes that the ligament diameter is linearly proportional to the wavelength,  $\Lambda_s$ , which breaks up the liquid sheet, i.e.,

$$d_L = C_L \Lambda_s = \frac{2\pi C_L}{K_s} \quad (5.31)$$

where  $C_L$  is the ligament constant, which is assumed to 0.5 in the present study.

In both long and short waves, the breakup of ligaments into drops is considered to behave according to the capillary instability analysis [130]. The wave number at the ligament breakup,  $K_L$ , corresponding to the maximum growth rate for the breakup of a cylindrical viscous liquid column is determined from

$$K_L d_L = \left[ \frac{1}{2} + \frac{3\mu_l}{2(\rho_l \sigma_l d_L)} \right]^{-\frac{1}{2}} \quad (5.32)$$

In general, it is considered that the breakup occurs when the amplitude of the unstable waves is equal to the radius of the ligament and one drop is formed per wavelength [130]. The relation between drop size wave number is established in the following form by mass balance.

$$d_l = \sqrt[3]{\frac{3\pi d_L^2}{K_L}} \quad (5.33)$$

where  $d_l$  and  $d_L$  are the drop diameter and ligament diameter, respectively.

Combining Eqns. 5.32 and 5.33 gives

$$d_l = 1.88d_L(1 + 3Oh)^{\frac{1}{6}} \quad (5.34)$$

where  $Oh$  is the Ohnesorge number, which is a combination of the Reynolds number and the Weber number, i.e.,

$$Oh = \frac{\sqrt{We_l}}{Re_l} = \frac{\mu_l}{\sqrt{\rho_l \sigma_l d_L}} \quad (5.35)$$

where  $We_l$  and  $Re_l$  are the liquid Weber number and the Reynolds number, respectively.

### 5.4.2 Drop Breakup Modeling

Over the years, several drop breakup models have been proposed owing to different physical mechanisms. Among them, the Taylor analogy breakup (TAB) model, the dynamic drop breakup (DDB) model, the Wave breakup model, and the Rayleigh-Taylor (RT) model are the most popular and widely used models for liquid spray drop breakup modeling.

The TAB [131] and the DDB [132] models are based on the dynamics of individual droplets in the surrounding medium. The TAB model is based upon Taylor’s analogy [133] between an oscillating and distorting droplet and a spring mass system. In other words, the breakup is due to the amplification of drop deformation resulting from vibrational resonance of the liquid surface. The model is generally well suited for low-Weber-number sprays [71]. The DDB model is a modified version of the TAB model that enforces mass conservation constraints as the drop distorts. In principle, this model is a deformation-induced secondary breakup model, which is appropriate for the bag breakup regime. The Wave model [134] considers Kelvin-Helmholtz (K-H) instability effects and is appropriate for breakup of drops in the stripping regime. The RT model [135] considers RT instabilities that arise on a very high-speed drop surface. Therefore, this model can be adopted to model droplet secondary breakup in the catastrophic regime. Nevertheless, it is hard to choose the right breakup model for a specific spray simulation. It has been found that with a proper selection of model constants, all the breakup models are capable of reproducing measured data. In the present study of the LDI reacting sprays, the Wave model has been selected, since the drop breakup is assumed to be in the shear regime. A brief description of the model is presented below.

#### Wave Breakup Model

The Wave breakup model is based on the stability analysis of round liquid jets, which describes stripping breakup of drops in sprays [128]. Therefore, it is more appropriate for high Weber number flows. The model is also capable of simulating the breakup of a liquid jet at the injector exit. Drop breakup time and the resulting drop size in the Wave model are related to the fastest growing K-H instability on the liquid surface.

The maximum growth rate,  $\Omega$ , for the corresponding wavelength,  $\Lambda$ , can be determined from

$$\Lambda = 9.02a \frac{(1 + 0.45Oh^{0.5})(1 + 0.4Ta^{0.7})}{(1 + 0.87We_g^{1.67})^{0.6}} \quad (5.36)$$

$$\Omega = \frac{0.34 + 0.38We_g^{1.67}}{(1 + Oh)(1 + 1.4Ta^{0.6})} \left( \frac{\sigma_l}{\rho_l a^3} \right)^{0.5} \quad (5.37)$$

where  $Ta = OhWe_g^{0.5}$  is the Taylor number,  $We_g = \rho_g U_{rel}^2 a / \sigma_l$  refers to the gas Weber number,  $a$  is the undisturbed jet radius, and  $U_{rel}$  is the relative velocity between the gas and the liquid drop.

The breakup of droplet parcels is modeled by assuming that the diameter of the new droplets is proportional to the wavelength of the fastest growing surface wave over the parent drop, i.e.,

$$d_l = 2B_0\Lambda \quad (5.38)$$

where  $B_0$  is a model constant set equal to 0.61 in the present study, based on the work of Reitz [134].

The characteristic radius of an unstable drop in the parent parcel changes continuously with time, and is determined from the following equation.

$$\frac{da}{dt} = -\frac{(a - \frac{d_l}{2})}{\tau_{bu}}, \quad \frac{d_l}{2} \leq a \quad (5.39)$$

where the breakup time,  $\tau_{bu}$  is computed from

$$\tau_{bu} = \frac{3.726B_1a}{\Lambda\Omega} \quad (5.40)$$

The values of  $\Lambda$  and  $\Omega$  can be obtained from Eqns. 5.36 and 5.37, respectively. In this study, the breakup time constant,  $B_1$ , is set to 1.73 as recommended in literature [69]. Nevertheless, values of  $B_1$  ranges between 1 and 60, depending on the injector characterization and the related drop breakup mechanism.

The Wave model considers an accumulation of mass from the parent parcel at a rate  $\tau_{bu}$  until the shed mass is equal to 5% of the initial parcel mass. When a new parcel is formed, its diameter can be determined using Eqn. 5.38.

In conjunction with the Wave model for drop breakup, the Dynamic Drag Model (DDM) is included in the present study to accurately determine drop drag. The model calculates the drop drag coefficient dynamically, thus accounting for variations in the drop shape. In the Fluent<sup>®</sup> solver, when the collision model is applied, collisions adjust the distortion and distortion velocities of the colliding drops. In the DDM, the drag coefficient varies between that of a sphere (see Eqn. 3.28) and the drag coefficient value corresponding to a disk [69]. The drop drag coefficient,  $C_D$ , is thus related to the magnitude of drop distortion by the expression

$$C_D = C_{D,sphere}(1 + 2.632y) \quad (5.41)$$

where  $y$  is the drop’s distortion from sphericity, which is obtained using Eqn. 3.31.

## 5.5 Drop Collision and Coalescence Modeling

The theory of drop collision and coalescence and the possible collision outcomes are discussed in Chapter 3. However, modeling drop collision for a large group of drops in liquid spray becomes computationally expensive unless an efficient method for particle representation is implemented. The collision model used in the Fluent<sup>®</sup> code for the present study is discussed below.

For example, if there are  $N$  drops present in a liquid spray, each drop can collide with the remaining  $N - 1$  drops. Therefore, the number of possible collision pairs is about  $\frac{1}{2}N^2$ . In a numerical simulation of spray, the collision algorithm has to calculate all the collision events at every time step, thereby increasing the computational cost. In order to reduce the time for collision calculation, the concept of parcels has been introduced. A parcel, in essence, corresponds to an ensemble of identical particles. Although the parcel concept significantly reduces the computational cost, the effort to calculate the possible interactions of many parcel trajectories would still be CPU and memory intensive. An alternative and more efficient method is O’Rourke’s algorithm [59], which suggests a stochastic estimate of parcel collisions. The algorithm also assumes that two parcels may collide only if they are located in the same continuous-phase cell. This assumption is valid when the size of the continuous-phase cell is small compared to the size of the spray. The assumption may prevent drops that are close to each other, but not in the same continuous-phase cell, from colliding. Nevertheless, the effect of this error is reduced by allowing some drops that are farther apart to collide. Overall, the accuracy of the O’Rourke’s algorithm is second-order in space.

Once it is determined that two parcels of drops collide, the algorithm detects the type of collision. However, it only considers coalescence and bouncing outcomes. In general, the outcome becomes coalescence if the drops collide head-on. On the other hand, bouncing occurs if the collision is more oblique. The probability of each outcome is computed from the collision Weber number,  $We_l$  (see Section 3.3.4). Subsequently, the state of the two colliding parcels is modified, depending on the outcome of the collision.

The O’Rourke’s algorithm uses the concept of collision volume to compute the probability of collision. The probability of collision of two drops is conducted in the frame of reference of the larger drop or collector drop so that its velocity is zero. The important term here is the relative distance between the two drops. The smaller drop is considered being engaged in a collision with the collector when the center of the smaller drop passes within a flat disk centered around the collector of area  $\pi(r_1 + r_2)^2$  perpendicular to the trajectory of the smaller drop. The area of this disk multiplied by the distance traveled by the smaller drop in one time step defines the collision volume, i.e.,

$$V_{coll} = \pi(r_1 + r_2)^2 \mathbf{v}_{rel} \Delta t \quad (5.42)$$

where  $(r_1 + r_2)$  is the distance between the drop centers,  $\mathbf{v}_{rel}$  is the relative velocity of the two drops (see Eqn. 3.33), and  $\Delta t$  refers to the time step.

The smaller drop is within the continuous-phase phase cell of volume  $V$ . Considering there is a uniform probability of the smaller drop being anywhere within the cell, the likelihood of the drop being within the collision volume is the ratio of the two

volumes. Therefore, the probability of the collector colliding with the smaller drop is

$$P_1 = \frac{V_{coll}}{V} = \frac{\pi(r_1 + r_2)^2 \mathbf{v}_{rel} \Delta t}{V} \quad (5.43)$$

This concept can be implemented in the parcel as well by modifying Eqn. 5.43. If  $n_1$  and  $n_2$  number of drops are present in the collector and smaller drop parcels, respectively, the mean number of collisions that the collector parcel undergoes is

$$\bar{n} = \frac{\pi(r_1 + r_2)^2 \mathbf{v}_{rel} \Delta t}{V} \quad (5.44)$$

where  $(r_1 + r_2)$  now refers to the distance between the centers of the two parcels.

The actual number of collision events that the collector experiences is the probability distribution of the number of collisions [59], which follows a Poisson distribution, i.e.,

$$P(n) = e^{-\bar{n}} \frac{\bar{n}^n}{n!} \quad (5.45)$$

where  $n$  is the number of collisions between the collector and other drops.

When the two parcels collide, the outcome of the collision is determined. To determine the outcome of a collision, a collision impact parameter,  $X$ , is calculated and compared to a critical value,  $X_{crit}$ . If  $X < X_{crit}$ , the result of the collision is coalescence. In principle, drop separation occurs following a collision if the rotational energy of the coalesced pair exceeds the surface energy required to reform the original drops from the pair. The probability that a collision event will result in permanent coalescence is given by the coalescence efficiency,  $E_{coll} = X/X_{crit}$ , which depends on the drop radii before collision and the Weber number based on the drop velocity difference,  $We_1$  [59]. The relevant parameters are given in formula form as

$$\begin{aligned} X &= \sqrt{Y}(r_1 + r_2) \\ X_{crit} &= (r_1 + r_2) \sqrt{\min \left[ 1.0, \frac{2.4(\gamma^3 - 2.4\gamma^2 + 2.7)}{We_1} \right]} \end{aligned} \quad (5.46)$$

where  $r_1$  and  $r_2$  are the radii of the collector and smaller drops, respectively,  $Y$  is a random number in the interval of  $(0, 1)$ ,  $\gamma = \frac{r_1}{r_2}$  is the drop size ratio and is always greater than or equal to unity, and the Weber number  $We_1 = \frac{\rho_l |\mathbf{v}_1 - \mathbf{v}_2|^2 d_1}{\sigma_l}$ .

Equation 5.46 indicates that drops of greatly unequal size are more likely to coalesce than drops of almost equal size [136]. When the coalescence is predicted, Eqn. 5.45 gives the number of smaller drops removed from parcel 2 (coalesce with a collector) and the size, velocity, and temperature of drops in parcel 1 are modified suitably to conserve mass, momentum, and energy.

In the case of a grazing collision,  $X$  exceeds  $X_{crit}$ . The drops do not combine, but maintain their sizes and temperatures. However, the drops undergo velocity changes, which is taken into account in the momentum conservation [59]. It is also assumed that some fraction of kinetic energy of drops is lost due to viscous dissipation. This fraction of energy lost can be related to the collision impact parameter,  $X$ , by the expression

$$\mathbf{v}'_1 = \frac{m_1 \mathbf{v}_1 + m_2 \mathbf{v}_2 + m_2 (\mathbf{v}_1 - \mathbf{v}_2)}{m_1 + m_2} \left( \frac{X - X_{crit}}{r_1 + r_2 - X_{crit}} \right) \quad (5.47)$$

where  $\mathbf{v}'_1$  is the new drop velocity and  $m_1$  and  $m_2$  are the drop masses for the collector and smaller drops, respectively.

Equation 5.47 can be used to determine all the components of drop velocity during grazing collision.

## 5.6 Drop Vaporization Modeling

In the present work, the mass-transfer vaporization law of a droplet as given in the Fluent manual<sup>®</sup> [71] is used in the DPM to account for evaporation of spray drops. The evaporation of drops continues until the drops reach the boiling point, or until the drops' volatile fraction is fully consumed. This model is based on gradient diffusion and is designed to model evaporation from airborne drops. A molar flux of evaporated vapor from a drop surface is calculated as

$$N_i = k_c(C_{i,s} - C_{i,\infty}) \quad (5.48)$$

where  $k_c$  is the mass transfer coefficient,  $C_{i,s}$  is the vapor concentration at the drop surface, and  $C_{i,\infty}$  is the vapor concentration in the bulk gas.

The mass transfer coefficient,  $k_c$ , is calculated from the Sherwood number shown in Eqn. 3.36.

The vapor concentration at the drop surface,  $C_{i,s}$ , is determined by assuming that the partial vapor pressure at the interface is equal to the saturated vapor pressure,  $p_{sat}$ , at the drop temperature,  $T_d$ , i.e.,

$$C_{i,s} = \frac{p_{sat}(T_d)}{RT_d} \quad (5.49)$$

where  $R$  is the universal gas constant.

The vapor concentration in the bulk gas is obtained from the PDF look-up table for non-premixed combustion calculations:

$$C_{i,\infty} = X_i \frac{p}{RT_\infty} \quad (5.50)$$

where  $X_i$  is the local bulk mole fraction of species  $i$ ,  $p$  refers to the local absolute pressure, and  $T_\infty$  is the local bulk temperature in the gas.

Due to vaporization, the mass of the drop becomes

$$m_d(t + \Delta t) = m_d(t) - N_i A_d M_{w,i} \Delta t \quad (5.51)$$

where  $M_{w,i}$  is the molecular weight of species  $i$ ,  $m_d$  is the mass of the drop, and  $A_d$  refers to the drop surface area.

The drop temperature,  $T_d$ , is updated by using the heat balance expression shown in Eqn. 3.38. In the present calculations, radiation heat transfer to the particle is not included.

## 5.7 Combustion Modeling

In the present study, combustion simulation of the reacting spray is performed using the Non-Premixed Combustion model combined with the mixture fraction- $\beta$  PDF approach [71]. The theory of the model is described in this section.

Non-premixed modeling solves transport equations for one or two scalars. In this model, instead of solving the equations for individual species, species concentrations are derived from the predicted mixture fraction fields. In non-premixed combustion, fuel and oxidizer separately enter the reaction zone. Under a certain set of assumptions, the instantaneous thermochemical state of fluid can be reduced to a conserved scalar quantity known as the mixture fraction,  $f_m$ , which is given by [137]

$$f_m = \frac{Y_i - Y_{i,ox}}{Y_{i,fuel} - Y_{i,ox}} \quad (5.52)$$

where  $Y_i$  is the elemental mass fraction for element,  $i$ ,  $Y_{i,ox}$  and  $Y_{i,fuel}$  are the mass fractions of the oxidizer and fuel, respectively.

In general, the mixture fraction is defined as the fraction of mass present locally, which originally is coming from the fuel stream.

For  $f_m = 0$ , Eqn. 5.52 gives  $Y_i = Y_{i,ox}$ , signifying the air inlet. On the other hand, for  $f_m = 1$ , the equation gives  $Y_i = Y_{i,fuel}$ , which implies the fuel inlet.

### Mixture Fraction Transport Equations

With the assumption of equal diffusivities, the species equations can be reduced to a single equation for the mixture fraction,  $f_m$ . The mixture fraction,  $f_m$ , is a conserved quantity, since the reaction source terms in the species equations cancel. The assumption of equal diffusivities is generally acceptable for turbulent flows as turbulent convection overcomes molecular diffusion. The mean (density-averaged) mixture fraction equation is

$$\frac{\partial(\rho_g \overline{f_m})}{\partial t} + \nabla \cdot (\rho_g \mathbf{u} \overline{f_m}) = \nabla \cdot \left( \frac{\mu_t}{\sigma_t} \nabla \overline{f_m} \right) + \dot{\rho}^s + S_{user} \quad (5.53)$$

where  $\dot{\rho}^s$  refers the source term as a result of mass transfer from liquid fuel drops to the gas-phase (see Eqn. 3.18),  $S_{user}$  is a user-defined source term,  $\mu_t$  is the turbulent viscosity, and  $\sigma_t$  is a constant. The above expression is also known as the Favre mean mixture fraction.

In addition to solving for the Favre mean mixture fraction, it is necessary to solve a conservation equation for the mixture fraction variance,  $\overline{f_m'^2}$  [138]:

$$\frac{\partial}{\partial t} \left( \rho_g \overline{f_m'^2} \right) + \nabla \cdot \left( \rho_g \mathbf{u} \overline{f_m'^2} \right) = \nabla \cdot \left( \frac{\mu_t}{\sigma_t} \nabla \overline{f_m'^2} \right) + C_g \mu_t (\nabla \overline{f_m})^2 - C_d \rho_g \frac{\epsilon}{k} \overline{f_m'^2} + S_{user} \quad (5.54)$$

where  $f_m' = f_m - \overline{f_m}$ ,  $C_g$  and  $C_d$  are the constants.

The mixture fraction variance,  $\overline{f_m'^2}$ , is used in the closure model to account for turbulence-chemistry interactions, as described later in this section.

In the mixture fraction modeling approach, under the assumption of chemical equilibrium, the thermochemical scalars, such as species mass fractions, density, and temperature are exclusively related to the mixture fraction.

For a single mixture fraction adiabatic system, the instantaneous values of species mass, density, and temperature are only dependent on the instantaneous mixture fraction,  $f_m$ :

$$\phi_i = \phi_i(f_m) \quad (5.55)$$

where  $\phi_i$  refers to the instantaneous species mass fraction, density, or temperature.

However, for non-adiabatic systems, the instantaneous values of species mass fraction, density, and temperature depend on both instantaneous mixture fraction,  $f_m$ , and the instantaneous enthalpy,  $H$ . The effect of heat loss or gain can be described using the following expression

$$\phi_i = \phi_i(f_m, H) \quad (5.56)$$

The non-adiabatic system has to be chosen for the systems involving radiation, heat transfer through the walls, multiple inlets at different temperatures, and heat transfer to or from liquid drops or particles. The present study includes the non-adiabatic model to account for the heat transfer between the discrete-phase and gas-phase, while assuming no radiation heat loss from the system. Therefore, the local thermochemical state is related to the instantaneous mixture fraction,  $f_m$ , and enthalpy,  $H$ .

Equations 5.55 and 5.56 describe the instantaneous relationships between mixture fraction and species fractions, density, and temperature under the assumption of chemical equilibrium. Nevertheless, in many reacting systems, combustion is not in chemical equilibrium. In the present work, using the Rich Flammability Limit (RFL) option in the non-premixed combustion model, a chemical non-equilibrium simulation is performed. By introducing the RFL option in the non-premixed combustion method, rich regions are modeled as a mixed but unburnt mixture of pure fuel and a leaner equilibrium burnt mixture [71]. In other words, the RFL allows to perform a partial equilibrium calculation, suspending the calculation when the mixture fraction exceeds the specified rich limit. This increases the efficiency of the Probability Density Function or PDF calculation by speeding up the preparation of the look-up tables and bypasses the complex equilibrium calculations in the fuel-rich region. Furthermore, it is physically more realistic than the assumption of full equilibrium.

The turbulence-chemistry interaction model in the Fluent<sup>®</sup> solver determines the relationships between the averaged and instantaneous values of the thermochemical scalars in the system. In the non-premixed model, the assumed-shape PDF approach is used as a closure model.

## Probability Density Function

The Probability Density Function,  $p(f_m)$ , is defined as the fraction of time that the fluid spends in the neighborhood of the state  $f_m$ . For instance, if the fluctuating value

of  $f_m$  spends some fraction of time within the range  $\Delta f_m$ , the area under the curve of  $p(f_m)$  is the fraction of time that  $f_m$  spends in this range, i.e.,

$$p(f_m)\Delta f_m = \lim_{T \rightarrow \infty} \frac{1}{T} \sum_i t_i \quad (5.57)$$

where  $T$  is the time scale and  $t_i$  is the amount of time that  $f_m$  spends in the range  $\Delta f_m$ . The shape of the function  $p(f_m)$  depends on the turbulent fluctuations in  $f_m$ .

The PDF,  $p(f_m)$ , describing the fluctuation of the mixture fraction,  $f_m$ , in the turbulent flow, can also be used to compute the average values of the thermochemical scalars. In an adiabatic system, density-weighted species mass fractions and temperature are calculated from

$$\overline{\phi_i} = \int_0^1 p(f_m)\phi_i(f_m) df_m \quad (5.58)$$

Likewise, the mean time-averaged fluid density,  $\overline{\rho_g}$ , can be computed from

$$\frac{1}{\overline{\rho_g}} = \int_0^1 \frac{p(f_m)}{\rho_g(f_m)} df_m \quad (5.59)$$

Therefore, in order to determine the local mean values of species mass fractions, density, and temperature at all points in the flow field, it is only required to specify the shape of the PDF,  $p(f_m)$ , and then use Eqns. 5.58 and 5.59.

The  $\beta$ -function can be used to describe the shape of the assumed PDF for both single and two mixture fraction types. The  $\beta$ -function represents the experimental PDF more accurately than another PDF, the double-delta function. The  $\beta$ -function PDF shape is determined by the following function of  $\overline{f_m}$  and  $\overline{f_m'^2}$ :

$$p(f_m) = \frac{f_m^{\alpha-1}(1-f_m)^{\beta-1}}{\int f_m^{\alpha-1}(1-f_m)^{\beta-1} df_m} \quad (5.60)$$

where

$$\alpha = \overline{f_m} \left[ \frac{\overline{f_m}(1-\overline{f_m})}{\overline{f_m'^2}} - 1 \right] \quad (5.61)$$

and

$$\beta = (1-\overline{f_m}) \left[ \frac{\overline{f_m}(1-\overline{f_m})}{\overline{f_m'^2}} - 1 \right] \quad (5.62)$$

From Eqns. 5.60-5.62, it can be observed that the PDF shape,  $p(f_m)$ , is a function of the mean mixture fraction,  $\overline{f_m}$ , and the mixture fraction variance,  $\overline{f_m'^2}$ . Therefore, applying Eqns. 5.53 and 5.54,  $\overline{f_m}$  and  $\overline{f_m'^2}$  at each point in the flow field can be computed, which in turn can be used to calculate the assumed PDF shape,  $p(f_m)$ . The assumed PDF shape,  $p(f_m)$ , can be used as the weighting function to determine the mean values of species mass fractions, density, and temperature applying Eqns. 5.58 and 5.59.

On the other hand, in non-adiabatic systems, the local thermochemical state is related to the instantaneous mixture fraction,  $f_m$ , and the enthalpy,  $H$  (see Eqn. 5.56). The

system enthalpy affects the chemical equilibrium calculation and the thermochemical state of the fluid flow. Turbulent fluctuations in these systems are accounted for using a joint PDF,  $p(f_m, H)$ , which however, is difficult to compute. Consequently, the problem is simplified by considering that heat losses do not significantly affect the turbulent enthalpy, i.e.,

$$p(f_m, H) = p(f_m)\delta(H - \overline{H}) \quad (5.63)$$

Based on the assumption above, the mean scalars are calculated using

$$\overline{\phi}_i = \int_0^1 \phi_i(f_m, \overline{H})p(f_m) df_m \quad (5.64)$$

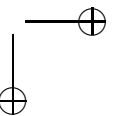
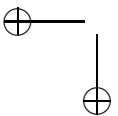
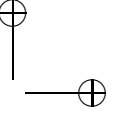
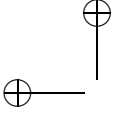
Therefore, to determine  $\overline{\phi}_i$  in a non-adiabatic system, it is required to solve the transport equation for mean enthalpy,  $\overline{H}$ :

$$\frac{\partial}{\partial t} (\rho_g \overline{H}) + \nabla \cdot (\rho_g \mathbf{u} \overline{H}) = \nabla \cdot \left( \frac{k_t}{c_p} \nabla \overline{H} \right) + S_h \quad (5.65)$$

where  $k_t$  is the turbulent thermal conductivity and  $S_h$  refers to the source terms due to radiation, heat transfer to wall, and heat exchange with the discrete-phase.

## Look-Up Tables

A significant amount of computational time can be reduced by calculating the integrals in Eqns. 5.58 and 5.64 for adiabatic and non-adiabatic single mixture fraction systems, respectively, storing the data in a look-up table, and finally recalling them during simulation. In an adiabatic system, from the predicted values of  $\overline{f}_m$  and  $\overline{f'_m{}^2}$  at a point in the flow, the mean values of species mass fractions, density, and temperature ( $\overline{\phi}_i$ ) at that point are obtained by table interpolation. Each scalar of interest has one look-up table. In adiabatic systems, the instantaneous enthalpy is a function of the instantaneous mixture fraction only. Therefore, a two-dimensional look-up table is required for each possible enthalpy value in the system. On the other hand, in non-adiabatic systems, the instantaneous enthalpy is not linearly related to the mixture fraction, but depends also on radiation, heat transfer to wall, and heat exchange with the discrete-phase. The look-up table becomes three-dimensional, which comprises layers of two-dimensional tables, each one representing a normalized heat loss or gain. The three-dimensional look-up tables are used to determine the value of each mass fraction, density, and temperature from the values of  $\overline{f}_m$ ,  $\overline{f'_m{}^2}$ ,  $\overline{H}$ , calculated from Eqns. 5.53, 5.54, and 5.65, respectively.



## 6. Non-Reacting Flow Study in the Single-Element LDI Combustor

### 6.1 Introduction

In this dissertation, two lean direct injection (LDI) combustor configurations are studied: a single-element LDI and a Multi-Point LDI (MPLDI) combustor. The results obtained from the numerical simulation of the LDI combustors are split into four chapters. The first two chapters are presented to validate the numerical results with the measurement data as reported in the literature. This is the foremost chapter that illustrates the computational results of the non-reacting flows in the single-element combustor [52], [139]. The non-reacting cold flow simulation is the very first step to investigate the aerodynamic characteristics of the flow associated with the LDI configuration. The insights obtained from the analysis of the swirling air flows in the single-element geometry are useful to model the combusting spray in the same set-up. In addition, the computed flow field of the single-element case are compared with that of the MPLDI case presented in Chapters 8 and 9. The results reported in this chapter are part of an effort to understand the underlying unsteady dynamics of mixing associated with this combustion concept, which are not completely explained by the experimental observations [47]. Furthermore, it is important to validate the numerical code with the available measurement data.

An unsteady Reynolds Averaged Navier Stokes (URANS) code is used to simulate the 3-D, turbulent, non-reacting, and confined swirling flow associated with the single-element LDI combustor. The numerical model encompasses the entire experimental flow field, including the flow passages through the swirler vanes, the flow development section, and the flame tube. Both mean and turbulent velocity components of the flow are calculated. The numerical results are compared with the available experimental data [47]. Furthermore, grid independency study is performed. In other words, the grid is refined several times until no appreciable change in the the computed flow field is noticed. The results presented are for the final refined grid.

The study shows that the numerical code is capable of resolving the complex swirling flow structures and the reverse flow regions with good accuracy. Overall, the computational results are in good agreement with the measurements. The consistency of the results offers confidence in the modeling and simulation strategies, which are used in the subsequent computations.

## 6.2 Geometrical Configuration and Grid

### Geometry

The LDI combustor concept is developed by the NASA Glenn Research Center [36]. The experimental data for the single-element LDI geometry is provided by Cai et al. [47]. The numerical model is shown in Fig. 6.1. The zoomed-in view in the figure depicts the swirler-fuel injector module. The geometry comprises a swirled-vaned inlet which has six helicoidal vanes of  $60^\circ$  vane exit angle, followed by a short converging-diverging venturi that ends at the dump plane of a square combustion chamber. The outer and inner diameters of the swirler are 22.5 mm and 8.8 mm, respectively. The calculated swirl number is 1.23. Both the converging and diverging

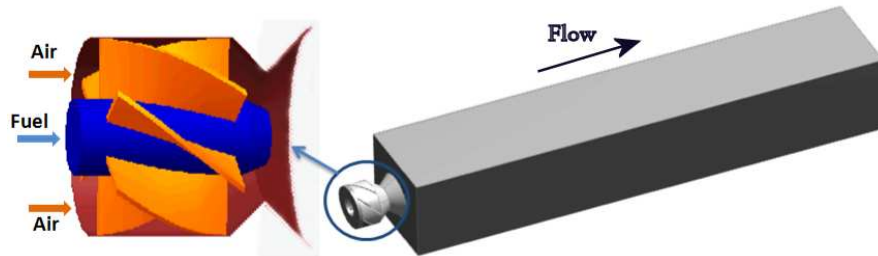


Figure 6.1: The single-element LDI combustor geometry with the air swirler-fuel injector configuration being zoomed into

angle of the venturi are  $45^\circ$ . The converging-diverging venturi is designed such that it can lower the chances of the return of the spray droplet from downstream and prevent flame flashback and auto ignition inside the swirler [47]. The fuel injector is inserted through the center of the swirler and the fuel tip is placed at the throat of the venturi. A simplex type fuel injector is used.

### Grid

Figure 6.2 shows the grid distribution used for the flow calculation in the single-element LDI configuration. Computation is performed for the entire geometry including the flow development section for the incoming air, six swirling passages for each injector module, converging-diverging venturi, and the rectangular flame tube. The grid consists of hexahedron and tetrahedron elements. Since the numerical code allows for unstructured elements, the elements can be constructed in any arrangements relative to each other. However, the storage requirement for such an unstructured mesh can be very large since the neighborhood connectivity needs to be explicitly stored. The final refined grid has 2.4 million elements. The grid is clustered normal to the walls to resolve the large change of gradients within the boundary layer. The maximum  $y^+$  along the walls is less than 5. The grid has been refined a few times to investigate the effects of grid density on the flow field.

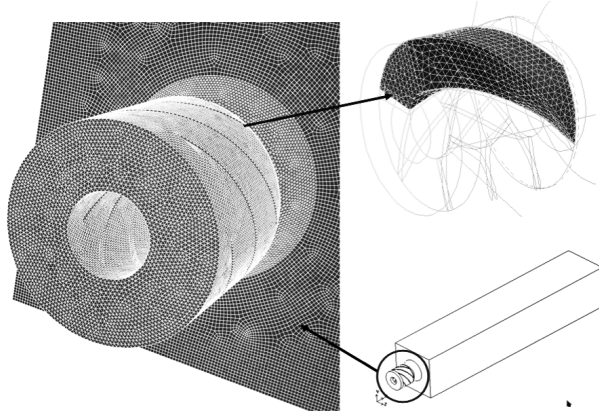


Figure 6.2: Grid distribution for the single-element configuration

## 6.3 Boundary Conditions and Numerical Procedure

### Initial and Boundary Conditions

The initial flow field for the URANS simulation is the solution of a steady RANS simulation, and no extra random fluctuations are imposed. Air at total temperature  $T_0 = 294.28$  K and 1 atmosphere pressure enters with a flow velocity of  $U_0 = 20.14$  m/s normal to the inlet face. Inlet air density is  $1.19$  kg/m<sup>3</sup>. Inlet turbulence is specified by turbulent intensity and length scale. Turbulent intensity is varied between 7% and 14% to examine its effect on the flow field. It is determined that a turbulent intensity of 10% yields more accurate results when compared with the measurements; therefore, this value is applied to calculate the flow field. The length scale is set to one tenth of the inlet diameter.

### Numerical Procedure

The pressure-based solver is used with the coupled pressure-velocity coupling scheme. The third-order MUSCL discretization method is specified to solve the momentum equations and the second-order upwind scheme is applied to solve the other equations. A higher-order convective discretization scheme is suitable for the present problems involving highly turbulent flows. Furthermore, as the flow is not aligned with the grid due to the presence of unstructured tetrahedral elements, a higher-order scheme is expected to yield greater accuracy and decrease the possibility of numerical discretization error.

Experimental data for the non-reacting single-element combustor [47] have been obtained for six stream-wise locations. Nevertheless, except for the inlet boundary conditions, all the experimental measurements are taken inside the combustion chamber, and no experimental data are available to prescribe the inlet to the combustion chamber. The computations are carried out until the solution becomes statistically stable.

At first, a steady flow state realizable  $k - \varepsilon$  model is used to create a realistic initial flow field. Once the flow field is reasonably converged, unsteady calculation is enabled. The unsteady  $k - \varepsilon$  calculation is continued until the flow becomes statistically stable. Thereafter, the computation is restarted using the Reynolds Stress Turbulence Model (RSTM). When the flow is fully developed and statistically stable, time-averages are calculated by sampling at a specified frequency to obtain both mean and root mean square values. The calculation is continued until statistically stable data is obtained. The duration of the computation is determined beforehand by estimating the mean flow residence time in the solution domain. In the present case, it is observed that when the residuals of continuity, momentum, and Reynolds stresses equations drop by more than four orders of magnitude, there is no appreciable change in the solution for the velocity components, and the solution is considered as converged. Nevertheless, while performing the unsteady RSTM calculations, the local unsteadiness in the flow owing to the highly swirling nature inhibits the residuals to drop significantly. In the URANS calculations, the physical time-step is  $1.0\mu s$  and the CFL number for time iteration is less than 1.

One quad dual-core AMD Opteron™ Linux cluster machine is employed for parallel computing. The machine has 8 processors and an InfiniBand architecture for data flow between processors. The total computation time for the single-element non-reacting case is 170 hours.

## 6.4 Non-Reacting Cold Flow Field Analysis

The results of the non-reacting cold flow simulation include the profiles of both time-averaged mean and turbulent velocity components. The data are also compared with the experimental results.

### Mean Velocity Field

Figures 6.3 and 6.4 show the URANS results for the axial mean velocity contours in the X-Y plane and the iso-surface of zero axial mean velocity, respectively. The iso-surface of the zero axial mean velocity is also known as the vortex breakdown bubble (VBB) [140]. The figures indicate the presence of a large recirculation zone in the central core region, which extends upstream up to the injector tip. At low swirl numbers, there may be a significant radial pressure gradient at any axial position caused by the centrifugal effects, but the axial pressure gradient is relatively low. Nevertheless, when increasing the swirl, a strong coupling develops between axial and tangential velocity components and the axial (adverse) pressure gradient increases. A point is reached, when the adverse pressure gradient along the jet axis cannot be further overcome by the kinetic energy of the fluid particles flowing in the axial direction, and a recirculation flow is set up in the central portion of the jet. The formation of the recirculation zone, a form of vortex breakdown, acts as an aerodynamic blockage or a three dimensional bluff body which stabilizes flames. This is essential to provide sufficient residence time, temperature, and turbulence for a complete combustion of the fuel. In addition to the major recirculation zone at the center, there are two

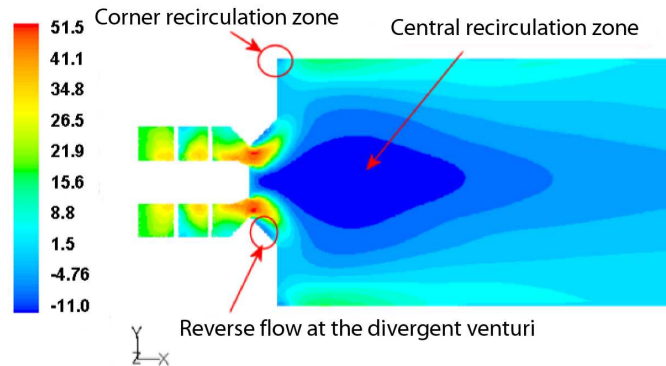


Figure 6.3: Non-reacting axial mean velocity (in m/s) distribution in the mid-plane (close-up view)

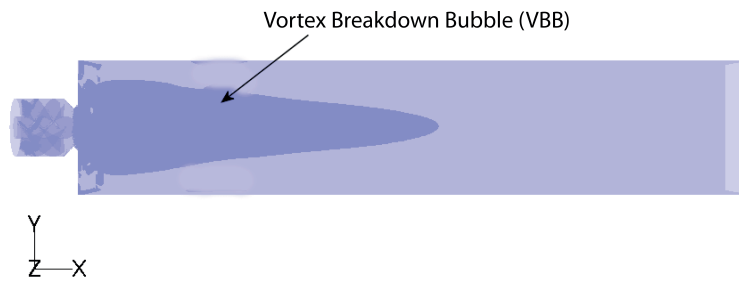


Figure 6.4: VBB of the single-element LDI combustor (side view)

other regions in which the flow is reversed, one is located in the diverging section of the venturi and the other one is found in the corners of the upstream wall of the combustion chamber. The presence and the interaction of these vortical structures make the mean flow unsteady in the frontal region. The highly fluctuating velocity, as illustrated later, further demonstrates the existence of a large degree of unsteadiness in this region. Figure 6.5 compares the computed axial mean velocity distribution along the length of the combustor to the experimental data. Both numerical and experimental data indicate that the recirculation region extends into the combustion chamber and ranges over as much as half of its axial length. From the dump plane of the combustion chamber up to 50 mm inside the chamber, a strong reverse flow region is observed. Thereafter, recirculation gets weaker and disappears at about 120 mm from the dump plane. Further downstream, the flow accelerates and at the exit, the axial velocity is close to 1 m/s.

The axial mean normal stress distribution at the centerline is compared to the measurements at various axial locations in Fig. 6.6. The axial normal stresses have the

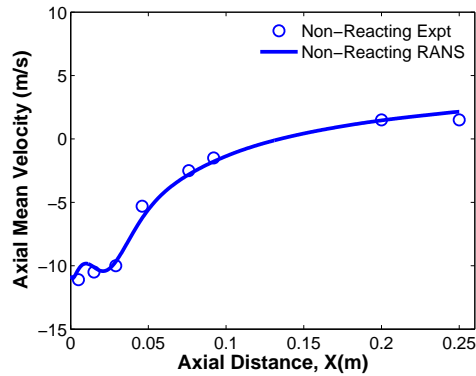


Figure 6.5: Computed centerline axial mean velocity vs. experimental data

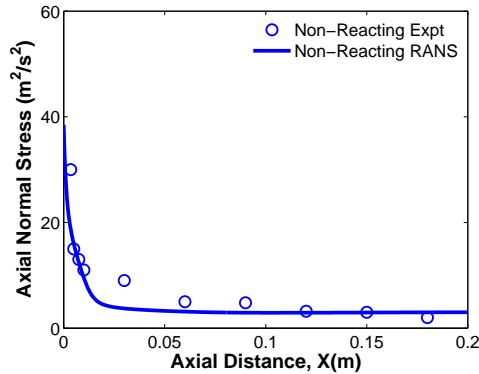


Figure 6.6: Computed centerline axial mean normal stress vs. experimental data

highest value at the swirler exit owing to the high level of turbulence resulting from the high degree of swirling flow. Thereafter, the axial normal stress decays rapidly and then becomes almost constant within the recirculation zone. Although it levels off, it still decays as the flow moves downstream.

Figure 6.7 compares the computed axial mean velocity distribution along the radial direction, with the measured data for several axial locations. At 5 mm downstream, both measurements and computed URANS data indicate the presence of an axial mean velocity peak away from the centerline and a reverse flow region in the central part. Nevertheless, the computed results exhibit symmetrical profiles unlike the measured data. The discrepancy at this location may be due to various reasons. Apart from the computational issues, such as grid resolution, there was also difficulty in obtaining accurate experimental data at this location as reported in the literature[47, 49]. Nevertheless, at all other locations, the computed data for the axial mean velocity profiles have good agreement with the measurements. Both measured and computed data exhibit axial velocity peaks near the wall of the combustion chamber when the

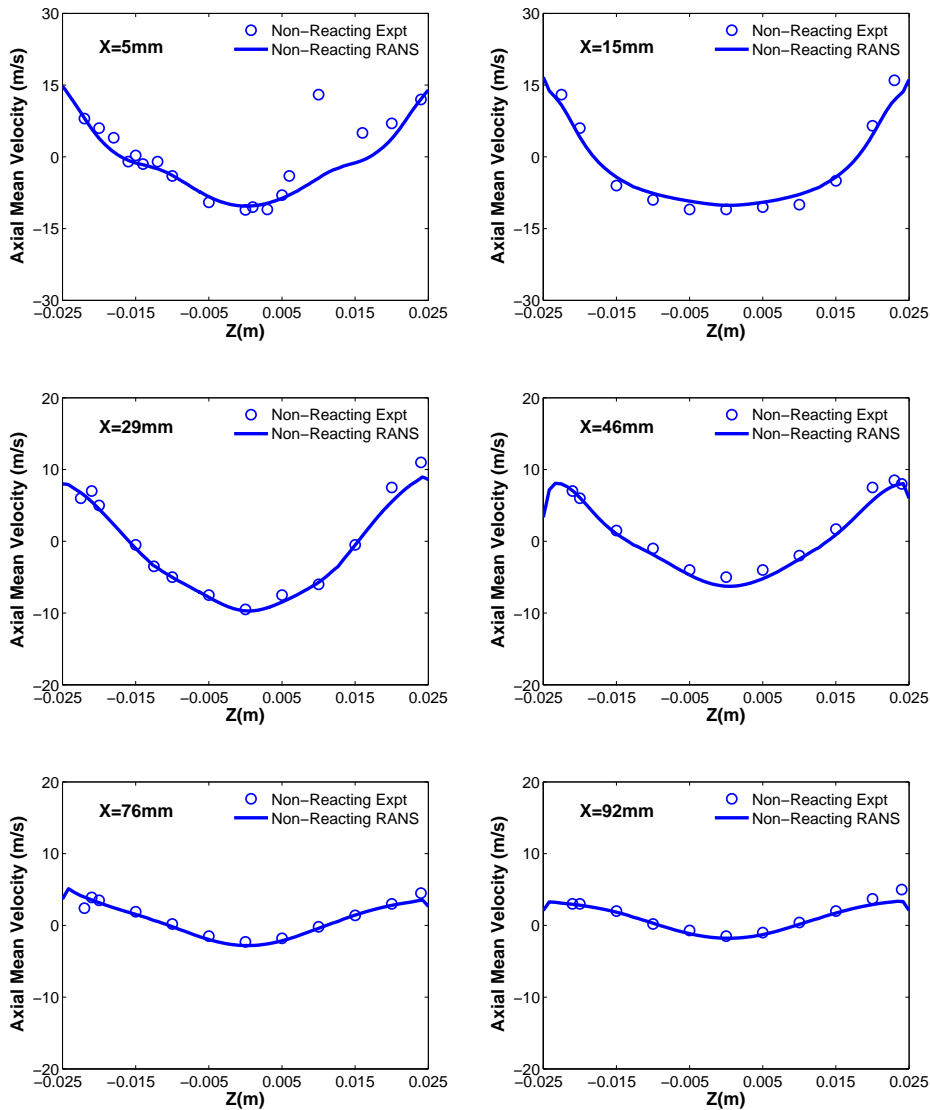


Figure 6.7: Computed non-reacting axial mean velocity at various axial locations compared with measurements

flow hits the wall. As the flow moves downstream, the axial mean velocity peak, which is observed away from the centerline at the location  $x=5$  mm, flattens out due to expansion of the recirculation zone in the central region. On the other hand, further downstream, the magnitude of the axial velocity peaks close to the chamber wall also decreases. At  $x=92$  mm, the axial velocity profile shows an almost flat velocity distribution.

Comparisons of the radial mean velocity at various axial stations are shown in Fig.

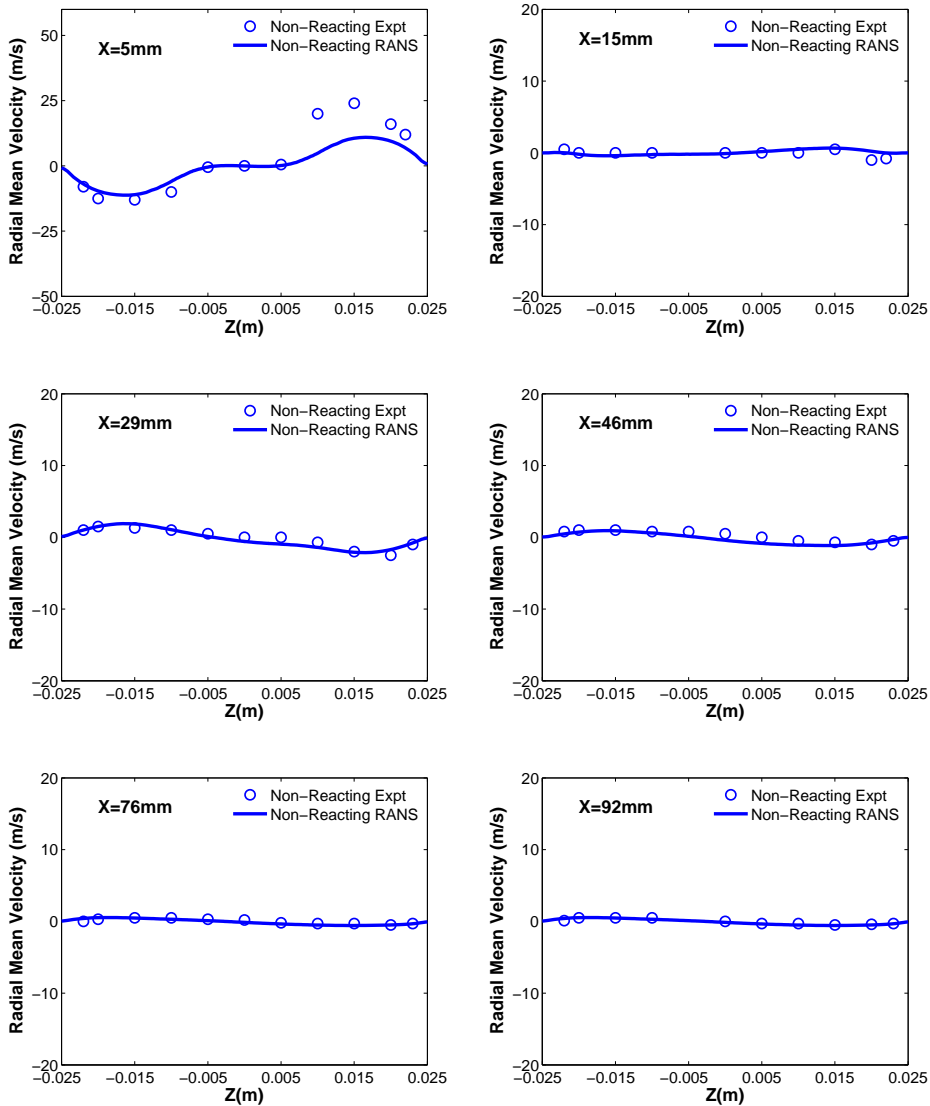


Figure 6.8: Computed non-reacting radial mean velocity at various axial locations compared with measurements

6.8. High radial velocity is observed as the flow enters the combustion chamber. At 5 mm downstream, the radial velocity has a higher magnitude than at other axial locations. The profile indicates a quick expansion of the flow in the radial direction. Some discrepancies with the measurements are observed at this station along the positive radial direction. Unfortunately, it is the same location where measurements are uncertain. At 15 mm downstream, the radial velocity is almost zero because the expansion of the flows stops. Further downstream, at 29 mm and 46 mm, the radial

velocities have a different direction owing to the shrinkage of the recirculation zone. The radial mean velocity profiles are relatively flat at 76 mm and 92 mm downstream of the combustion chamber inlet.

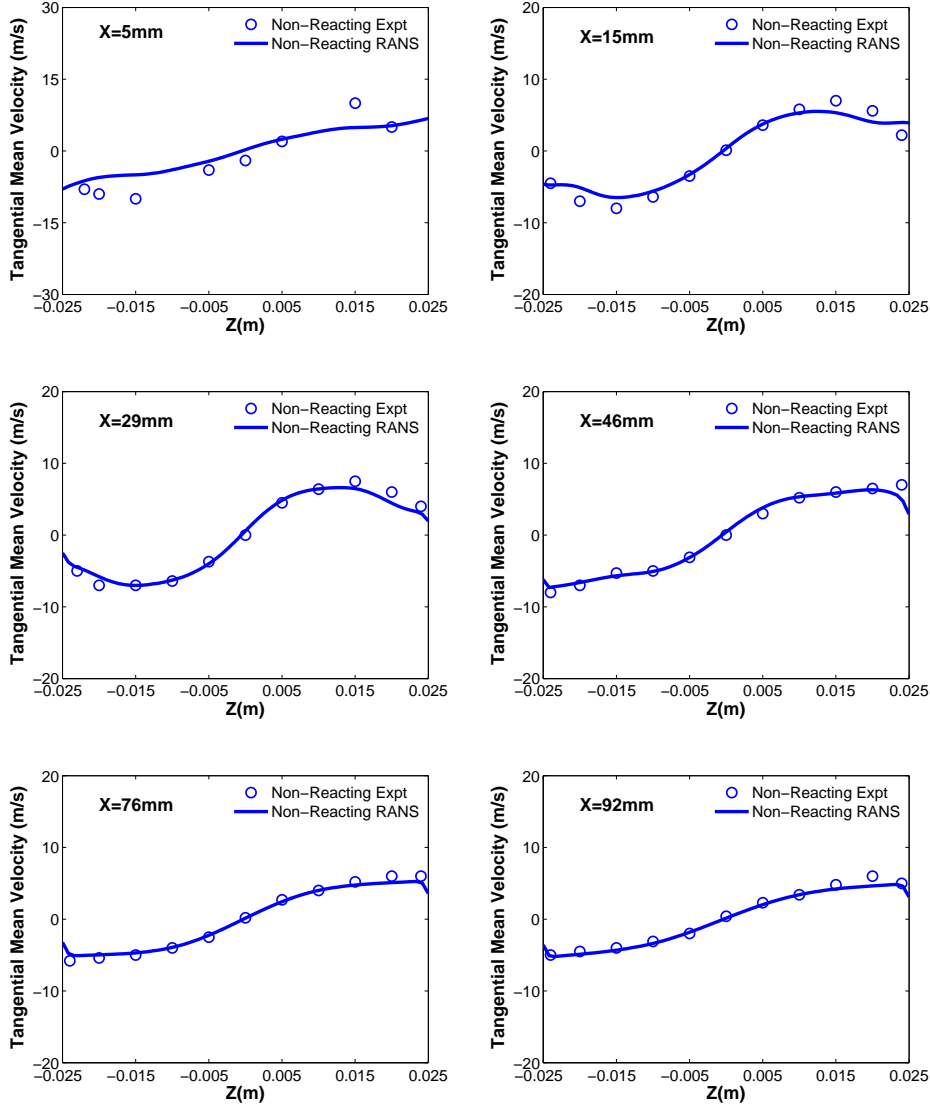


Figure 6.9: Computed non-reacting tangential mean velocity at various axial locations compared with measurements

Figure 6.9 compares the computed tangential mean velocity profiles to the measurements at different axial locations. This velocity component, which essentially represents the swirl of the flow, is important since the combustor is designed for creating high swirling flows to enhance the mixing of fuel and oxidizer. At the initial stations

(at 15 mm and 29 mm downstream), the tangential velocity profiles indicate the formation of a combined solid and free vortex structure. Further downstream, the peak of the swirling velocity moves outward and a solid vortex profile is established. In addition, it is observed that even in the regions far away from the combustion chamber inlet, the magnitude of tangential velocities is much higher than the magnitude of the radial velocities.

### Turbulent Velocity Field

Figures 6.10-6.12 show the components of the turbulent quantities at various axial

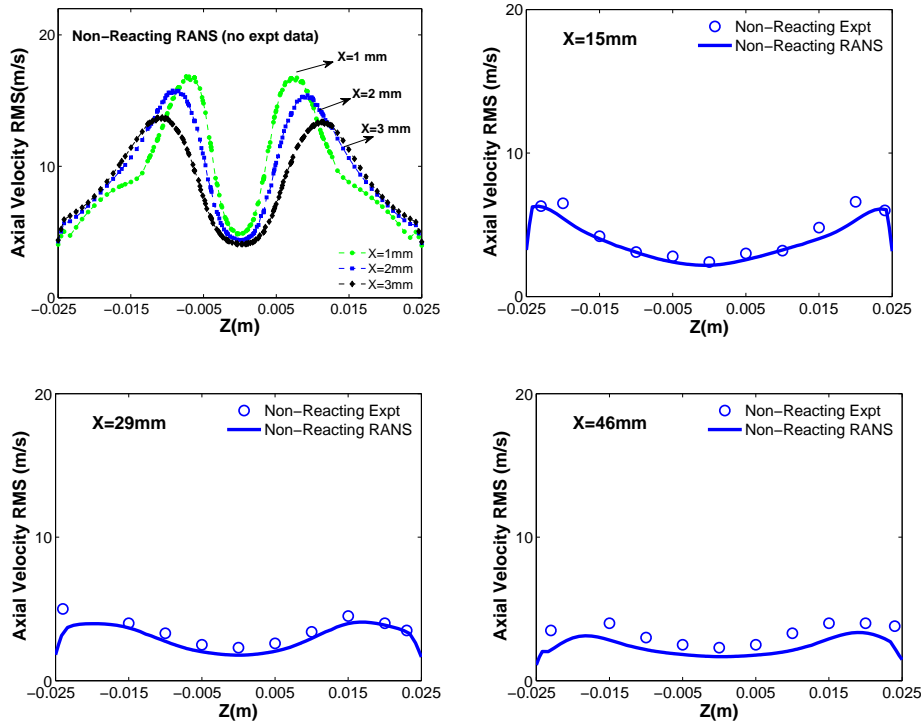


Figure 6.10: Computed non-reacting axial RMS velocity at various axial locations compared with measurements

locations. The root-mean-square (RMS) values presented here represent the turbulent velocities. Fluctuating velocities are computed at 3 additional stations in close proximity to the combustion chamber inlet, where experimental data are not available. The locations are 1 mm, 2 mm, and 3 mm downstream of the chamber inlet and the turbulent velocities at these locations are plotted together. Figure 6.10 shows stronger turbulent axial velocities close to the chamber inlet. However, they decay rapidly as the flow moves downstream. The turbulent radial and tangential velocity profiles are shown in Figs. 6.11 and 6.12, respectively. Similar to the axial turbulent velocity pro-

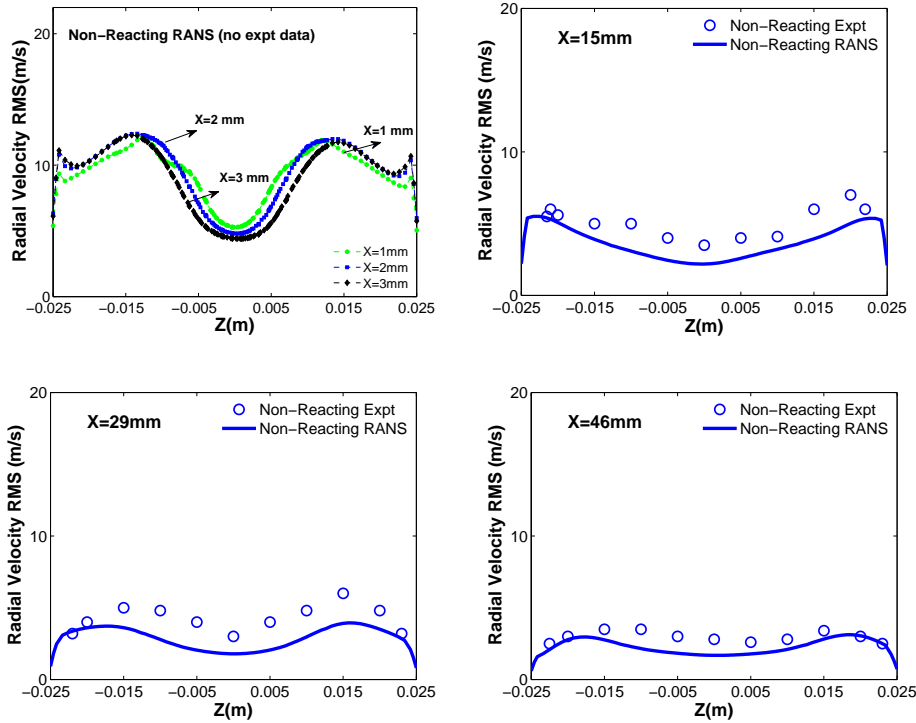


Figure 6.11: Computed non-reacting radial RMS velocity at various axial locations compared with measurements

files, the radial and tangential profiles exhibit higher peak values near the chamber inlet and decay quickly at downstream locations. At 1 mm downstream, comparing the turbulent profiles for the three velocity components, the results show that the peak axial turbulent velocity is around 17 m/s, while the peak radial turbulent velocity and tangential turbulent velocity are 12 m/s and 11 m/s, respectively. Such variations in the components of the turbulent velocity are also observed at the two other axial locations close to the chamber inlet. The different turbulent velocity profiles among three components found at these axial locations indicate the non-isotropic Reynolds stress distribution induced by the highly swirling flow.

The computed data for all the three mean and turbulent velocity components at various axial stations show a very good agreement with the experimental findings. Apart from the location  $x=5$  mm, overall, the numerical data differ less than 5% compared with the experimental data. The overall agreement offers confidence in the present simulation approach and in the strategy of simulating the entire swirler assembly to eliminate any uncertainty attributed to the computation.

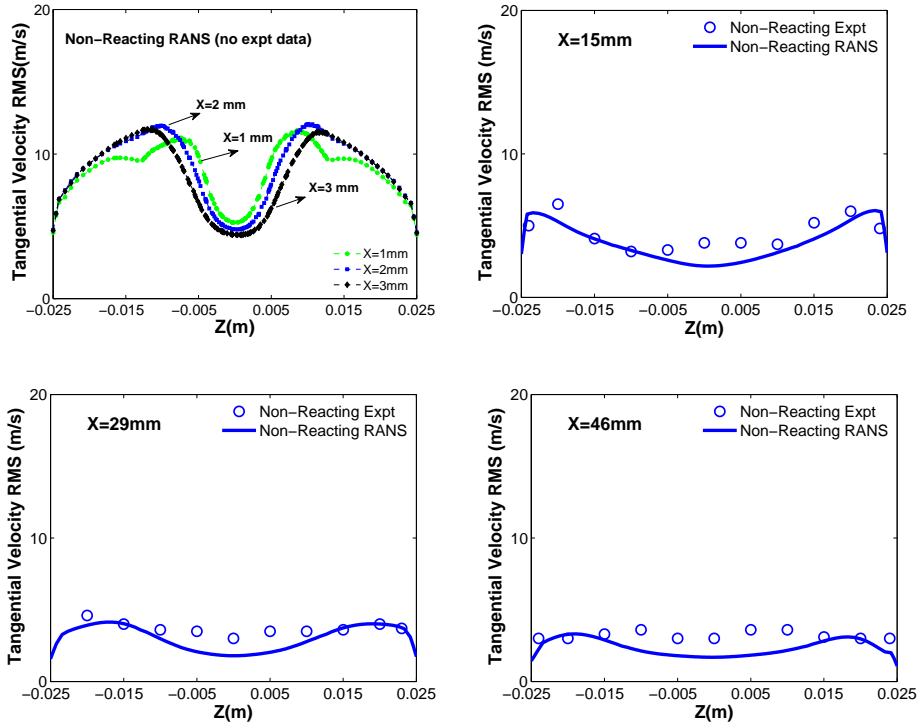


Figure 6.12: Computed non-reacting tangential RMS velocity at various axial locations compared with measurements

## 6.5 Concluding Remarks

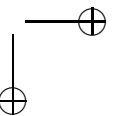
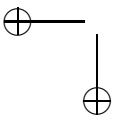
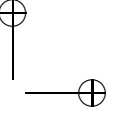
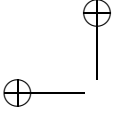
Numerical simulation is performed to characterize the non-reacting cold flow field in a single-element LDI combustor. The URANS code is used to compute the entire flow field of the combustor, encompassing six helicoidal air flow passages, the converging-diverging nozzle, and the square chamber section. The results are compared with the available experimental data.

The steady RANS solution is used as an initial condition for the URANS calculations. The unsteady calculations are performed using the realizable  $k - \varepsilon$  and subsequently the RSTM turbulence models. The solution captures the essential flow features of the LDI combustor, such as the complex swirling flow structures inside the swirler passages and combustion chamber, the single large recirculation zone originating from the tip of the fuel injector, and the reverse flow regions at the corners of the chamber wall and on the wall of the divergent venturi, with reasonable accuracy. Furthermore, the calculated mean and turbulent velocity components at various axial locations within the combustor exhibit good agreement with the measurements.

The computational results exhibit high tangential velocities at all the computed axial

locations, including far downstream, thus indicating a high degree of swirling flow inside the chamber. In a reacting flow, such a highly swirling velocity field assists liquid fuel atomization, and expedites the mixing of fuel and air by influencing liquid fuel stream breakup into small drops and dispersing the drops into the gaseous medium. The RMS velocity components record higher magnitudes in the vicinity of the chamber inlet, implying the presence of highly turbulent flow in this region. Nevertheless, the fluctuating velocities decay rapidly as the flow moves downstream. Furthermore, the RMS velocity components close to chamber inlet show a variation in fluctuation levels, suggesting the flow being anisotropic.

Overall, the agreement between the non-reacting numerical and experimental results demonstrates that the RANS code is capable of resolving the complex flow field in the LDI combustor. The results offer confidence to pursue the flow computation for the reacting field in the single-element LDI and non-reacting and reacting fields in a complex MPLDI system, described in the following chapters.



## 7. Spray Combustion Study in the Single-Element LDI Combustor

### 7.1 Introduction

This chapter reports the computational results of the reacting spray simulations in a single-element lean direct injection (LDI) combustor [53, 54]. The calculations for the reacting spray are carried out under the same air flow inlet conditions as for the non-reacting single-element case presented in the previous chapter. However, two-phase flow modeling is far more complex than modeling non-reacting cold flow. The presence of liquid spray compounds the complexity, since the development of a spray comprises several sub-processes that need to be explicitly modeled to perform the simulations. For the liquids, which react with the surrounding medium, a combustion model has to be introduced as well. Therefore, a numerical simulation of reacting spray could be computationally very expensive. In addition to the complexity in resolving spray combustion and associated computational challenges, the highly swirling flow field within the LDI combustor demands for an accurate modeling of spray-turbulence interactions.

The Discrete Phase Model (DPM) [71] of the Fluent<sup>®</sup> solver is applied to simulate the combusting liquid spray in the LDI combustor. The DPM implements the Euler-Lagrange approach to resolve the multiphase flow. For the liquid spray calculations, various sub-models are employed to describe the spray sub-processes, such as fuel atomization, drop breakup, drop collision and coalescence, drop drag and distortion, turbulent dispersion of spray, and drop evaporation. In addition, a combustion model is applied. For the gas-phase turbulence modeling, the Realizable  $k - \varepsilon$  model with is used.

Properties of both the liquid and gas phases are analyzed to get an insight into the effects of the highly swirling flows on the spray characteristics and the combustion process. The computational results are compared with the available experimental data [47]. In addition, a comparison is made between the non-reacting and reacting flow velocity fields. Overall, both the gas and drop velocity predictions are consistent with the experimental results. The computed size and distribution of the liquid fuel drops at various locations are also in good agreement with the measurements. The study indicates that the swirling flow strongly influences the spray velocity and the drop size distribution which reflects the momentum exchange between the two phases.

This chapter is organized as follows. In the next section, the geometrical configuration and the numerical grid are briefly described. In Section 7.3, the boundary conditions, mathematical models, and numerical approach are presented. This is followed by the results on the reacting spray calculations in Section 7.4. Finally, the chapter ends up with some concluding remarks in Section 7.5.

## 7.2 Geometrical Configuration and Grid

### Geometry

The geometry of the single-element LDI combustor used for the reacting flow calculations has been depicted in Chapter 6 (see Fig. 6.1). The figure also shows a close-up view of the air swirler-fuel injector module. The experimental data for the reacting spray is provided by Cai et al. [47]. A detailed description of the combustor geometry and the swirler design are given in Section 6.2. The fuel is injected through a simplex type fuel nozzle, and the tip of the injector is positioned at the throat of a converging-diverging venturi. A hollow conical spray is formed as the fuel is introduced into the gas stream. The initial half cone angle of the spray is  $45^\circ$ .

### Grid

The reacting flow simulation in the single-element LDI combustor is performed for the entire geometry by using the RANS code. The flow calculations are started with the grid being used for the non-reacting flow case. A view of the grid is shown in Fig. 6.2, which consists of hexahedron and tetrahedron elements. Nevertheless, during the computations, it is refined a few times in the regions of high temperature gradients. The final refined grid has 2.65 million elements. The maximum  $y^+$  along the walls is less than 5.

## 7.3 Boundary Conditions and Numerical Procedure

### Initial and Boundary Conditions

The inlet flow conditions applied to the RANS calculations are obtained from the experiments [47]. Air at a total temperature  $T_0 = 294.28$  K and 1 atmosphere pressure enters with a flow velocity of  $U_0 = 20.14$  m/s normal to the inlet face. Inlet air density is  $1.19$  kg/m<sup>3</sup>. Inlet turbulence is specified by turbulent intensity and length scale. The turbulent intensity at the inlet is set to 10% and the length scale is one tenth of the inlet diameter. Kerosene is injected through the fuel injector at a rate of 0.415 g/s, which in combination with the air mass flow rate gives an equivalence ratio of 0.75. The fuel atomizer is operated at a pressure of 110 kPa (16 Psi).

## Mathematical Models

Chapters 3 and 5 describe the theory of various spray sub-processes and the corresponding models being applied for the computations, respectively. The DPM of the Fluent<sup>®</sup> solver is used to simulate the reacting spray in the combustor. This model implements the Euler-Lagrange approach to describe the two-phase flow. The gas-phase is treated as a continuum and it is calculated by solving the Navier-Stokes equations. The Realizable  $k-\varepsilon$  model is used for turbulence modeling. The enhanced wall treatment method is used for near-wall modeling. The liquid-phase is resolved by tracking the liquid particles through the calculated flow field. The sub-models used for modeling various spray sub-processes are as follows.

The pressure-swirl atomizer model [122] is used for fuel atomization modeling. It is also known as the Linearized Instability Sheet Atomization (LISA) model. The modeling process has two stages: liquid film formation, and sheet breakup and atomization. A detailed description of this model is provided in Section 5.4. For drop breakup modeling, the Wave model [134] is selected. This model essentially considers the effects of the Kelvin-Helmholtz (K-H) instability on the liquid surface. Drop collision and coalescence modeling are executed by applying the O'Rourke's method [59], which introduces a concept of drop parcels to reduce the time for collision calculations. This method considers a stochastic estimate of parcel collision and its accuracy is second-order in space. Drop vaporization modeling is carried out using the mass-transfer vaporization law of a droplet as given in the Fluent Theory Guide [71], which is based on gradient diffusion. The Discrete Random Walk (DRW) model is applied to predict the turbulent dispersion of liquid spray drops. This approach predicts the dispersion of liquid drops by integrating the trajectory equations for individual drops and using the instantaneous fluid velocity along the drop's path during the integration process. To model combustion, the Non-Premixed Combustion model combined with the mixture fraction- $\beta$  PDF approach [71] is employed. In the Non-Premixed model, fuel and oxidizer enter the reaction zone in distinct streams. On the other hand, the thermochemistry is reduced to a single parameter called the mixture fraction, which essentially is the local mass fraction of burnt and unburnt fuel stream elements in all the chemical species (reactants and products). The Probability Density Function (PDF) describes the fluctuation of the mixture fraction in the turbulent flow. The  $\beta$ -function computes the mean mixture fraction ( $\overline{f_m}$ ) and mixture fraction variance ( $\overline{f_m'^2}$ ) at each point in the flow field to calculate the PDF shape. The assumed PDF shape is used to determine the mean values of species mass fractions, density, and temperature.

## Numerical Procedure

A steady RANS simulation is performed for the gas-phase calculations. The spray calculations are conducted with the unsteady particle tracking method and the particles are tracked in a Lagrangian reference frame. In the unsteady tracking, all the particles are tracked through the domain simultaneously and a particle time step is used to track them in an unsteady manner. The particles are represented by parcels that correspond to an ensemble of identical particles. Two user-defined-function (UDF) files are used to calculate the drop statistics. The first file is written to calculate drop

mean diameters in a spray simulation for each cell, and the second one is written to obtain drop velocity of each parcel crossing a plane within the combustor.

The pressure-based solver is used with the pressure-velocity coupled scheme. The second-order upwind discretization scheme is applied to solve all the equations. Simulations are run until the residuals of the continuity, momentum, and energy equations drop by more than four orders of magnitude and no significant changes are found in the solution. Once the reacting spray simulation is fully converged, the UDF files are compiled and a UDF library is created. After the library is built, the UDFs are loaded and hooked up to the current case/data files. Finally, more iterations are run to get statistics for spray particles.

One quad dual-core AMD Opteron™ Linux cluster machine is used for parallel computing. The machine has 8 processors and an InfiniBand architecture for data flow between processors. The total computation time for the single-element reacting spray simulation is 240 hours.

## 7.4 Reacting Spray Analysis

In this section, first, the reacting gas-phase flow field is discussed. The computed velocity field is compared with the non-reacting cold flow velocity field. Later, the predicted liquid spray characteristics are reported, which include the predictions for drop diameter distributions and drop velocity profiles at various locations. The numerical data are compared with the available experimental data [47].

### 7.4.1 Gas-Phase Flow Field

Figures 7.1 and 7.2 illustrate axial mean velocity contours in the mid plane ( $X - Y$

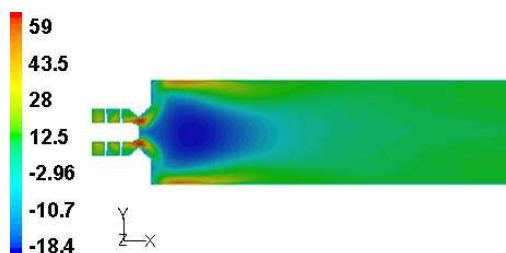


Figure 7.1: Reacting flow axial mean velocity (in m/s) distribution in the mid-plane (close-up view)

plane and  $Z = 0$ ) and the centerline axial velocity comparisons between the reacting and non-reacting cases, respectively. The central recirculation region of the reacting flow is significantly stronger compared with that of the non-reacting flow, due to the effect of heat release resulting from combustion. The combustion of the spray increases the axial momentum, which leads to a shorter and narrower recirculation

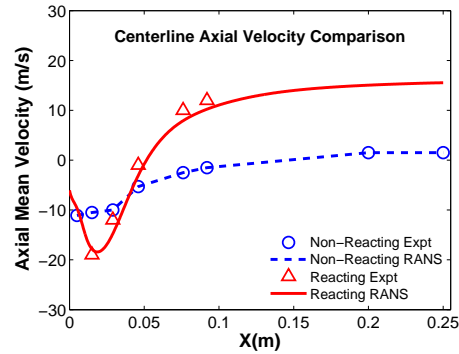


Figure 7.2: Centerline axial mean velocity comparison

region. Figure 7.2 shows that the central recirculation zone in the reacting flow is half the length of the central recirculation zone in the non-reacting flow. Further downstream, the figure illustrates flow acceleration to 15 m/s for the reacting case as compared to only 1 m/s for the non-reacting case. In addition to the central recirculation zone, Fig. 7.1 depicts the reverse flow regions in the diverging venturi and the corners of the upstream wall of the combustion chamber.

Figure 7.3 shows the computed axial mean velocities of the reacting flow at various axial locations inside the combustor. The corresponding gas-phase velocity profiles for the non-reacting flow are also illustrated alongside to make a comparison with the reacting flow. In general, the magnitudes of axial velocity in the reacting flow are higher both within the positive velocity and reverse flow regions when compared with the non-reacting flow. The heat release due to chemical reactions results in an expansion of the gas, which in turn increases the axial velocities significantly. At the first measurement station, i.e., at 5 mm downstream, the computed data for reacting gas-phase predict a strong recirculation zone in the central portion with almost symmetric peaks on either side. On the contrary, the measurement data do not reveal any flow reversal and the velocity magnitudes are relatively high. However, in the experimental study [47], the authors mentioned the difficulty in distinguishing the seeding particles from high momentum spray particles at this location. This could be the reason why no negative axial velocities are measured in the reverse flow zone. Further downstream, the reacting flow axial velocity comparison between the RANS and the measurements is quite reasonable. Compared with the non-reacting flow, at 15 mm and 29 mm downstream, where an intense reaction takes place, the expansion of hot reacting gas leads to narrow reverse flow zones with higher reverse velocities. At 46 mm downstream, the recirculation zone of reacting flow almost disappears due to the high axial momentum. Further downstream, at 76 mm and 92 mm, although the velocity profiles of the reacting case show a relatively flat velocity distribution, they still possess higher magnitude compared to the velocity magnitude in the non-reacting case at the corresponding locations.

The reacting flow axial mean velocity plots of the single-element LDI can be compared with that of the MPLDI combustor discussed in Chapter 9. The computed axial

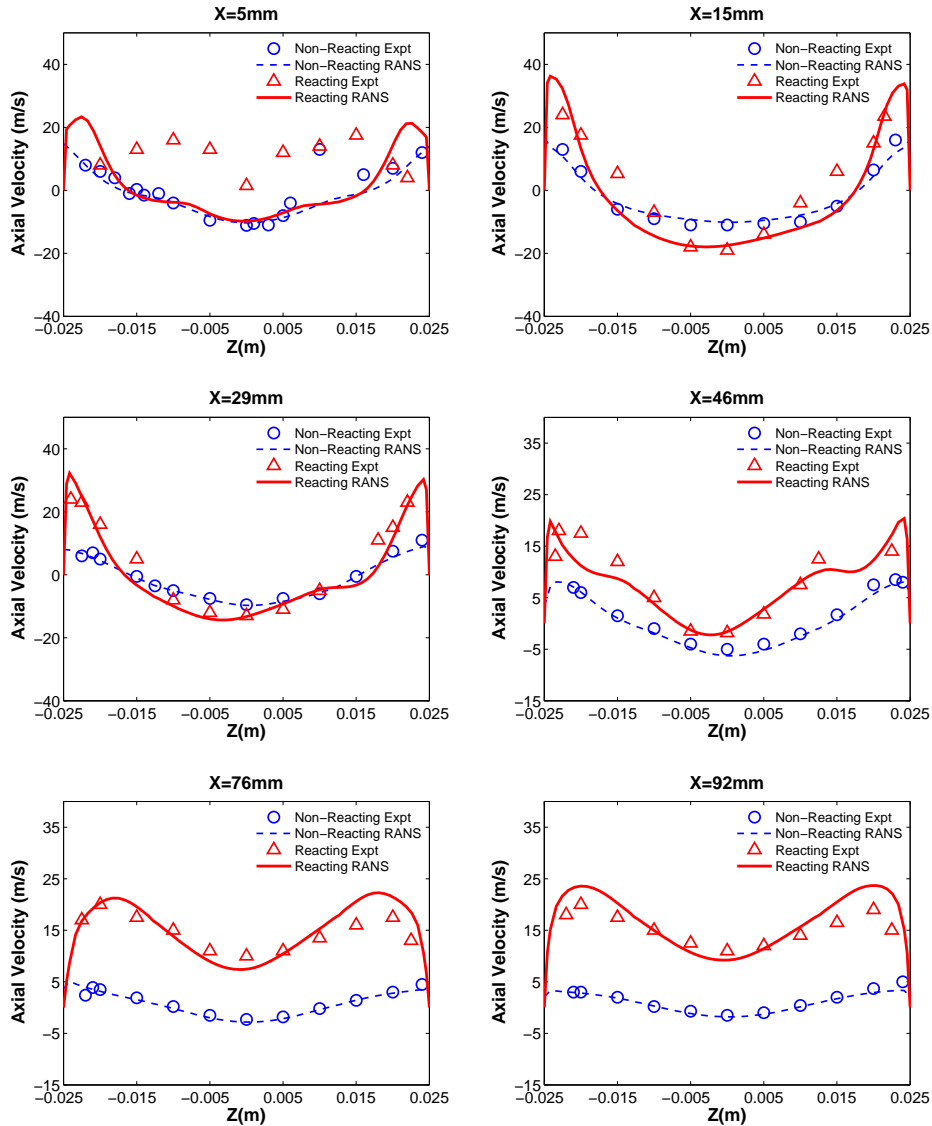


Figure 7.3: Computed axial mean velocity at various axial locations compared with measurements

velocity profiles of the single-element LDI illustrate a relatively large and wide central recirculation zone, as opposed to small and narrow recirculation zones generated from the individual swirlers in the MPLDI, due to strong flow interactions amongst the neighboring swirlers.

Figure 7.4 shows the tangential mean velocity profiles at several axial locations. The tangential velocity essentially represents the swirl of the flow. From the LDI’s perspective, it is important to generate high swirl velocities, so that a good quality

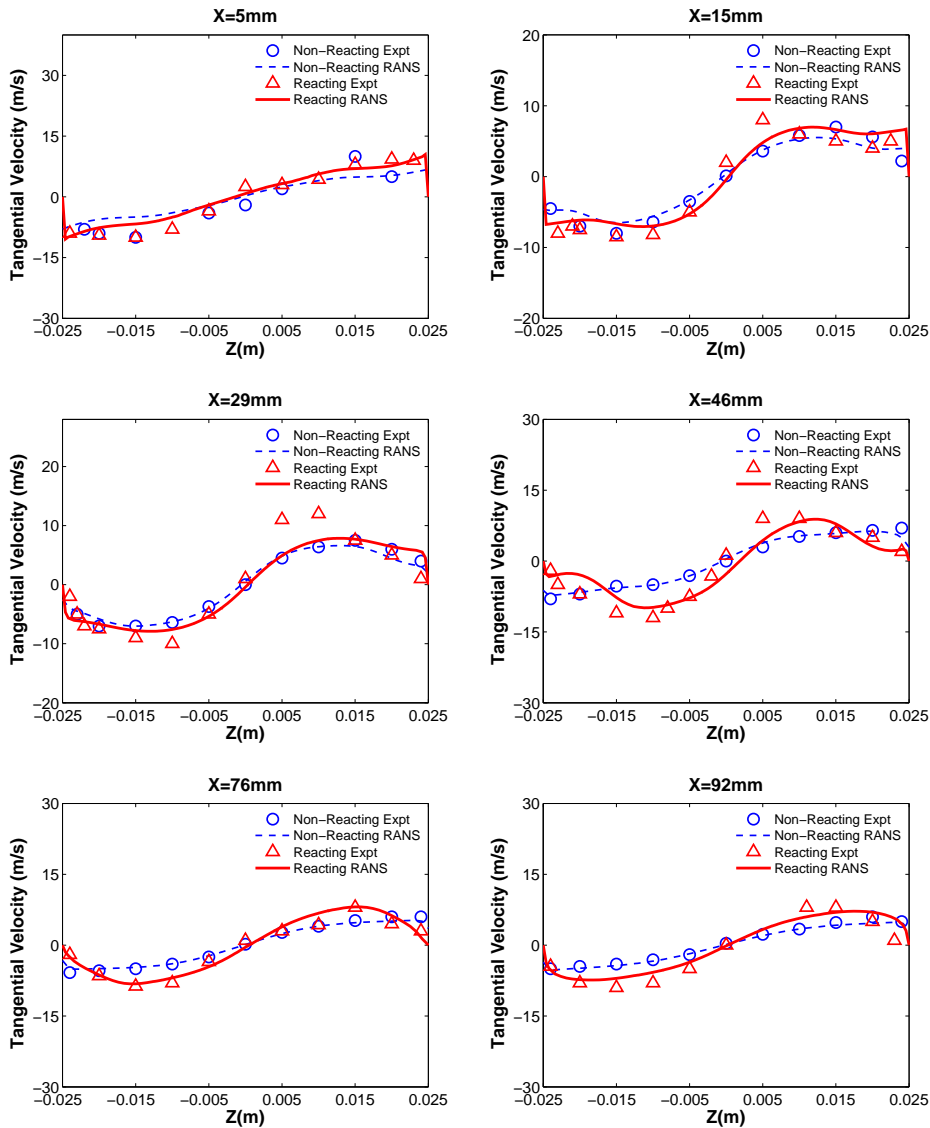


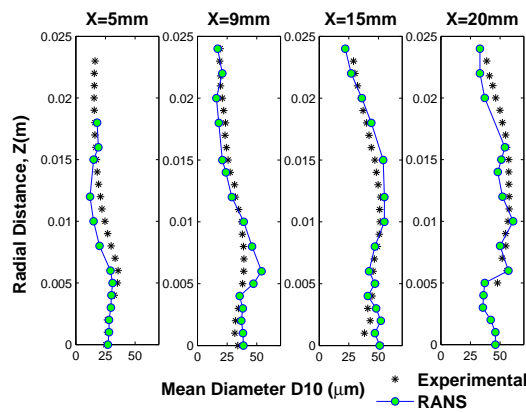
Figure 7.4: Computed tangential mean velocity at various axial locations compared with measurements

mixture of fuel and oxidizer can be achieved in the lowest possible mixing time and length prior to combustion. In general, the reacting gas-phase swirl velocities show higher magnitude compared with the non-reacting flow swirl velocities. This is due to chemical reactions within the combustor, which causes an increase in gas-phase temperature and velocity and a decrease in gas density. At 5 mm downstream, the reacting case shows a solid vortex profile. As the flow moves downstream, the peak swirl velocity moves toward the center and forms a combined vortex structure. This

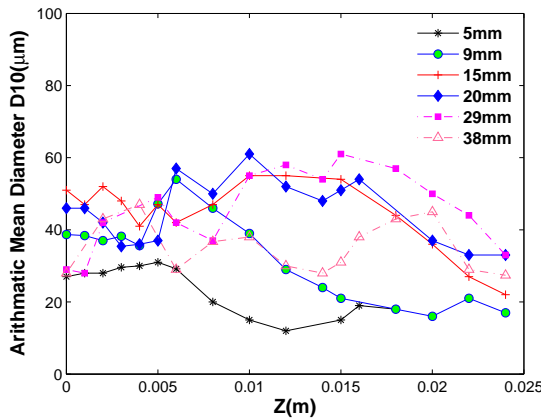
can be attributed to the short recirculation zone in the reacting case. On the other hand, at 15 mm and 29 mm downstream, the non-reacting flow exhibits a combined vortex structure. Further downstream, the peak tangential velocity moves radially outward and the velocity distribution makes a solid vortex profile. Overall, Fig. 7.4 shows that the computational results are in good agreement with the measurements.

### 7.4.2 Liquid Spray Characteristics

The liquid drop properties, such as drop mean diameter, size distribution, and velocity offer more insight into the development of a spray in the highly swirling flow field. The



(a) Radial profiles for  $D_{10}$  distribution compared with the experimental data



(b) Comparison of the computed  $D_{10}$  distribution in different axial planes

Figure 7.5: Mean diameter  $D_{10}$  distribution

DPM with the unsteady particle tracking method is applied in the RANS simulation

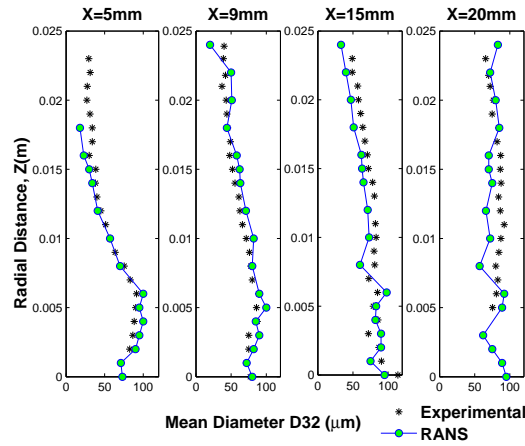


Figure 7.6: Radial profiles for  $D_{32}$  distribution compared with the experimental data

to compute the spray statistics. The DPM includes the essential spray models to describe various spray sub-processes. The numerical results are compared with the experimental results, which are obtained only on one half of the combustion chamber.

### Drop Diameter Distribution

Figure 7.5 demonstrates the arithmetic mean diameter (AMD),  $D_{10}$ , distribution of drops along the radial direction in various axial planes. At 5 mm downstream, the drop mean diameter reaches its maximum value at 5 mm from the center in the radial direction. The measurements illustrate the same. In addition, the experiments record the maximum liquid volume flux at this location, indicating that the large drops in the spray retain their original direction, due to high momentum. Away from this location on either side, smaller drops are predicted. This can be attributed to the strong interactions between the highly swirling air flow and small drops. As a consequence, the small drops are entrapped. The  $D_{10}$  profiles at the other locations downstream, by and large, keep a distribution similar to the  $D_{10}$  distribution at 5 mm downstream. However, with increasing axial distance, the mean diameter peak moves outward along the radial direction, which presumably is caused by the expansion of the main spray. The peak  $D_{10}$  is increased up to 20 mm downstream. This is attributed to vaporization of small drops and coalescence of drops after collision. Further downstream, at 29 mm and 38 mm, the sizes of the drops are decreased due to higher vaporization rate, caused by the higher temperature regions.

Figure 7.6 illustrates the Sauter mean diameter (SMD),  $D_{32}$ , distribution of drops along the radial direction in various axial planes. The  $D_{32}$  profiles exhibit the drop size distribution pattern at various axial locations similar to the  $D_{10}$  profiles at the corresponding locations. The numerical predictions for both AMD and SMD show good agreement with the experiments at almost all the measured locations.

### Drop Velocity Fields

Measurements for drop velocity components are acquired for five size groups based on the drop radius. In this study, the radial profiles of drop axial velocity are

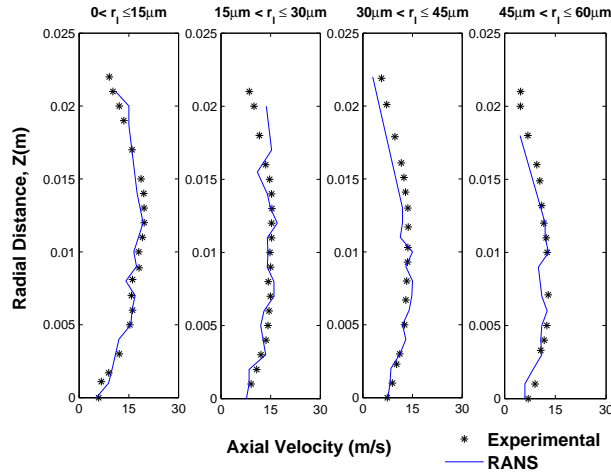


Figure 7.7: Computed spray axial velocity distribution at 5mm downstream and compared with the measurements

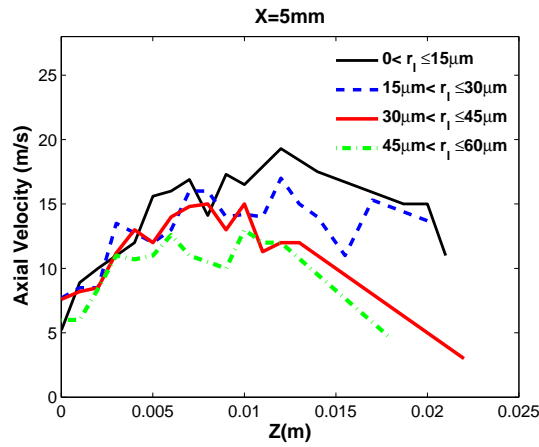


Figure 7.8: Comparison of computed axial velocity for different diameter groups at 5mm downstream

obtained for the following drop size groups:  $0 < r_l \leq 15\mu m$ ,  $15\mu m < r_l \leq 30\mu m$ ,  $30\mu m < r_l \leq 45\mu m$ , and  $45\mu m < r_l \leq 60\mu m$  (see Figs. 7.7-7.14). The velocity data for these drop size groups are recorded at four different axial locations along the

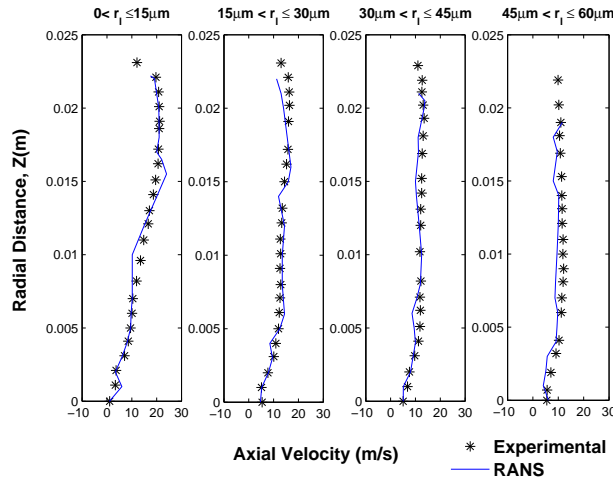


Figure 7.9: Computed spray axial velocity distribution at 9mm downstream and compared with the measurements

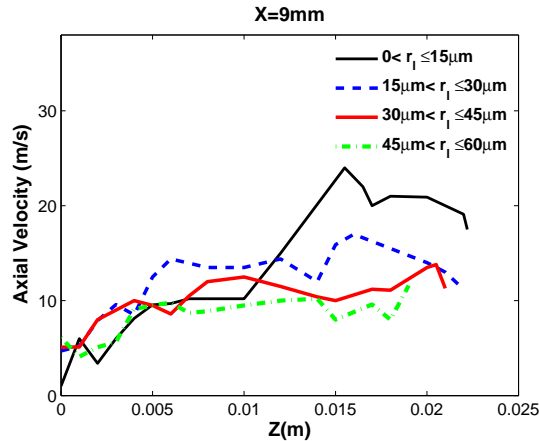


Figure 7.10: Comparison of computed axial velocity for different diameter groups at 9mm downstream

length of the combustor: 5 mm, 9 mm, 15 mm, and 20 mm. The results are compared with the experimental results. Figures 7.7 and 7.8 illustrate the axial velocity profiles of the drop size groups at 5 mm downstream. Large velocity differences are observed between various groups, which can be attributed to strong interactions between the swirling gas and the liquid spray. Figure 7.7 illustrates that the smaller drops possess a higher velocity than the larger drops. The numerical data show that the peak velocity of the smallest drop size group ( $0 < r_i \leq 15 \mu m$ ) is about 20 m/s. The peak velocities of the other three groups (in ascending order of drop sizes) are about 16 m/s, 14 m/s,

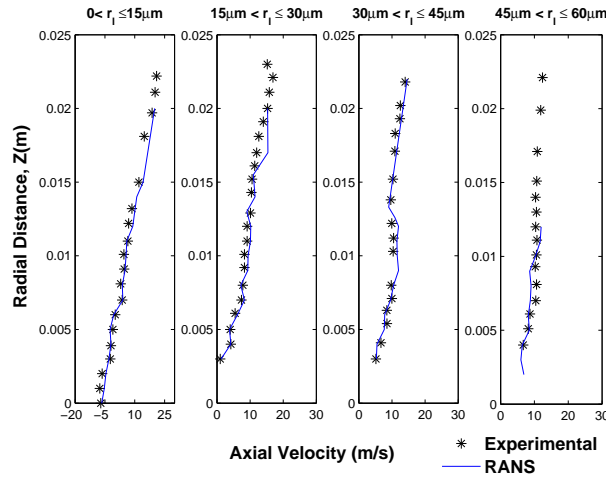


Figure 7.11: Computed spray axial velocity distribution at 15mm downstream and compared with the measurements

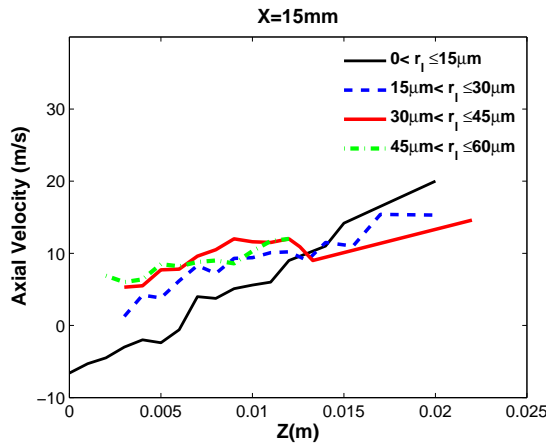


Figure 7.12: Comparison of computed axial velocity for different diameter groups at 15mm downstream

and 12 m/s, respectively. Nevertheless, very close to the center, the small size drops have a lower velocity than the large drops. The gas-phase velocity also has a low magnitude near the center (see Fig. 7.3). Both measurements and numerical data indicate that the small drops tend to follow the gas, while the large drops retain their original momentum due to higher inertia. At 9 mm downstream, similar developments are observed (see Figures 7.9 and 7.10). The peak velocity of the smallest drop group is about 25 m/s, while the peak velocity of the other drop groups decreases with increasing drop size. Furthermore, due to the presence of the recirculation region,

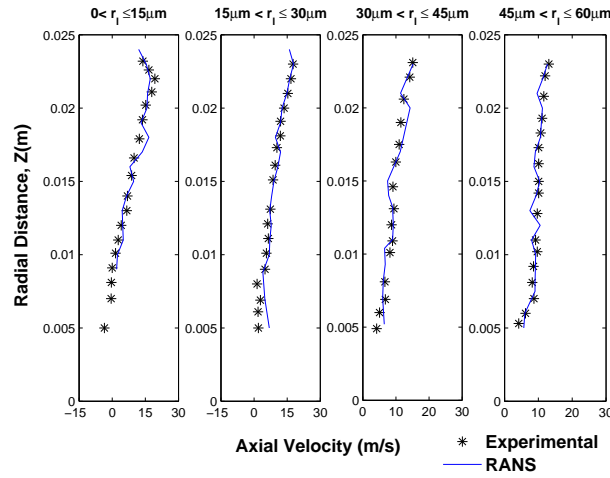


Figure 7.13: Computed spray axial velocity distribution at 20mm downstream and compared with the measurements

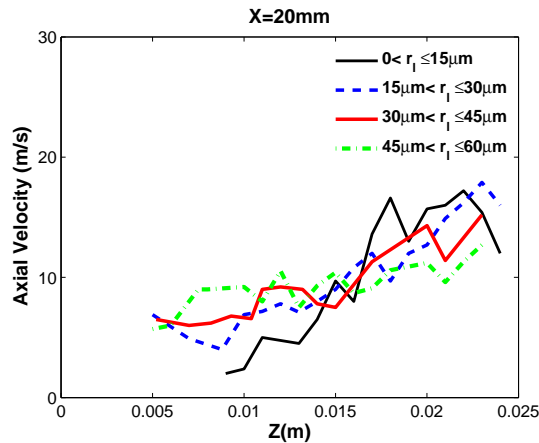


Figure 7.14: Comparison of computed axial velocity for different diameter groups at 20mm downstream

the drop velocities close to the center are much lower than the drop velocities away from the center with the smallest size group possessing the lowest velocity. At 15 mm downstream (see Figures 7.11 and 7.12), close to the center, small drops show negative velocities, indicating the effect of deceleration of the gas-phase on the spray. At this location, the gas-phase recirculation velocity reaches its maximum value (see Fig. 7.3). Further downstream, at 20 mm (see Figures 7.13 and 7.14), there are not many spray data available near the center in both the numerical and experimental cases, due to combustion. However, the velocity profiles of the drop groups in this plane

show similarities with that in the planes located upstream. Away from the center, the large drops are still lagging behind the small drops. In all the planes, there are a few radial locations in which not enough spray data are recorded. This problem can be overcome by tracking more drops, but at an added computational expense. Overall, the computed drop axial velocity profiles show reasonable agreement with the measurements.

## 7.5 Concluding Remarks

Numerical simulation is performed to characterize the reacting flow field associated with a single-element LDI combustor. A RANS code is used to compute the entire flow field of the combustor, encompassing six helicoidal air flow passages, the converging-diverging nozzle, and the square chamber section. A spray model is introduced which consists of several sub-models, such as the models for drop breakup, drop collision and coalescence, drop drag and distortion, turbulent dispersion of spray, and drop evaporation. In addition, a combustion model is applied. The Realizable  $k - \varepsilon$  model is used for turbulence modeling. Properties of both the gas and liquid phases are analyzed to get an insight into the effects of the highly swirling flows on the spray characteristics and the combustion process. The numerical results are compared with the measurements for validation.

The reaction of the spray greatly influences the gas-phase velocity distribution. The high axial momentum induced by combustion and momentum transfer between the liquid and gas phases decrease the size and length of the central recirculation zone in the reacting flow. On the other hand, the heat-release due to combustion gives rise to a strong reverse flow region at the center. In addition, the heat release leads to the expansion of the gas-phase, resulting in higher velocities compared with the non-reacting case.

The spray mean diameter profiles at various locations within the combustion chamber indicate a strong influence of the highly swirling flow on the spray drop distribution. The effect of vaporization of spray on the drop size distribution is noticed. The spray velocity profiles further illustrate the interactions between the gas-phase and the liquid drops of various size groups, which reflect a strong momentum exchange between the two phases. The spray velocity is significantly influenced by the swirling flow and the strong recirculation region. By and large, the smaller drops tend to follow the gas, while the larger drops retain their original momentum due to high inertia. Overall, the numerical results for both the gas-phase and liquid spray exhibit a good agreement with the measurements.

## 8. Non-Reacting Flow Study in the MPLDI Combustor

### 8.1 Introduction

This chapter presents the numerical results obtained from the non-reacting cold simulations of a Multi-Point Lean Direct Injection (MPLDI) combustor [52]. The non-reacting cold flow investigation is an initial step to study the flow field in the complex MPLDI configuration. The key insights obtained from the simulation and post-processing are utilized to perform a reacting spray simulation in the MPLDI combustor described in Chapter 9. The MPLDI has the same air swirler-fuel injector configuration as for the single-element setup. The geometry becomes more complex due to the arrangement of several swirler-fuel injector modules in a close proximity to each other. However, the multi-injector concept allows for several small flame zones within the combustor, resulting in a short flame residence time. The fuel atomization and fuel-air mixing process are supposed to be enhanced due to highly swirling flow and inter-swirler mixing inside the chamber, leading to a uniform temperature distribution and a good pattern factor at the chamber exit. The lean mixture and an efficient mixing process in the MPLDI will result in low  $\text{NO}_x$  production. In addition, this design allows for a variety of fuel staging possibilities appropriate for a wide range of engine operating conditions.

In the past, different flame-tube configurations were examined to determine an efficient design for the multi-injection strategy [43, 44, 141]. A large number of variables play an important role in the development of the MPLDI concept. Design choices include the number and size of injector elements, the type of air swirler (radial or axial), the number of swirl vanes per swirler, vane angle, rotational direction (co-rotation or counter-rotation), and the type of fuel nozzle. Considering these factors, experiments were conducted to compare combustion performance and emission characteristics. Various configurations, such as 3x3, 5x5, 6x6, and 7x7 array of elements, were experimentally studied [43, 15, 8]. The LTO  $\text{NO}_x$  has been reported well below the 1996 ICAO standard [8].

In this study, the MPLDI geometry comprises nine air swirler-fuel injector modules in a 3x3 arrangement at the inlet of the combustion chamber. This geometrical configuration is deemed the baseline design by the NASA for multi-injection LDI strategy and a few experiments have been performed on it [15, 8, 48]. Unfortunately,

no experimental cold flow results are reported on this baseline configuration, although a numerical cold flow study using the NASA National Combustion Code (NCC) was conducted by Davoudzadeh et al. [51]. Some non-reacting measurement data for MPLDI are presented by Cai et al. [141], but employing a different swirler geometry arranged in a 3x3 array, where each of the 9 swirlers has 8 flow passages and each swirl vane has 35° downstream vane angle. Therefore, the results from the present study cannot be compared directly with the measurements, however the general flow structures are compared with the relevant information available in the literature.

The unsteady RANS (URANS) and large eddy simulation (LES) methods are employed separately to characterize the non-reacting flow field of the MPLDI combustor. The results between the two methods are compared. Overall, the numerical simulations capture aerodynamic flow features, such as the recirculation regions, the highly complex flow structures at the chamber entrance, and in the intersections of the adjacent swirlers. The results confirm the flow being highly unsteady in the vicinity of the chamber inlet where the highly swirling flows emerge from the individual swirlers and interact with the neighboring ones.

## 8.2 Geometrical Configuration and Grid

### Geometry

Figure 8.1 shows the numerical model of the MPLDI combustor used for the computations, which also includes an enlarged view of the swirler-fuel injector module. The configuration comprises nine swirler-fuel injector modules in a 3x3 array that are designed to fit within a 76.2 mm square section. The center-to-center distance between the modules is 25.4 mm [15]. All the nine swirlers rotate in the same direction. The geometry and design of each module are the same as that of the single-element configuration. Each air swirler has six helicoidal vanes of 60° vane exit angle and the swirl number is 1.23. A simplex type fuel injector is inserted through the center of the swirler and its tip is positioned at the throat of a converging-diverging venturi section which encloses the swirler-fuel injector assembly.

### Grid

The numerical simulation is performed for the entire geometry of the MPLDI combustor by using two calculation methods: URANS and LES. For the URANS calculations, a study is conducted to determine the effects of grid resolution on the computed flow field. The grid is refined several times until no appreciable change is observed in the flow field. The final refined grid (see Fig. 8.2) for the URANS calculations has 3.5 million cells. It consists of both hexahedron and tetrahedron elements. The grid is clustered normal to the walls to resolve the large gradients within the boundary layer. The maximum  $y^+$  along the walls is less than 5.

On the other hand, for the LES calculations, the grid used for the URANS is refined further in the regions of high shear. Within the swirler assembly and the combustion

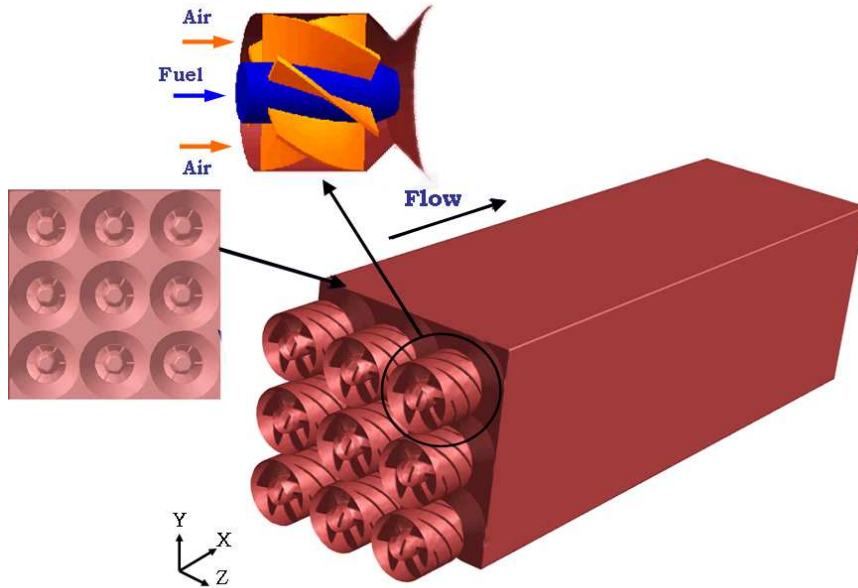


Figure 8.1: The MPLDI combustor geometry with the air swirler-fuel injector module being zoomed into

chamber, the maximum  $y^+$  along the wall is about 5. The final refined grid for the LES calculations has 8.9 million cells. The grid refinement study is performed only up to the limits posed by the available computational resources.

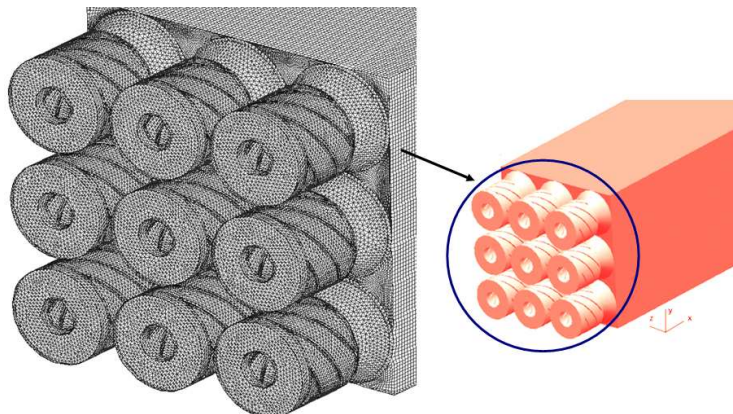


Figure 8.2: Grid distribution for the MPLDI configuration

## 8.3 Boundary Conditions and Numerical procedure

### Initial and Boundary Conditions

The initial flow field for the URANS and LES calculations is the solution of the steady-state RANS calculations, and no extra random fluctuations are imposed. The non-reacting inlet flow conditions are the same for the MPLDI as in the single-element LDI. Air at a total temperature  $T_0 = 294.28$  K and 1 atmosphere pressure enters with a flow velocity of  $U_0 = 20.14$  m/s normal to the inlet face. Inlet air density is  $1.19$  kg/m<sup>3</sup>. Inlet turbulence is specified by turbulent intensity and length scale. From the flow simulations of the single-element LDI under the same inlet conditions, it has been noticed that a turbulent intensity of 10% and one tenth of inlet diameter length scale yield the most accurate results when compared to the measurements. Therefore, the same turbulent intensity level and the length scale value of the single-element case are assigned to compute the MPLDI flow field.

### Numerical Procedure

The URANS and LES calculations are carried out using the pressure-based coupled algorithm, in which the momentum equations and the pressure-based continuity equations are solved in a coupled manner. The PRESTO [71] discretization scheme is used for pressure interpolation. For the URANS calculations, the second-order upwind scheme is applied to solve the momentum and turbulence equations. On the other hand, for the LES calculations, the central differencing discretization method is employed to solve the momentum equations.

In all cases, before performing unsteady flow calculations, a realistic initial flow field is obtained by running a steady state flow simulation using the realizable  $k - \varepsilon$  RANS turbulence model. When the solution is sufficiently converged, unsteady calculations are initiated. The URANS calculations comprise the following steps. At first, the steady state RANS solution is restarted in the unsteady mode using the realizable  $k - \varepsilon$  model. Once the flow becomes fully developed and statistically stable, the RSTM calculations are started. The simulation is continued until the solution becomes completely stable. It is followed by computation of the time-averages by sampling at a specified frequency to obtain mean and root mean-square values. The time-average calculations are continued until statistically stable data is obtained.

For the LES calculations, the following steps are followed.

1. The reasonably converged realizable  $k - \varepsilon$  RANS solution is used as an initial flow field. An instantaneous velocity field is generated out of the steady-state RANS results to create a more realistic initial field before the LES run. It also helps in shortening the time required for the LES solution to become statistically stable.
2. The LES mode is enabled and an appropriate time step size is set for the simulation.

3. The LES calculations are run until the flow becomes statistically steady.
4. The solution is restarted by enabling the time average calculations at a specified interval. The statistics collected at each sampling interval are post-processed to compute the mean and the root-mean-square values.
5. The calculations are continued until the solution becomes statistically stable.

For all the unsteady flow simulations, the duration of the calculations are pre-determined by estimating the mean flow residence time in the solution domain. To determine if the flow is fully developed and statistically steady, velocity components are monitored at a few locations close to the chamber inlet, where the flow field is highly unsteady. During the course of the simulations, when no substantial variations in velocity magnitude are found at those locations, the flow is considered to be statistically stable. At this point, the residuals of continuity, momentum, and Reynolds stresses equations drop by more than 5 orders of magnitude and the solution converges. For both the URANS and LES calculations, the physical time-step is  $1.0\mu\text{s}$  and the CFL number for time iteration is less than 1.

Two quad dual-core AMD Opteron Linux cluster machines, namely DUTW1424 (2.2 GHz and 16 GB memory) and DUTW1420 (1.8 GHz and 16 GB memory), are simultaneously employed for parallel computing. Each machine has eight processors with an InfiniBand architecture. The total computation time for the URANS and LES calculations are 320 and 672 hours, respectively.

## 8.4 Non-Reacting Cold Flow Field Analysis

URANS and LES methods are employed to simulate the non-reacting turbulent flow field of the MPLDI combustor. The axial mean velocity data obtained from the two methods are compared at various axial locations. However, only the LES results are presented to demonstrate the swirl velocities and the structures of the vortex cores.

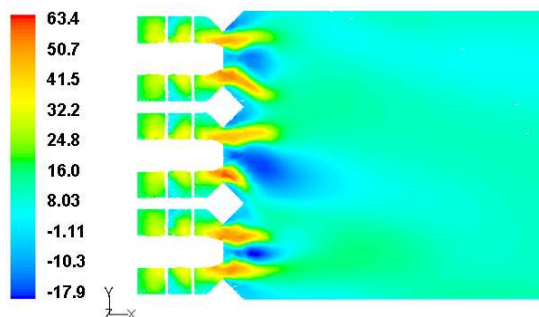


Figure 8.3: Axial mean velocity distributions (in m/s) shown at the mid-plane (x-y plane)

Figure 8.3 shows axial mean velocity contours in the X-Y plane. There is a recirculation region downstream of each of the 9 fuel injectors similar to the single-element flow case. However, the recirculation zones are smaller in size compared with the single-element recirculation zone mainly due to the geometry that allows for flow mixing amongst the neighboring swirlers. The size and shape of each of the 9 reversed flow regions can be further noticed in Fig. 8.4. The figure shows the iso-surface of the zero axial mean velocity or the vortex breakdown bubble (VBB), indicating all the recirculation zones inside the combustion chamber. The VBB of each injector is in the light blue surface, which is fairly smooth and asymmetric. The recirculation zone of the central element is distinctively larger than the recirculation zones of the surrounding elements. This is due to the fact that there is no wall adjacent to the central element, whereas all the other recirculation zones are bounded by the side walls of the combustion chamber. In addition to the central recirculation regions, Figs. 8.3 and 8.4 depict the reversed flow regions in the corners of the upstream wall of the combustion chamber, at the interfaces of the converging-diverging nozzles, and along the divergent section of the venturi. The results are consistent with the numerical data presented by Davoudzadeh et al. [51].

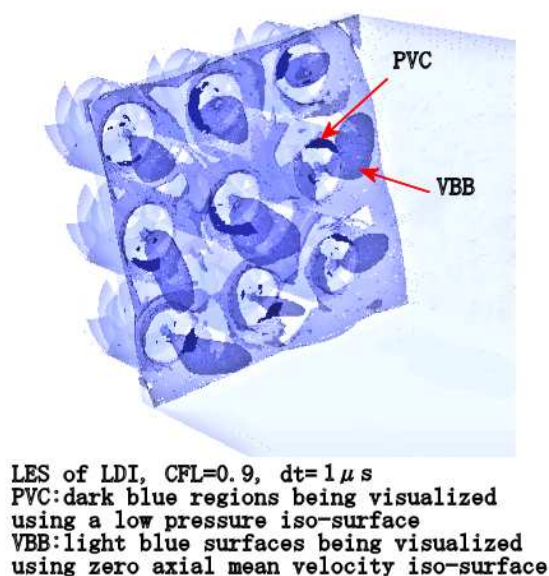


Figure 8.4: A perspective view of the PVC and VBB

Figure 8.4 also shows the precessing vortex core (PVC) together with the VBB. In this figure, the iso-surface of a relatively low pressure captures the PVC. The PVC essentially occurs in high Reynolds and swirl number flows. It is characterized by the regular precession of the large scale vortical structure typical of swirling jets around the geometrical axis of symmetry. The short dark blue regions in the figure represent the vortex core, which is formed near the tip of the fuel injectors and extends

into the combustion chamber. The vortex cores rotate and break, thereby creating hydrodynamic instability around the reverse flow regions. The LES data shows that the location and shape of the PVC are time dependent and it does not align with the centerline of each of the nozzles. Such behavior may explain why the axial mean velocity distribution at the dump plane and inside the chamber is asymmetric.

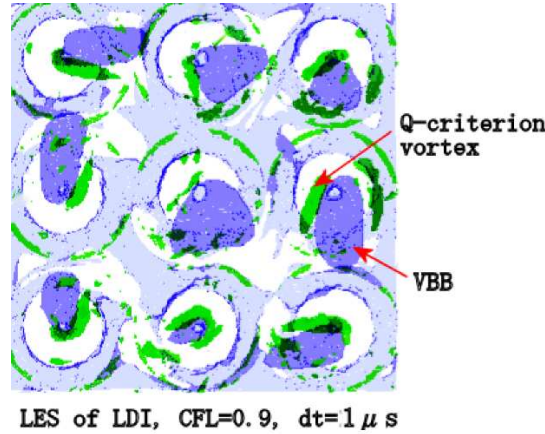


Figure 8.5: Iso-surface of the Q criterion and VBB at the chamber inlet

Figure 8.5 shows the instantaneous iso-surface of the Q-criterion vortex together with the VBB in the Y-Z plane. The iso-surfaces of the Q-criterion and the VBB are in the green and light blue surfaces, respectively. The Q criterion identifies vortices as flow regions with positive second invariant of the velocity gradient tensor, i.e.,  $Q > 0$ , and Q can be written in the following form [142]

$$Q = \frac{1}{2}(\|\Omega\|^2 - \|S\|^2) \quad (8.1)$$

where  $\Omega$  and  $S$  are the skew-symmetric and symmetric parts of the velocity gradient, respectively. Therefore, Q is a local measure of excess rotation-rate relative to strain-rate. The vortex breakdown phenomenon around the VBB can also be observed in the figure. The iso-surfaces of the PVC and Q-criterion indicate the presence of coherent structures in the vicinity of the combustion chamber inlet. The rotation and interactions of these coherent structures in the flow field play an effective role in the dispersion of liquid fuel particles, which in turn will cause an impact on turbulent mixing between fuel and oxidizer in the combustion chamber. The effects of vortex structures on liquid spray dispersion and mixing are presented in Chapter 9.

Figures 8.6- 8.12 exhibit the time-averaged axial velocity contours and the vector orientations (Figs. 8.7- 8.12) in the Y-Z plane at several locations, including the regions inside the swirler vanes and the combustion chamber.

The computed LES and URANS axial velocity contours inside the swirlers are illustrated in Fig. 8.6. Between the two models, there is only a small difference in the magnitude of the peak velocity. In both cases, the white radial lines represent the

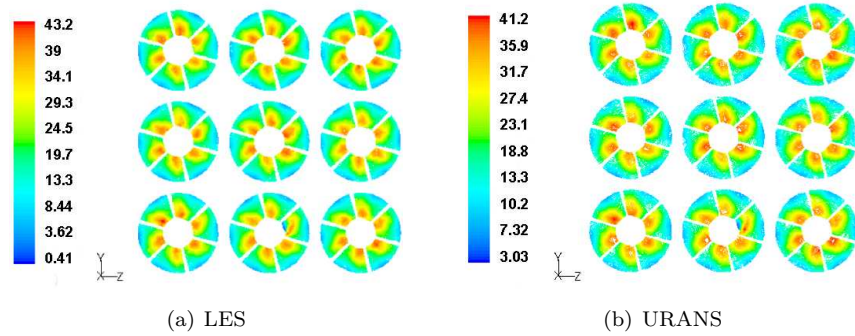


Figure 8.6: Axial mean velocity (in m/s) contours inside the nine swirlers

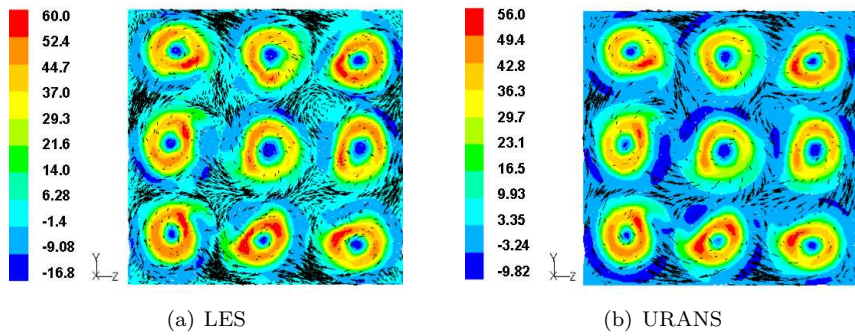


Figure 8.7: Axial mean velocity (in m/s) contours at the chamber inlet

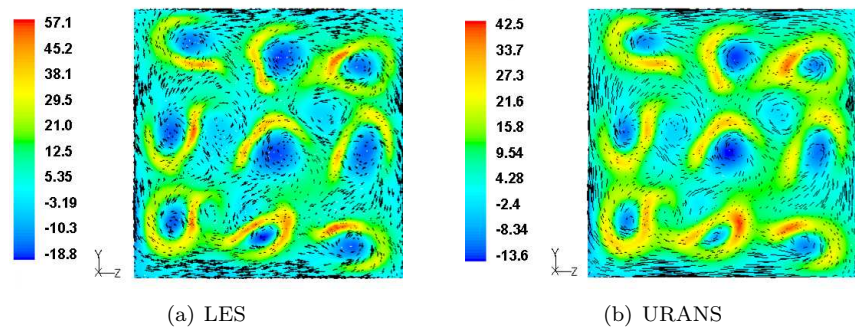


Figure 8.8: Axial mean velocity (in m/s) contours at 5 mm downstream

swirler blades. The flow is identical in each swirler passage, since all the passages are separated from each other. Likewise, all the 9 swirlers have the same flow pattern. However, at the chamber inlet (see Fig. 8.7), the magnitude of the velocities between the LES and URANS predictions differ significantly. For the LES calcula-

tions, the maximum reverse flow velocity in the recirculation zone is around  $-17$  m/s, whereas the URANS prediction of the maximum reverse flow velocity is just about  $-10$  m/s. In addition, each of the nine recirculation regions are quite conspicuous in the LES plot compared with the URANS plot. Nevertheless, both numerical methods show that each recirculation region is surrounded by a high velocity jet coming out of the swirler vane passages. Reversed flow regions are also observed at the boundary between any two swirlers and at the wall corners.

As shown in Fig. 8.8, at 5 mm downstream, the magnitude of the velocities and the size of the recirculation regions between the LES and URANS predictions continue to differ, although the vector orientations and the flow structures display similarities. The contour plots indicate that the recirculation zones are expanding. However, the shapes of these recirculation zones produced by the surrounding eight swirlers appear distorted. Low axial velocity regions are found in the areas adjoining four swirlers, which contain both positive and negative velocities. Furthermore, small reverse flow regions can be seen near the corners of the wall.

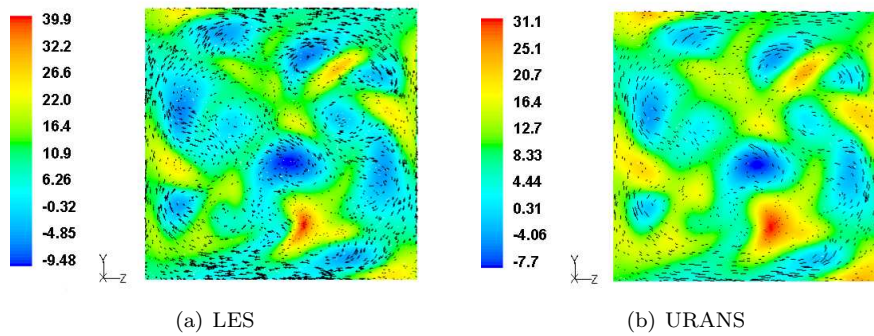


Figure 8.9: Axial mean velocity (in m/s) contours at 12 mm downstream

As the flow moves downstream, the jet streams from each swirler combine with each other and the velocity signatures of the original jet streams disappear along with recirculation zones at the wall corners and at the intersections. Figure 8.9 shows the LES and URANS predictions of the axial mean velocity contours at 12 mm downstream of the combustion chamber inlet. Differences in the magnitude of the velocities can be noticed between the two modeling approaches. In the URANS calculations, the reverse flow regions of the surrounding swirlers become weak, whereas LES predicts stronger reverse flow regimes. Nevertheless, except the recirculation zone from the central swirler, the recirculation regions of the surrounding swirlers are displaced outward from their original locations. In both models, the central recirculation region appears to be larger and more prominent with high recirculation velocities. On the other hand, the recirculation zones of the surrounding swirlers continue to stretch and deform due to the deformation of the swirling flows near the wall. Furthermore, the flows from all the swirlers begin to merge together at their intersections, indicating a high degree of mixing inside the combustion chamber.

Figure 8.10 compares the LES and URANS axial mean velocity contours in the Y-

Z plane at 18 mm downstream. The magnitude of the velocities between the two models still differs, although both models display almost identical flow structures and vector orientations. In addition, it can be noticed that the recirculation zone of the

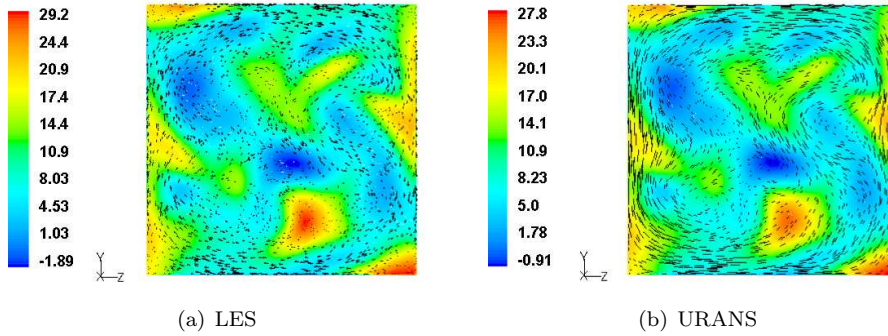


Figure 8.10: Axial mean velocity (in m/s) contours at 18 mm downstream

central swirler becomes a lot weaker, but it is still located at the center. However, it is deformed and no longer retains its initial roundness. The reverse flow regions of the surrounding swirlers almost vanish. The flow mixing among the adjacent swirlers is still fairly strong. The length of the recirculation zone of the central swirler differs between the two numerical approaches. LES predicts that the recirculation zone of the central swirler extends up to 22 mm from the dump plane, whereas URANS anticipates that the recirculation zone of the central swirler disappears at about 19 mm downstream.

At 29 mm downstream (see Fig. 8.11), the recirculation region of the central swirler does not exist anymore. Both LES and URANS calculations capture almost the same flow characteristics and only some minor differences are observed in the magnitude of the axial mean velocities between the two models.

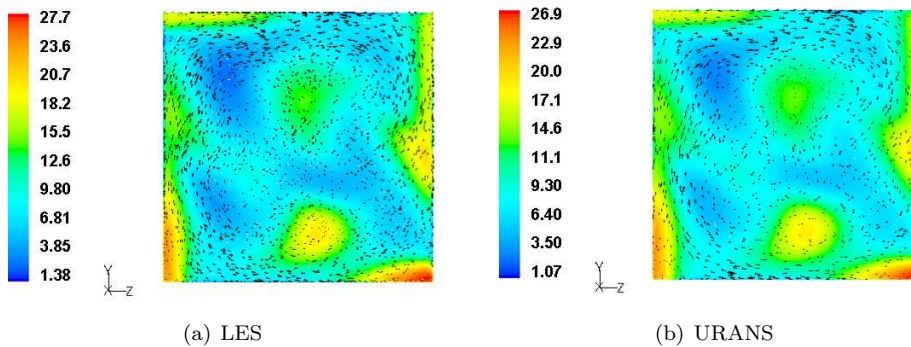


Figure 8.11: Axial mean velocity (in m/s) contours at 29 mm downstream

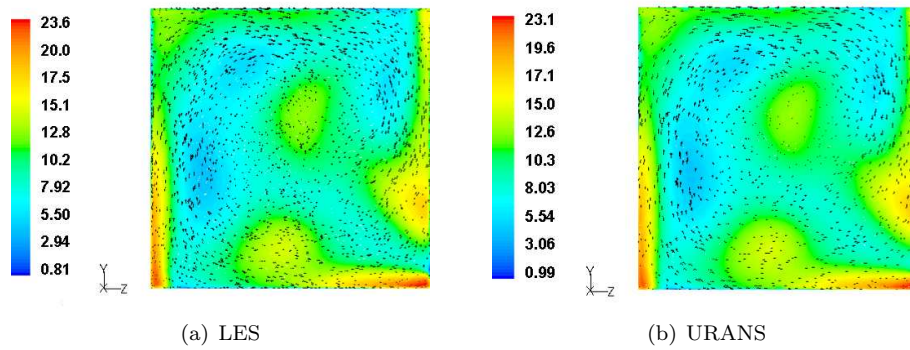


Figure 8.12: Axial mean velocity (in m/s) contours at 46 mm downstream

Further downstream, at 46 mm from the chamber inlet, the axial mean velocity field predictions by the two methods are almost identical (see Fig. 8.12). The vector orientations indicate that a unified swirling flow exists in the central region, whereas near the chamber wall, the axial velocities are higher than that of the central region. As the flow moves towards the exit, the unified swirling flow loses its strength.

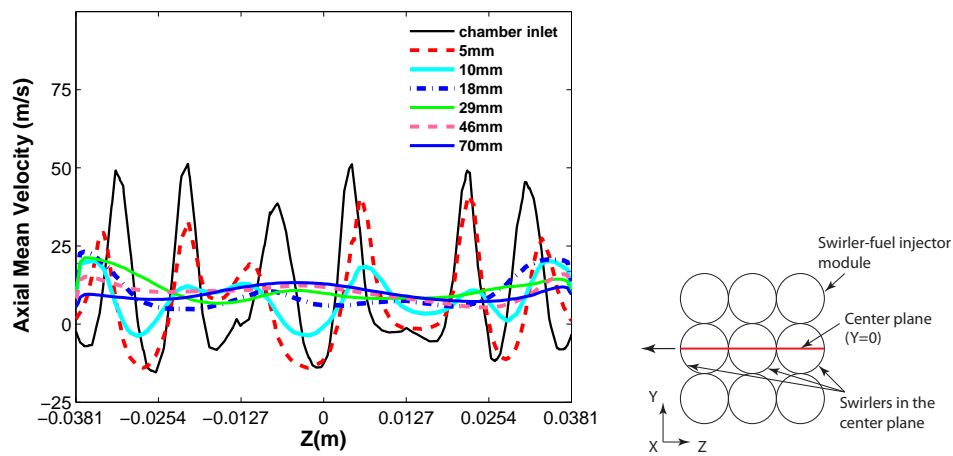


Figure 8.13: Axial mean velocity profiles (in m/s) at various axial locations in the Y-Z plane

To compare the axial mean velocity profiles at various axial locations, the LES data are plotted together (see Fig. 8.13). The velocity profiles are presented for the 3 swirlers located in the center plane ( $Y = 0$ ) as shown on the right side of Fig. 8.13. At the chamber inlet, the recirculation zone of each of the 3 swirlers can be identified. In addition, reverse flow regions at the intersections of the swirlers and the axial mean velocity peaks are observed. As the flow proceeds downstream, the velocity peaks move toward the intersections of the swirlers, indicating an expansion of the

swirling flow and a strong flow interaction between the adjacent swirlers. The axial velocity peaks move toward the wall as the flow travels along. Further downstream, no distinct velocity peaks can be found and the profile almost flattens out.

The mean axial velocity contours at various axial locations reveal some typical features in the flow field. Figures 8.7-8.10 mainly demonstrate clockwise rotation of the outer swirling structures around the central jet for each swirler-injector. On the other hand, Figs. 8.9-8.12 show high axial velocity at the corners and the sides of the wall, which might be induced by the overall swirling motion of the flow.

The numerical predictions of LES differ significantly with those of URANS in the neighborhood of the dump plane of the combustion chamber. The size of the recirculation zones and the magnitude of the velocity in the jet streams and recirculation zones can be compared between the two methods in the proximity of the dump plane. The LES results in this region show a higher magnitude of both positive and negative velocities compared with the URANS results. This is probably due to the limited capability of URANS to predict the flows accurately in the areas of large turbulence, which might result in an under prediction of energy estimation. On the other hand, it is noticed that the LES results for the resolved scale stresses in the vicinity of the chamber inlet are higher compared with the URANS results. Furthermore, SGS stresses modeled in LES give rise to subgrid-energy, which contributes to the total amount of energy in the domain. However, if the grid is coarse, there are also possibilities of having high subgrid-energy in the system. The grid size for the LES MPLDI simulation is almost three times the grid size for the URANS simulation, but it can be refined further to compare the contribution of subgrid energy to the system. In addition, higher-order SGS models need to be investigated to analyze and compare their influence on the LES results. Nevertheless, overall, the axial mean velocity structures and the vector orientation in the two methods exhibit some similarities. Far downstream, almost identical flow features with nearly the same magnitude of velocities are predicted by the two methods.

By and large, the LES and URANS computational methods are able to predict the following basic flow characteristics: (a) the progress of the recirculation zone of the central swirler, (b) the stretching and deformation of the recirculation regions of the surrounding swirlers, and (c) the complex flow field at the intersections of the adjoining swirlers and near wall. The computed results are in good qualitative agreement with the results of Cai et al. [141] and Davoudzadeh et al. [51].

Figure 8.14 shows the LES radial mean velocity profiles at various axial positions for the 3 swirlers located in the center plane ( $Y = 0$ ). Similar to the axial mean velocity profiles, the radial mean velocities in the vicinity of the chamber inlet are high, indicating a quick expansion of the flow in the radial direction. However, once the flow goes past the recirculation regions, the radial velocity peaks decay rapidly. The strong flow interactions among the swirlers lower the magnitude of radial velocity. At 29mm downstream, radial velocities change directions. Further downstream, at 70 mm, the radial mean velocity profile is relatively flat and the radial velocity magnitude at all the radial locations almost approaches to zero.

Figure 8.15 shows the LES vector plots of the tangential (swirl) mean velocity distribution at several axial locations inside the combustion chamber. The vector plots are in the Y-Z plane and viewed from the left with respect to Fig. 8.1. The vector

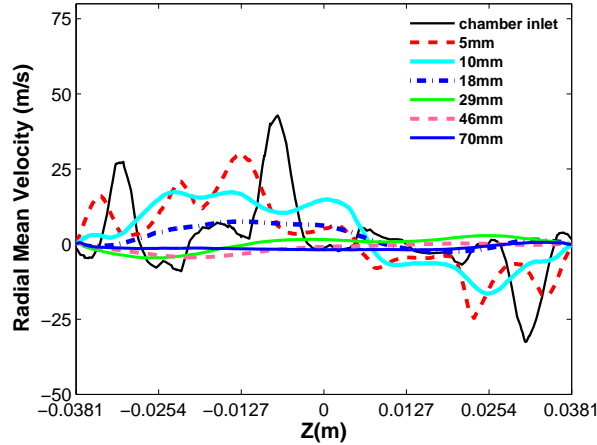


Figure 8.14: Radial mean velocity profiles (in m/s) at various axial locations in the Y-Z plane)

length is essentially proportional to the velocity magnitude. At the chamber inlet or the dump plane (see Fig. 8.15(a)), a swirling flow characterizes each swirler, because of the tangential jets relative to individual swirler axis. At this location, the swirling flow is not uniform. The peak tangential mean velocity is about 60 m/s, which is of the same order as to the corresponding LES peak axial mean velocity. When viewing from left, the rotation directions are clockwise for all the swirlers. As shown in Fig. 8.15(b), at 5 mm downstream, the flow structures between the swirlers start interacting. Furthermore, the original rotating flow structures of each swirler are partially deformed, thereby forming complex flow structures resulting from the opposing flow directions at the interface of the adjacent swirlers. Figure 8.15(c) shows that strong flow interactions take place amongst the neighboring swirlers at 12 mm downstream. The original swirl flow pattern of each swirler is almost completely destroyed and the flows at the boundaries of neighboring swirlers become more complex. The asymmetrical effects, due to the opposing flow directions at the boundaries between two adjacent swirlers, cause deformation of the swirling flows near the wall. In the downstream locations, the swirling flow structures continuously and gradually merge with each other, as illustrated in Figs. 8.15(d) and 8.15(e). At 70 mm downstream (see Fig. 8.15(f)), the vector orientations indicate the formation of a unified swirling flow field. The nine-swirler array now acts like a single swirler. Further downstream, the strength of this unified swirling stream diminishes.

Figure 8.16 compares the LES tangential (swirl) mean velocity profiles at different axial positions for the 3 swirlers located in the center plane ( $Y = 0$ ). The magnitude of tangential mean velocity is considerably higher in the upstream locations, such as at the chamber inlet and in the regions close to it. In the downstream locations, although the strength of the swirling flow decreases, yet the magnitude of swirl velocities are significantly higher than radial mean velocities at the corresponding locations. The swirl mean velocity structures predicted by the simulation exhibit good agreement

with the experimental cold flow data reported by Cai et al. [141].

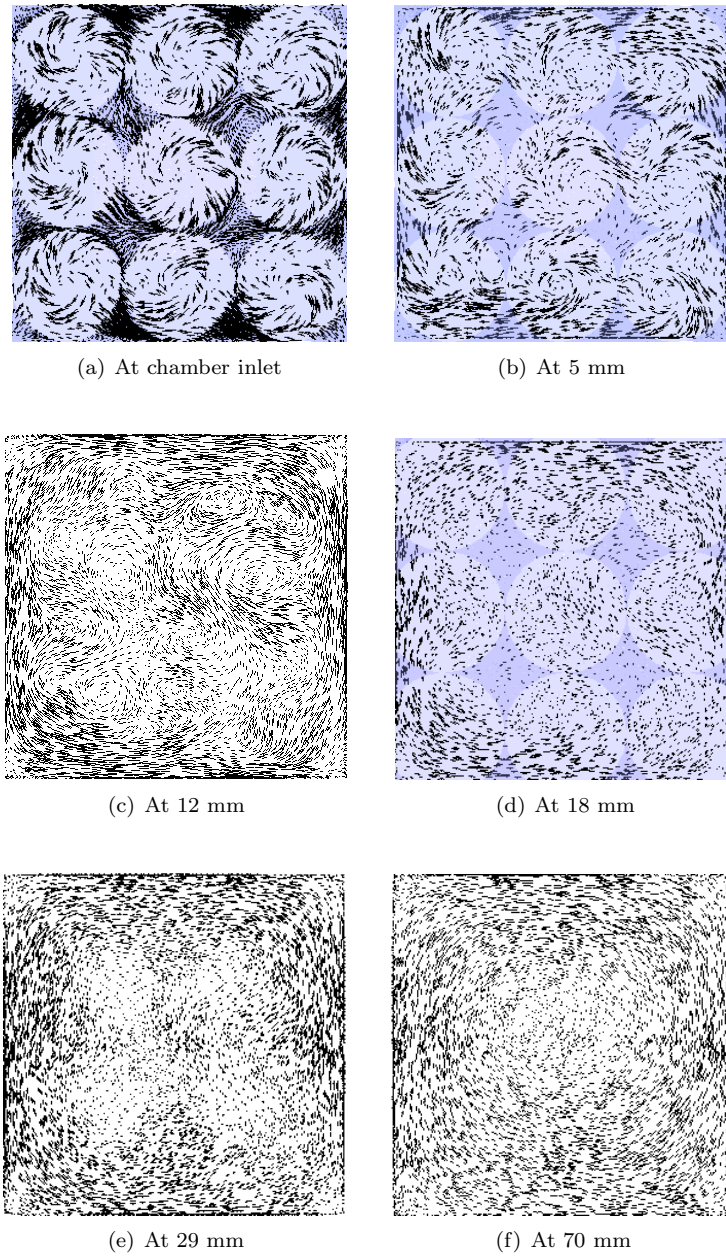


Figure 8.15: Tangential mean velocity vectors at different axial locations inside the combustion chamber

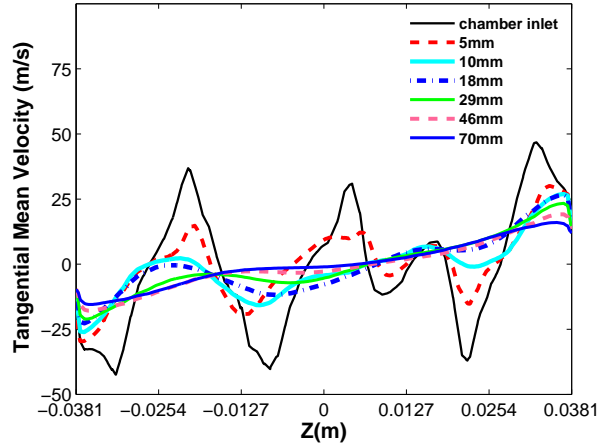


Figure 8.16: Tangential mean velocity profiles (in m/s) at various axial locations in the Y-Z plane)

## 8.5 Concluding Remarks

This chapter presents the non-reacting cold flow results of the baseline MPLDI combustor. The URANS and LES methods are employed separately to study the aerodynamic characteristics of the flow field for the same inlet flow conditions. The results of the two numerical methods are compared. Furthermore, the results are compared with the measurement data available in the literature. The steady RANS solution is used as the initial condition for the URANS and LES calculations. The solution captures the typical flow features of the MPLDI combustor, such as the complex swirling flow structures inside the swirlers and combustion chamber, the recirculation zones originating from the fuel injector tips, and the reverse flow regions in the corners of the chamber wall, intersections of the swirlers and on the wall of the divergent venturi.

In the vicinity of the chamber inlet, the LES predictions of the velocity magnitude and the recirculation volume and length of the reverse flow regions differ significantly from the URANS predictions. Nevertheless, the axial mean velocity structures and the vector orientation in the two methods display similarities. In the downstream part, both methods show identical flows with nearly the same magnitude of velocities. The computed axial mean and tangential mean velocity plots indicate very complex flow structures close to the combustion chamber inlet. In this region, highly turbulent flow structures exist due to the agitation of the incoming air flows and the flow interactions among the neighboring swirlers. Consequently, the flow generated by the co-rotating swirlers deforms rapidly inside the combustion chamber.

The LES results also reveal the dynamic behavior of the large-scale turbulent structures in the combustor, namely the PVC and VBB, which essentially indicate a large degree of unsteadiness in the flow field. The highly swirling flow field, the unsteady complex flows at the combustor inlet, and the presence of the dynamic vortex cores

might favorably influence the distribution, breakup, and dispersion of liquid fuel drops and the mixing of fuel and air in a combustion case. Overall, the numerical predictions for the mean velocity field and the flow structures show a good agreement with the experimental data available in the literature. Although LES holds promise in resolving the complex flow field of the MPLDI combustor, more detailed experimental data are required to validate the results.

## 9. Spray Combustion Study in the MPLDI Combustor

### 9.1 Introduction

This chapter discusses the numerical results of the reacting spray simulations in a Multi-Point Lean Direct Injection (MPLDI) combustor [55, 56]. The non-reacting cold flow results presented in the previous chapter provide some basic information about the complex flow field of the MPLDI system. However, the reacting flow study is necessary to understand the effects of the highly swirling flows and the complex arrangement of the swirler-fuel injector modules on temperature profiles and spray distribution. Furthermore, the reacting spray simulations provide an insight into the fuel and air mixing process in the combustion chamber which has a strong impact on combustion performance and emission characteristics.

The LDI concept has been developed as an ultra-low  $\text{NO}_x$  combustion technique for future aircraft gas turbines. Like other lean burn combustor concepts, LDI reduces thermal  $\text{NO}_x$  by minimizing flame temperature. To attain this, fuel and air are mixed at a low equivalence ratio. However, reducing flame temperature alone will not be sufficient to achieve the steep  $\text{NO}_x$  targets set for the future gas turbines. Flow residence time is another important parameter which influences  $\text{NO}_x$  production significantly. The MPLDI scheme is introduced by breaking up a few large fuel injectors into many small fuel injectors to produce several small flame zones. The small multi-zone burning provides shorter burning residence time, resulting in low- $\text{NO}_x$  formation. In addition to flame temperature and residence time, local hot spots influence  $\text{NO}_x$  formation. To eliminate local high temperature regions, lean combustion concepts generally rely on the fuel and air being well-mixed before burning takes place. Therefore, LDI also requires rapid fuel vaporization and fuel-air mixing. It achieves this by using a multi air swirler-fuel injector concept (MPLDI) which creates highly swirling flows with stronger turbulence inside the combustion chamber. The enhanced mixing and vaporization processes together with a fuel-lean operating condition are supposed to create a lean front end and uniform temperature distribution throughout the combustor, leading to low  $\text{NO}_x$  emissions and a good pattern factor at the burner exit.

In this chapter, by employing CFD, an effort is made to describe the underlying flow phenomena of reacting spray in the baseline MPLDI combustor. The Discrete Phase Model (DPM) [71] of the Fluent<sup>®</sup> solver is applied to simulate the combusting liquid

spray, which implements the Euler-Lagrange approach to treat the two-phase flow. For the liquid spray calculations, various spray sub-models are used. In addition, a combustion model is applied. Simulations are performed under different operating conditions and the results are compared. Furthermore, the numerical results are compared with the single-element LDI results for reacting flow. Unfortunately, no detailed experimental data are reported in the literature on gas-phase temperature profiles and liquid spray distribution. Therefore, the numerical results could not be compared with measurements. Experiments on the baseline MPLDI system are mostly limited to an observation of emission characteristics [8]. Although the measurements show that the MPLDI system has the potential to reduce  $\text{NO}_x$  to a great extent when compared with the 1996 ICAO standard, yet the experimental data have not completely described the dynamics of the mixing and the combustion process that resulted in low  $\text{NO}_x$ . Overall, the numerical results are able to capture and explain some of the fundamental features of the MPLDI combustor, such as the fuel-air mixing, drop size distribution, drop vaporization, and combustion process, which are primarily responsible for  $\text{NO}_x$  reduction.

The present chapter is structured as follows. In the next section, the geometrical configuration and the grid are briefly described. In Section 9.3, the boundary conditions, mathematical models, and numerical approach are summarized. This is followed by the results on the reacting spray in Section 9.4, and finally some concluding remarks in Section 9.5.

## 9.2 Geometrical Configuration and Grid

### Geometry

The geometry of the MPLDI used for the reacting flow calculations has been shown in Chapter 8 (see Fig. 8.1). It comprises nine swirler-fuel injector modules arranged in a 3x3 array to fit within a 76.2 mm x 76.2 mm flame-tube combustor. All the nine swirlers rotate in the same direction. The distance between the centers of the two adjacent modules is 25.4 mm. The fuel injector in each module is a simplex type nozzle, which is inserted through the center of the air swirler and the fuel tip is at the throat of a converging-diverging venturi section that encloses the swirler-fuel injector assembly. In the baseline MPLDI combustor, the fuel injectors are fed by two manifolds. One circuit feeds the four corner injectors and the central injector, and the second circuit feeds the remaining four injectors. Therefore, the MPLDI geometry allows for a variety of fuel staging possibilities. However, an equal fuel splitting is considered in the present work. Both the convergent and divergent angle of the venturi are  $45^\circ$ . The high air speed at the throat of the venturi enhances fuel atomization and fuel-air mixing inside the diverging venturi section and the combustion chamber, leading to an improvement in combustion performance and emission control. The air swirlers have helical, axial vanes with downstream vane angles of  $60^\circ$ . A detailed geometrical description of the swirler vanes can be found in Chapter 6.

## Grid

The reacting spray simulations are performed for the whole geometry of the MPLDI combustor by applying the RANS code. The final refined grid has 3.7 million cells. In the previous chapter, a view of the grid is shown in Fig. 8.2. It consists of both hexahedron and tetrahedron elements. During the reacting flow computation, the grid was refined a few times in the regions of high temperature gradients. The maximum  $y^+$  along the walls is less than 5.

## 9.3 Boundary Conditions, Mathematical Models, and Numerical approach

### Initial and Boundary Conditions

In order to investigate spray turbulent combustion in the MPLDI combustor, three different cases are simulated. The main purpose for choosing these cases is to study the effects of swirling air on fuel atomization and the impact of fuel-to-air ratio on spray characteristics and combustion. In all the events, air at a temperature of 776 K and of 1 atmospheric pressure enters normal to the inlet face of each swirler. The inlet boundary condition for air flow is velocity-inlet. The turbulence specification method is intensity and length scale with 10% turbulent intensity and one tenth of inlet diameter length scale. Kerosene ( $C_{12}H_{23}$ ) is set as a liquid fuel for the simulations, which is injected at a temperature of 300 K. All the nine fuel injectors have the same fuel inlet boundary conditions, since an even fuel splitting is specified amongst the injectors. The fuel atomizers are operated at a pressure of 180 kPa. The atomizers form hollow conical sprays and the initial half spray cone angle is set to  $45^\circ$ . The inlet flow conditions for the three specific cases are as follows.

In Case 1, air enters with a flow velocity of 38 m/s. The fuel through each injector is injected at a rate of 0.157 g/s, which in combination with the air mass flow rate gives an equivalence ratio ( $\phi$ ) of 0.41. In Case 2, the equivalence ratio is set to 0.41 (same as in Case 1). However, the air inlet velocity is reduced to 20.14 m/s. The fuel mass flow rate for each of the nine injectors is 0.0832 g/s. In Case 3, the inlet air velocity is the same as in Case 1, but the fuel flow rate is increased to 0.176 g/s, thereby creating a mixture equivalence ratio of 0.46.

### Mathematical Models

The mathematical models that are applied to perform the numerical simulations for spray combustion are described in Chapter 5 and the theory concerning spray and its sub-processes are explained in Chapter 3. The DPM of the Fluent<sup>®</sup> solver is used to simulate the multiphase flow in the MPLDI combustor. This model implements the Euler-Lagrange approach to describe the multiphase flow. The gas-phase is treated as a continuum and it is calculated by solving the Navier-Stokes equations. The Realizable  $k-\varepsilon$  model is used for turbulence modeling. On the other hand, the liquid-

phase is resolved by tracking the liquid particles through the calculated flow field. The sub-models of the DPM used to model the corresponding spray sub-processes are as follows.

The pressure-swirl atomizer model, which is also known as the Linearized Instability Sheet Atomization (LISA) [122] model, is used to specify the liquid sheet breakup and the atomization process. For drop breakup modeling, the Wave model [134] is selected, which takes into account the Kelvin-Helmholtz (K-H) instability effects on the liquid surface. To model drop collision and coalescence, O’Rourke’s method [59] is applied. Drop vaporization modeling is carried out using the mass-transfer vaporization law of a droplet as given in the Fluent Theory Guide [71]. The Discrete Random Walk (DRW) model is used to predict the turbulent dispersion of liquid spray drops. Finally, for combustion modeling, the Non-Premixed Combustion model combined with the mixture fraction- $\beta$  PDF approach is employed.

## Numerical Procedure

A steady RANS simulation is performed for the gas-phase calculations. The spray calculations are conducted with the unsteady particle tracking method and the particles are tracked in a Lagrangian reference frame. In the unsteady tracking, all the particles are tracked through the domain simultaneously and a particle time step is used to track them in an unsteady manner. The particles are represented by parcels that correspond to an ensemble of identical particles. A user-defined-function (UDF) is used to calculate mean diameters for each cell in the spray simulations.

The pressure-based solver is used with the coupled pressure-velocity coupling scheme. The second-order upwind discretization scheme is applied to solve all the equations. Simulations are run until the residuals of the continuity, momentum, and energy equations drop by more than four orders of magnitude and no significant changes are found in the solution. Once the reacting spray simulation is fully converged, the UDF file is compiled and a UDF library is created. After the library is built, the UDF is loaded and hooked up to the current case/data files. Finally, more iterations are run to get statistics for the spray particles.

One quad dual-core AMD Opteron™ Linux cluster machine is used for parallel computing. The machine has 8 processors and an InfiniBand architecture for data flow between processors. On the average, the total computation time for each reacting spray simulation is 408 hours.

## 9.4 Reacting Spray Analysis

The results of the reacting spray simulations of the MPLDI combustor are presented here for three different inlet boundary conditions as mentioned in Section 9.3. Each case is analyzed and the results of the three cases are compared with each other. In addition, these results are compared with the reacting flow results of the single-element LDI and the non-reacting flow results of the MPLDI as described previously in Chapters 7 and 8, respectively.

**A. Case 1:  $\phi = 0.41$ , Inlet flow velocity=38 m/s**

Amongst the 3 cases discussed in this section, the present case has the highest inlet air flow velocity and the lowest mixture equivalence ratio. This case is treated as an example to illustrate the features of the MPLDI combustor which explain its ability to reduce  $\text{NO}_x$ . The results are later compared with the results from the two other cases having lower swirling flow speed and higher equivalence ratio, respectively.

**Velocity Field**

Figure 9.1 shows the axial mean velocity profiles at various axial stations for the three swirlers located in the center plane ( $Y = 0$ ). At the chamber inlet, axial velocity peaks and the reverse flow regions at the intersections of the adjacent swirlers

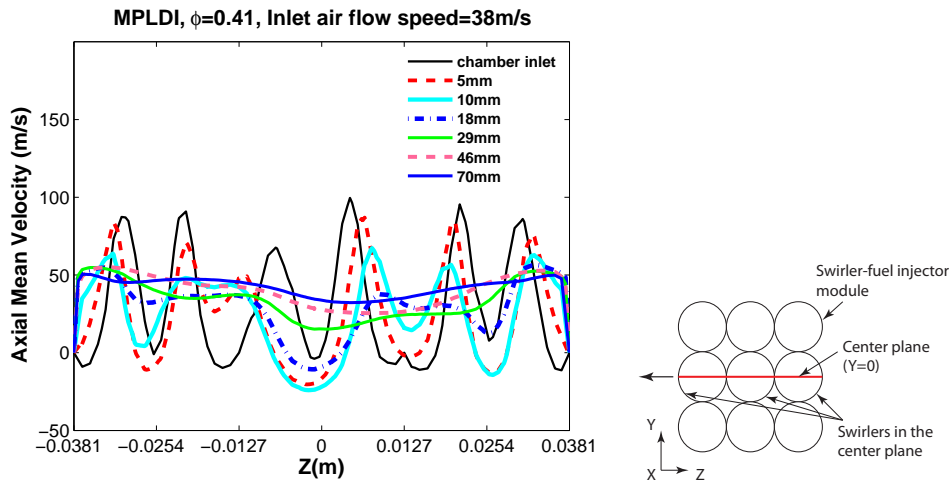


Figure 9.1: Axial mean velocity profiles (in m/s) at various axial locations in the Y-Z plane

can be observed, but there are no central recirculation regions. As the flow moves downstream, it reverses in the central regions of the swirlers. At 5 mm downstream, the recirculation zones generated from individual swirlers can be visualized with the center one being stronger and larger than others. However, the reverse flow regions at the swirler intersections disappear and the axial velocity peaks move toward the intersections, signifying that the flows from the swirlers begin to mix with each other. At 10 mm downstream, the recirculation zone of the center swirler expands in size, but the recirculation regions of the adjacent swirlers become shorter and weaker. The velocity peaks further shift radially outward, indicating a strong flow mixing between the individual swirlers. At 18 mm downstream, the recirculation zone of the center swirler also diminishes and the velocity peaks move toward the side-walls. The axial velocities at the swirler intersection become almost uniform. Further downstream, the axial velocity profiles flatten out, signifying that a uniform mixing has occurred inside the combustor and interactions between the individual swirlers are negligible.

The radial mean velocity profiles at various axial locations are shown in Fig. 9.2 for the three swirlers located in the center plane ( $Y = 0$ ). The figure exhibits that radial velocities of individual swirlers at the chamber inlet are significantly higher than at other downstream axial stations. The high radial velocities indicate a rapid expansion of the flow along the radial direction. The reacting flow possesses higher radial velocity gradients when compared with the radial velocity gradients of the non-reacting flow (see Fig. 8.14). Nevertheless, the radial velocities decay fast when the flows move past the recirculation zones, showing a similar trend as observed in the non-reacting case.

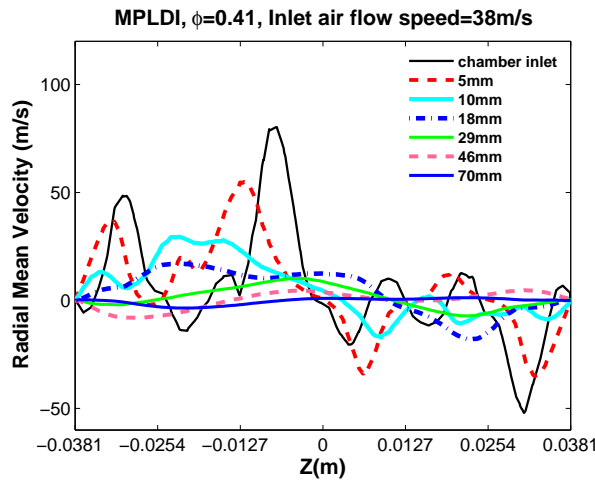


Figure 9.2: Radial mean velocity profiles (in m/s) at various axial locations in the Y-Z plane)

Figure 9.3 compares the tangential or swirl mean velocity profiles at different axial positions for the swirlers located in the center plane ( $Y = 0$ ). In the vicinity of the chamber inlet, a spiral motion of individual swirlers results in high tangential velocities, indicating that a strong swirling flow is generated from individual swirlers. As the flow moves downstream, the original rotating flow structures are destroyed. The swirling shear layer from the individual swirlers continually and gradually merges with each other with increasing axial distance, which causes a decrease in maximum swirl velocity strength. Finally, a unified swirling flow is formed, and the swirler array poses as a single swirler.

Figure 9.4 shows the instantaneous contours of turbulent kinetic energy in the mid-plane ( $X - Y$  plane and  $Z = 0$ ). High turbulent kinetic energy is distributed along the air streams of individual swirlers, due to the high velocity gradient between the jet and ambience. On the other hand, low turbulent intensity zones are located within the central recirculation zone of each swirler, where the low mean velocity magnitudes and small velocity gradients give rise to low turbulence levels. In the regions between 5 mm and 20 mm downstream of the chamber inlet, the swirling flows generated by the array interact with each other, causing the maximum levels of turbulence intensity to be distributed along the boundaries between swirlers. As the flow moves downstream,

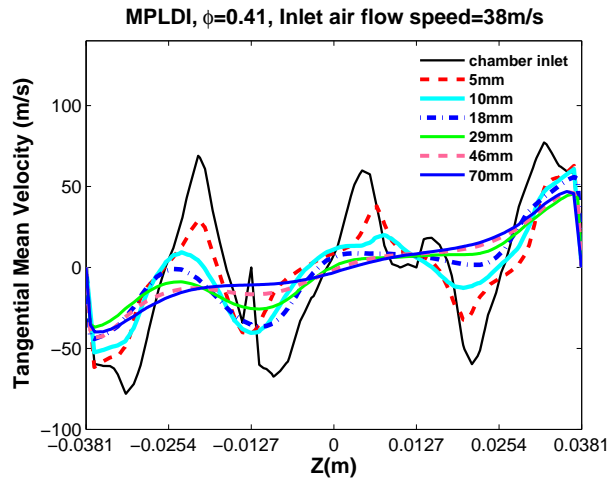


Figure 9.3: Tangential mean velocity profiles (in m/s) at various axial locations in the Y-Z plane)

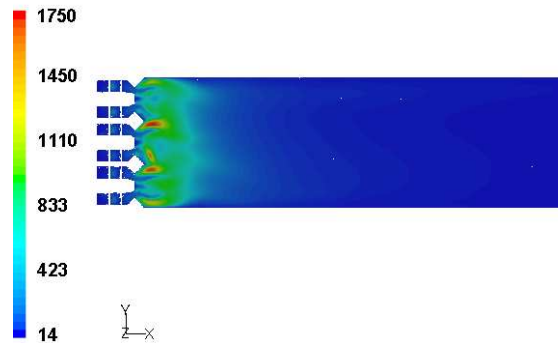


Figure 9.4: Turbulent kinetic energy (in  $m^2/s$ ) in the X-Y ( $Z=0$ ) plane

the turbulence intensity decays rapidly, and the turbulent energy distribution becomes more uniform across the array.

### Temperature Field, OH Mass Fraction, and Fuel Vaporization

Figure 9.5 shows the instantaneous temperature distribution at various axial locations within the combustor. Inside the diverging venturi (see Fig. 9.5(a)), there are relatively high temperature regions at the intersections of fuel and air streams. As the high degree of swirling flow enters the throat of the venturi, it interacts with the fuel stream and the fuel is atomized in the diverging section, resulting in disintegration of fuel stream into droplets. The fuel droplets evaporate and mix with the incoming air stream. This fuel-air mixing process continues up to a few millimeters downstream of the chamber inlet before a combustible mixture is produced. Therefore, the di-

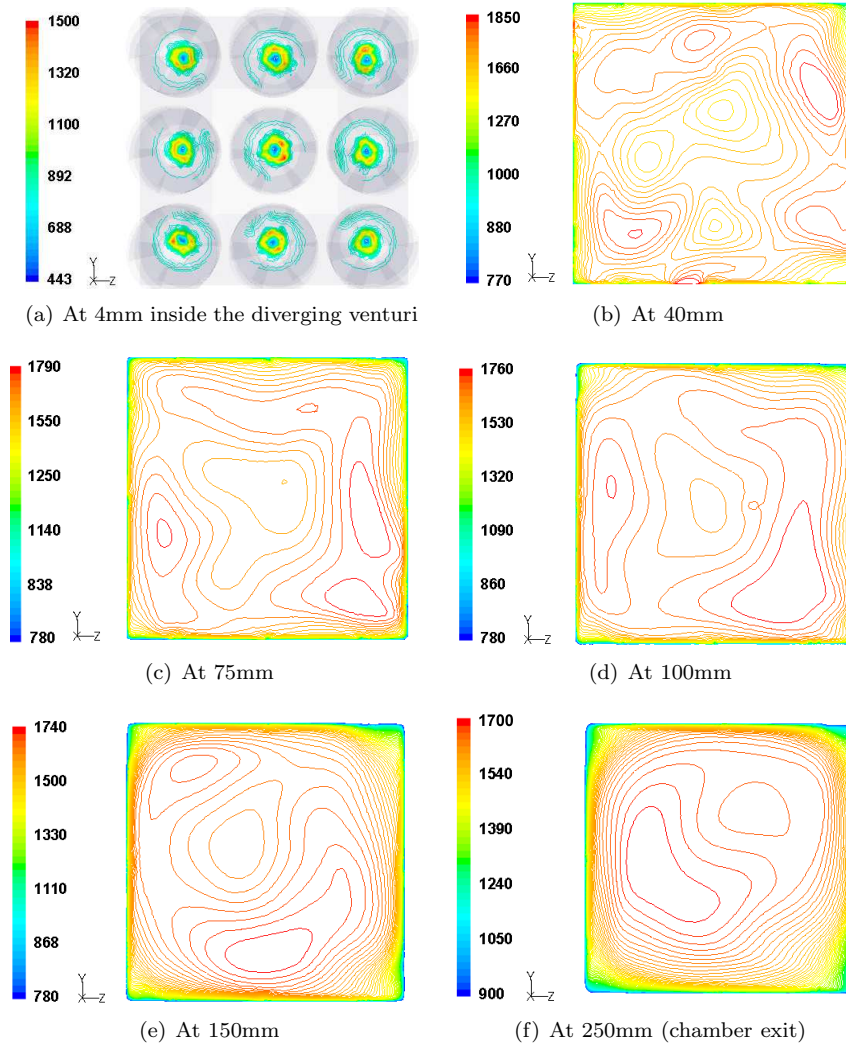


Figure 9.5: Instantaneous temperature (in K) contours in the Y-Z plane

verging venturi acts like a premixed section to some extent and the temperatures in this region is essentially lower than the regions downstream where combustion takes place. At 40 mm downstream, the temperature contours (see Fig. 9.5(b)) show higher temperature regions due to combustion in the central portions of individual swirlers, which spread and mix with low temperature regions at the intersection of the swirlers and close to the wall. The highly swirling shear layers generated by the individual swirlers play an important role in merging the different temperature zones. Further downstream, the temperature profiles show a rapid mixing between high and low temperature regimes caused by the unified swirling flow, thereby creating a uniform temperature distribution. In addition to the temperature plots at various axial locations, instantaneous temperature is plotted in the midplane as shown in Fig. 9.6.

The figure illustrates high temperature zones within the flames generated from the individual swirler-injectors.

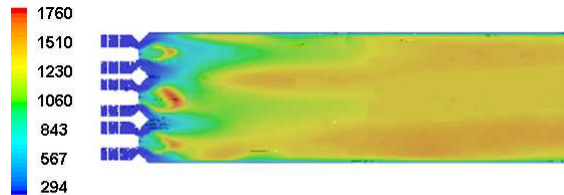


Figure 9.6: Instantaneous temperature profiles (in K) in the midplane

The instantaneous temperature profiles for different axial locations, including the chamber inlet or dump plane and the combustor exit, are plotted together inside the combustor in Fig. 9.7 to demonstrate the temperature variations along the combustor length. The figure exhibits a uniform gas temperature distribution in most of the regions inside the combustor, indicating that an efficient fuel atomization, fuel evaporation, and fuel vapor-air mixing have taken place prior to chemical reactions. In addition to a uniform temperature distribution and an absence of local fuel-rich regions, low instantaneous temperatures are recorded. At the chamber exit, the difference between the maximum temperature and the instantaneous spatial temperature average is small, leading to a small burner pattern factor index. The calculated burner pattern factor value is 0.07.

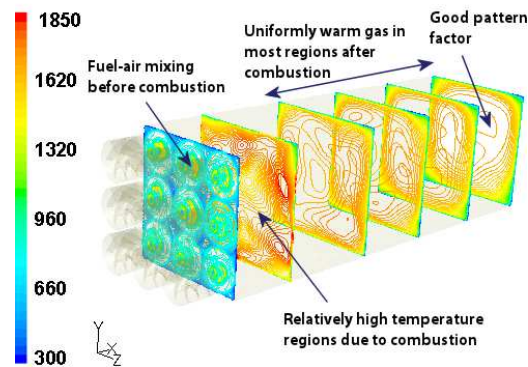


Figure 9.7: Perspective view of the MPLDI illustrating temperature profiles (in K) at various locations inside the combustor

Figure 9.8 shows strain-rate contours at two axial locations in the mixing flow field. Inside the diverging venturi, the flow is highly strained at the intersections where the fuel and air mix (see Fig. 9.8(a)), leading to an increase in mixing rates. The high strain rates in this region are due to the large velocity gradients resulting from the strong incoming swirling air flows from individual swirlers which increase the relative velocity between the liquid to be atomized and the surrounding air. At the chamber

inlet, the flow is also highly strained at the intersections where the fuel spray and the air/gas stream interact. In addition, high strain-rates are noticed at the boundaries between swirlers, signifying that the flow field has high fluid shear and large velocity gradients which result in an increase in fluid mixing rates and bulk transport rates.

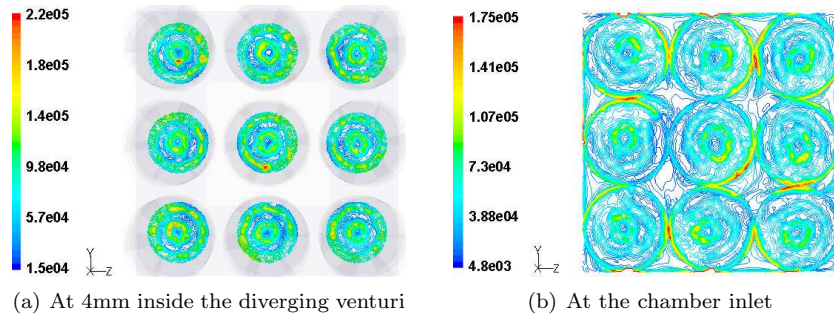


Figure 9.8: Instantaneous strain rate (in 1/s) contours in the Y-Z plane

Figure 9.9 shows the OH mass fraction distribution in the mid-plane ( $X - Y$  plane and  $Z = 0$ ), indicating that a short flame emanates from each injector, with the center one being relatively wider. The short flames reduce residence times in the flames. The average flame length is about 17% shorter than its single element counterpart.

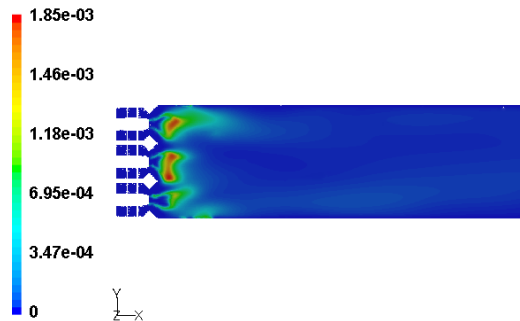


Figure 9.9: OH mass fraction distribution in the X-Y ( $Z=0$ ) plane

Figure 9.10 displays the contours of mixture fraction distribution in the mid-plane ( $X - Y$  plane and  $Z = 0$ ). The distribution shows where the vaporized fuel exists in the gas phase. It is significant in the fuel-rich portions of the flame. The small regions of fuel vapor close to individual injectors suggest that the vaporized fuel rapidly mixes with the oxidizer before undergoing chemical reactions.

To illustrate the fuel vaporization process inside the combustor, the vaporization rate contours (see Fig. 9.11) are plotted in the mid-plane ( $X - Y$  plane and  $Z = 0$ ). The vaporization rate is large only in the vicinity of the injector exits and on the circumferences of the hollow conical sprays. The fuel drop trajectories essentially

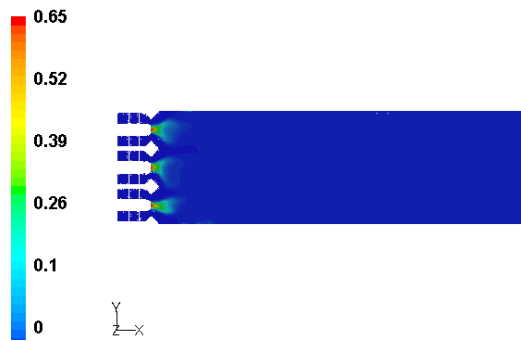


Figure 9.10: Mixture fraction distribution in the X-Y ( $Z=0$ ) plane

terminate when vaporization is finished. Figure 9.11 indicates that the liquid drops have traveled only a short distance from their initial injection location.

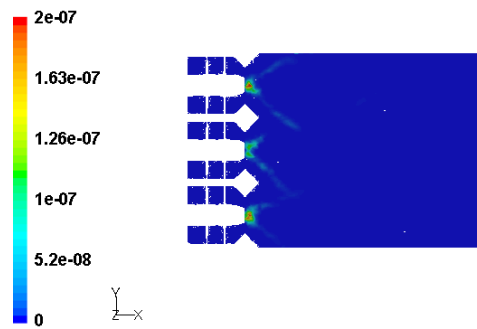


Figure 9.11: Liquid fuel vaporization rate (in kg/s) distribution in the X-Y ( $Z=0$ ) plane

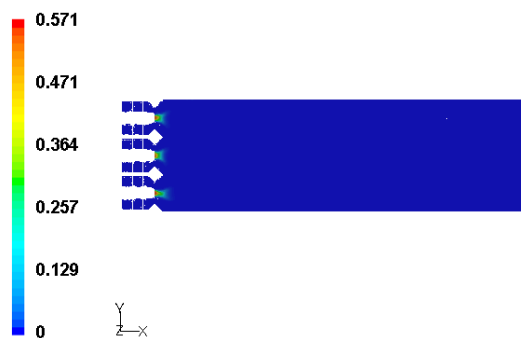


Figure 9.12:  $C_{12}H_{23}$  mass fraction distribution in the X-Y ( $Z=0$ ) plane

The species concentration distribution for kerosene ( $C_{12}H_{23}$ ) is plotted in the mid-

plane ( $X - Y$  plane and  $Z = 0$ ) of the combustor as shown in Fig. 9.12. The predicted  $C_{12}H_{23}$  mass fractions are low, because the vaporized fuel is rapidly converted into other chemical species.

### Spray Drop Distribution

Figure 9.13 illustrates the radial distribution of the arithmetic mean diameter (AMD),  $D_{10}$ , at various axial locations in the Y-Z plane. The plots are shown for only one half of the combustion chamber. In all the planes, the  $D_{10}$  profiles in the radial direction are nearly identical, and no distinct peak is observed. Furthermore, for each plane, the variations in the magnitudes of drop mean diameter are small along the radial direction. In other words, the size distribution of drops is uniform, due to the strong effect of the swirling shear layers and the complex flows generated from the swirler array at the boundaries of the individual swirlers. The distribution of  $D_{10}$  is markedly different from that of the single-element LDI (see Fig. 7.5), in which spray drops are influenced only by the incoming swirling flow generated from a single swirler. Figure 9.13 also shows that the magnitude of  $D_{10}$  increases with increasing axial distance.

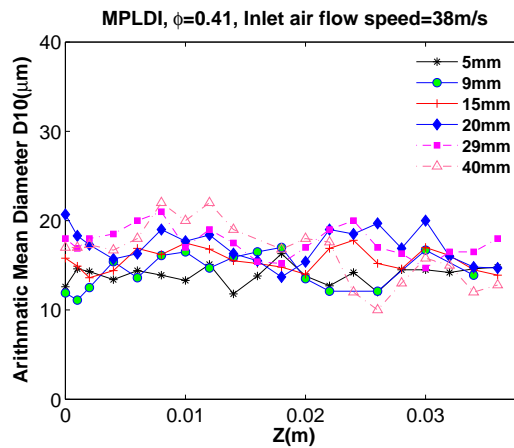


Figure 9.13: Radial profiles for  $D_{10}$  distribution in different axial planes

This is attributed to evaporation of small drops and coalescence of drops. This trend continues up to 20 mm downstream. Further downstream, the heat release due to combustion accelerates the vaporization of liquid drops, resulting in a decrease in mean drop diameters. The  $D_{10}$  magnitudes in the axial direction vary between  $12\mu\text{m}$  and  $21\mu\text{m}$ , with most of the drops have  $D_{10}$  values ranging from  $15\mu\text{m}$  to  $18\mu\text{m}$ , signifying the presence of a large number of small drops in the flow field. On the contrary, in the single-element reacting flow, the AMDs of spray drops vary between  $15\mu\text{m}$  and  $60\mu\text{m}$  (see Fig. 7.5(b)), with a majority of the drops have  $D_{10}$  magnitudes ranging from  $35\mu\text{m}$  to  $55\mu\text{m}$ .

Figure 9.14 shows the radial distribution of the Sauter mean diameter (SMD),  $D_{32}$ , at various axial locations in the Y-Z plane. The  $D_{32}$  profiles illustrate the features similar to the profiles for  $D_{10}$  distribution. The variation in the magnitudes of SMD is small in

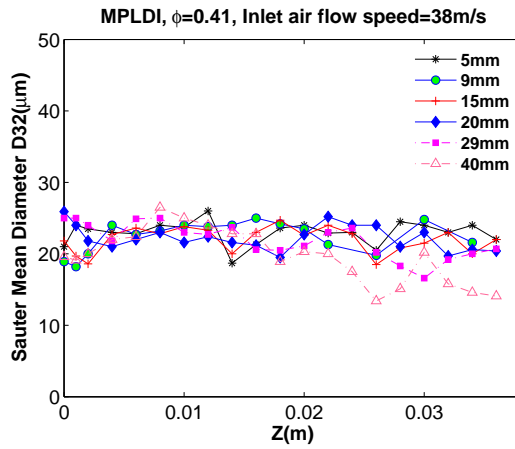


Figure 9.14: Radial profiles for  $D_{32}$  distribution in different axial planes

both radial and axial directions, further indicating a uniform dispersion of small drops in the MPLDI combustor. The SMDs of spray drops vary between  $15\mu\text{m}$  and  $25\mu\text{m}$ . However, a large number of drops have SMDs between  $18\mu\text{m}$  and  $22\mu\text{m}$ . The SMD profiles in the axial planes are more uniform when compared with the single-element SMD profiles in the corresponding planes (see Fig. 7.6). Furthermore, comparing with the single-element LDI,  $D_{32}$  magnitudes are much lower in the MPLDI, owing to the higher relative velocities between the air/gas and spray drops which result in stronger drop breakup.

The main differences in spray drop distribution between the MPLDI and single-element LDI are as follows.

MPLDI	Single-element LDI
Smaller drops are obtained.	Relatively large drops are obtained.
The ranges in which both $D_{10}$ and $D_{32}$ vary are small.	The mean diameter ranges are much wider.
The mean diameter profiles are mostly uniform along the axial and radial directions.	The mean diameter profiles are not smooth. Distinct diameter peaks are observed.

A rapid fuel-air mixing within the MPLDI is achieved by an efficient fuel atomization technique and fuel drop dispersion into the gas stream. The complex array of swirlers plays an important role in this mixing process. As shown in Fig. 9.15, the flow field in the vicinity of the chamber inlet becomes highly complex and instationary, due to the presence of vortical structures, such as precessing vortex cores (PVC) and vortex breakdown bubbles (VBB). The figure also illustrates the pathlines of the swirling flows generated from individual swirlers and the predicted spray drops of different sizes, suggesting that the vortex structures strongly interact with the spray drops. Precessing motion of the gas entrains the liquid drops, thus the PVCs

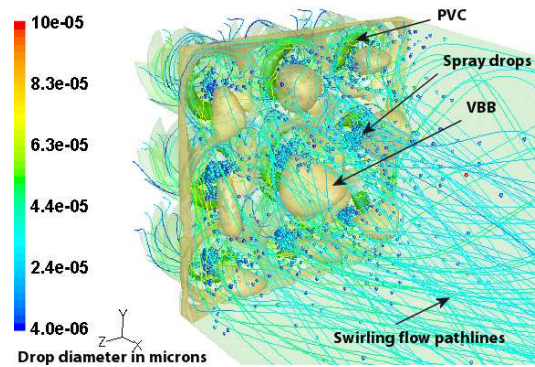


Figure 9.15: Interactions among swirling flows, PVC, VBB, and spray drops

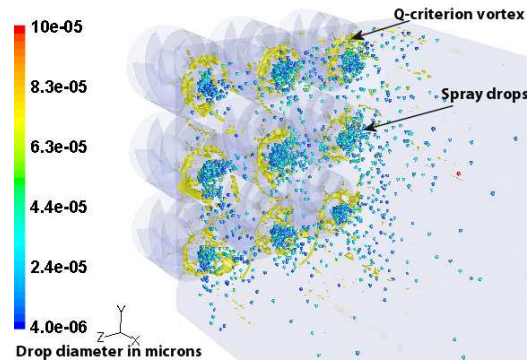


Figure 9.16: Interactions between Q-vortex and spray drops inside the combustion chamber

play an effective role in their dispersion. Figure 9.16 displays the instantaneous iso-surfaces of the Q-criterion vortex and the spray drops within the combustor, which also indicates the interactions between the vortex structures and drops. The highly complex and swirling flows generated from the swirler array and the motion of the coherent vortical structures influence the spray drop dispersion, resulting in a uniform drop size distribution and good mixing within the combustor.

### B. Case 2: $\phi = 0.41$ , Inlet flow velocity=20.14 m/s

In this case, the mixture equivalence ratio remains the same as in Case 1. However, the inlet air velocity is reduced to 20.14 m/s to study the effects of low swirling flow speed on the reacting spray. The fuel flow rate through each injector is set to 0.0832 g/s.

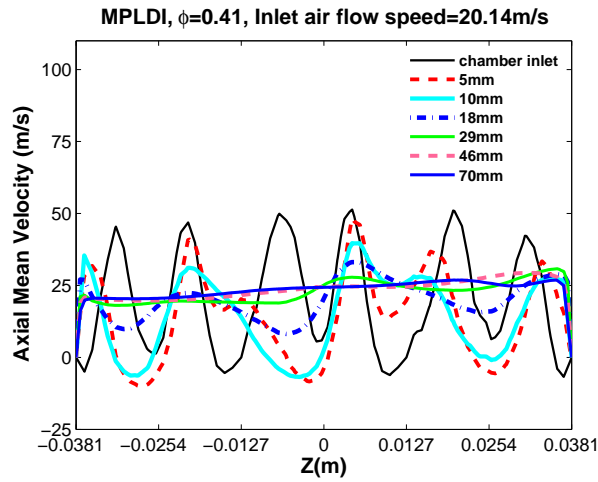


Figure 9.17: Axial mean velocity profiles (in m/s) at various axial locations in the Y-Z plane)

### Velocity Field

Figure 9.17 shows the axial mean velocity profiles at various axial locations for the three swirlers located in the center plane ( $Y = 0$ ). The basic features of the axial velocity profiles mostly resemble the features predicted in Case 1 (see Fig. 9.1).

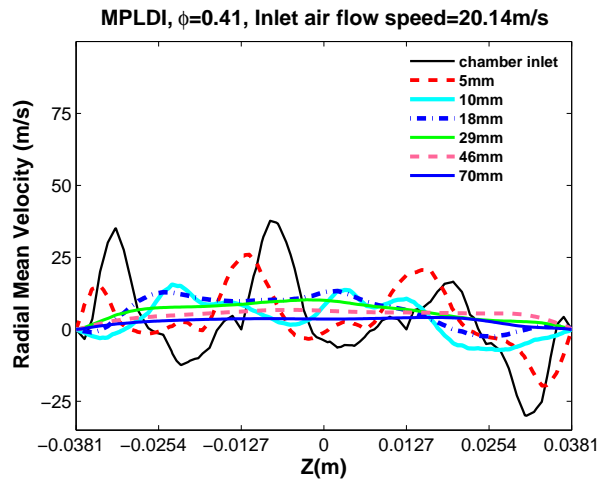


Figure 9.18: Radial mean velocity profiles (in m/s) at various axial locations in the Y-Z plane)

However, in the regions close to the dump plane, vast disparities in the velocity magnitudes are noticed between the two cases. For instance, at the chamber inlet,

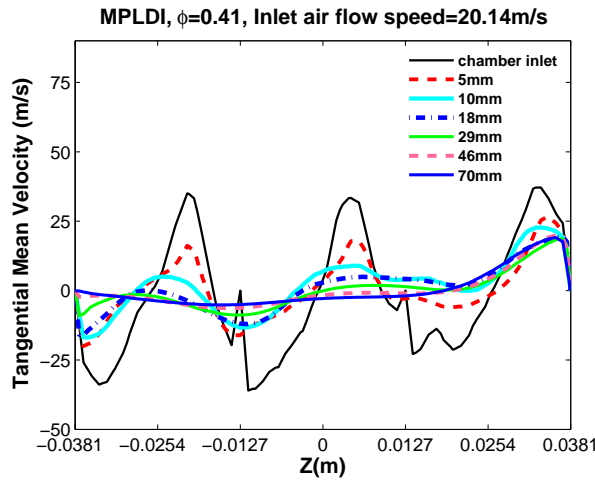


Figure 9.19: Tangential mean velocity profiles (in m/s) at various axial locations in the Y-Z plane)

the peak axial mean velocity of the central swirler in the present case is about 50 m/s, while the peak axial velocity of the central swirler in Case 1 is about 105 m/s. At 5 mm and 10 mm downstream, the central recirculation zones are narrower with lower strengths when compared with Case 1. Further downstream, the axial velocities decay more rapidly. At 70 mm downstream, the axial velocity profile becomes flat with an average velocity of 21 m/s. The radial (see Fig. 9.18) and tangential mean velocity (see Fig. 9.19) profiles also exhibit similarities with the corresponding velocity profiles in Case 1, but the magnitudes and gradients of velocities are comparatively low in Case 2. This is attributed to the low Reynolds number flow through the swirlers and the resulting low turbulent kinetic energy distribution along the air streams from individual swirlers and low levels of turbulence intensity along the boundaries between swirlers.

### Temperature Field

Figure 9.20 shows the predicted instantaneous temperature distribution at different axial locations within the combustor. When compared with the temperature plots of Case 1, some major differences are noticed. First, in the regions where the fuel-air mixing takes place prior to forming a combustible mixture, temperatures at the intersections of fuel and air streams are relatively low. For instance, at 4 mm inside the diverging venturi, the peak instantaneous temperature is 1370 K (see Fig. 9.20(a)), whereas in Case 1, the peak temperature in the same region is about 1500 K (see Fig. 9.5(a)). This is attributed to the low incoming swirling flow speed and low relative velocities between the air and fuel streams in Case 2, leading to a reduced fluid shear at the intersections of the two fluid streams. On the other hand, in Case 1, due to a relatively high incoming flow velocity, the velocity gradients and the relative velocities between the air and fuel streams are large, resulting in high flow strain rates

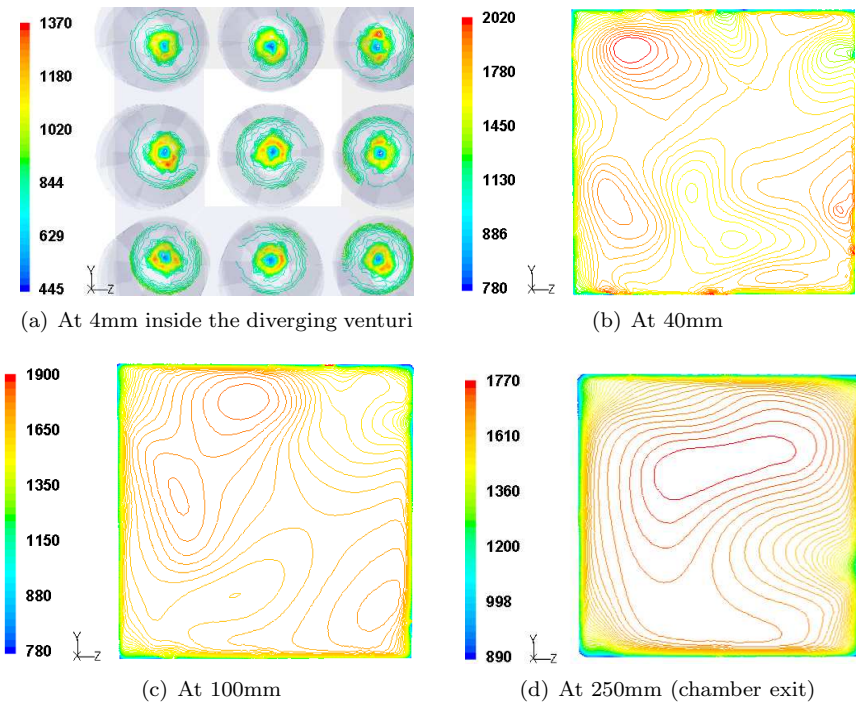


Figure 9.20: Instantaneous temperature (in K) contours in the Y-Z plane

and rapid mixing. Therefore, by increasing incoming swirling flow speed, the mixing

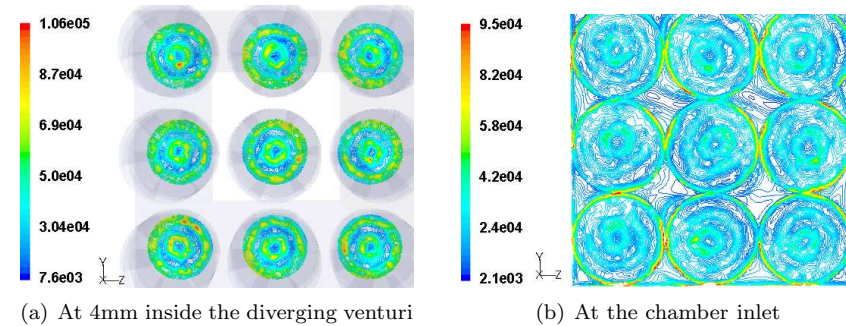


Figure 9.21: Instantaneous strain rate (in 1/s) contours in the Y-Z plane

process is expedited in Case 1, when compared with Case 2. As the flow moves downstream, combustion takes place. The peak temperature due to combustion is about 9.3% higher than in Case 1. In addition, it is noticed that the mixing between the various temperature regimes is not as quick as in the previous case, resulting in local high temperature regions and a delay in attaining a uniform temperature profile downstream. At the exit, a good temperature distribution is obtained, but the average

temperature is higher than in Case 1.

Figure 9.21 illustrates the instantaneous flow strain rate contours at two locations in the mixing flow field. In comparison with Case 1 (see Fig. 9.8), the predicted average strain rate value is 51.6% lower within the diverging venturi where fuel-air mixing most actively takes place along the interface between the two fluids. On the other hand, in the chamber inlet plane, Case 2 records 39% lower average flow strain rate at the boundaries between the swirlers compared to the average strain rate value in Case 1. The low fluid shear is attributed to small velocity gradients of the incoming swirling flows and low relative velocities between the fuel and air flow streams.

### Spray Drop Distribution

Figures 9.22 and 9.23 illustrate the predicted radial distribution of the AMD and SMD at various axial locations in the Y-Z plane, respectively. When compared with

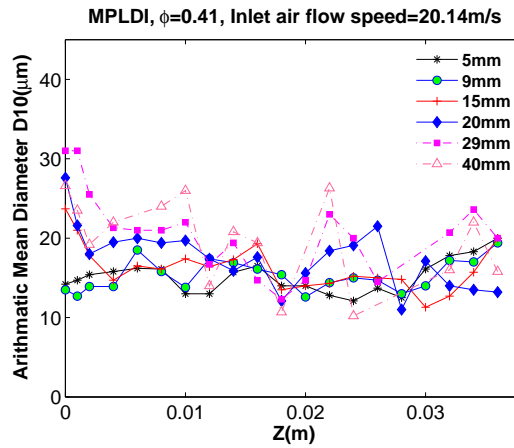


Figure 9.22: Radial profiles for  $D_{10}$  distribution in different axial planes

the AMD and SMD distributions at the corresponding locations in Case 1, some major differences are noticed. Both the AMD and SMD distributions in the radial directions are not as uniform as they are in the previous case, owing to the lower gas velocity. The swirl velocities are not strong enough to rapidly disperse the spray drops into the gas flow. Furthermore, the weak swirl velocities have less impact on spray drop breakup and collision, leading to the formation of moderately large-sized drops. The ranges over which the mean drop diameters AMD and SMD vary are  $12 - 30 \mu\text{m}$  and  $11 - 32 \mu\text{m}$ , respectively. In comparison with Case 1, the AMD and SMD distribution ranges are extended by 70% and 91%, respectively. However, the mean diameter distributions of spray drops in this case are more uniform compared to the distributions in the single-element LDI (see Figs. 7.5 and 7.6). In addition, the average drop size is smaller than in the single-element LDI. These characteristics are attributed to the inter-swirler mixing within the combustion chamber and the resulting increased velocity gradients along the boundaries of the swirlers.

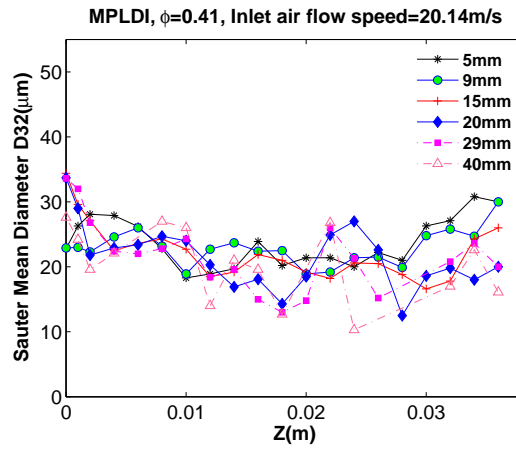


Figure 9.23: Radial profiles for  $D_{32}$  distribution in different axial planes

### C. Case 3: $\phi = 0.46$ , Inlet flow velocity=38 m/s

In this case, the mixture equivalence ratio is raised to 0.46 to study the effects of increasing equivalence ratio on spray combustion in the MPLDI. The inlet air flow velocity is 38 m/s, which is the same for Case 1. The fuel flow rate through each injector is 0.176 g/s.

#### Velocity Field

Figures 9.24-9.26 illustrate the axial, radial, and tangential mean velocity profiles of the three swirlers located in the center plane ( $Y = 0$ ). The mean velocity profiles display similarities with Case 1 (see Figs. 9.1-9.3), in terms of both the predicted flow features and the velocity magnitudes. On the other hand, the components of mean velocities and its gradients are fairly high close to combustion chamber when compared with Case 2 (see Fig. 9.17-9.19). The high tangential velocities indicate the presence of a large degree of swirling flow generated by the swirler array.

#### Temperature Field

Figure 9.27 shows the predicted instantaneous temperature distributions at different axial locations within the combustor. The magnitudes of temperature are higher at all locations when compared with the temperature profiles at the corresponding locations in Case 1. This is attributed to the higher equivalence ratio which increases the temperatures after combustion. Similar to the previous two cases, the exit temperature is uniform. However, the average exit temperature is about 4% higher than in Case 1.

Figure 9.28 illustrates strain rate plots at two locations in the mixing flow field. The profiles and the magnitudes of fluid strain rate display similarities with Case 1, as

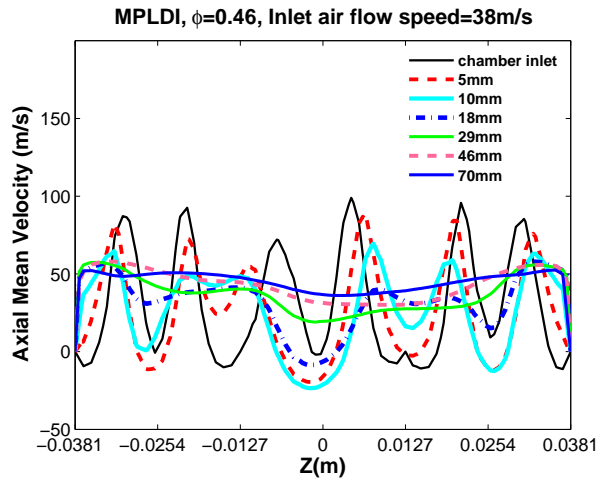


Figure 9.24: Axial mean velocity profiles (in m/s) at various axial locations in the Y-Z plane)

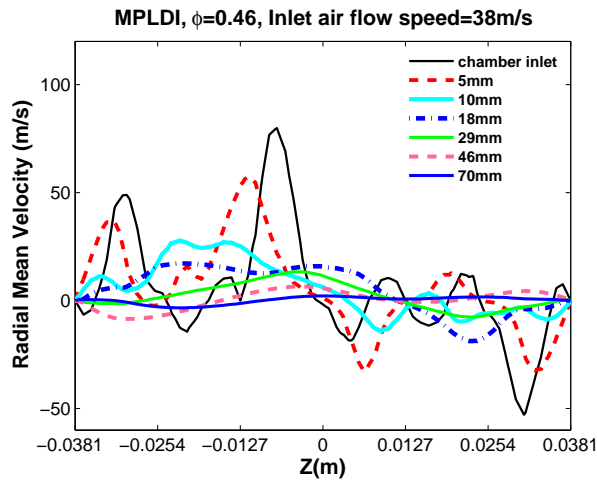


Figure 9.25: Radial mean velocity profiles (in m/s) at various axial locations in the Y-Z plane)

the air mass flow rate is identical in both cases. On the other hand, comparing with Case 2, the magnitudes of fluid shear are much larger at the fuel-air intersections within the diverging venturi, due to higher relative velocities between the air and fuel streams. In addition, fluid shear is high along the boundaries between the swirlers at the chamber inlet, owing to large velocity gradients in the incoming swirling flows generated from the individual swirlers.

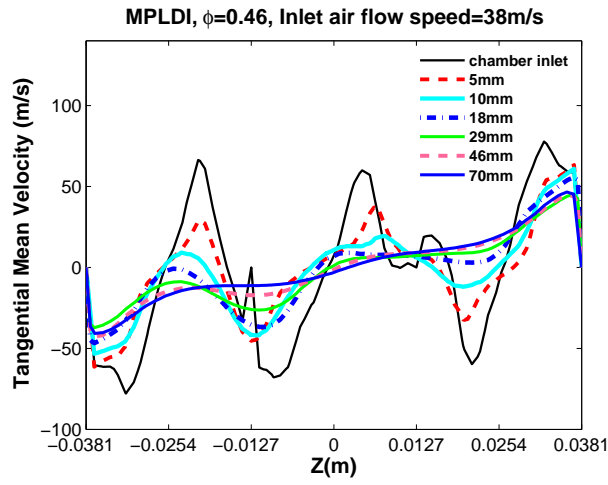


Figure 9.26: Tangential mean velocity profiles (in m/s) at various axial locations in the Y-Z plane)

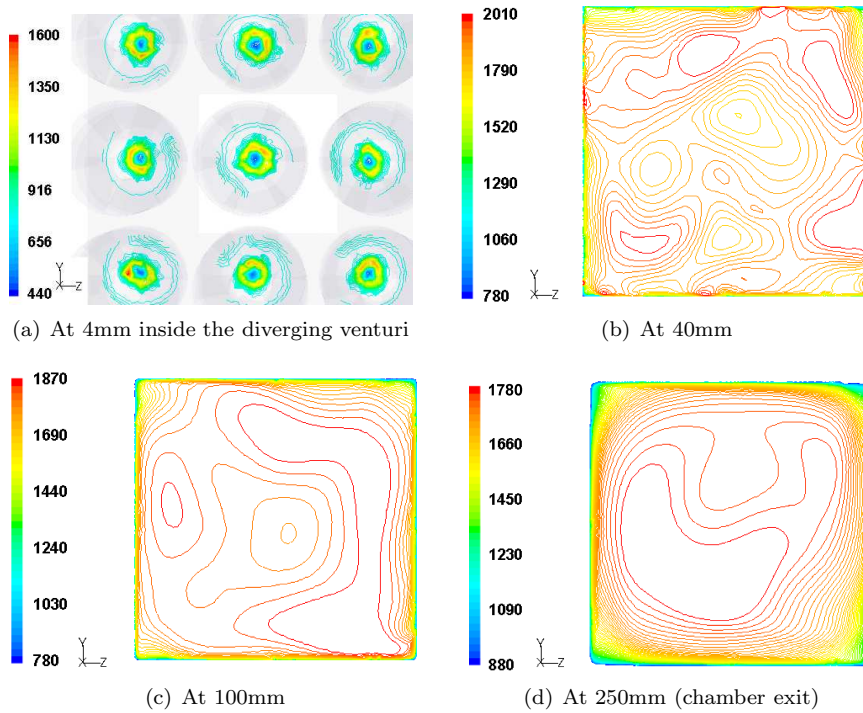


Figure 9.27: Instantaneous temperature (in K) contours in the Y-Z plane

### Spray Drop Distribution

Figures 9.29 and 9.30 depict the radial distributions of the AMD and SMD at various axial locations in the Y-Z plane, respectively. The mean diameter distributions

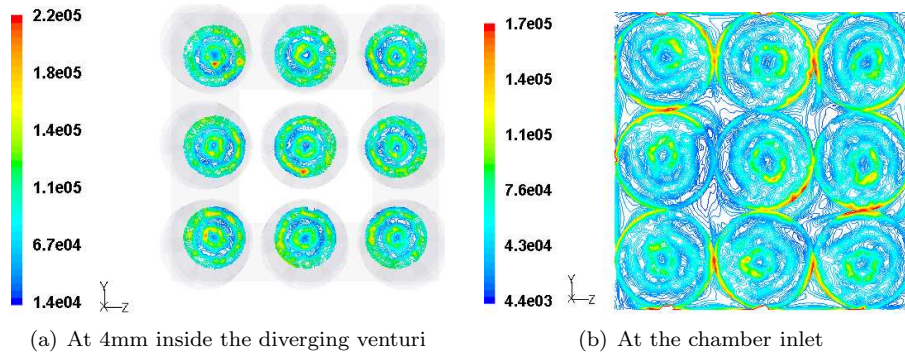


Figure 9.28: Instantaneous strain rate (in 1/s) contours in the Y-Z plane

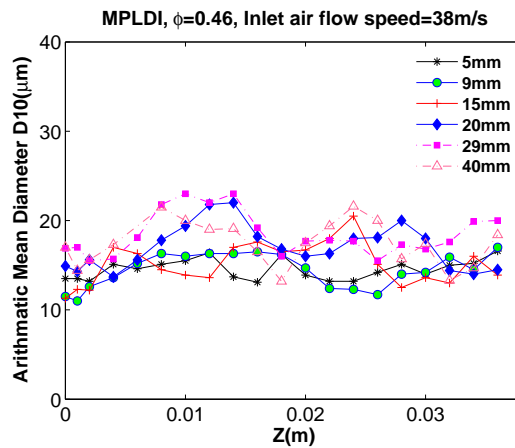


Figure 9.29: Radial profiles for  $D_{10}$  distribution in different axial planes

closely follow the profiles for Case 1 (see Figs. 9.13 and 9.14). Therefore, the explanations provided on the diameter profiles for Case 1 can be applied here to describe the drop size distribution. However, a few differences between the two cases can be noticed in the profiles of  $D_{10}$  and  $D_{32}$ . In Case 2, the ranges of  $D_{10}$  and  $D_{32}$  distributions are 10% and 27% wider than in Case 1, respectively. In addition, the drop mean diameters are larger at several axial and radial locations than the mean diameters at the corresponding locations in Case 1. These differences are attributed to the higher fuel mass flow rate under the same air inlet flow condition, leading to a larger number of fuel drops in the combustor and an increasing amount of collision events.

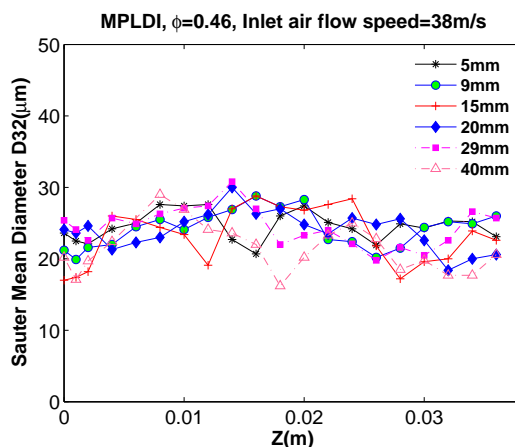


Figure 9.30: Radial profiles for  $D_{32}$  distribution in different axial planes

## 9.5 Concluding Remarks

This chapter reports the computational results of the reacting spray in a Multi-Point Lean Direct Injection (MPLDI) combustor to demonstrate some of its fundamental features that essentially explain its ability to achieve low  $\text{NO}_x$ . In this regard, three cases are studied under different operating conditions. Each case is analyzed and its results are compared with the results of the two other cases. In addition, the reacting spray results of the MPLDI are compared with that of the single-element LDI.

The Discrete Phase Model (DPM) of the Fluent<sup>®</sup> solver is used to simulate the flow field in the combustor. The model implements the Euler-Lagrange approach to describe the two-phase flow. The gas-phase is treated as a continuum and it is calculated by solving the Navier-Stokes equations. The Realizable  $k - \epsilon$  model is used for turbulence modeling. Several sub-models are employed to specify various spray sub-processes in combination with a model for combustion. The liquid-phase is resolved in an unsteady manner by tracking the liquid particles through the calculated flow field.

By analyzing the three cases, it is acknowledged that a high degree of swirling shear layer significantly influences liquid fuel atomization, fuel drop size distribution, drop vaporization, fuel vapor-air and/or gas mixing, and combustion. In addition, the complex array of the air swirler-fuel injector modules has a strong impact on the liquid spray characteristics. The results show that the fuel atomization process starts as soon as the fuel is introduced into the highly swirling air stream, resulting in the development of a hollow conical spray. The atomization process is enhanced with increasing swirl (tangential) velocities, thus producing a large number of small drops. Furthermore, the drop mean diameters and drop size distribution become more uniform along both the axial and radial directions with increasing swirl velocities. In other words, as the strength of the swirl increases, the ranges in which the mean drop diameters (AMD and SMD) vary become narrower. In addition to the highly swirling

shear layer, the geometry of the MPLDI favorably influences both the size of the drops and their distribution. The computations predict the dynamic vortex structures in the gas-phase near the chamber inlet. The rotating motions of these vortices entrain the liquid drops, thus playing an effective role in their dispersion. The small drops, being well dispersed into the flow field, expedite drop vaporization and improve the quality of fuel-air mixture.

The fuel-air mixing process within the MPLDI is quite significant as it determines the performance of the combustor. The results illustrate that the mixing process is predominant in the diverging section of the venturi and it continues up to a few millimeters downstream of the dump plane. However, the mixing length decreases with increasing swirl velocity, since the large number of small drops being produced by the shear breakup process evaporate faster to form a combustible mixture. The incoming highly swirling flow increases the velocity gradients and the relative velocities between the fuel and air streams within the divergent venturi. As a result, the flow field becomes extremely strained at the intersections of the two fluid streams and the liquid surface becomes unstable, due to the growth of surface waves. The unstable growth of surface waves disintegrates the fuel stream into ligaments and then into fine drops. The computations also predict high fluid shear at the chamber inlet, especially along the boundaries between the swirlers, in which the flows from individual swirlers mix with each other. In addition, the large velocity gradients and high turbulent activities are noticed in the vicinity of the dump plane where adjacent swirling flows interact, signifying a strong flow mixing inside the combustor.

The results indicate that the high fluid shear and rapid mixing have a significant influence on the temperature profiles. In the regions of high fluid shear, mixing rates and bulk transport rates are essentially faster than chemical reaction rates. Therefore, the local reactions are not completed before the flow carries the combustion radicals away from the reaction zone. The net result of this process is a reduction in peak flame temperature, which in turn reduces thermal  $\text{NO}_x$  production. On the other hand, a good mixture of fuel and air in the regions upstream promotes a uniform temperature distribution after combustion. In addition, a unified swirling flow in the downstream region assists the higher temperature zones to spread rapidly and mix with the lower temperature zones, thereby eliminating the local hot spots and making a uniform temperature profile within the combustor. The mixture with a low equivalence ratio and high velocity gradients illustrates evenly distributed low temperature regions up to the chamber exit. Nevertheless, all the three cases predict a uniform temperature distribution inside the combustion chamber and in the combustor exit plane.

The reacting flow simulations also predict short flames from the individual injectors, mainly due to the small size of the swirler-fuel injector modules and their complex arrangement in a 3x3 array. The short flames reduce the residence times in the flames.

In conclusion, the improved fuel-air mixing, due to highly swirling flows and the complex swirler array, diminishes the possibility of non-uniform combustion caused by direct fuel injection. In addition, the small swirlers reduce the required combustor length to have complete fuel-air mixing. As a consequence, the MPLDI concept decreases the combustion zone temperature and the flow residence time, thereby lowering the  $\text{NO}_x$  emissions.

## 10. Conclusions

*I think and think for months and years. Ninety-nine times, the conclusion is false. The hundredth time I am right.*

Albert Einstein

The main conclusions of this dissertation are discussed in this chapter. In addition, the chapter presents possible future research directions, based on the current work status.

This thesis has presented a detailed numerical analysis of the flow field in Lean Direct Injection (LDI) combustors, which explains its underlying features that are primarily responsible for the measured low  $\text{NO}_x$  emissions as reported in the literature. A single-element LDI and a Multi-Point LDI (MPLDI) configuration were investigated. Simulations were carried out in two stages. In the first stage, non-reacting cold flow calculations were performed in order to study the aerodynamic characteristics of the flow associated with the LDI combustors. In the second stage, reacting flow simulations were conducted for the two configurations to investigate the respective characteristics of liquid and gas phases, interactions between the gas-phase turbulence and spray drops, and the combustion process. In all cases, the flow field was resolved for the entire geometry, including the inlet flow paths through the swirl vanes and the combustion chamber. The results were validated with the available measurement data.

The non-reacting cold flow simulation for the single-element LDI was carried out using the Unsteady Reynolds-averaged Navier Stokes (URANS) code with the realizable  $k - \varepsilon$  and the Reynolds stress turbulence models. The results exhibited that the numerical code could predict the essential flow features of the LDI combustor, such as the complex swirling flow structures inside the swirler passages, the single large recirculation zone near the tip of the fuel injector, and the reverse flow regions at the corners of the chamber wall and on the wall of the diverging venturi, with good accuracy. The calculated mean and turbulent velocity components at various axial locations are in good agreement with the measurements. High tangential velocities were predicted at all the computed locations, including the regions far downstream, signifying the presence of a large degree of swirl inside the combustor. In the vicinity of the injector and the combustion chamber inlet, the results showed very high magnitudes of turbulent velocities. However, the fluctuation levels of the RMS velocity components displayed a significant amount of variation close to the dump plane of the combustor, indicating the non-isotropic Reynolds stress distribution induced by

the highly swirling flow.

The URANS and large eddy simulation (LES) methodologies were applied separately to characterize the non-reacting flow field in the MPLDI combustor. The computed results captured the compact recirculation zone generated by each of the nine air swirlers. The velocity magnitude close to the chamber inlet and the length and volume of the nine recirculation zones predicted by the LES scheme differed significantly from that of the URANS scheme. The differences were attributed to the limited capability of URANS in resolving the flow field with strong turbulence and a high degree of swirl. Nevertheless, the predicted axial mean velocity structures and the vector orientation obtained from the two methods displayed similarities. Farther downstream, the LES and URANS calculations showed identical flow structures with almost the same velocity magnitude. The LES results depicted the dynamic behavior of large scale turbulent structures such as the precessing vortex cores (PVC) and vortex breakdown bubbles (VBB), thus indicating a large degree of unsteadiness in the flow field. Overall, the numerical predictions for the mean velocity field and flow structures showed good agreement with the experimental data.

The numerical simulations of the reacting spray in the LDI combustors involved the modeling of several spray sub-processes and the combustion of the fuel-air mixture. The sub-processes include drop breakup, drop drag and distortion, turbulent dispersion of spray, drop collision and coalescence, and liquid spray evaporation. The Euler-Lagrange approach was implemented to resolve the two-phase flow. The gas-phase was treated as a continuum, which was calculated by solving the Navier-Stokes equations. The spray computations were performed by applying the unsteady particle tracking method. The simulations of the single-element LDI showed a significant influence of spray on the gas-phase velocity distribution. In contrast to the non-reacting flow, the high axial momentum induced by combustion and momentum transfer between the liquid and gas phases decrease the length and volume of the central recirculation zone in the reacting flow. The heat release due to combustion resulted in a stronger recirculation region in comparison with its non-reacting counterpart. The drop mean diameter distributions and spray velocity profiles indicated that the smaller drops tended to follow the gas flow path, while the larger drops retained their original momentum due to high inertia. The numerical results for both the gas-phase and liquid spray exhibited a good accuracy when compared with the measurements.

The reacting spray simulations for the MPLDI demonstrated that the complex array of air swirler-fuel injector modules had a strong impact on the liquid spray characteristics. The results showed that by increasing the swirl velocity, a large number of small liquid drops were produced, thereby enhancing the fuel atomization and fuel-air mixing processes. The drop mean diameters and drop size distribution were found to be more uniform along both the axial and radial directions with increasing swirl velocities. The complex geometry of the MPLDI also played an important role in the drop distribution process. This is in contrast to the drop size distribution profiles for the single-element LDI, in which distinct mean diameter peaks are visible along the axial and radial directions. The rotating motion of the vortex structures (PVC and VBB) in the vicinity of the injectors further enhances the drop dispersion into the gas, thereby expediting drop vaporization and improving the mixture quality.

In the MPLDI reacting flow, it was illustrated that the mixing between fuel vapor

and air was predominant in the diverging venturi and it continued only up to a few millimeters downstream of the chamber inlet. The mixing length was decreased with increasing swirl velocity, because a large number of small drops produced by the shear breakup process evaporate rapidly to form a combustible mixture. The results showed that the incoming highly swirling flow increased the velocity gradients and the relative velocity between the fuel and air streams within the diverging nozzle, leading to a highly strained flow field at the intersections of the two fluid streams. Consequently, the growth of the surface waves made the liquid surface very unstable and the fuel streams disintegrated into ligaments and then into fine drops. The computed results were also able to predict high fluid shear and large velocity gradients near the chamber inlet, especially along the boundaries between the swirlers, in which the flows from individual swirlers mix with each other, signifying a strong flow interaction inside the combustor.

The results further showed that the high fluid shear and rapid mixing influenced the instantaneous temperature profiles. The peak temperature was reduced with increasing fluid shear. This was attributed to the faster mixing rates induced by the high strain and fluid shear, which would not allow the local reactions to go to completion before the flow carried the combustion radicals away from the reaction zone. It was found that the unified swirling flow downstream of the reaction zone aided the higher temperature zones to rapidly spread out and mix with the lower temperature zones, thereby eliminating the local hot spots and making a uniform temperature profile inside the combustor. The simulations illustrated that the mixture with a low equivalence ratio and high velocity gradients produced a uniformly low temperature distribution in almost the entire volume of the MPLDI combustion chamber. At the chamber exit, the difference between the maximum temperature and the instantaneous spatial temperature average is small, leading to a small burner pattern factor index.

The OH mass fraction distribution in the MPLDI combustor illustrated short flames from the individual injectors, due to the presence of relatively small swirler-fuel injector modules and their complex arrangement upstream of the combustion chamber. The MPLDI simulations predicted much shorter flames than the flame generated from the single-element LDI. By restricting the flames to a short region, the residence time within the flames is reduced significantly. The short residence time at peak temperature keeps the vast majority of nitrogen in flue gas from becoming ionized.

Therefore, it can be concluded that the improved fuel-air mixing, due to highly swirling flows and the complex swirler-fuel injector array, decreases the possibility of non-uniform combustion caused by direct fuel injection. The small swirlers reduce the mixing length that is required to achieve a complete fuel-air mixing, resulting in a shorter combustor. This decreases the flow residence time, leading to low  $\text{NO}_x$ . Overall, the MPLDI flow field simulations illustrated low flame temperatures, rapid fuel vaporization and fuel-air mixing, short flame and flow residence times, and uniformly warm temperature distribution without local hot spots. All these features contribute to a significant reduction in the  $\text{NO}_x$  emissions. The results prove that the MPLDI concept has the potential to become the low  $\text{NO}_x$  combustion scheme for future aviation gas turbines.

## Contribution of the Thesis to the State-of-the-art

This thesis proposes an essential guideline on the numerical models and the solution strategies required to simulate the complex flow field in the LDI combustors. The study successfully captures the underlying features of the LDI technique, which offer a physical insight into the dynamics of the mixing and spray combustion processes, and in turn, help to understand how LDI is able to achieve low  $\text{NO}_x$ . The contribution of this dissertation to the state-of-the-art are listed below.

State-of-the-art	Thesis contribution
1) Only the reacting flow field for single-element LDI was numerically modeled. 2) Temperature profiles for MPLDI were not reported.  3) Non-reacting cold flow within the baseline MPLDI geometry was not studied in detail. 4) PVC, VBB, and Q-criterion vortex for MPLDI were not described.	1) Two-phase flow for both single-element LDI and MPLDI is modeled. 2) Temperature profiles for MPLDI are studied under various initial flow conditions . 3) Non-reacting cold flow for the baseline MPLDI is analyzed by using the URANS and LES methodologies. 4) Computational results capture PVC, VBB, and Q-criterion vortex and their interactions with the swirling flow field in MPLDI.

## Future Research Perspectives

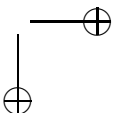
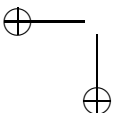
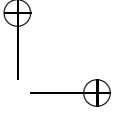
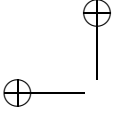
On the basis of the present research and its outcomes, a few possible future research directions can be proposed. First, this work can be extended further to analyze the flow field at higher operating pressures. Both the gas and liquid phases need to be studied explicitly in order to evaluate the effect of higher combustion chamber pressure on spray characteristics and combustion process.

In this study, only the Non-Premixed model combined with the mixture fraction- $\beta$  PDF approach was applied to simulate the combustion process and no other combustion model was tested. However, as a part of future work, other available numerical models for combustion can be examined to study the performances of individual combustion models when applied in combination with the spray sub-models. In addition, the coupling between the two phases for each combustion model must be studied.

In the present study, the reacting spray simulations were performed using the Fluent<sup>®</sup> solver, which has limitations in using the Discrete Phase Model (DPM) with the LES methodology. As a result, only the RANS code was examined while implementing the DPM for spray calculations. However, scalar mixing and combustion processes generally occur at small scales that are not typically resolved in the RANS code. Therefore, to obtain the additional details on sub-grid scale mixing, inter-phase exchange, and turbulent combustion, LES has to be applied with the spray models by using an advanced solver.

In the current work,  $\text{NO}_x$  was not modeled during the simulations. The  $\text{NO}_x$  characteristics were only determined from the calculated flow field. Nevertheless, in order to make more precise  $\text{NO}_x$  estimations, a dedicated model needs to be incorporated and the results have to be validated with the measurements. Furthermore, the computed  $\text{NO}_x$  can be compared with the  $\text{NO}_x$  data calculated from the  $\text{EINO}_x$  correlation developed for the baseline MPLDI combustor.

The simulations of the MPLDI showed that the mixing of the fuel and air could be improved by increasing flow strain rate, which is generally obtained by increasing the air jet velocities and/or the relative velocity between the fuel and air streams. However, this will also cause an increased combustor pressure drop. In addition, the static stability of the flame is a strong function of the incoming velocities of the fuel and air jets. If the incoming air velocity is too high, it may result in flame blowout. Therefore, flame stability concerns impose limits on allowable levels of strain rate and fluid shear. As a future work, it may be important to determine an injector configuration that maximizes flame strain while minimizing flame stability and combustor pressure drop concerns.



## Bibliography

- [1] J. E. Penner, D. H. Lister, D. J. Griggs, D. J. Dokken, and M. McFarland. *Aviation and the Global Atmosphere - A Special Report of IPCC working Groups I and III*. Cambridge University Press, U.K., 2000.
- [2] S. C. Herndon, J. H. Shorter, M. S. Zahniser, D. D. Nelson, J. Jayne R. C. Brown, R. Miake-Lye, I. Waitz, P. Silva, T. Lanni, K. Demerjian, and C. E. Kolb. NO and NO<sub>2</sub> emission ratios measured from in-use commercial aircraft during taxi and takeoff. *Environ. Sci. and Tech.*, 38(22):60786084, 2004.
- [3] M. Gauss, I. S. A. Isaksen, D. S. Lee, and O. A. Sovde. Impact of aircraft NO<sub>x</sub> emissions on the atmosphere tradeoffs to reduce the impact. *Atmos. Chem. Phys.*, 6:15291548, 2006.
- [4] P. J. Crutzen. The influence of nitrogen oxides on atmospheric ozone content. *Q. J. R. Meteorol. Soc.*, 96:320–325, 1970.
- [5] A. H. Lefebvre. *Gas Turbine Combustion*. Taylor & Francis, 2<sup>nd</sup> edition, 1998.
- [6] N.K. Rizk and H.C. Mongia. A three-dimensional analysis of gas turbine combustors. *AIAA J. Prop. Power*, 7(3):445–451, 1991.
- [7] G. L. Leonard and S. M. Correa. NO<sub>x</sub> formation in lean premixed high- pressure methane flames. *2<sup>nd</sup> ASME Fossil Fuel Combustion Symposium*, 30:69–74, 1990.
- [8] C.-M. Lee, K. M. Tacina, and C. Wey. High pressure low NO<sub>x</sub> emissions research: Recent progress at NASA Glenn Research Center. ISABE-2007-1270. ISABE, 2007.
- [9] S.A. Mosier and R.M. Pierce. Advanced combustor systems for stationary gas turbine engines: Vol. 1. Review and preliminary evaluation. Technical Report EPA-600/7-80-017a, U.S. Environmental Protection Agency, 1980.
- [10] D.W. Bahr. Technology for the design of high temperature rise combustors. *AIAA J. Prop. Power*, 3(2):179–186, 1987.
- [11] H. C. Mongia. TAPS - A 4<sup>th</sup> generation propulsion combustor technology for low emissions. AIAA Paper 2003-2657, 2003.
- [12] L. Spadaccini and J. TeVelde. Autoignition characteristics of aircraft type fuels. *Comb. Flame*, 46:283–300, 1982.

- [13] J. Fritz, M. Kröner, and T. Sattelmayer. Flashback in a swirl burner with cylindrical premixing zone. ASME Paper GT2001-0054, 2001.
- [14] M. P. Boyce. *Gas Turbine Engineering Handbook*. Butterworth-Heinemann, 4<sup>th</sup> edition, 2012.
- [15] M. C. Heath, R. Y. Hicks, R. C. Anderson, and R. J. Locke. Optical characterization of a multipoint lean direct injector for gas turbine combustors: Velocity and fuel drop size measurements. ASME Paper GT2010-22960, 2010.
- [16] R. Tacina, C. Wey, P. Laing, and A. Mansour. Sector tests of a low-  $\text{NO}_x$ , lean direct injection, multipoint integrated module combustor concept. ASME Paper GT-2002-30089, 2002.
- [17] L. Khezzar. Velocity measurement in the near field of a radial swirler. *Exp. Thermal Fluid Sci.*, 16:230–236, 1998.
- [18] A. K. Gupta, D. G. Lilley, and N. Syred. *Swirl Flow*. Abacus Press, 1984.
- [19] J. M. Beer and N. Chigier. *Combustion Aerodynamics*. Applied Science Publishers, 1972.
- [20] N. Syred and M. Beer. Combustion in swirling flow: A review. *Comb. Flame*, 23:143–201, 1974.
- [21] H. S. Al-Kabie. *Radial Swirler for Low Emissions Gas Turbine Combustion*. PhD thesis, Univ. of Leeds, 1989.
- [22] K. O. Smith, F. R. Kurzynske, and L. C. Angello. Experimental evaluation of fuel injection configurations for a lean-premixed low  $\text{NO}_x$  gas turbine combustor. ASME Paper GT1987-0141, 1987.
- [23] L. H. Cowell and K. O. Smith. Development of a liquid-fueled lean-premixed gas turbine combustor. *J. Eng. Gas Turb. Power*, 115:55462, 1993.
- [24] S. Etemad and B. C. Forbes. CFD modeling of a gas turbine combustor air swirler effect, computational fluid dynamics in aero-propulsion. In *Proceedings of the ASME international mechanical engineering congress and exposition*, 1995.
- [25] S. Wang, V. Yang, G. Hsiao, and H. Mongia. Large eddy simulation of gas turbine swirl injector flow dynamics. *J. Fluid Mech.*, 583:99–122, 2007.
- [26] K. Merkle, H. Haessler, H. Buchner, and N. Zarzalis. Effect of co- and counter-swirl on the isothermal flow- and mixture-field of an airblast atomizer nozzle. *Int. J. Heat Fluid Flow*, 24:529–537, 2003.
- [27] G. Li and E. J. Gutmark. Effect of swirler configurations on flow structures and combustion characteristics. ASME Paper GT2004-53674, 2004.
- [28] T. C. Claypole and N. Syred. The effect of swirl burner aerodynamic on  $\text{NO}_x$  formation. 18<sup>th</sup> *Symposium on Combustion*. The Combustion Institute, 1981.

- [29] H. S. Al-Kabie and G. E. Andrews. An ultra low  $\text{NO}_x$  pilot combustor for staged low  $\text{NO}_x$  combustion. 1993-7020. ISABE, 1993.
- [30] H. S. Al-Kabie and G. E. Andrews. Ultra low  $\text{NO}_x$  emissions for gas and liquid fuels using radial swirlers. ASME Paper 89-GT-322, 1989.
- [31] H. S. Al-Kabie, G. E. Andrews, and N. T. Ahmad. Lean low  $\text{NO}_x$  primary zones using radial swirlers. ASME Paper 88-GT-245, 1988.
- [32] G. E. Andrews, Escott N. H., Al-Shaikhly A. F. A., and Al-Kabie H. S. Counter-rotating radial swirlers for low  $\text{NO}_x$  emissions with passage fuel injection. 95-7113. ISABE, 1995.
- [33] D. N. Anderson. Ultra lean combustion at high inlet temperatures. ASME 81-GT-44, 1981.
- [34] S. W. Shaffer and G. S. Samuelsen. A liquid fueled, lean burn, gas turbine combustor injector. *Comb. Sci. Tech.*, 139:41–47, 1998.
- [35] T. Terasaki and S. Hayashi. Lean non-premixed combustion for low- $\text{NO}_x$  gas turbine combustor. Yokohama International Gas Turbine Congress, 1995.
- [36] R. Tacina. Low  $\text{NO}_x$  potential of gas turbine engines. AIAA Paper 90-0550, 1990.
- [37] U. S. Hussain, G. E. Andrews, W. G. Cheung, and A. R. Shahabadi. Low  $\text{NO}_x$  primary zones using jet mixing shear layer combustion. ASME Paper 88-GT-308, 1988.
- [38] A.S. Novick and D. L. Troth. Low  $\text{NO}_x$  heavy fuel combustor concept. Technical Report CR-165367, NASA, 1981.
- [39] H. G. Lew, D. R. Carl, G. Vermes, and E. A. DeZubay. Low  $\text{NO}_x$  heavy fuel combustor concept program. phase 1: Combustion technology generation. Technical Report CR-165482, NASA, 1981.
- [40] T. J. Rosfjord. Evaluation of synthetic fuel character effects on rich-lean stationary gas turbine combustion systems. Vol. 1: Subscale test program. Technical Report AP-2822, Electric Power Research Institute, Feb. 1981.
- [41] D. F. Schultz and G. Wolfbrandt. Flame tube parametric studies for control of fuel bound nitrogen using rich-lean two stage combustion. Technical Report TM-81472, NASA, 1980.
- [42] L. H. Nguyen and D. A. Bittker. Investigation of low  $\text{NO}_x$  staged combustor concept in high-speed civil transport engines. Technical Report TM 101977, NASA, 1989.
- [43] R. Tacina, C. Wey, P. Laing, and A. Mansour. A low  $\text{NO}_x$  lean-direct injection, multipoint integrated module combustor concept for advanced aircraft gas turbines. Technical Report NASA/TM2002-211347, NASA, 2002.

- [44] R. Tacina, C. P. Mao, and C. Wey. Experimental investigation of a multiplex fuel injector module with discrete jet swirlers for low emission combustors. Technical Report NASA/TM2004-212918, NASA, 2004.
- [45] R. Tacina, C.-P. Mao, and C.-M. Wey. Experimental investigation of a multiplex fuel injector module for low emission combustors. AIAA Paper 20030827, 2003.
- [46] C. J. Marek, T. D. Smith, and K. Kundu. Low emission hydrogen combustors for gas turbines using lean direct injection. AIAA Paper 2005-3776, 2005.
- [47] J. Cai, S.-M. Jeng, and R. Tacina. The structure of a swirl-stabilized reacting spray issued from an axial swirler. AIAA-2005-1424. 43rd AIAA Aerospace Sciences Meeting and Exhibit, 2005.
- [48] Y. R. Hicks, C. M. Heath, R. C. Anderson, and K. M. Tacina. Investigations of a combustor using a 9-point swirl-venturi fuel injector: Recent experimental results. ISABE-2011-1106. ISABE, 2011.
- [49] N. Patel and S. Menon. Simulation of spray-turbulence-flame interactions in a lean direct injection combustor. *Comb. Flame*, 153:228–257, 2008.
- [50] N.-S. Liu, T.-H. Shih, and T. Wey. Comprehensive combustion modeling and simulation: Recent progress at NASA Glenn Research Center. ISABE-2007-1268. ISABE, 2007.
- [51] F. Davoudzadeh, N.-S. Liu, and J. P. Moder. Investigation of swirling air flows generated by axial swirlers in a flame tube. ASME Paper GT2006-91300, 2006.
- [52] D. Dewanji, A. G. Rao, M. Pourquie, and J. P. van Buijtenen. Investigation of flow characteristics in lean direct injection combustors. *AIAA J. Prop. Power*, 28(1):181–196, 2012.
- [53] D. Dewanji, A. G. Rao, M. Pourquie, and J. P. van Buijtenen. Numerical study of non-reacting and reacting flow characteristics in a lean direct injection combustor. ASME Paper GT2011-45263, 2011.
- [54] D. Dewanji, A. G. Rao, M. Pourquie, and J. P. van Buijtenen. Numerical investigation of reacting spray in a lean direct injection combustor. 2011-1104. ISABE, 2011.
- [55] D. Dewanji, A. G. Rao, M. Pourquie, and J. P. van Buijtenen. Numerical investigation of multiphase flow in the single-element and multi-point lean direct injection combustors. pages 55–56. COMBURA, 2011.
- [56] D. Dewanji, A. G. Rao, M. Pourquie, and J. P. van Buijtenen. Simulation of reacting spray in a multi-point lean direct injection combustor. AIAA Paper 2012-4324, 2012.
- [57] N.-S. Liu. Assessment and improvement of engineering simulation for multi-phase turbulent combustion in a lean direct injection combustor. ISABE-2011-1108. ISABE, 2011.
- [58] F. A. Williams. *Combustion Theory*. Addison-Wesley Publishing Co., Reading, MA, 2<sup>nd</sup> edition, 1985.

- [59] P. J. O’Rourke. *Collective Drop Effects on Vaporizing Liquid Sprays*. PhD thesis, Princeton University, Princeton, NJ, 1981.
- [60] G. M. Faeth. Evaporation and combustion of sprays. *Prog. Energy Combust. Sci.*, 9:1–76, 1983.
- [61] G. M. Faeth. Current status of droplet and liquid combustion. *Prog. Energy Combust. Sci.*, 3:191–224, 1977.
- [62] C. P. Mao, Y. Wakamatsu, and G. M. Faeth. A simplified model of high pressure spray combustion. 18<sup>th</sup> Symposium (International) on Combustion, The Combustion Institute, Pittsburgh, 1981.
- [63] F. C. Lockwood and A. S. Naguib. The prediction of the fluctuations in the properties of free, round-jet, turbulent, diffusion flames. *Comb. Flame*, 24:109–124, 1975.
- [64] C. P. Mao, G. A. Szekeley, and G. M. Faeth. Evaluation of locally homogeneous flow model of spray combustion. *J. Energy*, 4:78, 1980.
- [65] G. M. Faeth. Spray combustion phenomena. *Symposium (International) on Combustion*, 26:1593–1612, 1996.
- [66] Z. Liu and R. D. Reitz. An analysis of the distortion and breakup mechanisms of high speed liquid drops. *Int. J. Multiphase Flow*, 23(4):631–650, 1997.
- [67] P.-K. Wu, L.-P. Hsiang, and G. M. Faeth. Aerodynamic effects on primary and secondary spray breakup. *1<sup>st</sup> Int. Symposium on Liquid Rocket Combustion Instability*, 1993.
- [68] S. S. Hwang, Z. Liu, and R. D. Reitz. Breakup mechanisms and drag coefficients of high speed vaporizing liquid drops. *Atomization and Sprays*, 6:353–376, 1996.
- [69] A. B. Liu, D. Mather, and R. D. Reitz. Modeling the effects of drop drag and breakup of fuel sprays. SAE Technical Paper 930072, SAE, 1993.
- [70] P. J. O’Rourke and F. V. Bracco. Modeling drop interactions in thick sprays and a comparison with experiments. In *Stratified Charge Automotive Engine*, IMechE. Conference, 1980-9, 1980.
- [71] ANSYS, Inc. *Ansys Fluent 12.0 Theory Guide*, April 2009.
- [72] C. T. Crowe. Modeling turbulence in multiphase flows. *Elsevier Science*, 2:899–913, 1993.
- [73] Z. Yuan and E. E. Michaelides. Turbulence modulation in particulate flows - A theoretical approach. *Int. J. Multiphase Flow*, 18:779–785, 1992.
- [74] C. T. Crowe, J. N. Chung, and T. R. Trout. Particle mixing in free shear flows. *Prog. Energy Combustion. Sci.*, 14:171–194, 1988.
- [75] N. Ashgriz and P. Givi. Binary collision dynamics of fuel droplets. *Int. J. Heat Fluid Flow*, 8:205–210, 1987.

- [76] N. Ashgriz and J. Y. Poo. Coalescence and separation in binary collisions of liquid drops. *J. Fluid Mech.*, 221:183–204, 1990.
- [77] Y. J. Jiang, A. Umemura, and C. K. LAW. An experimental investigation on the collision behaviour of hydrocarbon droplets. *J. Fluid Mech.*, 234:171–190, 1992.
- [78] A. A. Amsden, P. J. O’Rourke, and T. D. Butler. KIVA-II - A computer program for chemically reactive flows with sprays. Technical Report LA-11560-MS, Los Alamos National Labs, 1989.
- [79] C. K. Law. Recent advances in droplet vaporization and combustion. *Prog. Energy Combust. Sci.*, 8:171–201, 1982.
- [80] W. E. Ranz and W. R. Marshall. Evaporation from drops. *Chem. Eng. Prog.*, 48:141–146, 1952.
- [81] S. M. Frolov, V. S. Posvianskii, and V. Ya. Basevich. Evaporation and combustion of hydrocarbon fuel. Part I: Nonempirical model of single-component drop evaporation. *Adv. Chem. Phys.*, 21:58–67, 2002.
- [82] A. H. Lefebvre. Fuel effects on gas turbine combustion-Ignition, stability and combustion efficiency. *ASME J. Eng. Gas Turbine and Power*, 107:24–37, 1985.
- [83] A. Radcliffe. Fuel injection in high speed aerodynamics and jet propulsion. Technical Report XIX, Princeton University Press, Princeton, N.J, 1960.
- [84] A. K. Jasuja. Atomization of crude and residual fuel oils. *ASME J. Eng. Power*, 100.2:250–258, 1979.
- [85] J. B. Kennedy. High Weber number SMD correlations for pressure atomizers. ASME Paper 85-GT-37, 1985.
- [86] A. H. Lefebvre. The prediction of sauter mean diameter for simplex pressure-swirl atomizers. *Atomization and Spray Tech.*, 3:37–51, 1987.
- [87] X. F. Wang and A. H. Lefebvre. Mean drop sizes from pressure-swirl nozzles. *AIAA J. Propul. Power*, 3(1):11–18, 1987.
- [88] E. Giffen and A. Muraszew. *The Atomization of Liquid Fuels*. John Wiley and Sons, New York, 1953.
- [89] M. Suyari and A. H. Lefebvre. Film thickness measurements in a simplex swirl atomizer. *AIAA J. Prop. Power*, 2:528–533, 1986.
- [90] H. C. Simmons and C. E. Harding. Some effects on using water as a test fluid in fuel nozzle spray analysis. ASME Paper 80-GT-90, 1980.
- [91] A. H. Lefebvre. Properties of sprays. *Part. Part. Syst. Charact.*, 6:176–186, 1989.
- [92] G. E. Lorenzetto and A. H. Lefebvre. Measurements of drop size on a plain jet airblast atomizer. *AIAA J.*, 15:1006–1010, 1977.

- [93] A. K. Jasuja. Plain-jet airblast atomization of alternative liquid petroleum fuels under high ambient air pressure conditions. ASME Paper 82-GT-32, 1982.
- [94] N. K. Rizk and A. H. Lefebvre. Spray characteristics of plain-jet airblast atomizers. *ASME J. Eng. Gas Turbine and Power*, 106:639–644, 1984.
- [95] M. S. M. R. El-Shanaway and A. H. Lefebvre. Airblast atomization: The effect of linear scale on mean drop size. *J. Energy*, 4:184–189, 1980.
- [96] S. Nukiyama and Y. Tanasawa. Experiments on the atomization of liquids in an airstream. *Trans. SOC. Mech. Eng. Jpn.*, 5:68–75, 1939.
- [97] P. Rosin and E. Rammler. The laws governing the fineness of powdered coal. *J. Inst. Fuel*, 31:29–36, 1933.
- [98] N. K. Rizk and A. H. Lefebvre. Drop-size distribution characteristics of spill-return atomizers. *AIAA J. Propul. Power*, 1:16–22, 1985.
- [99] J. R. Custer and N. K. Rizk. Effect of design concept and liquid properties on fuel injector performance. *AIAA J. Propul. Power*, 4(4):378–384, 1988.
- [100] N. K. Rizk and H. C. Mongia. Calculation approach validation for airblast atomizers. *ASME J. Eng. Gas Turbine and Power*, 114:386–394, 1992.
- [101] N. K. Rizk and H. C. Mongia. Performance of hybrid airblast atomizers under low power conditions. AIAA Paper 1992-0463, 1992.
- [102] A. H. Lefebvre. *Atomization and Sprays*. Hemisphere Publishing Corporation, 1989.
- [103] N. K. Rizk and A. H. Lefebvre. Prediction of velocity coefficient and spray cone angle for simplex swirl atomizers. In *Proc. 3<sup>rd</sup> Int. Conf. Liquid Atomization and Spray Systems*, 111C/2/1-16, 1985.
- [104] J. Ortman and A. H. Lefebvre. Fuel distributions from pressure-swirl atomizers. *AIAA J. Propul. Power*, 1(1):11–15, 1985.
- [105] A. H. Lefebvre. Factors controlling gas turbine combustion performance at high pressures. *Cranfield International Symposium Series*, 10:211–226, 1968.
- [106] A. E. German and T. Mahmud. Modelling of non-premixed swirl burner flows using a Reynolds-stress turbulence closure vol. 84, 2005, pp. 583–594. *Fuel*, 84:583–594, 2005.
- [107] S. Undapalli, S. Srinivasan, and S. Menon. LES of premixed and non-premixed combustion in a stagnation point reverse flow combustor. *Proceedings of the Combustion Institute*, 32(1):1537–1544, 2009.
- [108] Shis T-H., W. W. Liou, A. Shabbir, Z. Yang, and J. Zhu. A new  $\kappa - \varepsilon$  eddy viscosity model for high reynolds number turbulent flows-model development and validation. *Computers & Fluids*, 24(3):227–238, 1995.
- [109] J. O. Hinze. *Turbulence*. McGraw-Hill Publishing Co., New York, 1975.

- [110] F. S. Lien and M. A. Leschziner. Assessment of turbulent transport models including non-linear RNG eddy viscosity formation and second-moment closure. *Computers & Fluids*, 23(8):893–1004, 1994.
- [111] M. M. Gibson and B. E. Launder. Ground effects on pressure fluctuations in the atmospheric boundary layers. *J. Fluid Mech.*, 86:491–511, 1978.
- [112] S. Fu, B. E. Launder, and M. A. Leschziner. Modeling strongly swirling recirculating jet flow with Reynolds-stress transport closures. 6<sup>th</sup> Symposium on Turbulent Shear Flows, 1987.
- [113] B. E. Launder. Second-moment closures and its use in modeling turbulent industrial flows. *Int. J. Numerical Methods in Fluids*, 9:963–985, 1989.
- [114] B. E. Launder, G. J. Reece, and W. Rodi. Progress in the development of a Reynolds-stress turbulence closure. *J. Fluid Mech.*, 68:537–566, 1975.
- [115] J. Smagorinsky. General circulation experiments with the primitive equations. I. The basic experiment. *AMS J.*, 91:99–164, 1963.
- [116] S-E. Kim. Large eddy simulation using unstructured meshes and dynamic subgrid-scale turbulence models. AIAA-2004-2548. Fluid Dynamics Conference and Exhibit, June 2004.
- [117] A. J. Chorin. Numerical solution of Navier-Stokes equations. *Math. Computation*, 22:745–762, 1968.
- [118] T. J. Barth and D. Jespersen. The design and application of upwind schemes on unstructured meshes. technical report , , 1989. Technical Report AIAA-89-0366, AIAA 27<sup>th</sup> Aerospace Sciences Meeting, Reno, Nevada, 1989.
- [119] H. P. Trinh and C. P. Chen. Modeling of turbulence effects on liquid jet atomization & breakup. AIAA-2005-0154. 43rd AIAA Aerospace Sciences Meeting and Exhibit, 2005.
- [120] G. M. Faeth. Mixing, transport and combustion in sprays. *Prog. Energy Combust. Sci.*, 13:293–345, 1987.
- [121] W. Feller. *An Introduction to Probability Theory and its Applications*, volume 1. Wiley, 3<sup>rd</sup> edition, 1968.
- [122] D. P. Schmidt, I. Nouar, P. K. Senecal, C. J. Rutland, J. K. Martin, and R. D. Reitz. Pressure-swirl atomization in the near field. SAE Paper 01-0496. SAE, 1999.
- [123] P. K. Senecal, D. P. Schmidt, I. Nouar, C. J. Rutland, and M.L. Corradini R. D. Reitz. Modeling high-speed viscous liquid sheet atomization. *Int. J. Multiphase Flow*, 25:1073–1097, 1999.
- [124] Z. Han, S. Perrish, P. V. Farrell, and R. D. Reitz. Modeling atomization processes of pressure-swirl hollow-cone fuel sprays. *Atomization and Sprays*, 7(6):663–684, 1997.

- [125] H. B. Squire. Investigation of the instability of a moving liquid film. *British J. Applied Physics*, 4:167–169, 1953.
- [126] W. W. Hagerty and J. F. Shea. A study of the stability of plane fluid sheets. *J. Appl. Mech.*, 22:509–514, 1955.
- [127] P. K. Senecal, D. P. Schmidt, I. Nouar, C. J. Rutland, R. D. Reitz, and M. L. Corradini. Modeling high-speed viscous liquid sheet atomization. *Int. J. Multiphase Flow*, 25:1073–1097, 1999.
- [128] R. D. Reitz and F. V. Bracco. Mechanism of atomization of a liquid jet. *Phys. Fluids*, 25:1730–1742, 1982.
- [129] N. Dombrowski and P. C. Hooper. The effect of ambient density on drop formation in sprays. *Chem. Eng. Sci.*, 17:291–305, 1962.
- [130] N. Dombrowski and W. R. Johns. The aerodynamic instability and disintegration of viscous liquid sheets. *Chem. Eng. Sci.*, 18:203–214, 1963.
- [131] P. J. O’Rourke and A. A. Amsden. The TAB method for numerical calculation of spray droplet breakup. SAE Paper 872089. SAE, 1987.
- [132] E. A. Ibrahim, H. Q. Yang, and A. J. Przekwas. Modeling of spray droplets deformation and breakup. *AIAA J. Propul. Power*, 9:651–654, 1993.
- [133] G. I. Taylor. The shape and acceleration of a drop in a high speed air stream. Technical Report, Scientific papers of G. I. Taylor, 1963.
- [134] R. D. Reitz. Modeling atomization processes in high-pressure vaporizing sprays. *Atomization and Spray Tech.*, 3:309–337, 1987.
- [135] M. A. Patterson and R.D. Reitz. Modeling the effects of fuel spray characteristics on diesel engine combustion and emission. SAE Paper 980131. SAE, 1998.
- [136] J. M. Maclnnes and F. V. Bracco. Comparisons of deterministic and stochastic computations of drop collisions in dense sprays. *AIAA Prog. Astronautics and Aeronautics*, 135:615–642, 1991.
- [137] Y. R. Sivathanu and G. M. Faeth. Generalized state relationships for scalar properties in non-premixed hydrocarbon/air flames. *Comb. Flame*, 82:211–230, 1990.
- [138] W. P. Jones and J. H. Whitelaw. Calculation methods for reacting turbulent flows: A review. *Comb. Flame*, 48:1–26, 1982.
- [139] D. Dewanji, A. G. Rao, M. Pourquie, and J. P. van Buijtenen. Study of swirling air flow characteristics in a lean direct injection combustor. ASME Paper GT2010-22602, 2010.
- [140] O. Lucca-Nergo and T. O’Doherty. Vortex breakdown: A review. *Prog. Energy Combust. Sci.*, 27(4):431–481, 2001.

- 
- [141] J. Cai, S.-M. Jeng, and R. Tacina. Multi-swirler aerodynamics: Comparison of different configurations. ASME Paper GT2002-30464, 2002.
- [142] G. Haller. An objective definition of a vortex. *J. Fluid Mech.*, 525:1–26, 2005.

## Appendix A. Code for Calculating Drop Mean Diameters

```
% Once the spray simulation is converged, this UDF file is compiled and hooked
% up to calculate the mean diameters such as D10 and D32 for all liquid drops
% passing through a computational cell.
%
% A number of iterations are run to obtain many sampling particles.

#include "udf.h"
#include "surf.h"
#include "dpm.h"

static int counter=0;

DEFINE_ADJUST(adjust_spray, d)
{
  Thread *t;
  cell_t c;

  if (counter==0)
  {counter=1;
  thread_loop_c (t,d)
  {
    begin_c_loop (c,t)
    {
      C_UDMI(c,t,0)=0.0;
      C_UDMI(c,t,1)=0.0;
      C_UDMI(c,t,2)=0.0;
      C_UDMI(c,t,3)=0.0;
      C_UDMI(c,t,4)=0.0;
      C_UDMI(c,t,5)=0.0;
    }
    end_c_loop (c,t)
  }
}
```

```
thread_loop_c (t,d)
{
begin_c_loop (c,t)
{
C_UDMI(c,t,6) = C_UDMI(c,t,1)/MAX(C_UDMI(c,t,0),DPM_SMALL);
C_UDMI(c,t,7) = sqrt(C_UDMI(c,t,2)/MAX(C_UDMI(c,t,0),DPM_SMALL));
C_UDMI(c,t,8) = pow(C_UDMI(c,t,3)/MAX(C_UDMI(c,t,0),DPM_SMALL),0.333333);
C_UDMI(c,t,9) = C_UDMI(c,t,3)/MAX(C_UDMI(c,t,2),DPM_SMALL);
}
end_c_loop (c,t)
}
}

DEFINE_DPM_BODY_FORCE(body_force_spray, p, i)
{
Thread *t;
cell_t c;
real num_p, dia;

c = P_CELL(p);
t = P_CELL_THREAD(p);
if(P_USER_REAL(p,0) != (float) c)
{num_p = p->number_in_parcel;
dia = p->state.diam;
C_UDMI(c,t,0) += num_p;
C_UDMI(c,t,1) += num_p * dia;
C_UDMI(c,t,2) += num_p * dia * dia;
C_UDMI(c,t,3) += num_p * dia * dia * dia;
C_UDMI(c,t,4) += num_p * dia * dia * dia * dia;
C_UDMI(c,t,5) += 1;
P_USER_REAL(p,0)=(float) c;}

return 0.0;
}
```

## Appendix B. Code for Computing Drop Velocity Distributions

```
% This UDF code samples the size and velocity of discrete-phase particles
% (liquid drops) at selected planes downstream of the liquid injection.

% The liquid drops are sampled at planes corresponding to constant streamwise
% locations (x).

% The UDF code is compiled and hooked up in the GUI.

#include "udf.h"

#define REMOVE_PARTICLES FALSE

DEFINE_DPM_OUTPUT(Discrete_phase_sample,header,fp,p,t,plane)
{
  real flow_time = solver_par.flow_time;
  real r, y, z;

  if(header)
    par_fprintf_head(fp," #Time[s] R [m] Y[m] Z[m] x-velocity[m/s] y-velocity[m/s]
z-velocity[m/s] Drop Diameter[m] Number of Drops Temperature [K] Initial Diam
[m] Injection Time [s] \n");

  if(NULLP(p))
    return;

  y = p->state.pos[1];
  z = p->state.pos[2];
  r = sqrt(SQR(y) + SQR(z));

  #if PARALLEL
  par_fprintf(fp,"%d %d %e %f %f %f %f %f %f %e %e %f %e %f \n",
p->injection->try_id, p->part_id, P_TIME(p), r,y,z,p->state.V[0],
```

```
p->state.V[1],p->state.V[2],P_DIAM(p),p->number_in_parcel,P_T(p),
P_INIT_DIAM(p), p->time_of_birth);
#else
par_fprintf(fp,"%e %f %f %f %f %f %f %e %e %f %e %f \n",
P_TIME(p), r,y,z,p->state.V[0],p->state.V[1],p->state.V[2],P_DIAM(p),
p->number_in_parcel,P_T(p), P_INIT_DIAM(p), p->time_of_birth);
#endif

#endif

#if REMOVE_PARCELS
p->stream_index=-1;
#endif
}
```

## Acknowledgements

It’s been quite a journey so far! I am extremely grateful to many people who supported me over the years and I sure would try my best to mention everyone to whom I owe a debt of gratitude.

First and foremost, I offer my sincerest gratitude to my promotor and principal supervisor, Prof. Jos P. van Buijtenen. This dissertation would not have been possible without your encouragement, support and patience, not to mention your advice and unparalleled knowledge that gave it a nudge in the right direction. The excellent guidance and friendship of my daily supervisor, Dr. Arvind Rao, have been priceless on both an academic and a personal level, for which I am extremely thankful. I also would like to thank Dr. Arvind for spending countless hours with me to discuss on several practical issues beyond the textbooks and for patiently correcting my articles.

I am most grateful to my advisor, Dr. Mathieu Pourquie, for his excellent guidance and support, helping me to overcome some tough hurdles that I confronted while conducting this research. In addition to his invaluable technical inputs, Dr. Mathieu was kind enough to allow me to use the high performance cluster machines and the Fluent licenses of his department over the entire period of my PhD research. There is no denying the fact that without this computational support, it would not have been possible to study the complex cases. Dr. Mathieu, I also appreciate your taking the time to read and correct my thesis and the scientific papers.

I wish to thank Prof. Dirk Roekaerts for giving a very informative and insightful course entitled: ‘Turbulent Reacting Flows’, which helped me enormously to develop my background in computational methods for turbulent combustion.

I would like to acknowledge the financial, academic, and technical support of the Delft University of Technology and CleanEra. In fact, this research was performed within the framework of CleanEra. The group not only provided me with an excellent atmosphere for doing my research, but it also introduced me a bunch of wonderful friends. Thank you Ronald, Francois, Durk, Marcel, Michiel, Marios, Hui, Farid, Chara, Gustavo, and Sonell for your continuous encouragement and very valuable advice, which helped me to complete this dissertation.

I am particularly indebted to Lin Pijpaert, Michiel Haanschoten, Bettie Ratuhaling, and Gemma van der Windt for all the matters that kept my research going.

Special thanks go to my past officemate, Maarten Foeken. You were very pleasant to work with since the very first day I met you, although our research areas were very

different from each other. I will always remember your willingness to help me during my time of need and I consider myself extremely fortunate to have met someone like you.

I wish to sincerely thank my current officemates, Haiqiang Wang and Peijian Lv, for their encouragement and friendship. You made the last year of my PhD a memorable one. I am also grateful to my housemate and colleague Li Mo for his measureless support. Peijian, Li and Haiqiang, you were the ones who graciously helped me when I was seriously down, for which I am extremely grateful to all of you.

My sincere and special thanks go to Jan Vriend, Feijia Yin, and Wim van Hoydonck for always being helpful, kind, and supportive.

I am especially grateful to my friend, Muhammad Iftikhar Faraz, for several reasons. More importantly, you were always there when I needed your help and you never left my side. Your friendship means a lot to me.

Thank you dear Gerry and Ben van der Walt for comforting me when I badly needed it. I shall never forget your kindness as long as I live.

I save the words of deepest gratitude to those who have given me their unequivocal support throughout. My dear father Milan, the person who I am today is someone you molded. You ensured I had everything I needed to succeed in my life, even in trying times. You made a special effort to make sure everything was there. I had to work hard, but I knew that I had your strong support. Dad, you had been like a roof over my head for so many years. My biggest pain was when you unfortunately left me just three months prior to my PhD defense day. Life has been very tough since you left me. However, I hope that you are around somewhere watching my success and I am sure you would be very proud of your dear son. My dear mother Krishna, you are my inspiration in many ways. I am eternally grateful to you for your love, affection, encouragement, and support. I also thank you for the wisdom that you pass down to me. Thanks very much, my dear brother Sunny, for always being supportive and proud of your brother. Many thanks go to my grandmother, Puspa, who is like my mother with extra frosting. To me, you are a delightful blend of laughter, caring deeds, wonderful stories and love. Special thanks go to my uncle, late Subodh Chowdhury, for introducing me the wonderful world of mathematics and teaching me several interesting tricks to solve many complex problems when I was in junior high school.

Last, but by no means least, I owe my sincere gratitude to my beloved wife Pia for always standing by me through the good and bad times. Your constant support, incredible patience, and care made these last few years a whole lot easier. I cannot thank you enough for that.

# Publications

## Publications related to this thesis

*D. Dewanji, A. G. Rao, M. Pourquie, and J. P. van Buijtenen.* Simulation of reacting spray in a multi-point lean direct injection combustor. 48<sup>th</sup> AIAA/ASME/SAE/ASEE Joint Propulsion Conference and Exhibit, AIAA-2012-4324, Atlanta, USA, 2012.

*D. Dewanji, A. G. Rao, M. Pourquie, and J. P. van Buijtenen.* Reacting flow characteristics in lean direct injection combustors. Submitted to AIAA J. Prop. Power, 2012.

*D. Dewanji, A. G. Rao, M. Pourquie, and J. P. van Buijtenen.* Investigation of flow characteristics in lean direct injection combustors. AIAA J. Prop. Power, 28(1):181196, 2012.

*D. Dewanji, A. G. Rao, M. Pourquie, and J. P. van Buijtenen.* Numerical investigation of multiphase flow in the single-element and multi-point lean direct injection combustors. COMBURA-11, pages 55-56, Ede, The Netherlands, 2011.

*D. Dewanji, A. G. Rao, M. Pourquie, and J. P. van Buijtenen.* Numerical investigation of reacting spray in a lean direct injection combustor. 2011-1104. ISABE, Gothenberg, Sweden, 2011.

*D. Dewanji, A. G. Rao, M. Pourquie, and J. P. van Buijtenen.* Numerical study of non-reacting and reacting flow characteristics in a lean direct injection combustor. Proceedings of ASME Turbo Expo 2011: Power for Land, Sea and Air, GT2011-45263, Vancouver, Canada, 2011.

*D. Dewanji, A. G. Rao, M. Pourquie, and J. P. van Buijtenen.* Study of swirling air flow characteristics in a lean direct injection combustor. Proceedings of ASME Turbo Expo 2010: Power for Land, Sea and Air, GT2010-22602, Glasgow, UK, 2010.

*D. Dewanji, A. G. Rao, and J. P. van Buijtenen.* Conceptual Study of Future Aero-engine Concepts. International Journal of Turbo and Jet Engines, Vol. 26(4):263-276, 2009.

*D. Dewanji, A. G. Rao, and J. P. van Buijtenen.* Feasibility Study of Some Novel Concepts for High Bypass Ratio Turbofan Engines. Proceedings of ASME Turbo Expo 2009: Power for Land, Sea and Air, GT2009-59166, Orlando, USA, 2009.

## Other publications

*D. Dewanji*, T. S. D. OMahoney, and A. Twerda. Numerical Investigation of Particle Deposition in Oscillatory Baffled Reactors. 23<sup>rd</sup> International Symposium on Transport Phenomena, Auckland, New Zealand, 2012.

## The Author

Dipanjay Dewanji was born on 5<sup>th</sup> of November in Calcutta, India. After finishing his studies from high school, he started his Aeronautical Engineering studies, which he completed in June 2003 and obtained a Bachelor of Engineering degree. During the bachelor course, he was specialized in aerospace propulsion. In August of the same year, he joined the Engine Division of Hindustan Aeronautics Limited in Bangalore as a graduate trainee. He was primarily involved in reverse engineering studies for various turbofan and turbojet engines used in combat aircrafts. In July 2004, he started his master studies in Rocket Propulsion from Birla Institute of Technology, India. The title of his master project is “Regression rate studies of paraffin wax fuel in a hybrid propulsion system”. For this project, he built a small-scale hybrid rocket motor and ‘fired’ it by using paraffin wax-gaseous oxygen hybrid propellant combination. In June 2006, he received his Master of Engineering degree with distinction.

In November 2006, Dipanjay was assigned as a methods engineer for Snecma HAL Aerospace Private Limited. A year later, he joined ESI Group as an application engineer for welding and heat treatment related applications. He worked in this company for one and half year and during this tenure he was assigned to work in Bangalore, Lyon, and Munich. While working at ESI Group, he was offered a PhD position in the faculty of Aerospace Engineering, TU Delft. In May 2008, he moved to Delft to pursue his PhD research. After submitting his draft thesis in February 2012, he joined the fluid dynamics department of TNO as a research scientist.

